

AWARD NUMBER: **W81XWH-12-1-0282**

TITLE: Monoamine Oxidase A: A Novel Target for Progression and Metastasis of Prostate Cancer

PRINCIPAL INVESTIGATOR: **Jean C. Shih, Ph.D.**

CONTRACTING ORGANIZATION: **University of Southern California
Los Angeles, CA 90089-0001**

REPORT DATE: **December 2015**

TYPE OF REPORT: **Final**

PREPARED FOR: U.S. Army Medical Research and Materiel Command
Fort Detrick, Maryland 21702-5012

DISTRIBUTION STATEMENT: Approved for Public Release;
Distribution Unlimited

The views, opinions and/or findings contained in this report are those of the author(s) and should not be construed as an official Department of the Army position, policy or decision unless so designated by other documentation.

REPORT DOCUMENTATION PAGE

Form Approved
OMB No. 0704-0188

Public reporting burden for this collection of information is estimated to average 1 hour per response, including the time for reviewing instructions, searching existing data sources, gathering and maintaining the data needed, and completing and reviewing this collection of information. Send comments regarding this burden estimate or any other aspect of this collection of information, including suggestions for reducing this burden to Department of Defense, Washington Headquarters Services, Directorate for Information Operations and Reports (0704-0188), 1215 Jefferson Davis Highway, Suite 1204, Arlington, VA 22202-4302. Respondents should be aware that notwithstanding any other provision of law, no person shall be subject to any penalty for failing to comply with a collection of information if it does not display a currently valid OMB control number. **PLEASE DO NOT RETURN YOUR FORM TO THE ABOVE ADDRESS.**

1. REPORT DATE December 2015		2. REPORT TYPE Final		3. DATES COVERED 30 SEP 2012 - 29 SEP 2015	
4. TITLE AND SUBTITLE Monoamine Oxidase A: A Novel Target for Progression and Metastasis of Prostate Cancer				5a. CONTRACT NUMBER	
				5b. GRANT NUMBER W81XWH-12-1-0282	
				5c. PROGRAM ELEMENT NUMBER	
6. AUTHOR(S) Dr. Jean C. Shih E-Mail: jcshih@usc.edu				5d. PROJECT NUMBER	
				5e. TASK NUMBER	
				5f. WORK UNIT NUMBER	
7. PERFORMING ORGANIZATION NAME(S) AND ADDRESS(ES) UNIVERSITY OF SOUTHERN CALIFORNIA 3720 S. FLOWER STREET LOS ANGELES, CA 90089-0001				8. PERFORMING ORGANIZATION REPORT NUMBER	
9. SPONSORING / MONITORING AGENCY NAME(S) AND ADDRESS(ES) U.S. Army Medical Research and Materiel Command Fort Detrick, Maryland 21702-5012				10. SPONSOR/MONITOR'S ACRONYM(S)	
12. DISTRIBUTION / AVAILABILITY STATEMENT Approved for Public Release; Distribution Unlimited				11. SPONSOR/MONITOR'S REPORT NUMBER(S)	
13. SUPPLEMENTARY NOTES					
14. ABSTRACT The purpose of this project is to investigate the key roles of the monoamine oxidase A (MAO A) enzyme in the progression and metastasis of prostate cancer (PCa). During this funding period, we delineated the functional and mechanistic roles of MAO A in promoting tumor metastasis, determined MAO A functions in PCa by defining its roles in reactive oxygen species production and augmentation of HIF1 α -mediated signaling, and developed a MHI-clorgyline, a novel pharmacological inhibitor of MAO A for targeted therapy and noninvasive imaging of PCa. Throughout the Year 3, we investigated the effect of hypoxia on MAO A and found that hypoxia induces MAO A expression and activity. We assessed the tumor-targeting properties of NIR-clorgyline for PCa <i>in vivo</i> and demonstrated its tumor-specificity in mouse xenograft model through NIR (near infrared) imaging. We generated MAO A/Pten double KO mice and showed that deletion of MAO A delays PCa development and facilitates an immunostimulatory environment in the Pten KO mouse model of prostate adenocarcinoma.					
15. SUBJECT TERMS Monoamine oxidase, prostate cancer, targeted therapy					
16. SECURITY CLASSIFICATION OF:			17. LIMITATION OF ABSTRACT Unclassified	18. NUMBER OF PAGES 105	19a. NAME OF RESPONSIBLE PERSON USAMRMC
a. REPORT Unclassified	b. ABSTRACT Unclassified	c. THIS PAGE Unclassified			19b. TELEPHONE NUMBER (include area code)

Table of Contents

	<u>Page</u>
1. Introduction	2
2. Keywords	2
3. Accomplishments	2
4. Impact	22
5. Changes/Problems	23
6. Products	23
7. Participants and Other Collaborating Organizations	27
8. Special Reporting Requirements	27
9. Appendices	27

- 1. INTRODUCTION: Monoamine Oxidase A (MAOA)**, the subject of the present study, is a mitochondria-bound enzyme that oxidatively deaminates monoamine neurotransmitters and dietary amines and produces hydrogen peroxide, a major source of reactive oxygen species (ROS).¹⁻² ROS causes DNA damage and tumor initiation.³⁻⁵ **The purpose of this research** is 1) to seek fundamental mechanistic insights on the functional roles of MAOA in human prostate cancer (PCa) progression and metastasis, and 2) to design and develop novel and effective tumor-specific pharmacological inhibitor of MAOA and to determine its effect on PCa tumor growth and metastasis in tumor xenograft mouse models. **The scope of this research** involves experiments and assays to study the role of MAOA in PCa progression and metastasis *in vitro* [LNCaP (androgen-sensitive) and C4-2B (derived from LNCaP, androgen-insensitive) and PC-3 (androgen-insensitive) PCa cells] and in mice [tumor growth studies, and tumor metastasis to bone and soft tissues].⁶⁻⁷
- 2. KEYWORDS:** Prostate cancer (PCa), monoamine oxidase A (MAOA), MHI-clorgyline, near-infrared (NIR) emitting compound, novel target, novel therapeutic agent, HIF1 α , reactive oxygen species (ROS), hydrogen peroxide (H₂O₂).
- 3. ACCOMPLISHMENTS:**

The objective of this study is to investigate the functional and mechanistic roles of MAOA in human PCa growth and metastasis, with the focus on epithelial-to-mesenchymal transition (EMT), reactive oxygen species (ROS), hypoxia-inducible factor 1 α (HIF1 α) and biomarkers associated with PCa progression. Furthermore, we designed, synthesized and tested *in vitro* and *in vivo* a novel tumor-specific MAOA inhibitor-near infrared (NIR) dye inhibitor (NIR-MAOA inhibitor), called MHI-clorgyline, with the goal to target and image advanced and metastatic PCa in our animal models. The reported study was conducted by three collaborating labs from two organizations (the Shih lab at USC, the Zhou lab at CSMC, and the Olenyuk lab at USC). **The Shih lab** was responsible for determining MAOA effects on PCa tumor growth and metastasis in tumor xenograft mouse models and assessing the efficacy of NIR-MAOA inhibitor on tumor growth and metastasis in tumor xenograft mouse models. **The Zhou lab** was responsible for generating different genetically manipulated human PCa cell lines and assisting with extensive immunohistochemical (IHC) analysis of tumor specimens with PCa-associated biomarkers for tumor xenograft studies. **The Olenyuk lab** was responsible for chemically synthesizing and characterizing NIR-MAOA inhibitor and assisting with determination of their pharmacological effects on PCa in tumor xenograft models.

The progress for the entire duration of this project in accordance with the detailed task assignments, as presented in SOW, is described below:

Task 1. (Specific Aim 1A): Determination of the effects of MAOA on human prostate tumor growth and metastasis.

- 1a. Establishment, validation and characterization of stable wild-type (WT) and MAOA-knockdown (KD) PCa cells (LNCaP, C4-2 and ARCaP_M) genetically engineered with luciferase (luc) for tumor xenograft studies. Investigator: Haiyen Zhou (CSMC) Months 1-6

- 1b. Prostate tumor growth studies: **orthotopic injection** of WT and MAOA-KD PCa cells into the athymic nude mice, determination of tumor growth post-injection by serial imaging of luciferase bioluminescence, determination of tumor ROS levels at sacrifice, and IHC analysis of tumor specimens post-sacrifice (cell proliferation, EMT and hypoxia markers). Investigators: Haiyen Zhau (CSMC) and Jean Shih (USC) Months 7-12
- 1c. Prostate tumor metastasis studies: **intracardiac injection** of PCa cells into athymic nude mice, determination of tumor bone metastasis status and tumor osteolesion post-injection by serial imaging of luc bioluminescence and X-ray, and IHC analysis of tumor/bone specimens post-sacrifice (osteoclastic, osteoblastic, EMT and hypoxia markers). Investigators: Haiyen Zhau (CSMC) and Jean Shih (USC) Months 7-12
- 1d. Prostate tumor bone metastasis studies: **intratibial injection** of PCa cells into athymic nude mice, determination of tumor growth, tumor bone metastasis status and tumor osteo-lesion post-injection by serial imaging of luc bioluminescence and X-ray, determination of tumor ROS levels at sacrifice, and IHC analysis of tumor/bone specimens post-sacrifice (cell proliferation, osteoclastic, osteoblastic, EMT and hypoxia markers).
WT and MAOA-KD luc-tagged C4-2 and ARCaP_M cells will be used.
Mice have been housed at the USC animal facility.
Investigators: Haiyen Zhau (CSMC) and Jean Shih (USC) Months 13-18

Task 2. (Specific Aim 1B): Investigation of the molecular mechanisms underlying the MAOA functions in PCa by defining its roles in ROS- and HIF1 α -mediated signaling.

- 2a. Investigation of the effect of MAOA on PHD and HIF1 α activity in human PCa cells (LNCaP, C4-2 and ARCaP_M) and the accompanying regulation mediated by ROS generated through the MAOA action. Investigator: Jean Shih (USC) Months 19-27
- 2b. Determination of the effect of hypoxia/HIF1 α on MAOA activity in human PCa cells (LNCaP, C4-2 and ARCaP_M). Investigator: Jean Shih (USC) Months 19-27

Task 3 (Specific Aim 2): Synthesis and characterization of novel near-infrared (NIR) dye-chlorgyline conjugate, and determination of its *in vivo* inhibitory effects on tumor growth and metastasis in tumor xenograft mouse models.

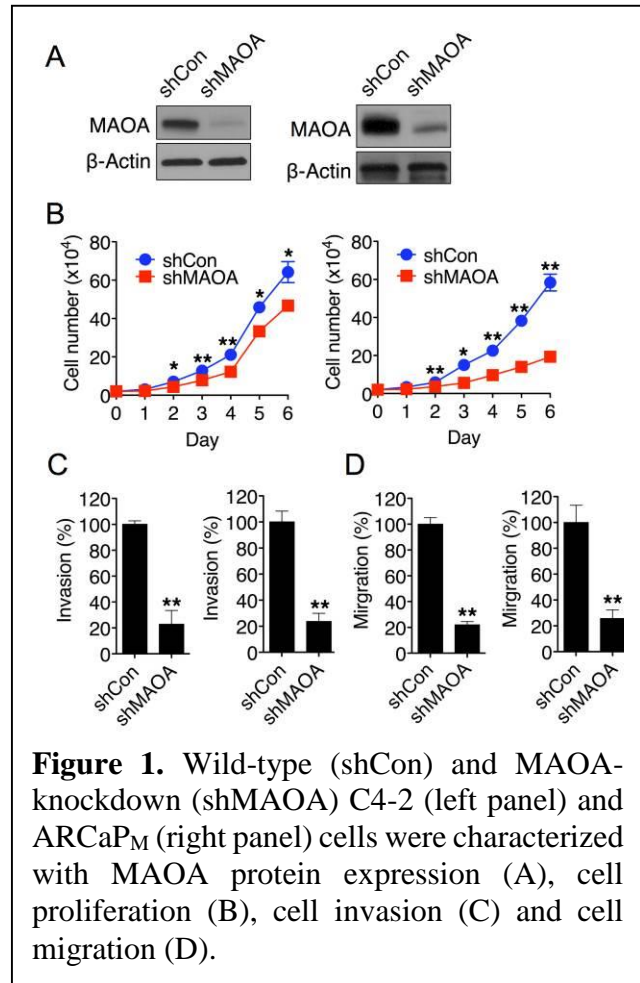
- | | | |
|-----|---|--------------|
| 3a. | Design, synthesis and chemical characterization of NIR-clorgyline.
Investigator: Bogdan Olenyuk (USC) | Months 1-6 |
| 3b. | Determination of MAOA inhibition curves in human PCa cells.
Investigator: Jean Shih (USC) | Months 7-8 |
| 3c. | Determination of the cellular uptake and localization of MAOA inhibitor – NIR dye conjugate (NIR-clorgyline) in human PCa cells.
Investigator: Bogdan Olenyuk (USC) | Months 9-12 |
| 3d. | Determination of the <i>in vivo</i> effect of NIR-clorgyline on prostate tumor metastasis: intracardiac injection of PCa cells into athymic nude mice, assessment of NIR-clorgyline targeting of metastatic tumors by superimposing both images of luc bioluminescence and NIR fluorescence, determination of tumor metastasis status and osteo-lesion post-injection of NIR-clorgyline by serial imaging and X-ray, and IHC analysis of tumor/bone specimen post-sacrifice (e.g. EMT markers)
Luc-tagged WT ARCaP _M cells will be used.
Mice have been housed at the USC animal facility.
Investigator: Bogdan Olenyuk (USC), Haiyen Zhau (CSMC) and Jean Shih (USC) | Months 13-24 |
| 3e. | Determination of the <i>in vivo</i> effect of NIR-clorgyline on prostate tumor growth:
subcutaneous injection of PCa cells into athymic mice, assessment of tumor-targeting of NIR-clorgyline by superimposing both images of luc bioluminescence and NIR fluorescence, determination of tumor growth post-injection of NIR-clorgyline by serial imaging, and IHC analysis of tumor specimens post-sacrifice (e. g. cell proliferation markers).
Luc-tagged WT LNCaP and C4-2 cells will be used.
Mice count: 2 cell lines, 10 mice per cell line, each cell line with 3 treatments: (1) NIR dye, (2) clorgyline, and (3) NIR-clorgyline
Luc-tagged WT ARCaP _M cells will be used.
Mice have been housed at the USC animal facility.
Investigator: Bogdan Olenyuk (USC), Haiyen Zhau (CSMC) and Jean Shih (USC) | Months 24-36 |

Task 3-2: We developed a Pten/MAOA double knockout (DKO) mouse model by combining prostate-specific conditional Pten knockout mice with MAOA knockout mice. We hypothesized that MAOA may act like a tumor promoter in the context of PCa through its induction of ROS and hypoxia. The resulting effect of hypoxia and ROS may result in the immune system suppression, facilitating tumor evasion from detection by the immune system. Thus, we expect that Pten/MAOA DKO mice would show a delayed formation of

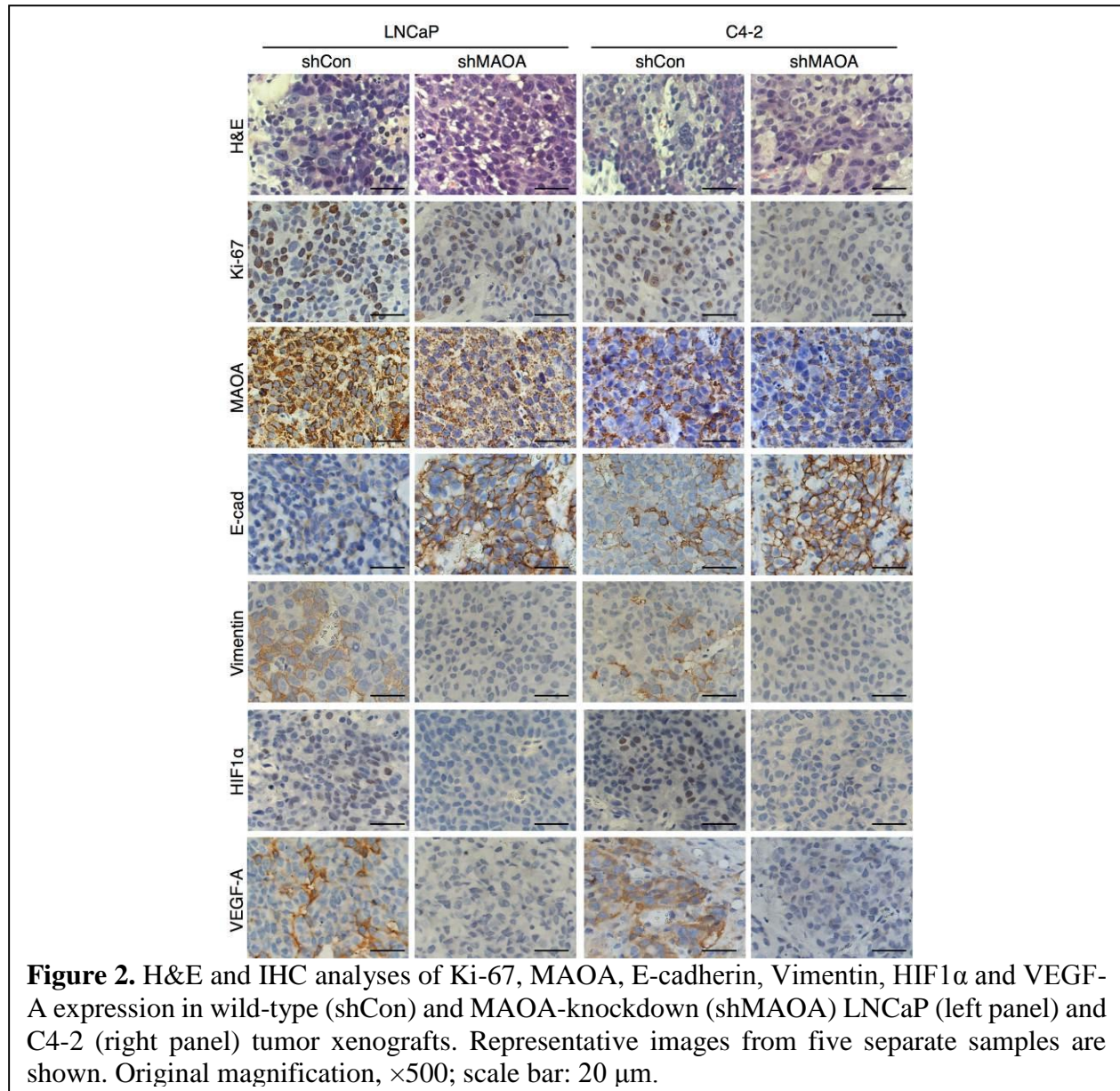
PCa tumors. This animal model will help us better understand MAOA in vivo functions in PCa progression and metastasis.

The detailed report of our progress during the entire period of grant support is outlined below.

Task 1a: We established and characterized stable wild-type and MAOA-knockdown human prostate cancer cells (C4-2 and ARCaP_M) for animal studies. We utilized lentiviral particles that express pGL4 Luciferase Reporter Vectors (Promega) to infect both C4-2 and ARCaP_M cells followed by selection for stable clones with hygromycin. Successful stable engineering of luciferase gene into the genome of these cells was validated by luciferase assay. These luc-labeled cells, when injected into mice, will be visualized by bioluminescence imaging. Next, these cells were infected with lentiviral particles that express specific shRNAs targeting MAOA (Sigma-Aldrich) followed by selection for stable clones with puromycin, and wild-type control cells were infected with control lentiviral particles (Sigma-Aldrich) accordingly. Successful knockdown of MAOA in these cells were examined by Western blot by probing MAOA protein. Furthermore, cell proliferation, invasion and migration were determined in these wild-type and MAOA-knockdown cells, and knockdown of MAOA significantly reduced these indices in both C4-2 and ARCaP_M cells (Figure 1). These cells are now ready to be used in proposed animal studies, such as intracardiac injection for determining MAOA effect on human prostate cancer bone metastases as well as intratibial injection for investigating MAOA-mediated prostate cancer-bone cell interaction.



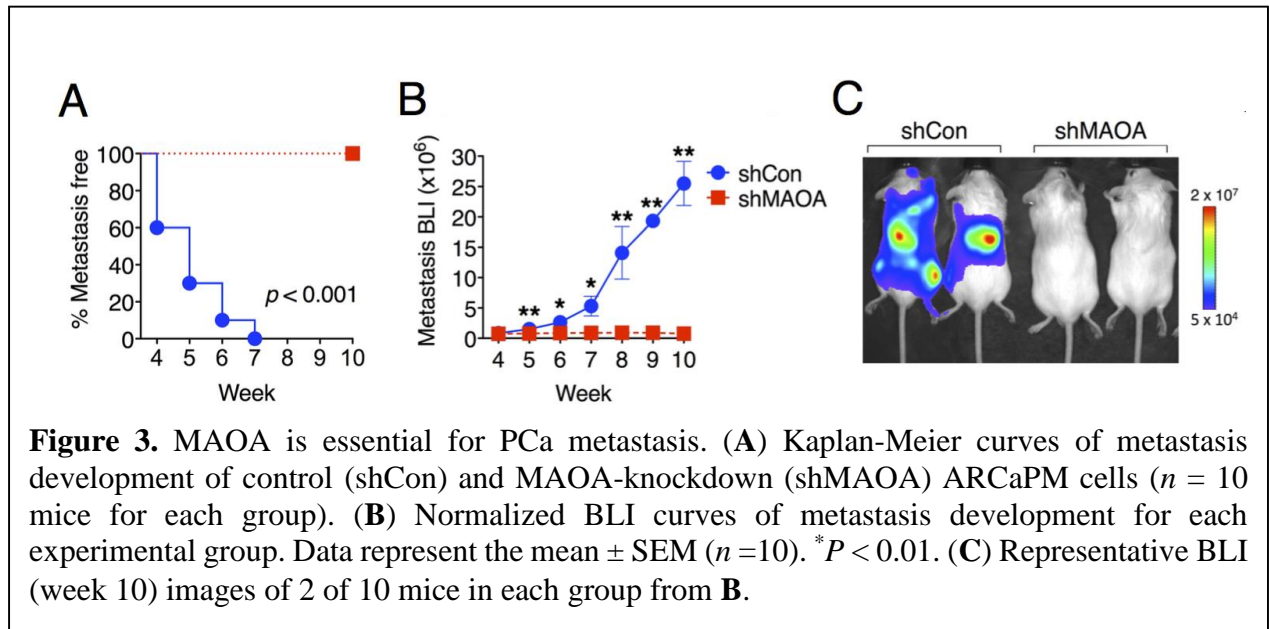
Task 1b: We analyzed wild-type and MAOA-knockdown human prostate cancer xenograft specimens with focuses on cell proliferation, epithelial-mesenchymal transition (EMT) and hypoxia signaling. Our preliminary *in vitro* results showed that MAOA is engaged in EMT induction and HIF1 α stabilization in human prostate cancer cells, we therefore analyzed wild-type and MAOA-knockdown human prostate LNCaP and C4-2 subcutaneous tumor xenograft specimens with select EMT and hypoxia markers by immunohistochemical (IHC) analyses. Our results showed that knockdown of MAOA significantly decreased the expression levels of Ki-67 (a



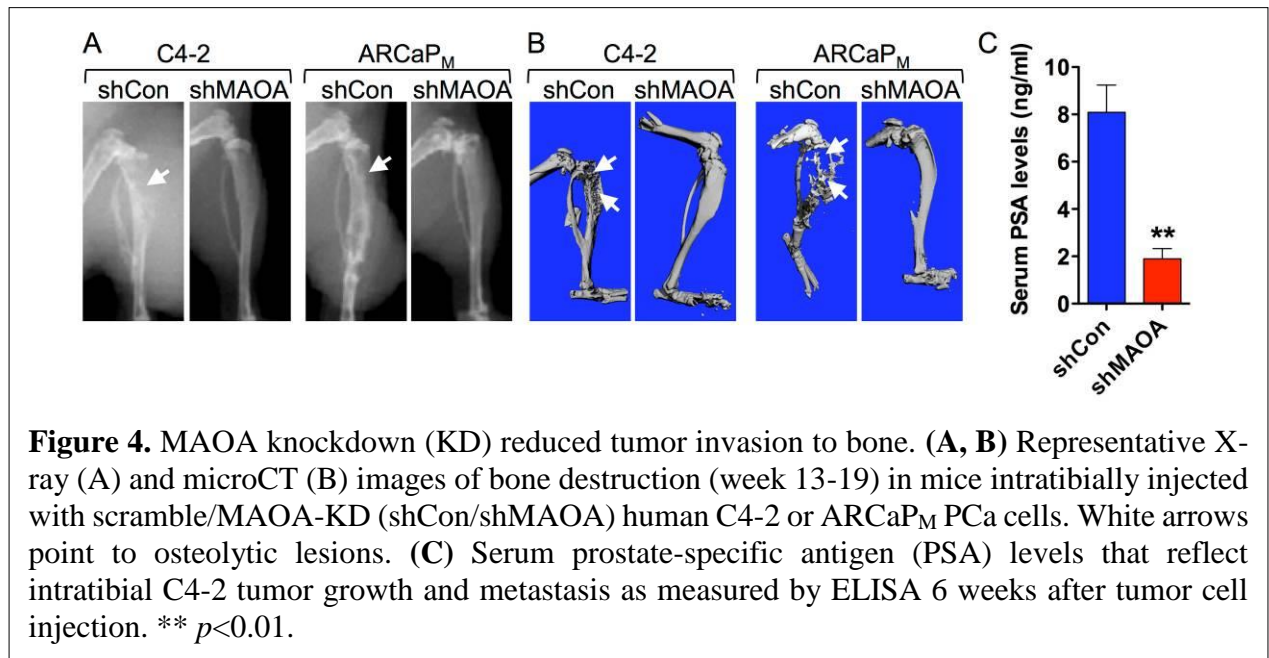
cell proliferation marker), Vimentin (a mesenchymal marker), HIF1 α and VEGF-A (a HIF1 α target gene), but increased E-cadherin (an epithelial marker) (Figure 2), which are consistent to the *in vitro* findings and confirm MAO A effect in driving EMT and hypoxia.⁸

Task 1c: We studied prostate tumor metastasis through **intracardiac injection** of PCa cells into the athymic nude mice. Briefly, mice were injected intracardially with MAO A knockdown

ARCaP_M cells⁹ and control wild-type cells. Our preliminary studies show that knockdown of MAOA in ARCaP_M cells reduced the rate of prostate cancer cell metastasis (Figure 3).



Task 1d: We performed prostate tumor bone metastasis studies through **intratibial injection** of PCa cells into athymic nude mice, and tumor growth and tumor-invading bone destruction were determined.



Human C4-2 or ARCaP_M PCa cells subjected to either a scrambled control shRNA (shCon) or a MAOA-targeting shRNA (shMAOA) were injected intratibially into male athymic nude mice. Tumor invasion to bone was examined routinely by X-ray during the period of tumor growth

(Figure 4A) and further assessed by microCT at the endpoint of experiments (Figure 4B). Serum PSA levels in mice implanted with PSA-producing C4-2 cells, which correlates to tumor growth, were collected biweekly and measured by ELISA (Figure 4C). Tumor ROS levels at sacrifice remain to be measured. Tumor specimens were fixed in formalin, embedded in paraffin, and ready for further IHC analyses of cell proliferation, osteoblastic, osteoclastic, EMT and hypoxia markers.

Conclusion: MAOA KD cells (shMAOA) have shown markedly reduced invasiveness to bone, as compared to control cells (shCon). As indicated in the Figure 1A-1B, the intratibially injected control cells produced marked bone destruction as evidenced by X-ray and microCT examination. In comparison, the bone remains essentially intact when MAOA-KD cells were used. Analysis of the serum PSA levels showed that intratibial tumor growth rate is reduced for MAOA-KD cells. This suggests that MAOA plays an essential role in promoting bone invasive properties of the PCa cells.

Task 2a: We investigated the molecular mechanisms underlying the MAOA functions in PCa by defining its roles in ROS- and HIF1 α -mediated signaling. We also studied the effect of MAOA on PHD and HIF1 α activity in human PCa cells (LNCaP, C4-2 and ARCaP_M) and the accompanying regulation mediated by ROS generated through the MAOA action.

The MAOA effect on hydroxylation-dependent HIF1 α protein stability was determined by Western blot in PC-3 cells with the addition of proteasomal inhibitor (Figure 5A). The MAOA effect on PHDs enzymatic activity was examined by qPCR analysis of select HIF1 α target gene expression in PC-3 cells under PHD inhibitor treatment (Figure 5B). The MAOA effect on the protein expression of all four PHD isoforms was directly measured in PC-3 cells by Western blot (Figure 5C). The interplay among MAOA-regulated HIF1 α , PHD and ROS was further studied by Western blot coupled with FACS analysis of ROS levels (Figures 5D-F). The ROS effect by which MAOA mediates EMT and hypoxia was examined by qPCR analysis of select EMT and HIF1 α target gene expression (Figure 5G). The role of ROS in mediating the MAOA effect on cancer cell proliferation under either normoxia or hypoxia was determined by cell number counting assays (Figure 5H).

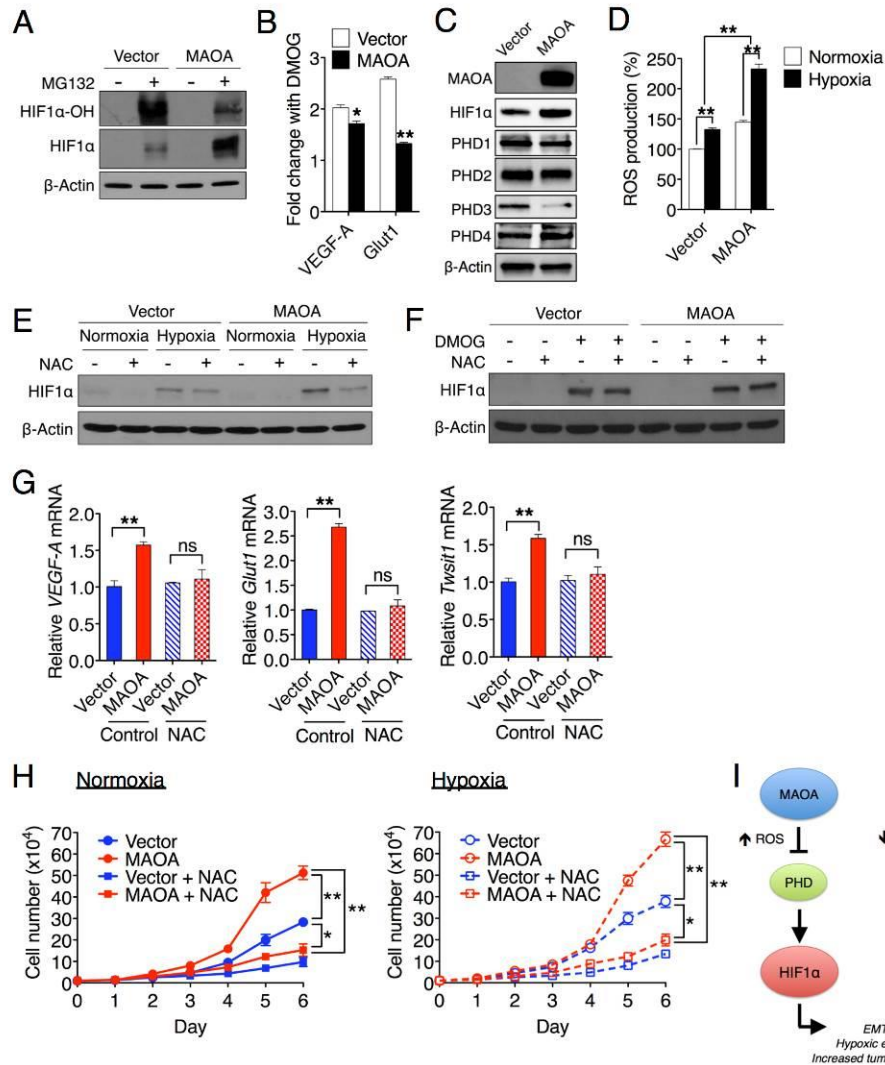


Figure 5. MAOA regulates HIF1 α stability through ROS. **(A)** Immunoblots of PC-3 (vector and MAOA-overexpression) cells treated with or without MG132 (1 μ M, 6 hours) for hydroxylated HIF1 α (HIF1 α -OH) and total HIF1 α . **(B)** Fold induction of HIF1 α target genes in PC-3 (vector and MAOA-overexpression) cells treated with DMOG (1 mM, 24 hours) was measured by qPCR, and the ratio (mean \pm SEM, n=3) of DMOG-treated to untreated gene expression is shown. **(C)** Immunoblots of PC-3 (vector and MAOA-overexpression) cells with hypoxia for PHD1-4. **(D)** The increase in ROS production in PC-3 (vector and MAOA-overexpression) cells with hypoxia was calculated as the percentage changes (mean \pm SEM, n=3) in ROS levels in hypoxic cells relative to normoxic cells. **(E)** Immunoblots of PC-3 (vector and MAOA-overexpression) cells incubated with 10 mM NAC and cultured under normoxia and hypoxia. **(F)** Immunoblots of PC-3 (vector and MAOA-overexpression) cells cultured at 21% O₂ with 10 mM NAC or 1 mM DMOG as indicated. **(G)** qPCR analysis of *VEGF-A*, *GLUT1*, and *TWIST1* expression (mean \pm SEM, n=3) in PC-3 (vector and MAOA-overexpression) cells incubated with 10 mM NAC and cultured under hypoxia. **(H)** Growth curves of PC-3 (vector and MAOA-overexpression) cells cultured in standard media supplemented with or without 10 mM NAC under either normoxia (left panel) or hypoxia (right panel) (mean \pm SEM, n=3). **(I)** A schematic diagram outlining MAOA stabilization of HIF1 α by repression of PHD activity through ROS production. * $p < 0.05$, ** $p < 0.01$.

Task 2b: We determined the effect of hypoxia/HIF α on MAOA activity in human PCa cells PC3, DU145, and C42B.

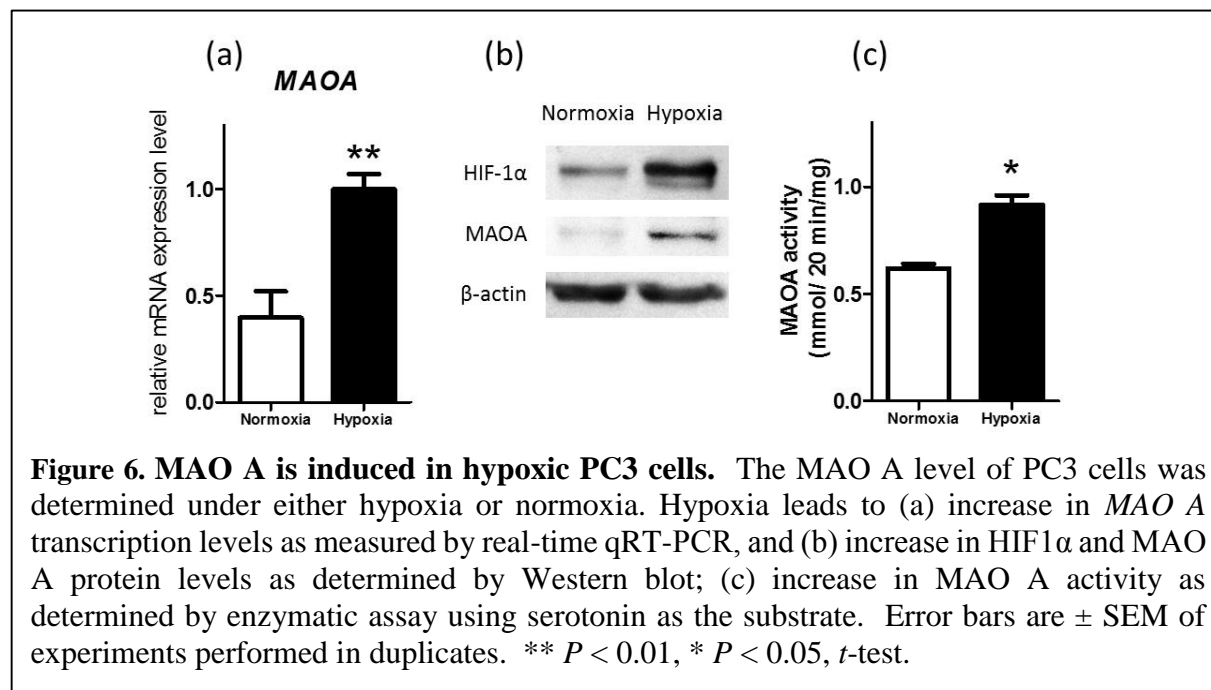


Figure 6. MAO A is induced in hypoxic PC3 cells. The MAO A level of PC3 cells was determined under either hypoxia or normoxia. Hypoxia leads to (a) increase in MAO A transcription levels as measured by real-time qRT-PCR, and (b) increase in HIF1 α and MAO A protein levels as determined by Western blot; (c) increase in MAO A activity as determined by enzymatic assay using serotonin as the substrate. Error bars are \pm SEM of experiments performed in duplicates. ** $P < 0.01$, * $P < 0.05$, t -test.

We found that MAO A is induced by hypoxia in human prostate cancer PC3 cells expressing a low level of MAO A (Figure 6). The level of MAO A mRNA increased 2.6-fold in PC3 cells under hypoxia (Figure 6a), which correlated with 5.7-fold increase in the MAO A protein level (Figure 6b) and 1.5-fold increase in MAO A activity (Figure 6c) as determined by the enzymatic activity assay using serotonin as the substrate.

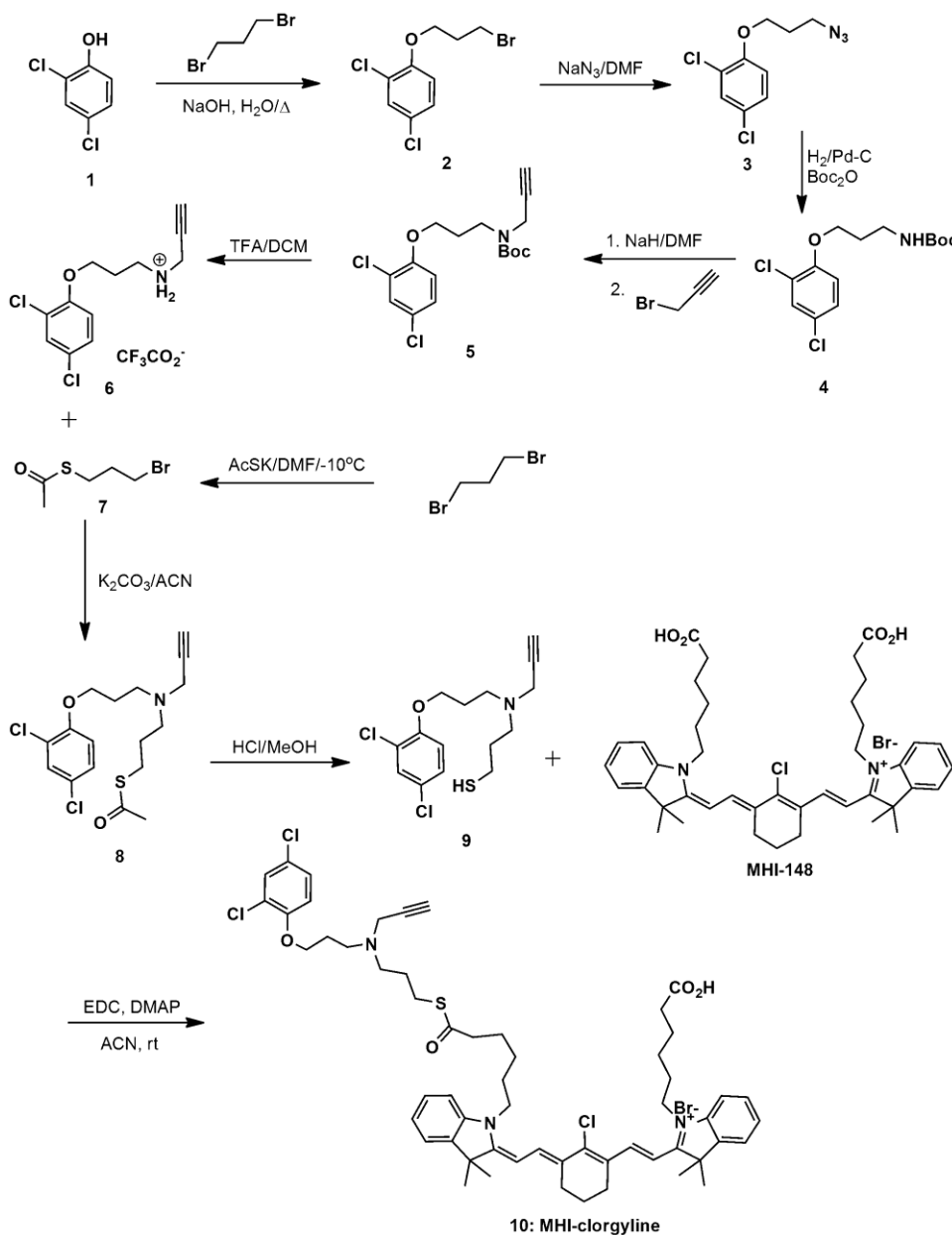
We have also established a similar relationship between the elevated MAO A levels (2.3-fold) and the levels of its enzymatic activity (3.7-fold) in DU145 cells with a moderate level of MAO A as well. The increase of MAO A correlates with the increase in HIF1 α protein levels in PC3 (Figure 6a-b) and DU145 cell lines.

In C42B cells expressing a high level of MAO A, HIF1 α is induced by hypoxia; however, it is abundant under normoxia as well at 63% of its hypoxic amount. As to the MAO A expression in C42B cells, its mRNA levels are not increased appreciably and reliably under hypoxia.

Conclusion: Our data suggest that hypoxia induces MAO A mRNA and protein in PC3 cells and DU145 cells expressing a low and moderate level of MAO A, respectively.

Task 3 (Specific Aim 2): This Specific Aim was focused on novel clorgyline (a potent MAOA inhibitor) - near-infrared (NIR) dye conjugate (NIR-clorgyline) specifically targeting tumors. We determined the inhibitory effect of this conjugate on metastasis of human PCa in mouse models.

Task3a: Based on crystal structure of MAOA¹⁰ we designed a novel clorgyline-NIR dye conjugate and prepared it through a series of synthetic steps as shown in Scheme 1. A modified clorgyline functionality was prepared first in order to accomplish this conjugation:



Scheme 1. Synthesis of NIR dye MHI-148 –clorgyline conjugate (MHI-clorgyline).

Task 3b: We determined inhibitory activity of the MHI-clorgyline using MAOA inhibition assays with radiolabeled substrates in LNCaP cell line (Figure 7). In parallel, clorgyline was used as a positive control. Surprisingly, MAOA catalytic activity was inhibited by clorgyline at a lower concentration than that of MHI-clorgyline. To test the efficacy of the MHI-clorgyline in inhibiting PCa cell growth we conducted an MTS assay in LNCaP, C4-2B and MAO-overexpressing PC3

cell lines after 96 h of incubation with MHI-clorgyline. Clorgyline was used as a positive control. The results are presented in Figure 8.

Remarkably, MHI-clorgyline has shown significantly higher activity as compared to clorgyline. We next conducted cell number counting assay in the same cell lines treated with clorgyline and MHI-clorgyline (Figure 9).

Again, treatment with MHI-clorgyline was more effective than that of the clorgyline. We also tested MHI-clorgyline and clorgyline in LNCaP cells in a standard colony formation assay and compared the results to shRNA treatment (Figure 10). In this assay both MHI-clorgyline and clorgyline showed significant reduction in the colony numbers (~50%) and were more effective than shRNA (~25%).

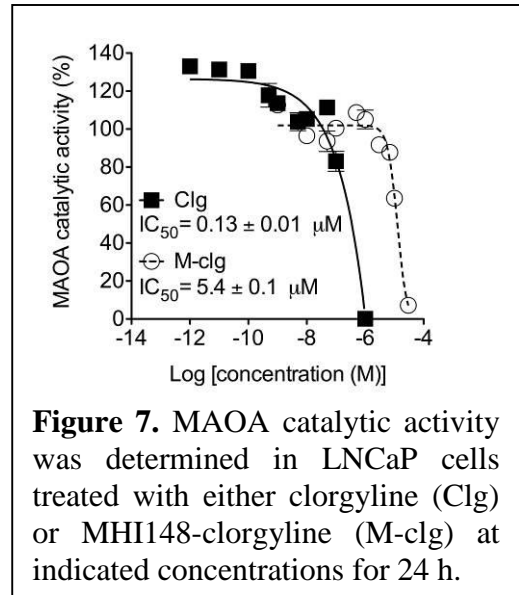


Figure 7. MAOA catalytic activity was determined in LNCaP cells treated with either clorgyline (Clg) or MHI148-clorgyline (M-clg) at indicated concentrations for 24 h.

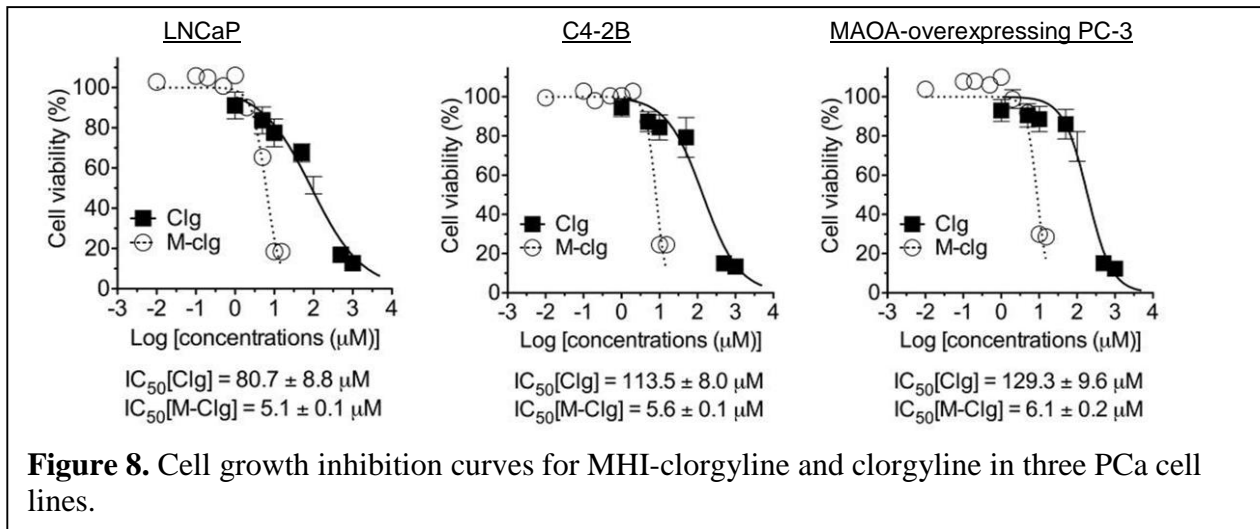


Figure 8. Cell growth inhibition curves for MHI-clorgyline and clorgyline in three PCa cell lines.

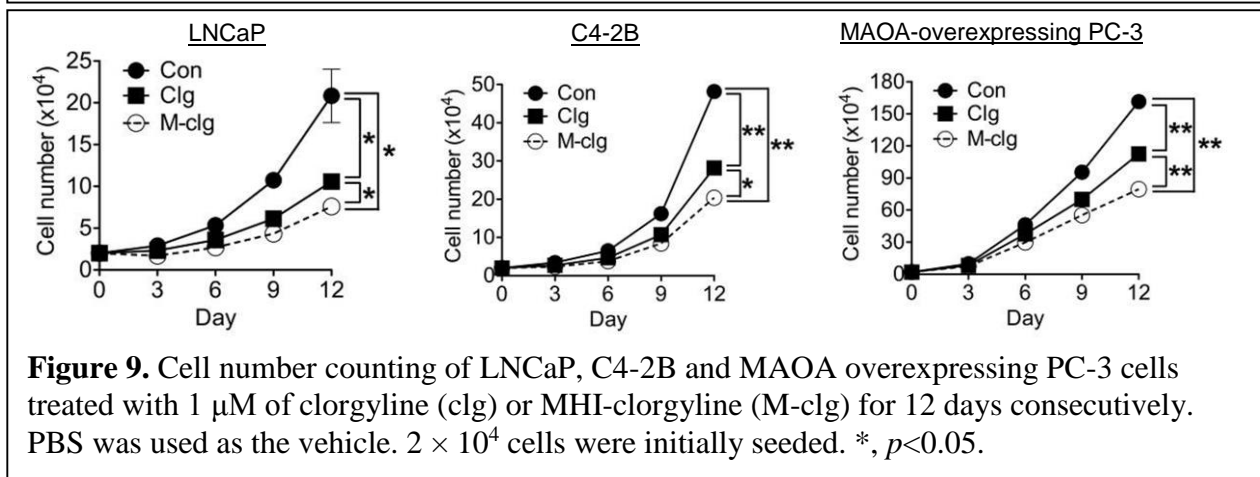


Figure 9. Cell number counting of LNCaP, C4-2B and MAOA overexpressing PC-3 cells treated with 1 μM of clorgyline (clg) or MHI-clorgyline (M-clg) for 12 days consecutively. PBS was used as the vehicle. 2×10^4 cells were initially seeded. *, $p < 0.05$.

Task 3c: We utilized laser-scanning confocal microscopy (LSCM) to determine the extent of targeting and intracellular localization of the MHI-clorgyline in PCa cells. Heptamethine cyanine dyes, such as MHI-148 and its conjugate MHI-clorgyline emit strong fluorescence in the near-IR region at 820-860 nm upon excitation at 750-780 nm.⁸ This fluorescence can be used to visualize the intracellular location of the dye or the conjugate. Since MAOA is mitochondria-bound, we anticipate that MHI-clorgyline will also localize there. The compound rapidly accumulated in C4-2B PCa cells and, as expected, localized in the mitochondria, as determined by co-staining cells with mitochondria-specific dye, Mitotracker Green (Figure 11).

Task 3d-1: We studied the *in vivo* effect of NIR-clorgyline on prostate tumor growth and metastasis. We recently discovered a novel class of NIR heptamethine carbocyanine dyes, IR-783 and MHI-148, which are effective cancer-specific imaging agents. These agents show preferential uptake and retention in cancer but not normal cells. By conjugating chemotherapeutic agents with these dyes, we observed tumor-specific cell kill without cytotoxicity in host mice, suggesting the potential use of these carbocyanine dyes as carriers for

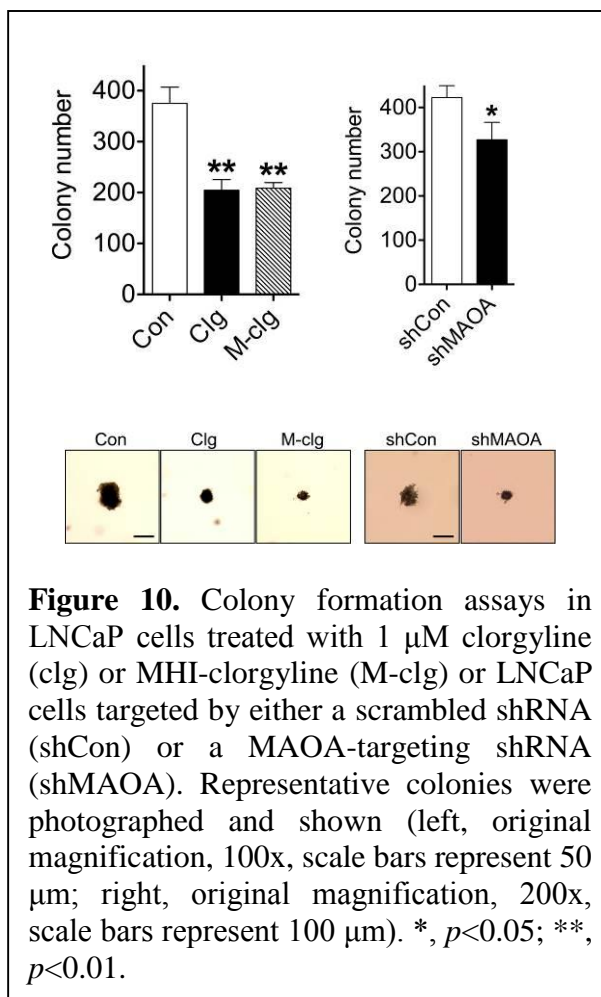


Figure 10. Colony formation assays in LNCaP cells treated with 1 μ M clorgyline (clg) or MHI-clorgyline (M-clg) or LNCaP cells targeted by either a scrambled shRNA (shCon) or a MAOA-targeting shRNA (shMAOA). Representative colonies were photographed and shown (left, original magnification, 100x, scale bars represent 50 μ m; right, original magnification, 200x, scale bars represent 100 μ m). *, $p < 0.05$; **, $p < 0.01$.

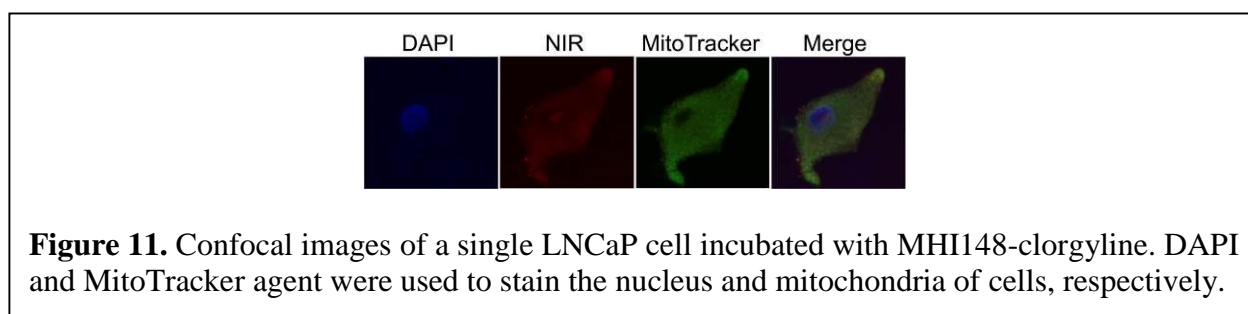
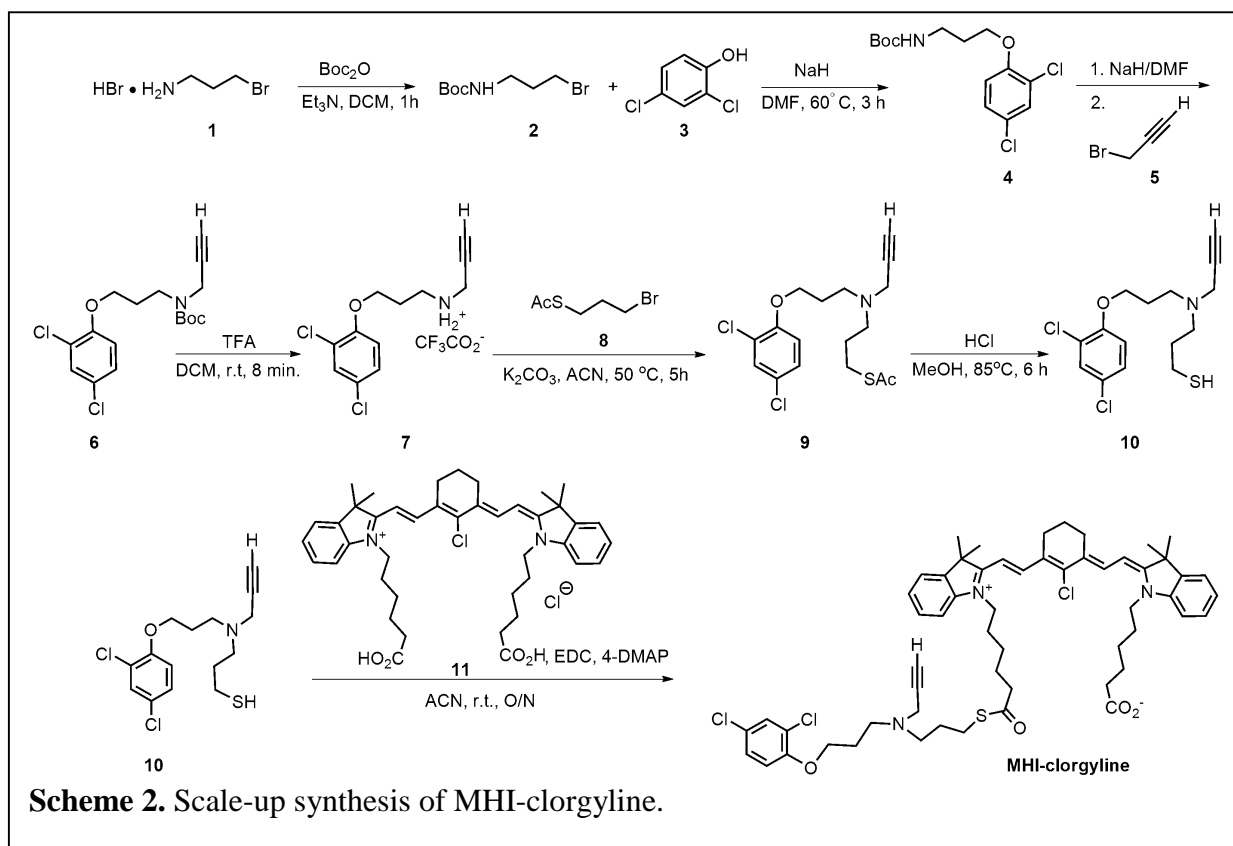


Figure 11. Confocal images of a single LNCaP cell incubated with MHI148-clorgyline. DAPI and MitoTracker agent were used to stain the nucleus and mitochondria of cells, respectively.

cancer-specific targeting by small molecules. The advantages of this new class of dyes as imaging agents are: (I) They have relatively low molecular weights that facilitate their effective uptake into both localized and metastatic tumors; (II) They can be synthesized in pure form and are stable upon storage; (III) They are taken up by many different types of cancer cells, including circulating or disseminated tumor cells and tumor tissues regardless of their cell-surface properties and their plasticity; and (IV) They have the potential of recognizing live versus dead cells and therefore can be used for follow-up in patients subjected to treatment by hormonal, radiation and chemotherapeutic agents.

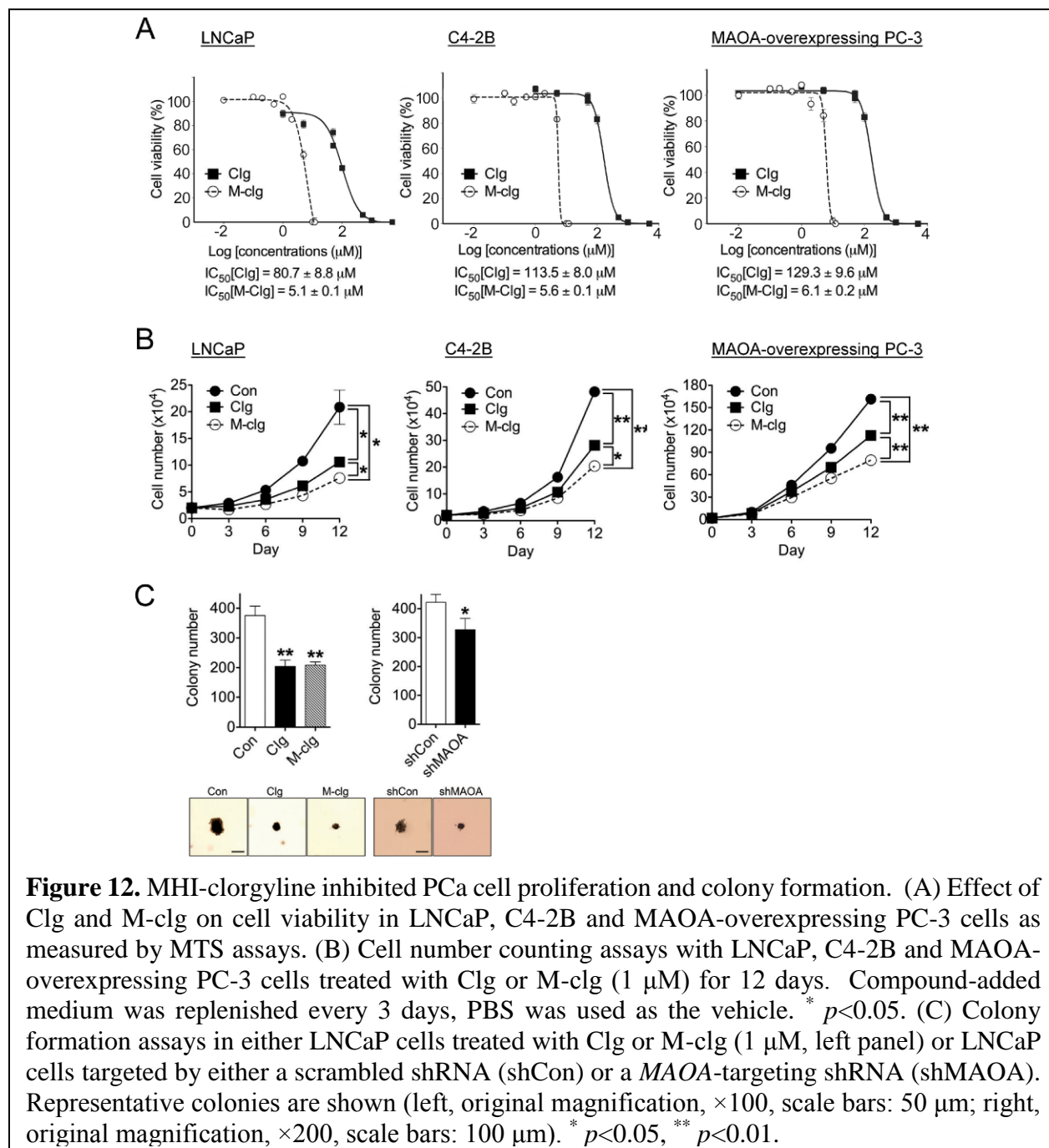
These dyes can be retained in established PCa cell lines (C4-2, PC-3 and ARCaP_M) with the dyes enriched in the mitochondria and lysosomes, but not in normal prostatic epithelial and fibroblast cells. In an orthotopic ARCaP_M xenograft mouse model receiving intraperitoneal injection of low dose of IR-783 (10 nmol/20 g), the near-infrared signals were specifically detected in the primary tumor and its associated bone metastases within 24 hours by fluorescence optical imaging. Additionally, this novel class of dyes showed no systemic toxicity when mice were given a 100-fold excess of the imaging dose of the dye.

By using the structure-guided design we developed MHI-clorgyline, a novel tumor-targeting MAOA inhibitor that would preferentially accumulate in the PCa lesions. This inhibitor contains a tumor-targeting NIR dye and a moiety of MAOA inhibitor. We reasoned that including a NIR imaging functionality could be useful for measuring uptake and cellular localization of the conjugate and possibly for future image-guided drug delivery and diagnosis. We chose small molecule clorgyline as a MAOA-targeting functionality because of the high affinity and selectivity of this compound towards MAOA. The presence of high-resolution crystal structure of clorgyline-MAOA complex¹⁰ facilitated our design. For tumor-targeting and NIR-imaging function we chose a MHI-148 dye¹¹⁻¹³. The high selectivity in targeting of these dyes to tumors, mediated by tumor hypoxia and organic anion-transporting polypeptides¹⁴, has been demonstrated in human PCa¹⁵. First, we developed an effective, scale-up procedure for the synthesis of MHI-clorgyline on the



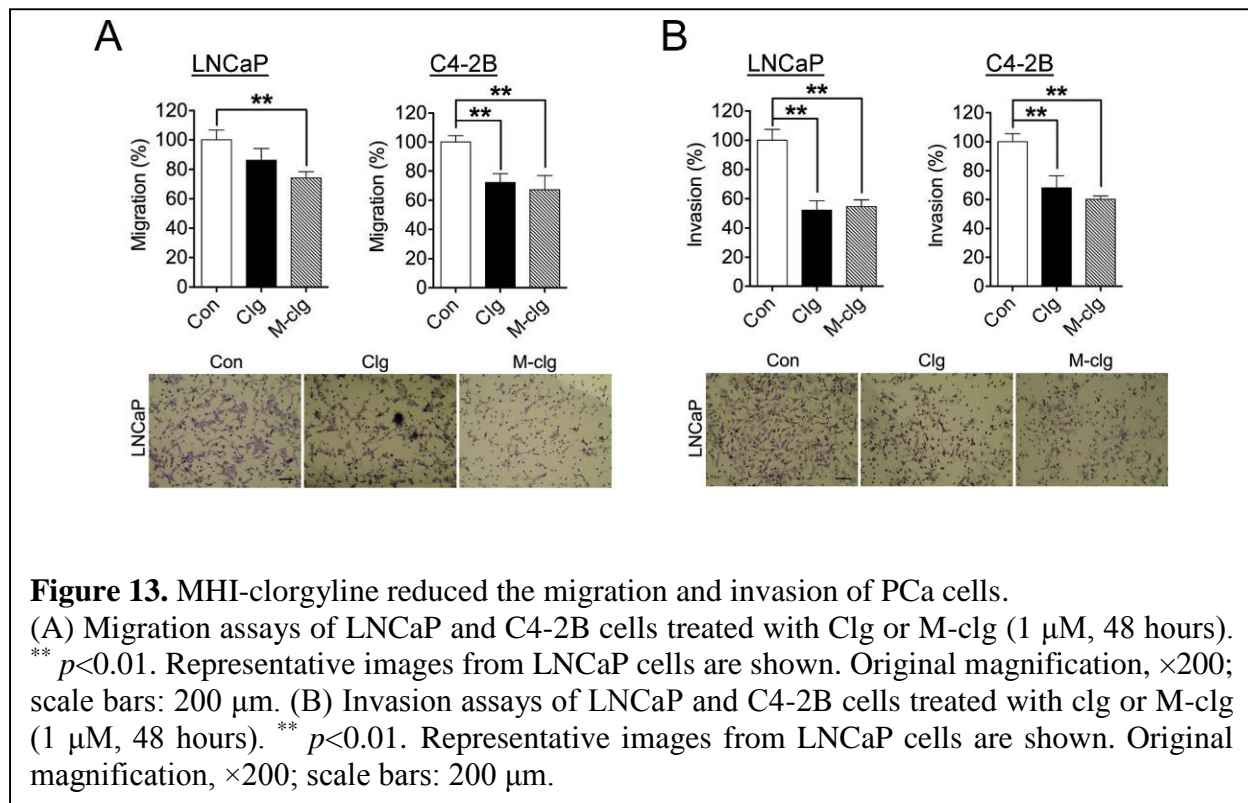
scale from hundreds on milligrams to 1 gram. It has been synthesized in a sequence of steps outlined in Scheme 2. The synthesis started with commercially available 3-bromopropylamine hydrobromide **1**. This compound was converted into *t*-butyl (3-bromopropyl)carbamate **2**, which

was used in the subsequent step to alkylate the commercially available 2,4-dichlorophenol, giving an intermediate **4**. Deprotonation of the amide in **4** was carried out with sodium hydride, followed by alkylation with propargyl bromide **5**, producing Boc-protected alkyne **6**. The protecting group was removed under acidic conditions using TFA in dichloromethane. The product **7** was alkylated with 1-bromo-3-thioacetylpropane **8**, resulting in the formation of compound **9**. Removal of the acetyl protective group in **9** was carried out in methanolic HCl, affording an intermediate **10**. This intermediate was then coupled to MHI-148 dye **11** using EDC and 4-DMAP to give MHI-clorgyline. The product was purified on preparative TLC and its identity and purity were confirmed by NMR and mass spectrometry.



We first demonstrated that MHI-clorgyline reduced colony formation, migration and invasion of PCa cells. PCa LNCaP, C4-2B and MAOA-overexpressing PC-3 cells¹⁶ were used for cell viability (Figure 12A) and cell proliferation assays (Figure 12B). Treatment with clorgyline produced dose response curves with 50% inhibitory concentrations (IC₅₀) of 80.7 ± 8.8 μM in LNCaP, 113.5 ± 8.0 μM in C4-2B, and 129.3 ± 9.6 μM in MAOA-overexpressing PC-3 cells. By comparison, treatment with MHI-clorgyline produced curves with IC₅₀ of 5.1 ± 0.1 μM in LNCaP, 5.6 ± 0.1 μM in C4-2B, and 6.1 ± 0.2 μM in MAOA-overexpressing PC-3 cells, indicating 12-20 times higher efficacy for MHI-clorgyline in inhibiting PCa cells growth as compared to clorgyline. In cell number counting assays we observed that both clorgyline and MHI-clorgyline reduced the number of proliferating cells after 12 days. MHI-clorgyline also showed higher efficacy as compared to clorgyline (Figure 12B).

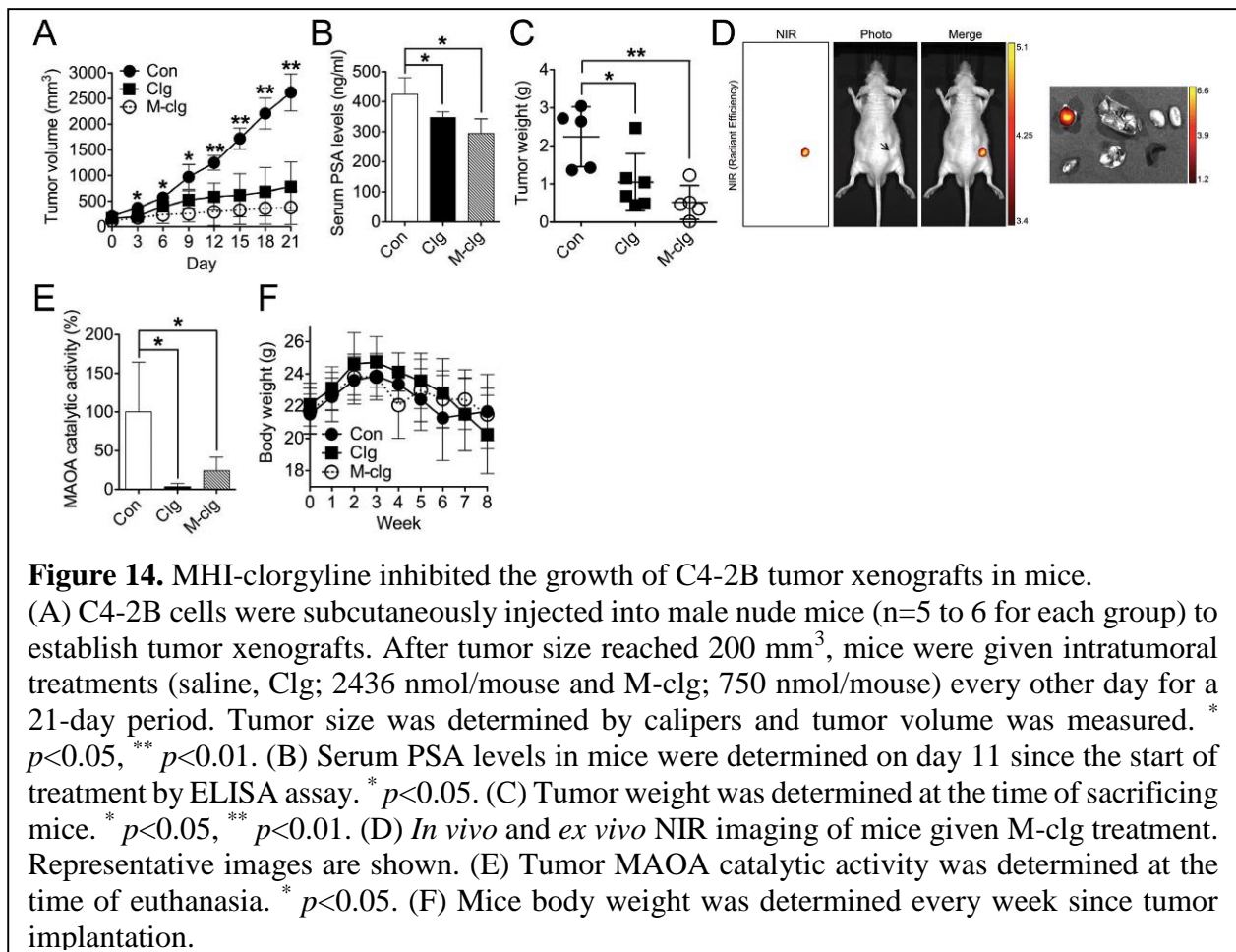
Colony formation assays were performed in LNCaP cells treated with clorgyline or MHI-clorgyline (Figure 12C). In a parallel setup, LNCaP cells were targeted by either a MAOA-targeting shRNA (shMAOA) or a scrambled shRNA (shCon). Treatment with clorgyline and MHI-clorgyline resulted in a reduction of the colony number by as much as 45%, although in this assay the difference between the activities of clorgyline or MHI-clorgyline was not statistically significant (left panel). Treatment with the MAOA-targeting shRNA reduced colony number by only 25%, as compared to treatment with scrambled shRNA (right panel).



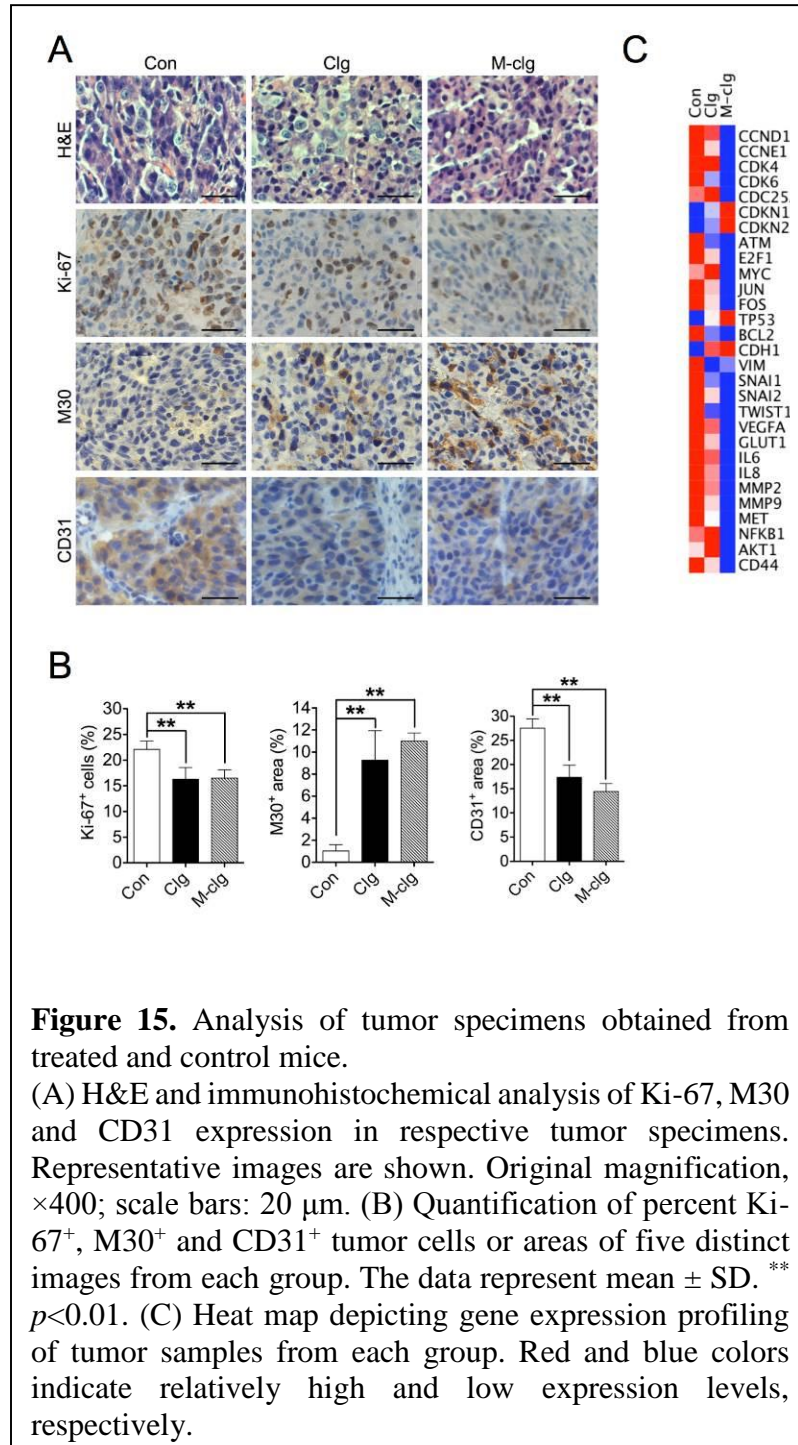
We determined the ability of MHI-clorgyline and clorgyline to inhibit migration of LNCaP and C4-2B cells. After treatment with compounds at 1 μM concentration for 48 hours the LNCaP cells showed statistically significant reduction in migration (20% for clorgyline, 35% for MHI-clorgyline, Figure 13A, left panel). A similar result was observed for C4-2B cells (Figure 13A,

right panel). In invasion assays, cells treated with MHI-clorgyline and clorgyline also showed 50% reduction in LNCaP and 40-45% in C4-2B cells (Figure 13B).

In order to assess the efficacies of MHI-clorgyline *in vivo*, subcutaneous tumor xenograft mouse models were used. After being implanted subcutaneously into male nude mice, C4-2B cells formed tumors in 3-4 weeks. After tumors reached 200 mm³, mice were randomly assigned into three groups to receive treatments every other day: 1) control, 2) clorgyline and 3) MHI-clorgyline. Two routes of administration were used to test the tumor-specific targeting ability of MHI-clorgyline: intratumoral and intraperitoneal. We explored an intratumoral injection because for clorgyline, the MAOA inhibitor without tumor-targeting specificity, this route could produce higher clorgyline concentration inside the tumor's interstitium, making more stringent conditions for comparison with the treatment efficacy of tumor-targeting MHI-clorgyline. Tumors were measured with calipers and tumor volume was calculated every three days during the 21-day treatment. Serum PSA levels in mice were determined on day 11, the middle of treatment course, and tumor MAOA activity was determined at the end of treatment. Mice body weights were monitored on a weekly basis since the time of inoculation. At the experiment endpoint mice were euthanized, tumors were excised, and tumor weights were determined. MHI-clorgyline- and clorgyline-treated mice showed significant delays in tumor growth (Figure 14A), reduction in PSA levels (Figure 14B) and decreases in tumor weight as compared to control mice (Figure 14C). It is noteworthy that even under the stringent conditions of intratumoral injection designed to improve efficacy of clorgyline,



MHI-clorgyline still showed superior results. NIR imaging of the whole body *in vivo* and individual tumor and normal organs *ex vivo* clearly showed MHI-clorgyline localization within the tumor (Figure 14D). Measurements of MAOA activity in tumors showed its significant reduction in both MHI-clorgyline- and clorgyline-treated mice (Figure 4E). All mice in treated and control groups showed similar changes in body weight that did not exceed 18% throughout the entire duration of experiment (Figure 14F), suggesting that this treatment regimen was well tolerated by the animals.



We next performed hematoxylin and eosin staining (H&E) and immunohistochemical analysis of protein expression patterns of Ki-67 (a cell proliferation marker), M30 (a cell apoptosis marker) and CD31 (an angiogenesis marker) in tumor specimens from control and treated groups (Figure 15A). H&E staining showed a decrease in the nucleus to cytoplasm ratios in cells from tumors treated by MHI-clorgyline and clorgyline, as compared to control group, suggesting reduced malignancy in treated tumors¹⁷. Ki-67 staining of tumor specimens revealed a 30%–35% decrease of Ki-67⁺ cells in MHI-clorgyline- and clorgyline-treated tumors (Figure 7B, left panel). We observed 10-12 fold increase of M30⁺ area (middle panel) and 30-40% decrease in CD31⁺ area (right panel) in the treated specimens as compared to controls (Figure 15B), suggesting increased apoptosis and reduced angiogenesis occurring in treated tumors. Gene expression profiling further indicated downregulation in expression of such proto-oncogenes or oncogenes as *FOS*, *JUN*, *NFKB1* and *MYC* and upregulation of *TP53* tumor suppressor gene expression in

response to treatment. Cell-cycle regulator genes that activate cell cycle progression, such as *CCND1*, *CCNE1*, *CDK4*, and *CDK6*, were also downregulated, whereas expression of select cell-cycle inhibitors, including *CDKN1A* and *CDKN2A* increased in the MHI-clorgyline- and clorgyline-treated tumors as compared to controls. In contrast, decreased expression of anti-apoptotic *BCL2* gene was revealed in treated tumor samples. In addition, genes involved in MAOA-downstream signaling demonstrated to promote EMT (*VIM*, *SNAI1*, *SNAI2* and *TWIST1*), tumor hypoxia (*VEGFA* and *GLUT1*) and cancer cell migration, invasion and metastasis (*IL6*, *IL8*, *MMP2*, *MMP9* and *MET*)¹⁶ all showed reduced expression by treatment (Figure 15C).

Conclusion: MHI-clorgyline targets tumor with no detectable accumulation in normal tissues, providing effective reduction of the tumor growth rate and tumor metastasis. Analysis of the tumor specimens shows reduction in Ki-67⁺ and CD31⁺ markers, suggesting reduction of cell proliferation and angiogenesis, and increase in M30⁺ markers, indicating an increased apoptosis. Furthermore, gene expression profiles of tumors treated with MHI-clorgyline showed a reduction in expression of oncogenes *FOS*, *JUN*, *NFKB*, *MYC*, cell cycle regulators *CCND1*, *CCNE1*, *CDK4/6*, and an increase in the levels of tumor suppressor gene *TP53* and cell cycle inhibitors *CDKN1A* and *CDKN2A*. The genes downstream of MAOA, which promote EMT, tumor hypoxia and cancer cell invasion and migration, were also reduced in expression. This indicates anti-metastatic activity of MHI-clorgyline.

Task 3e: We assessed the tumor-targeting properties of NIR-clorgyline for prostate cancer *in vivo*.

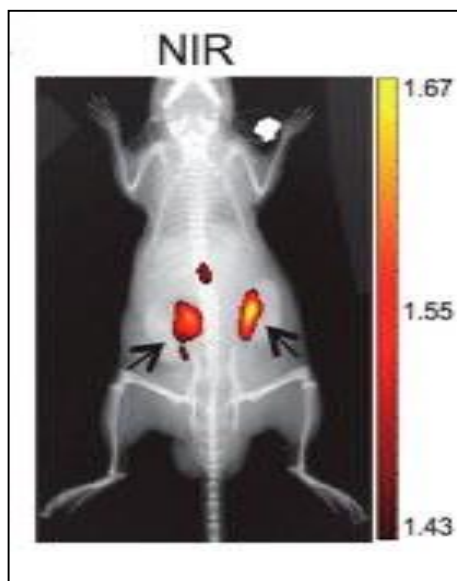


Figure 16. Tumor-targeting properties of NIR-MAOA inhibitor in mouse xenografts. C4-2B cells were subcutaneously implanted into both flanks of male nude mice to form tumor xenografts. Mice bearing C4-2B tumor xenografts were intraperitoneally injected with NIR-MAOA inhibitor (50 nmol/mouse) and 24 h later subjected to NIR imaging. One representative image is shown. Tumors are indicated by the arrows. NIR fluorescence color scales denote $\times 10^9$ and $\times 10^{10}$ for intratumoral and intraperitoneal injections, respectively, in the units of radiant efficiency ($[\text{p}/\text{sec}/\text{cm}^2/\text{sr}]/[\mu\text{W}/\text{cm}^2]$).

We demonstrated the tumor-targeting properties of NIR-MAOA inhibitor. C4-2B cells were subcutaneously implanted contralaterally into both flanks of male nude mice. After the formation of two tumor xenografts in each mouse, NIR-MAOA inhibitor was injected intraperitoneally. Figure 16 shows that NIR-MAOA inhibitor selectively targets two tumors when administered in an intraperitoneal injection. NIR imaging showed no observable NIR signals in other body parts, further confirming the tumor-specific targeting of NIR-MAOA inhibitor and its systemic circulation.

The determination of tumor growth post-injection of NIR-clorgyline by serial imaging, as well as the IHC analysis of tumor specimens post-sacrifice (e.g. cell proliferation markers) were previously completed and described in our Year 2 report.

In our recent report, the therapeutic effect of a NIR dye-gemcitabine conjugate was assessed in a 22Rv1 prostate tumor brain metastasis xenograft model, which may help address whether NIR dye-drug works for prostate cancer metastasis as we originally proposed (1).

Conclusion: These results suggest that NIR-MAO A inhibitor exerts its effect through tumor-targeted delivery of a MAO A-inactivating group, namely clorgyline, making it a valuable anti-tumor agent.

Task 3-2: We examined the hypothesis that MAOA may act like a tumor promoter in the context of PCa through its induction of ROS and hypoxia.

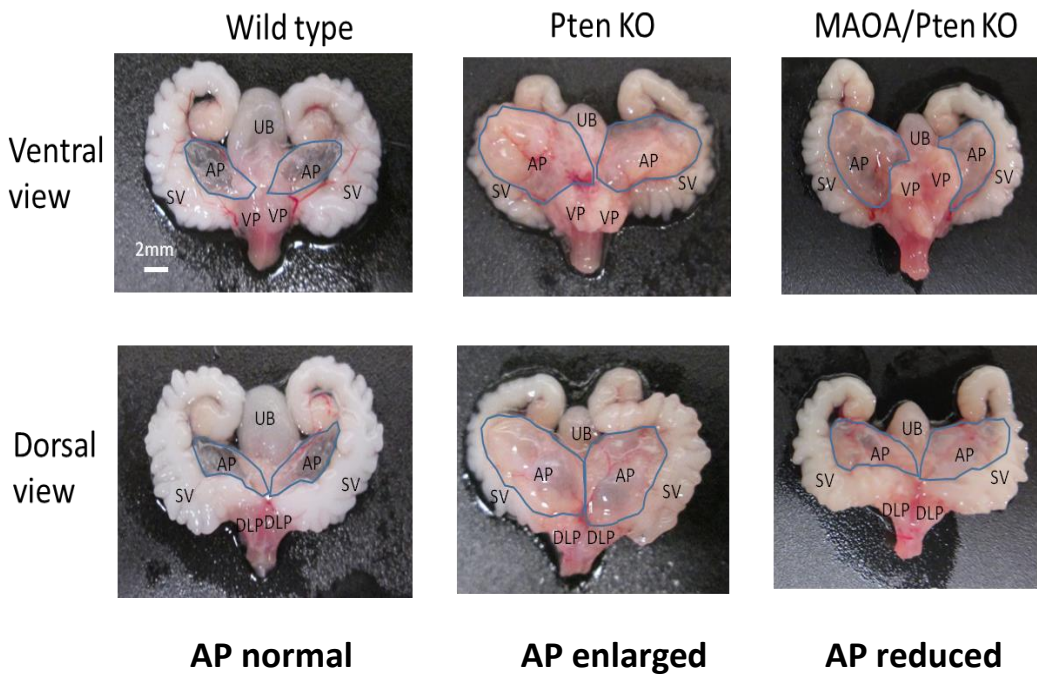


Figure 17. Prostate-specific deletion of MAOA reduced prostate enlargement resulting from Pten inactivation in Anterior prostate (AP). The gross anatomy of prostate of wild type, Pten KO and MAOA/Pten double KO mice (6 months old) are shown.

Since monoamine oxidase A (MAO A) has been implicated in prostate cancer growth and metastasis, we have studied the effects of MAO A on immune cells in the tumor microenvironment. To understand the role of MAO A in prostate cancer progression *in vivo*, MAO A/Pten double knockout mice were generated and demonstrated that deletion of MAO A delayed prostate tumor development and supported an immunostimulatory environment in the Pten knockout mouse model of prostate adenocarcinoma (Figure 17). Paraffin embedded prostate tissues from MAO A/Pten knockouts had elevated staining for markers of immune stimulation (CD8⁺ cytotoxic T cells, granzyme B, and IFN γ) and decreased expression of markers of immune

suppression (FoxP3, CD11b, HIF-1-alpha, and arginase 1) compared to parental *Pten* knockouts (*MAO A* wildtype). Multiple antigen immunostaining showed that cells contributing to immune suppression were mostly CD11b⁺ myeloid derived suppressor cells (MDSC). The data suggests that deletion of *MAO A* reduces immune suppression in prostate tumors and enhances antitumor immunity.

Conclusion: Our results suggest that inactivation of MAO A delays prostate cancer progression in *Pten* KO mice. This mouse model sets a stage for future studies with prostate-specific *Pten/MAOA* DKO mouse model will enhance our understanding of the functional roles of the MAOA in prostate cancer progression and metastasis.

In summary,

- We established MAOA-knockdown (KD) PCa cells: LNCaP, C4-2 and ARCaP_M.
- We have shown that MAOA effect is driving epithelial-to-mesenchymal transition (EMT) and hypoxia in human prostate cancer xenografts.
- We demonstrated that MAO A knockdown reduces the rate of growth and metastasis of PCa cells.
- We showed that MAOA drives tumor invasion to bone.
- We demonstrated that MAOA knockdown in both human C4-2 or ARCaP_M PCa cells reduced tumor-invading bone lesions.
- We established that MAOA regulates HIF1 α stability through ROS.
- The elevated levels of HIF1 α result in upregulated expression of *VEGF-A*, *GLUT1* and *TWIST1* genes, resulting in an increased tumorigenesis.
- We designed an efficient organic synthetic route leading to novel tumor-targeting agent – MHI-clorgyline.
- We showed that MHI-clorgyline targets mitochondria of prostate cancer cells.
- We demonstrated a remarkable efficacy of MHI-clorgyline in inhibiting MAOA activity in PCa cells, resulting in a suppression of cell growth and the rate of colony formation.
- We showed that MHI-clorgyline reduced PCa angiogenesis, increases apoptosis *in vitro* and *in vivo*.
- We showed that the NIR dye-drug conjugate was an effective approach to target and inhibit prostate cancer metastasis to distant organs, such as brain.

- MHI-clorgyline also reduced the expression of oncogenes and cell cycle regulators that promote EMT, tumor hypoxia and cancer cell invasion and migration, indicating anti-metastatic activity of the conjugate.
- We developed *Pten/MAOA* double-knockout mouse models to study the effect of *Pten* and MAOA loss on the onset and progression of PCa.

4. IMPACT:

During three years of the grant support, we established the role of MAOA in human PCa progression and metastasis. Through our experimental work we defined the molecular basis of MAOA functions in PCa. We found that hypoxia induces MAO A expression in prostate cancers cells contacting a low to moderate level of MAO A, which correlates with the increase in HIF1 α protein.

The significant efforts of synthetic chemistry, imaging and molecular pharmacology allowed us to develop an effective MAOA targeting strategy in tumors as well as means of inhibition of its downstream targets. Our novel MAOA inhibitor, MHI-clorgyline, is selectively delivered to PCa cells using a dye-drug conjugate platform to specifically target tumors without collateral damage to central nervous systems and the impairment of the normal tissue functions. The dye-drug conjugates can be visualized in tumors through the use of NIR imaging, which could also be utilized as a monitoring tool for the assessment of the drug efficacy, its delivery, and its impact on tumor growth and metastasis. We found that treatment with MHI-clorgyline resulted in a reduction of cell proliferation and angiogenesis, and increase in apoptosis of PCa cells. Gene expression profiles of tumors treated with MHI-clorgyline also indicated reduction in expression of oncogenes and cell cycle regulators downstream of MAOA and increase in the levels of tumor suppressor gene *TP53* and cell cycle inhibitors. This suggests that MHI-clorgyline decreased proliferative and metastatic potential of PCa cells and tumors.

We further demonstrated the tumor-targeting property of NIR-MAO A inhibitor that we developed. Following the intraperitoneal injection, NIR-MAO A inhibitor selectively localized to tumors in the mice bearing tumor xenografts formed by human prostate cancer cells as determined by serial NIR imaging. The results from the above studies were disseminated to the public through multiple means including internet-based news media, journal and/or book publication, conference presentation, etc.

In order to further study the role of MAOA in PCa progression, we generated a *Pten/MAOA* double knockout mouse model through the deletion of *MAOA* in a conditional *Pten* knockout mouse model. These mice showed reduction in myeloid-derived suppressor cells and a delayed formation of PCa tumors, suggesting that MAOA has an immunosuppressive effect in hypoxic prostate tumors, facilitating the evasion of tumor cells from detection by the immune system.

Based on the research findings, MAO-A activity increases with prostate cancer progression, metastasis, and in patients treated with chemotherapy. MAO-A inhibitors have been used as anti-depressants so they are safe for human use. Currently, a Phase II clinical trial

(ClinicalTrials.gov Identifier: NCT02217709; <https://clinicaltrials.gov/ct2/show/study/NCT02217709>) is ongoing, evaluating the efficacy of MAO inhibitor in non-metastatic recurrent prostate cancer.

5. CHANGES/PROBLEMS

Throughout our studies, we have encountered difficulties in performing orthotopic injections of PCa cells in order to establish orthotopic PCa models for evaluation of the MAO A role in PCa growth and metastasis. These difficulties were circumvented by taking alternative approaches where we generated prostate-specific Pten/MAOA double knockout mice. Prostate-specific Pten KO mice grow prostate tumors due to the deletion of tumor suppressor Pten gene. This transgenic mouse model by harboring spontaneous tumors better mimics prostate tumor growth than tumor xenograft mouse models. We showed that genetic knockout of MAOA in Pten-null background significantly impeded prostate enlargement and prostate tumor growth in the primary site, which along with results from other injections models (subcutaneous, intracardiac and intratibial) strongly indicate MAOA's role in promoting prostate tumor growth and metastasis.

In addition, we performed gene expression profiling on tumors from classical mouse xenografts with the emphasis on profiles of genes leading to PCa metastasis. We have shown that treatment with MAO inhibitor MHI-clorgyline results in a downregulation of genes that promote EMT (*VIM*, *SNAI1*, *SNAI2* and *TWIST1*), and cancer cell migration, invasion and metastasis (*IL6*, *IL8*, *MMP2*, *MMP9* and *MET*), suggesting the role of MAO A in PCa metastasis.

6. PRODUCTS:

a.

(1) Lay Press (selected from over 50 news reports):

“Antidepressant May Also Fight Prostate Cancer”, USC News, June 2, 2014.
<https://pressroom.usc.edu/antidepressant-may-also-fight-prostate-cancer/>

“Enzyme used in antidepressants could help researchers develop prostate cancer treatments”, HSC News, June 10, 2014.
<http://hscnews.usc.edu/enzyme-used-in-antidepressants-could-help-researchers-develop-prostate-cancer-treatments/>

“Antidepressants show promise for treating prostate cancer”, Futurity. org , June 4, 2014.
http://www.futurity.org/antidepressants-prostate-cancer-enzyme/?utm_source=rss&utm_medium=rss&utm_campaign=antidepressants-prostate-cancer-enzyme

“Enzyme used in antidepressants could help researchers develop prostate cancer treatments”, MedicalXpress, June 2, 2014.
<http://medicalxpress.com/news/2014-06-enzyme-antidepressants-prostate-cancer-treatments.html>

“Enzyme used in antidepressants could help researchers develop prostate cancer treatments”, Science Daily, June 1, 2014.
<http://www.sciencedaily.com/releases/2014/06/140601113953.htm>

“Enzyme Used In Antidepressants Could Help Researchers Develop Prostate Cancer Treatments”, News-Line Publishing, June 4, 2014.
http://www.newlinepublishing.com/NL_news18603_Enzyme-Used-In-Antidepressants-Could-Help-Researchers-Develop-Prostate-Cancer-Treatments

(2) Peer-Reviewed Scientific Journals: 5 Publications

Wu JB, Pan DF, Chung LWK. Near-infrared fluorescence and nuclear imaging and targeting of prostate cancer. *Transl Androl Urol* **2013**;2(3):254-264.

Wu JB, Shao C, Li X, Hu P, Chen Y-T, Li Q, Yin F, Li Y, Zhou HE, Shih JC, and Chung LWK. Monoamine oxidase A mediates prostate tumorigenesis and cancer metastasis. *J Clin Invest* **2014**, 124(7):2891-2908.

Wu JB, Shao C, Li X, Shi C, Li Q, Hu P, Chen Y-T, Dou X, Sahu D, Li W, Wang R, Zhou HE, Chung LWK. Near-infrared fluorescence imaging of cancer mediated by tumor hypoxia and HIF1 α /OATPs signaling axis. *Biomaterials* **2014**, 35:8175-8185.

Wu JB, Lin T-P, Gallagher JD, Kushal S, Zhou HE, Chung LWK, Olenyuk BZ, Shih JC. Monoamine oxidase A inhibitor – near-infrared dye conjugate reduces prostate tumor growth. *J Am Chem Soc* **2015**, 137:2366-2374.

Wu JB, Shi C, Chu GC, Xu Q, Zhang Y, Li Q, Yu JS, Zhou HE, Chung LW. Near-infrared fluorescence heptamethine carbocyanine dyes mediate imaging and targeted drug delivery for brain tumor. *Biomaterials* **2015**, 67:1-10.

Invited Articles:

Nothing to report

(3) Abstracts:

Wu JB, Zhou HE, Chung LW. Monoamine oxidase A promotes prostate cancer neuromimicry by activation of axon guidance genes. The Society for Basic Urologic Research Fall Symposium. Fort Lauderdale, FL. (2015)

Wu JB, Zhou HE, Posadas E, Chung LW. Monoamine oxidase A reciprocally interacts with androgen receptor and mediates castration-resistant prostate cancer progression. Cedars-Sinai Research Day VI. Los Angeles, CA. (2015)

b. Presentations and posters made:

Jean C. Shih:

1. International Symposium on Water, California Institute of Technology, Pasadena, CA (2013), “MAO A, a Novel Target for Prostate Cancer Progression”.
2. National Taiwan University, Taipei, Taiwan (2014), “MAO, Cancer and Autism”
3. Taipei Medical University, Taipei, Taiwan (2014), “MAO, Cancer and Autism”
4. National Yang-Ming University, Taipei, Taiwan (2014), “MAO, Cancer and Autism”
5. China Medical University, Taichung, Taiwan (2014), “MAO, Cancer and Autism”
6. 15th SCBA (Society of Chinese Bioscientist in America) International Symposium, Taipei, Taiwan (2015), “MAO A mediates neuroendocrine differentiation and autophagy activation of relapsed prostate cancer”

Boyang Jason Wu:

1. Cancer Biology Work-In-Progress Seminar Series, Cedars-Sinai Medical Center, Los Angeles, CA (2014), “Novel function for monoamine oxidase A in human prostate cancer”.
2. CSMC – RECOOP Nanomedicine Workshop, Cedars-Sinai Medical Center, Los Angeles, CA (2015), “Exploration of near-infrared dye-drug conjugate as dual imaging and therapeutic agents for solid tumors”.
3. Computational Biology Workshop, Cedars-Sinai Medical Center, Los Angeles, CA (2015), “Novel functions and targeting of monoamine oxidase in prostate cancer”.

c. Patent Applications

Inventors: Shih JC, Chung LW, Zhou HE, Wu B, Olenyuk BZ

Invention Title: Monoamine Oxidase Inhibitors and Methods for Treatment and Diagnosis of Prostate Cancer

Patent Application Number: PCT/US2012/048407

Filing Date: Jul 26, 2012

Publication Number: WO2013016580 A3

Publication Date: Mar 28, 2013

d. REPORTABLE OUTCOMES:

Phase II Clinical Trial of phenelzine on non-metastatic recurrent prostate cancer. PIs: Mitch Gross, MD , Ph.D., Jean C. Shih, Ph.D

e. OTHER ACHIEVEMENTS:

Facilitated US-Taiwan International Student Exchange
Trained Ph.D. candidates in Pharmaceutical Sciences

f. REFERENCES:

1. Bortolato, M.; Chen, K.; Shih, J. C., Monoamine oxidase inactivation: from pathophysiology to therapeutics. *Adv Drug Deliv Rev* **2008**, *60* (13-14), 1527-1533.
2. Shih, J. C.; Chen, K.; Ridd, M. J., Monoamine oxidase: from genes to behavior. *Annu Rev Neurosci* **1999**, *22*, 197-217.
3. Jossion, S.; Nomura, T.; Lin, J. T.; Huang, W. C.; Wu, D.; Zhau, H. E.; Zayzafoon, M.; Weizmann, M. N.; Gururajan, M.; Chung, L. W., Beta2-microglobulin induces epithelial to mesenchymal transition and confers cancer lethality and bone metastasis in human cancer cells. *Cancer Res* *71* (7), 2600-2610.
4. Sung, S. Y.; Hsieh, C. L.; Law, A.; Zhau, H. E.; Pathak, S.; Multani, A. S.; Lim, S.; Coleman, I. M.; Wu, L. C.; Figg, W. D.; Dahut, W. L.; Nelson, P.; Lee, J. K.; Amin, M. B.; Lyles, R.; Johnstone, P. A.; Marshall, F. F.; Chung, L. W., Coevolution of prostate cancer and bone stroma in three-dimensional coculture: implications for cancer growth and metastasis. *Cancer Res* **2008**, *68* (23), 9996-10003.
5. Trachootham, D.; Alexandre, J.; Huang, P., Targeting cancer cells by ROS-mediated mechanisms: a radical therapeutic approach? *Nat Rev Drug Discov* **2009**, *8* (7), 579-591.
6. Flamand, V.; Zhao, H.; Peehl, D. M., Targeting monoamine oxidase A in advanced prostate cancer. *J Cancer Res Clin Oncol* *136* (11), 1761-1771.
7. True, L.; Coleman, I.; Hawley, S.; Huang, C. Y.; Gifford, D.; Coleman, R.; Beer, T. M.; Gelmann, E.; Datta, M.; Mostaghel, E.; Knudsen, B.; Lange, P.; Vessella, R.; Lin, D.; Hood, L.; Nelson, P. S., A molecular correlate to the Gleason grading system for prostate adenocarcinoma. *Proc Natl Acad Sci U S A* **2006**, *103* (29), 10991-10996.
8. Yang, X.; Shi, C.; Tong, R.; Qian, W.; Zhau, H. E.; Wang, R.; Zhu, G.; Cheng, J.; Yang, V. W.; Cheng, T.; Henary, M.; Strekowski, L.; Chung, L. W., Near IR heptamethine cyanine dye-mediated cancer imaging. *Clin Cancer Res* *16* (10), 2833-2844.
9. Zhau, H. Y.; Chang, S. M.; Chen, B. Q.; Wang, Y.; Zhang, H.; Kao, C.; Sang, Q. A.; Pathak, S. J.; Chung, L. W., Androgen-repressed phenotype in human prostate cancer. *Proc Natl Acad Sci U S A* **1996**, *93* (26), 15152-15157.
10. De Colibus, L.; Li, M.; Binda, C.; Lustig, A.; Edmondson, D. E.; Mattevi, A., Three-dimensional structure of human monoamine oxidase A (MAO A): relation to the

- structures of rat MAO A and human MAO B. *Proc Natl Acad Sci U S A* **2005**, *102* (36), 12684-12689.
11. Luo, S.; Zhang, E.; Su, Y.; Cheng, T.; Shi, C., A review of NIR dyes in cancer targeting and imaging. *Biomaterials* **2011**, *32* (29), 7127-7138.
 12. Tan, X.; Luo, S.; Wang, D.; Su, Y.; Cheng, T.; Shi, C., A NIR heptamethine dye with intrinsic cancer targeting, imaging and photosensitizing properties. *Biomaterials* **2012**, *33* (7), 2230-2239.
 13. Luo, S.; Tan, X.; Qi, Q.; Guo, Q.; Ran, X.; Zhang, L.; Zhang, E.; Liang, Y.; Weng, L.; Zheng, H.; Cheng, T.; Su, Y.; Shi, C., A multifunctional heptamethine near-infrared dye for cancer theranosis. *Biomaterials* **2013**, *34* (9), 2244-2251.
 14. Wu, J. B.; Shao, C.; Li, X.; Shi, C.; Li, Q.; Hu, P.; Chen, Y.-T.; Dou, X.; Sahu, D.; Li, W.; Harada, H.; Zhang, Y.; Wang, R.; Zhau, H. E.; Chung, L. W. K., Near-infrared fluorescence imaging of cancer mediated by tumor hypoxia and HIF1 α /OATPs signaling axis. *Biomaterials* **2014**, *35* (28), 8175-8185.
 15. Yang, X.; Shi, C.; Tong, R.; Qian, W.; Zhau, H. E.; Wang, R.; Zhu, G.; Cheng, J.; Yang, V. W.; Cheng, T.; Henary, M.; Strekowski, L.; Chung, L. W., Near IR heptamethine cyanine dye-mediated cancer imaging. *Clin Cancer Res* **2010**, *16* (10), 2833-2844.
 16. Wu, J. B.; Shao, C.; Li, X.; Li, Q.; Hu, P.; Shi, C.; Li, Y.; Chen, Y. T.; Yin, F.; Liao, C. P.; Stiles, B. L.; Zhau, H. E.; Shih, J. C.; Chung, L. W., Monoamine oxidase A mediates prostate tumorigenesis and cancer metastasis. *J Clin Invest* **2014**, *124* (7), 2891-2908.
 17. Foraker, A. G., An analysis of nuclear size and nuclear: cytoplasmic ratio in the histological diagnosis of intraepithelial carcinoma of the cervix uteri. *Cancer* **1954**, *7* (5), 884-892.

7. PARTICIPANTS & OTHER COLLABORATING ORGANIZATIONS

There were no changes for the personnel.

8. SPECIAL REPORTING REQUIREMENTS

9. APPENDICES

Copies of the published articles:

Wu JB, Pan DF, Chung LWK. Near-infrared fluorescence and nuclear imaging and targeting of prostate cancer. *Transl Androl Urol* **2013**;2(3):254-264.

Wu JB, Shao C, Li X, Hu P, Chen Y-T, Li Q, Yin F, Li Y, Zhau HE, Shih JC, and Chung LWK. Monoamine oxidase A mediates prostate tumorigenesis and cancer metastasis. *J Clin Invest* **2014**, 124(7):2891-2908.

Wu JB, Shao C, Li X, Shi C, Li Q, Hu P, Chen Y-T, Dou X, Sahu D, Li W, Wang R, Zhau HE, Chung LWK. Near-infrared fluorescence imaging of cancer mediated by tumor hypoxia and HIF1 α /OATPs signaling axis. *Biomaterials* **2014**, 35:8175-8185.

Wu JB, Lin TP, Gallagher JD, Kushal S, Chung LW, Zhau HE, Olenyuk BZ, Shih JC. Monoamine oxidase A inhibitor – near-infrared dye conjugate reduces prostate tumor growth. *J Am Chem Soc* **2015**, 137(6):2366-74.

Wu JB, Shi C, Chu GC, Xu Q, Zhang Y, Li Q, Yu JS, Zhau HE, Chung LW. Near-infrared fluorescence heptamethine carbocyanine dyes mediate imaging and targeted drug delivery for brain tumor. *Biomaterials* **2015**, 67:1-10.



Published in final edited form as:

Transl Androl Urol. 2013 September ; 2(3): 254–264. doi:10.3978/j.issn.2223-4683.2013.09.05.

Near-infrared fluorescence and nuclear imaging and targeting of prostate cancer

Jason Wu¹, Dongfeng Pan², and Leland W.K. Chung¹

¹Uro-Oncology Research Program, Department of Medicine, Cedars-Sinai Medical Center, Los Angeles, CA 90048, USA

²Department of Radiology, The University of Virginia, Charlottesville, VA 22908, USA

Abstract

Despite advances in the treatment of castration-resistant and bone metastatic prostate cancer (PCa), there is still no clear demonstration that PCa growth and metastases can be unambiguously detected. We review recent advances including our own development of near-infrared fluorescence (NIRF) and near-infrared nuclear (NIRN) imaging approaches. We validated our results in experimental models of PCa bone and soft tissue metastases including PCa colonization at metastatic sites by injecting PCa cells either intratibially or intracardiacally. We describe our experience using noninvasive imaging and targeting modalities to probe PCa tumors grown at metastatic sites, molecular studies to understand the multiple molecular and cellular processes within tumor cells and their interactions with the tumor microenvironment, and targeting tumor growth at metastatic bone site. In this review, current knowledge and emerging technologies based on NIRF and NIRN disciplines will be summarized. Additionally the mechanisms of differential uptake of these agents by normal and cancerous cells will be described.

Keywords

Bone metastasis; heptamethine cyanine dyes; near-infrared fluorescence (NIRF); nuclear imaging; positron emission tomography (PET); prostate cancer (PCa)

Introduction

Prostate cancer (PCa) is a heterogeneous disease with the biological potential to develop an aggressive and lethal phenotype (1). PCa is the most common cancer diagnosed in men in the Western countries but only one of every 8–10 patients diagnosed with PCa will die from this disease (2,3). Thus it is important to develop effective methods not only to diagnose PCa but also to effectively select patients who need to be treated and avoid unnecessary treatment. It is also vital to target tumors that have recurred, escaping initial treatments and

© AME Publishing Company. All rights reserved.

Corresponding to: Leland W.K. Chung, Ph.D. 8750 Beverly Blvd., Atrium 103, Los Angeles, CA 90048. Leland.Chung@cshs.org; Dongfeng Pan, Ph.D. Department of Radiology, The University of Virginia, Charlottesville, VA 22908. DP3R@hscmail.mcc.virginia.edu.

Disclosure: The authors declare no conflict of interest.

developing into metastatic disease. Molecular imaging of PCa using such conventional imaging methodologies as X-ray computed tomography (CT), magnetic resonance imaging (MRI) and ultrasound has been successful for detecting organ-confined or metastatic disease for disease staging and companion diagnosis and prognosis (4,5). However, these techniques also show the limitations of current cancer-specific imaging and cannot reliably delineate the occurrence, the location, and the biochemical status of cancer and cancer metastases. Positron emission tomography (PET)/single-photon emission computed tomography (SPECT) for nuclear imaging have distinct advantages over conventional imaging, with unique noninvasive properties capable of monitoring the metabolic and molecular characteristics of cancer cells. These approaches utilize short-lived nuclear tracers and acquire signals emanating from the body after administration of imaging agents that target cancer-specific alterations, including glucose, amino acid and fatty acid metabolism, receptor status, cellular proliferation, tumor hypoxia and blood flow (6). Currently, several PET tracers have been applied for clinical imaging of both early- and late-stage PCa, such as ^{18}F -fluorodeoxyglucose (FDG), choline (^{11}C and ^{18}F labeled), ^{18}F -dihydrotestosterone (FDHT) and sodium ^{18}F -fluoride (NaF). These molecular imaging agents can potentially greatly elevate our ability to diagnose, prognose and monitor treatment responses in PCa patients.

Near-infrared fluorescence (NIRF) imaging agents can potentially increase the sensitivity and specificity of cancer diagnosis because NIRF have low autofluorescence, tissue absorbance, and scatter at NIR wavelengths (700–900 nm) (7). Once the specificity of these agents is established, a number of modifications can be made including the conversion of these agents into effective nuclear imaging probes, or conjugating these agents with effective therapeutic drugs to target cancer metastasis. The NIRF approach shares common physical properties with nuclear imaging techniques, such as the potential use of tracer administration of a contrast agent, which enables the development of combinational use of both techniques for cancer imaging (see below). Most conventional approaches for utilizing NIR dyes in cancer imaging require chemical conjugation of NIR fluorophores with appropriate cancer-targeting moieties such as peptides, antibodies, aptamers, growth factors and metabolic substrates (8–11). However, these approaches are less efficient because of tumor cell heterogeneity. Only a limited number of cancer cells may express the specified cell surface receptors or ligands, and the constant evolution of cancer cells known to occur within a tumor could alter cancer cell surface properties (12,13). The specificity and affinity of targeting ligands also be altered subtly following chemical conjugation (14). Our group has recently discovered a novel class of NIR heptamethine carbocyanine dyes that can be used as dual imaging and targeting agents, and demonstrated their preferential accumulation and retention in cancer but not normal cells, enabling cancer-specific targeting without the need for chemical conjugation (15,16). These agents greatly fulfill the unmet needs for specific imaging of PCa despite its heterogeneity, which to some extent is inadequately assessed by conventional methods. In this review, we will discuss recent advances in the development of novel NIRF, NIRN and NIRF-derived agents and techniques for imaging and targeting localized and metastatic PCa.

NIRF imaging of prostate cancer

NIRF imaging agents

Indocyanine green (ICG) is a noninvasive NIRF imaging dye that has been used clinically for more than 50 years for ophthalmic angiography and to determine cardiac output and liver blood flow and function (7,17). This tricyanocyanine dye is also used in cancer patients to map sentinel lymph nodes, for the detection of some tumors due to their enhanced angiogenesis, and for angiography during reconstructive surgery as the only NIRF agent approved by the United States Food and Drug Administration (FDA) (18–21). Most human NIR imaging studies employ ICG within the blood and lymphatic vasculatures. ICG and its derivatives are widely used clinically and show reasonable NIR features (ex/em 760–785/820–840 nm) and the capability to image normal but not cancerous tissues, generating weaker fluorescent properties (i.e., lower extinction coefficients) in comparison to the NIRF described herein (7,17). Several new NIRF agents have been developed including heptamethine carbocyanine dyes. Some of these agents have become commercially available in recent years, such as Cy5.5 (22) and IRDye 800-CW (23), which have been coupled with peptides or antibodies and successfully used for the targeted visualization of neoplastic tumors in animal models. Marshall *et al.*, for example, reported a safety and toxicity study of the NIRF dye IRDye 800CW in rats that showed no evidence of organ toxicity based on the hematologic, clinical chemistry and histopathologic analyses of tissues harvested from the experimental animals (23). These new NIRF agents offer great promise for future clinical applications of NIRF imaging agents.

NIRF imaging of prostate cancer

Conventional application of NIRF agents in PCa imaging use the chemical conjugation of specified NIRF agents to cancer cell-surface targeting moieties, such as peptides and antibodies recognized as tumor-specific biomarkers (19). One such biomarker is prostate-specific antigen (PSA), an androgen receptor (AR) target gene expressed almost exclusively by prostate epithelium. PSA, expressed by both benign and malignant prostate epithelium, potentially reflects active AR signaling activity (24). Since AR-mediated cell signaling pathways are known to determine human PCa initiation and progression, and AR expression and activity are elevated in some castration-resistant PCa (CRPC) (25), many groups have sought to image PCa through the use of PSA as a biomarker. PSA is initially produced as a catalytically active serine protease (free PSA), released subsequently into the perivascular space, by rapid and irreversible conversion to non-catalytic forms (26,27). In a recent study, Ulmert *et al.* described a new approach to specifically image tumor-associated free PSA in multiple preclinical models with ⁸⁹Zr-labeled 5A10, a novel radiotracer consisting of a monoclonal antibody that specifically recognizes an epitope adjacent to the catalytic cleft of PSA (28). In line with the same principle, Ho *et al.* developed an enzymatically cleavable peptide sequence labeled with NIR fluorophores (ex/em 740/770 nm), PSA750, which is optically quenched (>95%) and only becomes fluorescent upon cleavage by enzymatically-active PSA, yielding a significantly increased NIR signal from the site where PSA is secreted or deposited (29). Currently, serum PSA levels are widely used clinically as an indicator for primary screening and a biomarker for therapeutic responses, but PSA expression alone cannot distinguish benign from malignant prostate epithelium (30,31). The

noninvasive imaging tools developed for measuring tumor-associated PSA expression could more clearly reflect AR-driven changes in PSA expression and could be used to supplement the current clinical PSA test.

Another cell-surface antigen for PCa is prostate-specific membrane antigen (PSMA). PSMA, elevated in CRPC, is a plausible target for imaging probe development (32–34). Radioactive ^{111}In -labeled PSMA antibody has been used as a reagent in SPECT imaging. In addition to being a biomarker of PCa, PSMA has been proposed as a target for image-guided surgery due to its cell surface-expressing characteristics. To better identify prostate tumor margins during surgery, Nakajima *et al.* synthesized an activatable anti-PSMA monoclonal antibody (J591)-NIR fluorophore (ICG) conjugate and tested it in a PC-3 prostate tumor xenograft mouse model (35). Prior to binding to PSMA and cellular internalization, the conjugate yielded little light. However, upon internalization and cleavage, NIR-ICG intensity in PCa was elevated by 18-fold, permitting the detection of PSMA+ PC-3 but not PSMA– PC-3 tumors for up to 10 days after a low-dose (0.25 mg/kg) injection. In another study, Humblet *et al.* synthesized a single nucleophile-containing small molecule specific for the active site of PSMA enzyme that is chemically conjugated to an ICG derivative (10). This conjugate shows high-affinity binding to PSMA in xenograft prostate tumors by NIRF imaging. These NIRF-based PSMA-targeting imaging approaches are reproducible at the cellular level in PCa as well. Liu *et al.* developed a NIRF imaging probe (Cy5.5-CTT-54.2) by chemical conjugation of a Cy5.5 derivative with a potent PSMA inhibitor (CTT-54.2) (36). The probe displays high potency against PSMA and has demonstrated successful application for specifically labeling PSMA+ LNCaP PCa cells in both 2D and 3D cell culture conditions.

Another approach to developing targeted molecules relies on the aberrant metabolic pathways established by cancer cells. Cancer cells have been observed to exhibit altered metabolism and increased requirements for glucose and glutamine, which is facilitated by the overexpression of glucose transporter proteins (GLUTs) (37–39). FDG is a glucose analog that has been used extensively in cancer detection and therapeutic monitoring in the form of a ^{18}F -FDG probe, detected by PET (40,41). The ^{18}F -FDG probe, however, has several limitations, such as an extremely short half-life for following by positron-emitting nuclides, exhibiting low spatial resolution, being a radioactive compound, and is also abundantly taken up by tissues with high basal metabolic rates, such as the brain. To overcome these intrinsic PET imaging limitations, an NIRF imaging approach has been proposed and developed as a replacement for metabolic imaging using a similar targeting principle. Korotcov *et al.* (42) designed an NIRF probe (cypate) chemically conjugated to one or more glucosamine (GlcN) moieties, a common substrate for all 4 isoforms of GLUTs with higher affinity for GLUT2 than glucose (39,42,43), and demonstrated good uptake of the GlcN-linked NIRF probe in both PC-3 cell culture and live mice. In summary, diverse molecular imaging approaches from different research groups have demonstrated the effectiveness of targeting cell surface-based biomarkers or the metabolic differences between normal and cancer cells for monitoring PCa growth and recognizing the surgical margins of PCa tumors during surgery.

NIRF imaging of metastases in experimental prostate cancer models

Imaging of lymph node metastases

Early-stage PCa develops seminal vesicle invasion and micrometastases to surrounding lymph nodes (LNs). Pelvic LN dissection (PLND) is widely used in the clinic for nodal staging and assessing LN metastases in PCa (44). However, this method is invasive and underestimates LN involvement; 40–50% of patients are found to have metastatic LNs outside the standard resection area (45,46). There is an unmet need for more accurate noninvasive diagnostic techniques. Abnormal lymphatic function has been associated with a wide spectrum of diseases and is also intimately involved in cancer metastases (7,47). Preclinical cancer studies show apparent dilation and proliferation of tumor-draining lymphatic vessels and tumor-draining lymph node remodeling (47), which offers a targeting opportunity for noninvasive lymphatic imaging with NIRF probes. As the only NIRF agent approved by the FDA, ICG has been used noninvasively in humans to uniquely detect blood and lymphatic vasculatures and used intraoperatively in sentinel LN mapping for visualization of tumor-draining LNs in several types of cancers including PCa (7). Van der Poel *et al.* recently reported an approach integrating ICG with a radioisotope (^{99m}Tc) and nanoparticles for injection into the prostate prior to surgery for improved surgical guidance via multimodal imaging, particularly fluorescence imaging (48). *Ex vivo* analysis further revealed a strong correlation between the radioactive and fluorescent content in the excised LNs. Similar detection outcomes in the percentages of PCa metastases to LNs by NIRF imaging (63%) and $\mu\text{PET}/\text{CT}$ (64%) were also reported by Hall *et al.*, further confirmed by pathological examination (49). Alternatively, targeting PCa biomarker molecules as a conventional approach facilitates NIRF detection of LN metastases. Cai *et al.* (50) synthesized NIRF dye (Alexa Fluor 680) conjugated BBN[7-14] NH_2 peptides that target gastrin-releasing peptide receptors (GRPRs), which showed high densities on the cell membranes of prostatic intraepithelial neoplasia (PIN), primary PCa and invasive prostatic carcinomas with predominately negative expression in normal prostate tissue and benign prostatic hyperplasia (BPH) (51,52), in an orthotopic PC-3 xenograft mouse model. Within 2-hour post-injection, the conjugate reached the highest binding specificity and affinity in GRPR+ cancer *in vivo*, and LN and peritoneal metastases were detected by NIRF imaging, which was later confirmed by histopathology. These studies across different groups suggest the promising future clinical utility of NIRF imaging in PCa staging and laparoscopic LN dissection, which would be boosted by improved imaging devices with better signal capture from deep tissue in the near future.

Imaging of bone metastases

PCa patients develop lethal bone metastases in the late stage of disease progression. Current clinical examinations of PCa bone metastases rely on PET/SPECT/CT scans. While potential limitations in the use of these radiotracers in PET and SPECT imaging including exposure to radiation, difficulty in synthesizing radioactive tracers, and short interval of tracer retention in tumors, they are nevertheless preferred in patients due to the variability of tumor depth in patients. NIRF imaging, however, offers companion diagnostic and prognostic value by having a potentially better safety profile, lower cost and desirable sensitivity for the diagnosis of cancer metastasis. Recent advances have been made in

multiple NIRF imaging approaches to the visualization of bone metastases utilizing different targeting strategies. We previously synthesized a NIR quantum dot (QD) probe (QD800) conjugated to an anti-PSMA antibody and demonstrated the specific recognition of C4-2B xenografts residing in mouse tibia by this NIRF conjugate using the IVIS Imaging System (53). The maximal light emission was detected 30 minutes after intravenous injection of QD800 conjugate in mice. In addition to the conventional chemical conjugation method, we were also able to detect metastatic PCa cells in either bone metastases or in the precursor state as circulating tumor cells (CTCs) by a novel class of heptamethine carbocyanine dyes (see below) in an orthotopic ARCaP_M xenograft mouse model (16).

Novel heptamethine carbocyanine fluorescence dye-based imaging of prostate cancer

Heptamethine carbocyanine fluorescence imaging agents

We recently discovered a novel class of NIRF heptamethine carbocyanine dyes, IR-783 and MHI-148, which is an effective cancer-specific imaging agent. These agents show preferential uptake and retention in cancer but not normal cells (15,16). By conjugating chemotherapeutic agents with these dyes, we observed tumor-specific cell kill without cytotoxicity in host mice, suggesting the potential use of these carbocyanine dyes as carriers for cancer-specific targeting by small molecules (see below). The advantages of this new class of NIRF as imaging agents are: (I) They have relatively low molecular weights that facilitate their effective uptake into both localized and metastatic cancers; (II) They can be synthesized in pure form and are stable upon storage; (III) They are taken up by many different types of cancer cells, including circulating or disseminated tumor cells and cancer tissues regardless of their cell-surface properties and their plasticity; and (IV) They have the potential of recognizing live versus dead cells and therefore can be used for follow-up in patients subjected to treatment by hormonal, radiation and chemotherapeutic agents. We found that these dyes can be retained in established PCa cell lines (C4-2, PC-3 and ARCaP_M) with the dyes enriched in the mitochondria and lysosomes, but not in normal prostatic epithelial and fibroblast cells. In an orthotopic ARCaP_M xenograft mouse model receiving intraperitoneal injection of low dose of IR-783 (10 nmol/20 g), the NIRF signals were specifically detected in the primary tumor and its associated bone metastases within 24 hours by fluorescence optical imaging. Similar targeting was also found in spontaneously developed prostate and colon tumors in the TRAMP PCa and ApcMin/+ colon cancer mouse models, respectively (16). Recently, we extended these studies to demonstrate successful detection of dye uptake in freshly harvested human PCa tissue xenografts as well as CTCs using these novel NIRF agents. Additionally this novel class of NIRF showed no systemic toxicity when mice were given a 100-fold excess of the imaging dose of NIRF.

Near-infrared nuclear imaging of prostate cancer using novel heptamethine carbocyanine dyes conjugated to ⁶⁴Cu as PET probes

Although early detection of PCa by blood tests for elevated levels of PSA has led to early treatment and a reduction in death rates, PSA level alone does not distinguish between PCa and normal conditions that cause elevated PSA (30,31). Because PCa can be a very slow-growing cancer, even confirmation of PCa cells in a biopsy gives no indication whether an

active disease will progress within the individual's lifetime. As a result many patients receive painful repeated needle biopsies when PSA is found to be elevated. Successful management of prostate cancer requires early detection, appropriate risk assessment, and optimal treatment to avoid the development of CRPC with potential of lethal progression (54). Nuclear imaging is an attractive modality for the detection and characterization of disease because it is non-invasive, quantitative, provides dynamic real-time data, and allows the diagnosis and follow-up of patients undergoing therapy (6). Whether the development of new nuclear imaging probes could offer the opportunity of differentiating indolent from aggressive prostate tumors remains untested.

Different radionuclide-based imaging agents for planar, PET and SPECT imaging are currently used in the clinic with some under development for PCa. Clinical agents include the bone agent methylene diphosphonate (MDP, ^{99m}Tc labeled), the metabolic agent ^{18}F -FDG, and receptor targeted radiolabeled monoclonal antibodies including the PSMA-based ProstaScint. Agents in development for PCa include acetate (^{11}C labeled), choline (^{11}C and ^{18}F labeled), 1-aminocyclobutane-1-carboxylic acid (^{11}C and ^{18}F labeled), radiolabeled AR binding compounds, radiolabeled peptides and small molecules for receptors overexpressed in PCa or PCa-associated tumor neovasculature. Despite a variety of probes using nuclear imaging modalities, neither the detection of minimal disease nor the prediction of indolent versus aggressive PCa has been accomplished. A simple, accurate method for localizing cancer within the prostate for focal therapy also remains elusive.

As part of our extensive search for agents that might have cancer-specific uptake in PCa, we reported the discovery of a new class of heptamethine carbocyanine dyes that allow detection of human and mouse tumors with a high degree of sensitivity and specificity(15,16). To further improve the sensitivity and clinical utility of this class of carbocyanine dyes for deep-tissue detection of tumors, we modified the dye by conjugating it with a positron-emitting radionuclide (see below) and tested its feasibility in cultured human PCa cells and metastatic prostate tumors in mice.

We synthesized a PET/NIRF probe PC-1001 by conjugating MHI-148 with a DOTA chelator and subsequent chelating with ^{64}Cu for independent PET and fluorescence imaging (Figure 1). This two-component probe is the first example of novel tumor-specific fluorescent dye with both targeting and detection properties in one component and a second component (^{64}Cu -DOTA) with the capability to perform nuclear imaging. In contrast to all other multimodal probes reported to date, the tumor-targeting component is separate from the detection component and thus needs a minimum of three components. The NIRF imaging modality has the merits of simplicity, convenience, and high throughput. The NIRF property of the probe simplifies the early stages of its development for *in vitro* and *in vivo* optimization of parameters and its validity prior to final live animal PET imaging. NIRF alone has inherent shortcomings such as its low resolution and non-quantitative nature. The sensitivity and resolution of NIRF imaging is severely influenced by position and depth of the imaging probes in the body. The positron emitting property of the conjugated probe can overcome the shortcomings of NIRF and provide high sensitivity and deep-tissue spatial resolution for initial detection of primary tumors and their metastatic lesions. Tumor size can then be monitored over time with NIRF imaging. Our recent results showed successful

PC-1001/NIRF image of a mouse with a metastatic RANKL-overexpressing LNCaP tumor demonstrating two superficial tumors in the mouse (55) (Figure 2A), while the PC-1001/PET image of the same mouse revealed an extra tumor in a deep location (Figure 2B).

The dual-modality PC-1001 molecular imaging probe described above has demonstrated its applicability for tumor detection and quantitative image analysis in a metastatic PCa mouse model. The PC-1001 probe is accumulated specifically in cancerous tissue with good contrast to normal tissue. This probe could be useful in assisting the evaluation of anti-cancer therapies, anti-cancer drug discovery, and cancer-related biological studies. Further biological and toxicological evaluation of this imaging agent is ongoing, with the aim of advancing into clinical trials. Other laboratories have also designed dual-modality PCa imaging probes. In a recent study, Ghosh *et al.* designed a multimodality chelation scaffold (MMC) that combined a radiometal chelating agent (^{64}Cu) and NIRF dye (a IRDye 800CW derivative) (56). Using MMC-immunoconjugate to target an epithelial cell adhesion molecule (EpCAM), which shows elevated expression with PCa biochemical recurrence and correlation with Gleason scores (57,58), multimodal imaging studies indicated higher tumor accumulation of the dual-labeled conjugate compared to either single-labeled agent in a PC-3 tumor-bearing mouse model. Another example is EphB4, a key member of the Eph receptors overexpressed in numerous tumor types including PCa (59–61), which has been developed as a promising imaging target. Zhang *et al.* reported the visualization of EphB4+ PC-3M PCa xenografts with an EphB4-binding peptide (TNYL-RAW)-nanoparticle conjugate dually labeled with NIRF fluorophores (Cy7) and a radioisotope ^{111}In , with both NIRF and NIRM imaging (62). The high accumulation of dually labeled peptide in PC-3M tumor could be significantly reduced after co-injection with an excess amount of unlabeled peptide, suggesting the specificity of this imaging probe for recognizing EphB4 receptor. These reports support the promise of dual labeling imaging approaches for improved sensitivity and depth of imaging compared to NIRF imaging alone.

Novel heptamethine carbocyanine drug conjugates for targeting castration-resistant and bone metastatic prostate cancer

Because CRPC is considered as the most advanced and lethal form of PCa, we synthesized a number of heptamethine carbocyanine drug conjugates to target metastatic PCa more efficiently. The basic principle of these studies is to use heptamethine carbocyanine dyes as the drug carriers. They will be covalently conjugated to drugs through a linker composed of either an ester or a peptide bond. Upon uptake, these dye-drug conjugates accumulate exclusively in tumor tissues. Results using IR-783-docetaxel conjugate showed metastatic PCa tumor shrinkage in mouse tibia (Figure 3). While mice treated with this dye-drug conjugate showed no visible toxicity or reduced body weights, control mice treated with docetaxel alone had dramatically reduced body weights and over 50% mortality. These encouraging results have been shown to be repeatable using other dye-drug conjugates. Future safety studies are necessary before moving this concept into the clinic.

Mechanisms of uptake of heptamethine carbocyanine dyes by prostate cancer cells

We have studied the underlying mechanisms by which heptamethine carbocyanine dyes are taken up specifically into cancer but not normal cells. We investigated the effects of tumor hypoxia, a common condition found in a wide range of cancer cells or solid tumors, on the uptake of heptamethine cyanines into cancer cells. In our unpublished studies (Wu and Shao *et al.* 2013), unlike ICG that has a relatively low value of tumor-to-background ratio at 1.4–1.7 (63), measured at 24 hours after the administration of the dye into tumor-bearing mice, we showed that this ratio increased to 9.1 in tumors when MHI-148 was used, which was further enhanced by 2-fold when cells were maintained under hypoxic conditions. We found that a superfamily of organic anion carrier transporters, named organic anion-transporting peptides (OATPs), plays key roles accounting for the differential uptake of these dyes into cancer but not normal cells. We conducted microarray analyses and later confirmed by qRT-PCR, western blots and immunohistochemistry that specific isoforms of OATPs might be responsible for cancer-specific dye uptake. Currently there are 11 known human OATPs classified into 6 families and subfamilies on the basis of their amino acid sequence homologies, which facilitate the transport of a large number of substrates, including organic acids, drugs and hormones into cells in a highly substrate- and pathophysiologic-dependent manner (64). The dye uptake and retention in cancer cells can be blocked completely by several competitive inhibitors of OATPs, such as bromosulfophthalein (16). Increased expression of select OATPs, such as OATP1B3 and OATP2B1, by either aberrant gene regulation or genetic variation, has been reported in clinical PCa, particularly during progression to a CRPC state (64–67). Notably, OATP1B3 also serves as a testosterone transporter (68,69), and its transporting activity may be further exacerbated by low levels of testosterone in CRPC (67,70,71). In addition, we and another group dissected a direct regulatory mechanism of OATP1B3 expression by hypoxia through HIF1 α in PCa cells, which provides a functional link among different mediators that enhance dye uptake. Specific accumulation of dye and dye-drug conjugates in cancer cells can also be attributed to the high-affinity binding of this class of dyes once they enter into cells to interact with nucleic acids and proteins, which warrants further investigation.

Conclusions and future perspectives

We demonstrated the specific uptake and retention of a novel class of NIRF imaging agents, heptamethine carbocyanine dyes that can be used for imaging solid tumors and CTCs freshly harvested from human patients. This new class of NIRF imaging agents has been successfully tested as dual NIRF and NIRN agents using PET/SPECT to detect PCa bone and soft tissue metastases in experimental models. By further conjugating this class of NIRF/NIRN agents with cancer therapeutic drugs, we found that they can serve as drug carriers for the safe delivery of chemotherapies to experimental tumors. We found also that the differential uptake of this class of negatively charged carbocyanine dyes into cancer but not normal cells was largely due to the presence of specific isoforms of OATPs, coupled with specific metabolisms regulated by hypoxia and mitochondrial membrane potentials and the physical chemical reactions of this class of dyes when in close contact with nucleic acids and proteins in cancer cells. While promising data have accumulated thus far, crucial evaluation of the PK, PD and toxicity of the dyes and dye-drug conjugates are needed before

this group of novel compounds can be moved into the clinic for improved cancer diagnosis, prognosis and treatment.

Acknowledgments

This work was supported by NIH Grants 5P01CA098912, R01CA122602, Prostate Cancer Foundation Challenge Award, and Board of Governors Chair in Cancer Research fund (L.W-K.C.). The authors thank Mr. Gary Mawyer for his editorial assistance.

Dr. Dongfeng Pan and Dr. Leland W. K. Chung are the co-owner of Imol Radiopharmaceuticals, LLC (Charlottesville, Virginia) and Dr. Leland W. K. Chung is a co-owner of Da Zen Theranostics, LLC (Los Angeles, California).

References

1. Scher HI, Heller G. Clinical states in prostate cancer: toward a dynamic model of disease progression. *Urology*. 2000; 55:323–7. [PubMed: 10699601]
2. Siegel R, Naishadham D, Jemal A. Cancer statistics, 2012. *CA Cancer J Clin*. 2012; 62:10–29. [PubMed: 22237781]
3. Cooperberg MR, Carroll PR, Klotz L. Active surveillance for prostate cancer: progress and promise. *J Clin Oncol*. 2011; 29:3669–76. [PubMed: 21825257]
4. O'Donoghue PM, McSweeney SE, Jhaveri K. Genitourinary imaging: current and emerging applications. *J Postgrad Med*. 2010; 56:131–9. [PubMed: 20622393]
5. Marks L, Young S, Natarajan S. MRI-ultrasound fusion for guidance of targeted prostate biopsy. *Curr Opin Urol*. 2013; 23:43–50. [PubMed: 23138468]
6. Fox JJ, Schöder H, Larson SM. Molecular imaging of prostate cancer. *Curr Opin Urol*. 2012; 22:320–7. [PubMed: 22617062]
7. Sevcik-Muraca EM. Translation of near-infrared fluorescence imaging technologies: emerging clinical applications. *Annu Rev Med*. 2012; 63:217–31. [PubMed: 22034868]
8. Gao X, Cui Y, Levenson RM, et al. In vivo cancer targeting and imaging with semiconductor quantum dots. *Nat Biotechnol*. 2004; 22:969–76. [PubMed: 15258594]
9. Hintersteiner M, Enz A, Frey P, et al. In vivo detection of amyloid-beta deposits by near-infrared imaging using an oxazine-derivative probe. *Nat Biotechnol*. 2005; 23:577–83. [PubMed: 15834405]
10. Humblet V, Lapidus R, Williams LR, et al. High-affinity near-infrared fluorescent small-molecule contrast agents for in vivo imaging of prostate-specific membrane antigen. *Mol Imaging*. 2005; 4:448–62. [PubMed: 16285907]
11. Wu X, Liu H, Liu J, et al. Immunofluorescent labeling of cancer marker Her2 and other cellular targets with semiconductor quantum dots. *Nat Biotechnol*. 2003; 21:41–6. [PubMed: 12459735]
12. Edwards PA. Heterogeneous expression of cell-surface antigens in normal epithelia and their tumours, revealed by monoclonal antibodies. *Br J Cancer*. 1985; 51:149–60. [PubMed: 2578284]
13. Heppner GH, Miller FR. The cellular basis of tumor progression. *Int Rev Cytol*. 1998; 177:1–56. [PubMed: 9378615]
14. Rao J, Dragulescu-Andrasi A, Yao H. Fluorescence imaging in vivo: recent advances. *Curr Opin Biotechnol*. 2007; 18:17–25. [PubMed: 17234399]
15. Yang X, Shao C, Wang R, et al. Optical imaging of kidney cancer with novel near infrared heptamethine carbocyanine fluorescent dyes. *J Urol*. 2013; 189:702–10. [PubMed: 23000848]
16. Yang X, Shi C, Tong R, et al. Near IR heptamethine cyanine dye-mediated cancer imaging. *Clin Cancer Res*. 2010; 16:2833–44. [PubMed: 20410058]
17. Zhu B, Rasmussen JC, Lu Y, et al. Reduction of excitation light leakage to improve near-infrared fluorescence imaging for tissue surface and deep tissue imaging. *Med Phys*. 2010; 37:5961–70. [PubMed: 21158309]
18. Crane LM, Themelis G, Buddingh KT, et al. Multispectral real-time fluorescence imaging for intraoperative detection of the sentinel lymph node in gynecologic oncology. *J Vis Exp*. 2010; (44): pii: 2225.

19. Sevick-Muraca EM, Sharma R, Rasmussen JC, et al. Imaging of lymph flow in breast cancer patients after microdose administration of a near-infrared fluorophore: feasibility study. *Radiology*. 2008; 246:734–41. [PubMed: 18223125]
20. Kaibori M, Ishizaki M, Matsui K, et al. Intraoperative indocyanine green fluorescent imaging for prevention of bile leakage after hepatic resection. *Surgery*. 2011; 150:91–8. [PubMed: 21514613]
21. Chen SF, Kato Y, Oda J, et al. The application of intraoperative near-infrared indocyanine green videoangiography and analysis of fluorescence intensity in cerebrovascular surgery. *Surg Neurol Int*. 2011; 2:42. [PubMed: 21541008]
22. The MICAD Research Team. Bombesin peptide conjugated–cross-linked iron oxide-Cy5.5.
23. Marshall MV, Draney D, Sevick-Muraca EM, et al. Single-dose intravenous toxicity study of IRDye 800CW in Sprague-Dawley rats. *Mol Imaging Biol*. 2010; 12:583–94. [PubMed: 20376568]
24. Lilja H, Ulmert D, Vickers AJ. Prostate-specific antigen and prostate cancer: prediction, detection and monitoring. *Nat Rev Cancer*. 2008; 8:268–78. [PubMed: 18337732]
25. Tsao CK, Galsky MD, Small AC, et al. Targeting the androgen receptor signalling axis in castration-resistant prostate cancer (CRPC). *BJU Int*. 2012; 110:1580–8. [PubMed: 22985411]
26. Lilja H. A kallikrein-like serine protease in prostatic fluid cleaves the predominant seminal vesicle protein. *J Clin Invest*. 1985; 76:1899–903. [PubMed: 3902893]
27. Christensson A, Laurell CB, Lilja H. Enzymatic activity of prostate-specific antigen and its reactions with extracellular serine proteinase inhibitors. *Eur J Biochem*. 1990; 194:755–63. [PubMed: 1702714]
28. Ulmert D, Evans MJ, Holland JP, et al. Imaging androgen receptor signaling with a radiotracer targeting free prostate-specific antigen. *Cancer Discov*. 2012; 2:320–7. [PubMed: 22576209]
29. Ho G, Morin J, Delaney J, et al. Detection and quantification of enzymatically active prostate-specific antigen in vivo. *J Biomed Opt*. 2013; 18:101319. [PubMed: 23933968]
30. Ulmert D, Serio AM, O'Brien MF, et al. Long-term prediction of prostate cancer: prostate-specific antigen (PSA) velocity is predictive but does not improve the predictive accuracy of a single PSA measurement 15 years or more before cancer diagnosis in a large, representative, unscreened population. *J Clin Oncol*. 2008; 26:835–41. [PubMed: 18281654]
31. Ulmert D, Cronin AM, Björk T, et al. Prostate-specific antigen at or before age 50 as a predictor of advanced prostate cancer diagnosed up to 25 years later: a case-control study. *BMC Med*. 2008; 6:6. [PubMed: 18279502]
32. Bostwick DG, Pacelli A, Blute M, et al. Prostate specific membrane antigen expression in prostatic intraepithelial neoplasia and adenocarcinoma: a study of 184 cases. *Cancer*. 1998; 82:2256–61. [PubMed: 9610707]
33. Wright GL Jr, Haley C, Beckett ML, et al. Expression of prostate-specific membrane antigen in normal, benign, and malignant prostate tissues. *Urol Oncol*. 1995; 1:18–28. [PubMed: 21224086]
34. Mannweiler S, Amersdorfer P, Trajanoski S, et al. Heterogeneity of prostate-specific membrane antigen (PSMA) expression in prostate carcinoma with distant metastasis. *Pathol Oncol Res*. 2009; 15:167–72. [PubMed: 18802790]
35. Nakajima T, Mitsunaga M, Bander NH, et al. Targeted, activatable, in vivo fluorescence imaging of prostate-specific membrane antigen (PSMA) positive tumors using the quenched humanized J591 antibody-indocyanine green (ICG) conjugate. *Bioconjug Chem*. 2011; 22:1700–5. [PubMed: 21740058]
36. Liu T, Wu LY, Hopkins MR, et al. A targeted low molecular weight near-infrared fluorescent probe for prostate cancer. *Bioorg Med Chem Lett*. 2010; 20:7124–6. [PubMed: 20947349]
37. Macheda ML, Rogers S, Best JD. Molecular and cellular regulation of glucose transporter (GLUT) proteins in cancer. *J Cell Physiol*. 2005; 202:654–62. [PubMed: 15389572]
38. Shaw RJ. Glucose metabolism and cancer. *Curr Opin Cell Biol*. 2006; 18:598–608. [PubMed: 17046224]
39. Calvo MB, Figueroa A, Pulido EG, et al. Potential role of sugar transporters in cancer and their relationship with anticancer therapy. *Int J Endocrinol*. 2010; 2010 pii: 205357.
40. Gambhir SS. Molecular imaging of cancer with positron emission tomography. *Nat Rev Cancer*. 2002; 2:683–93. [PubMed: 12209157]

41. Pysz MA, Gambhir SS, Willmann JK. Molecular imaging: current status and emerging strategies. *Clin Radiol*. 2010; 65:500–16. [PubMed: 20541650]
42. Korotcov AV, Ye Y, Chen Y, et al. Glucosamine-linked near-infrared fluorescent probes for imaging of solid tumor xenografts. *Mol Imaging Biol*. 2012; 14:443–51. [PubMed: 21971932]
43. Uldry M, Ibberson M, Hosokawa M, et al. GLUT2 is a high affinity glucosamine transporter. *FEBS Lett*. 2002; 524:199–203. [PubMed: 12135767]
44. Briganti A, Larcher A, Abdollah F, et al. Updated nomogram predicting lymph node invasion in patients with prostate cancer undergoing extended pelvic lymph node dissection: the essential importance of percentage of positive cores. *Eur Urol*. 2012; 61:480–7. [PubMed: 22078338]
45. Heesakkers RA, Jager GJ, Hövels AM, et al. Prostate cancer: detection of lymph node metastases outside the routine surgical area with ferumoxtran-10-enhanced MR imaging. *Radiology*. 2009; 251:408–14. [PubMed: 19401573]
46. Heidenreich A, Varga Z, Von Knobloch R. Extended pelvic lymphadenectomy in patients undergoing radical prostatectomy: high incidence of lymph node metastasis. *J Urol*. 2002; 167:1681–6. [PubMed: 11912387]
47. Tammela T, Alitalo K. Lymphangiogenesis: Molecular mechanisms and future promise. *Cell*. 2010; 140:460–76. [PubMed: 20178740]
48. van der Poel HG, Buckle T, et al. Intraoperative laparoscopic fluorescence guidance to the sentinel lymph node in prostate cancer patients: clinical proof of concept of an integrated functional imaging approach using a multimodal tracer. *Eur Urol*. 2011; 60:826–33. [PubMed: 21458154]
49. Hall MA, Kwon S, Robinson H, et al. Imaging prostate cancer lymph node metastases with a multimodality contrast agent. *Prostate*. 2012; 72:129–46. [PubMed: 21538422]
50. Cai QY, Yu P, Besch-Williford C, et al. Near-infrared fluorescence imaging of gastrin releasing peptide receptor targeting in prostate cancer lymph node metastases. *Prostate*. 2013; 73:842–54. [PubMed: 23280511]
51. de Visser M, van Weerden WM, de Ridder CM, et al. Androgen-dependent expression of the gastrin-releasing peptide receptor in human prostate tumor xenografts. *J Nucl Med*. 2007; 48:88–93. [PubMed: 17204703]
52. Markwalder R, Reubi JC. Gastrin-releasing peptide receptors in the human prostate: relation to neoplastic transformation. *Cancer Res*. 1999; 59:1152–9. [PubMed: 10070977]
53. Shi C, Zhu Y, Xie Z, et al. Visualizing human prostate cancer cells in mouse skeleton using bioconjugated near-infrared fluorescent quantum dots. *Urology*. 2009; 74:446–51. [PubMed: 19428067]
54. Zaheer A, Cho SY, Pomper MG. New agents and techniques for imaging prostate cancer. *J Nucl Med*. 2009; 50:1387–90. [PubMed: 19690043]
55. Hu P, Chu GC, Zhu G, et al. Multiplexed quantum dot labeling of activated c-Met signaling in castration-resistant human prostate cancer. *PLoS One*. 2011; 6:e28670. [PubMed: 22205960]
56. Ghosh SC, Ghosh P, Wilganowski N, et al. Multimodal chelation platform for near-infrared fluorescence/nuclear imaging. *J Med Chem*. 2013; 56:406–16. [PubMed: 23214723]
57. Benko G, Spajić B, Krušlin B, et al. Impact of the EpCAM expression on biochemical recurrence-free survival in clinically localized prostate cancer. *Urol Oncol*. 2013; 31:468–74. [PubMed: 21514185]
58. Mukherjee S, Richardson AM, Rodriguez-Canales J, et al. Identification of EpCAM as a molecular target of prostate cancer stroma. *Am J Pathol*. 2009; 175:2277–87. [PubMed: 19850885]
59. Dodelet VC, Pasquale EB. Eph receptors and ephrin ligands: embryogenesis to tumorigenesis. *Oncogene*. 2000; 19:5614–9. [PubMed: 11114742]
60. Nakamoto M, Bergemann AD. Diverse roles for the Eph family of receptor tyrosine kinases in carcinogenesis. *Microsc Res Tech*. 2002; 59:58–67. [PubMed: 12242697]
61. Lee YC, Perren JR, Douglas EL, et al. Investigation of the expression of the EphB4 receptor tyrosine kinase in prostate carcinoma. *BMC Cancer*. 2005; 5:119. [PubMed: 16171530]
62. Zhang R, Xiong C, Huang M, et al. Peptide-conjugated polymeric micellar nanoparticles for Dual SPECT and optical imaging of EphB4 receptors in prostate cancer xenografts. *Biomaterials*. 2011; 32:5872–9. [PubMed: 21612822]

63. Kosaka N, Mitsunaga M, Longmire MR, et al. Near infrared fluorescence-guided real-time endoscopic detection of peritoneal ovarian cancer nodules using intravenously injected indocyanine green. *Int J Cancer*. 2011; 129:1671–7. [PubMed: 21469142]
64. Obaidat A, Roth M, Hagenbuch B. The expression and function of organic anion transporting polypeptides in normal tissues and in cancer. *Annu Rev Pharmacol Toxicol*. 2012; 52:135–51. [PubMed: 21854228]
65. Pressler H, Sissung TM, Venzon D, et al. Expression of OATP family members in hormone-related cancers: potential markers of progression. *PLoS One*. 2011; 6:e20372. [PubMed: 21625523]
66. Fujimoto N, Kubo T, Inatomi H, et al. Polymorphisms of the androgen transporting gene *SLCO2B1* may influence the castration resistance of prostate cancer and the racial differences in response to androgen deprivation. *Prostate Cancer Prostatic Dis*. 2013; 16:336–40. [PubMed: 23896625]
67. Yang M, Xie W, Mostaghel E, et al. *SLCO2B1* and *SLCO1B3* may determine time to progression for patients receiving androgen deprivation therapy for prostate cancer. *J Clin Oncol*. 2011; 29:2565–73. [PubMed: 21606417]
68. Sharifi N, Hamada A, Sissung T, et al. A polymorphism in a transporter of testosterone is a determinant of androgen independence in prostate cancer. *BJU Int*. 2008; 102:617–21. [PubMed: 18537956]
69. Hamada A, Sissung T, Price DK, et al. Effect of *SLCO1B3* haplotype on testosterone transport and clinical outcome in caucasian patients with androgen-independent prostatic cancer. *Clin Cancer Res*. 2008; 14:3312–8. [PubMed: 18519758]
70. Wright JL, Kwon EM, Ostrander EA, et al. Expression of *SLCO* transport genes in castration-resistant prostate cancer and impact of genetic variation in *SLCO1B3* and *SLCO2B1* on prostate cancer outcomes. *Cancer Epidemiol Biomarkers Prev*. 2011; 20:619–27. [PubMed: 21266523]
71. Pressler HM, Figg WD. Androgen synthesis and steroid transporters in prostate cancer: rethinking the transition to CRPC. *Cancer Biol Ther*. 2010; 9:1043–5. [PubMed: 20818170]

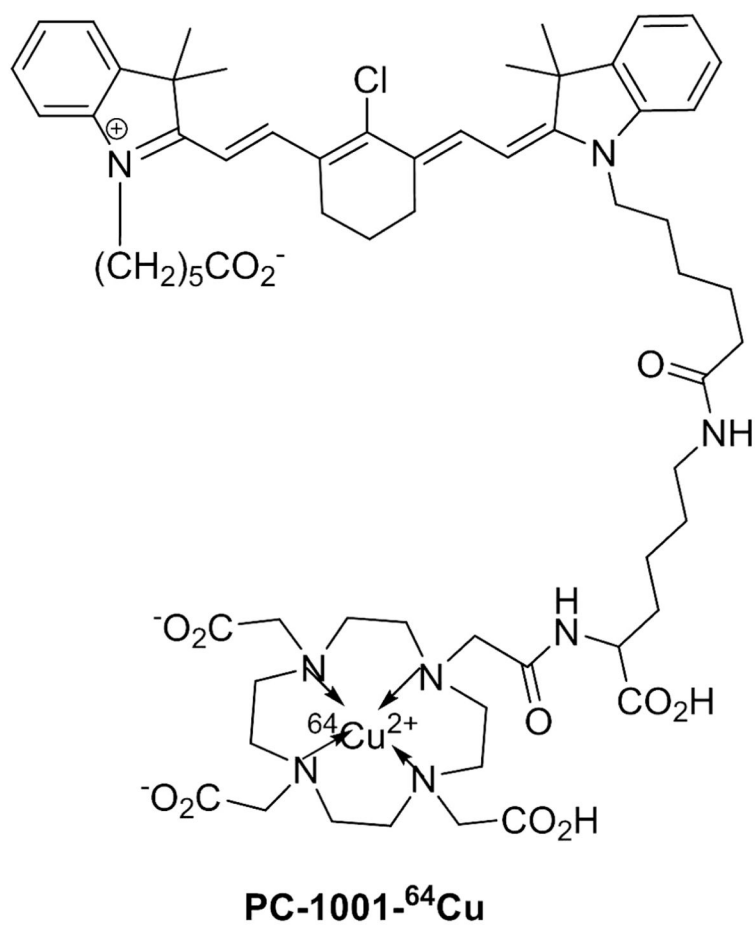


Figure 1.
The chemical structure of a PET/NIRF probe, PC-1001-⁶⁴Cu

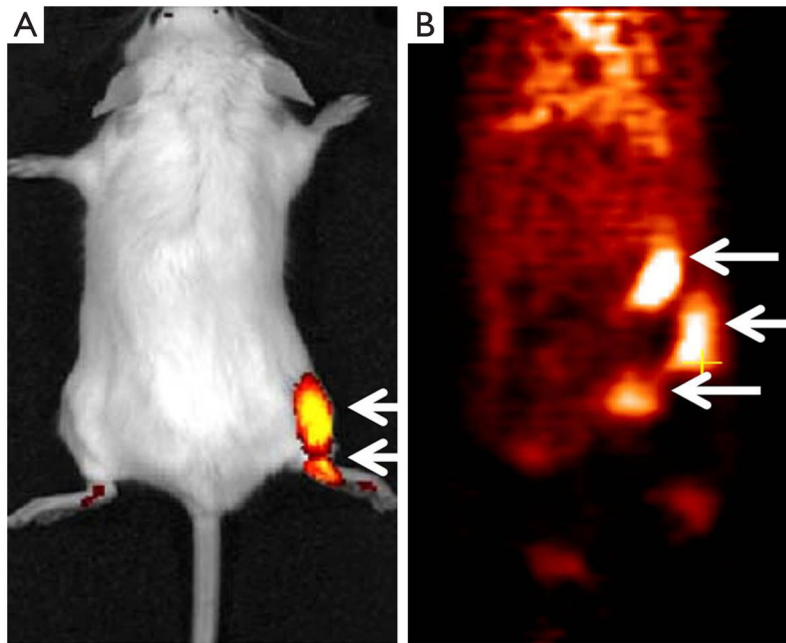


Figure 2.

Dual-modality NIRF/PET imaging of prostate tumors in a mouse model. A SCID mouse was intratibially inoculated with RANKL-overexpressing LNCaP tumors (arrows). Twenty-four hours after PC-1001-⁶⁴Cu (~17 MBq) was i.p injected, NIRF and PET scans were performed with a Caliper Spectrum System and a Focus-120 microPET scanner, respectively. A. NIRF (ex/em 745/820 nm) image shows two superficial tumor spots; B. Coronal slice of PET image reveals three isolated tumors. Similar results were obtained using the intracardiac injection of cancer cells to study cancer bone and soft tissue metastases in which more tumors were detected by PET than bioluminescence or NIRF staining, providing further evidence that PET has the advantage of detecting deep-seeded cancer metastases

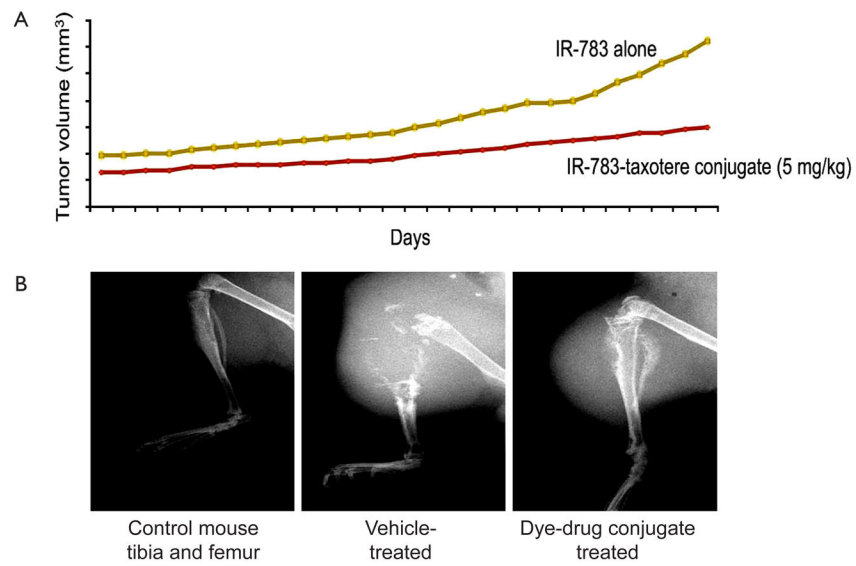


Figure 3. IR-783-docetaxel conjugate reduced prostate tumor growth in mouse skeleton. Nude mice were intratibially inoculated with osteolytic human PC-3 tumors followed by treatment with IR-783-docetaxel conjugate (5 mg/kg). A. Tumor growth was determined by measuring tumor volume; B. Bone lesions assessed by X-ray, showed improvement upon IR-783-docetaxel treatment. Note IR-783-docetaxel treated mouse has improved bone lesions when compared to mouse injected with vehicle

Monoamine oxidase A mediates prostate tumorigenesis and cancer metastasis

Jason Boyang Wu,¹ Chen Shao,^{1,2} Xiangyan Li,¹ Qinlong Li,^{1,3} Peizhen Hu,^{1,3} Changhong Shi,¹ Yang Li,⁴ Yi-Ting Chen,¹ Fei Yin,⁴ Chun-Peng Liao,^{1,5} Bangyan L. Stiles,⁴ Haiyen E. Zhau,¹ Jean C. Shih,^{4,6} and Leland W.K. Chung¹

¹Uro-Oncology Research Program, Department of Medicine, Cedars-Sinai Medical Center, Los Angeles, California, USA. ²Department of Urology and ³Department of Pathology, Xijing Hospital, Fourth Military Medical University, Xi'an, Shaanxi, China. ⁴Department of Pharmacology and Pharmaceutical Sciences, School of Pharmacy, and ⁵Center for Applied Molecular Medicine, Department of Medicine, Keck School of Medicine, University of Southern California, Los Angeles, California, USA. ⁶USC-Taiwan Center for Translational Research, University of Southern California, Los Angeles, California, USA.

Tumors from patients with high-grade aggressive prostate cancer (PCa) exhibit increased expression of monoamine oxidase A (MAOA), a mitochondrial enzyme that degrades monoamine neurotransmitters and dietary amines. Despite the association between MAOA and aggressive PCa, it is unclear how MAOA promotes PCa progression. Here, we found that MAOA functions to induce epithelial-to-mesenchymal transition (EMT) and stabilize the transcription factor HIF1 α , which mediates hypoxia through an elevation of ROS, thus enhancing growth, invasiveness, and metastasis of PCa cells. Knockdown and overexpression of MAOA in human PCa cell lines indicated that MAOA induces EMT through activation of VEGF and its coreceptor neuropilin-1. MAOA-dependent activation of neuropilin-1 promoted AKT/FOXO1/TWIST1 signaling, allowing FOXO1 binding at the *TWIST1* promoter. Importantly, the MAOA-dependent HIF1 α /VEGF-A/FOXO1/TWIST1 pathway was activated in high-grade PCa specimens, and knockdown of MAOA reduced or even eliminated prostate tumor growth and metastasis in PCa xenograft mouse models. Pharmacological inhibition of MAOA activity also reduced PCa xenograft growth in mice. Moreover, high MAOA expression in PCa tissues correlated with worse clinical outcomes in PCa patients. These findings collectively characterize the contribution of MAOA in PCa pathogenesis and suggest that MAOA has potential as a therapeutic target in PCa.

Introduction

Prostate cancer (PCa) is the second leading cause of male cancer death in the Western world (1). It can be clinically categorized into different risk groups primarily based on histological grade (Gleason score), clinical TNM stage, and levels of serum prostate-specific antigen (2). Aggressive, poorly differentiated high-grade PCa is incurable and potentially lethal, underscoring the need for a greater understanding of the molecular basis of PCa progression and improved opportunities to eliminate the development of the lethal phenotype of PCa.

Monoamine oxidase A (MAOA) is a mitochondria-bound enzyme that catalyzes the degradation of monoamine neurotransmitters and dietary amines by oxidative deamination, which produces a by-product, hydrogen peroxide, a major source of ROS (3–5). ROS can predispose cancer cells to DNA damage and cause tumor initiation and progression (6). In the last several decades, MAOA has been widely studied in the context of neuropsychiatric disorders, such as aggressive behaviors and mental depression (3, 5). Recently, a significant correlation was established between increased levels of MAOA expression and high Gleason grade or poorly differentiated human prostate tumors (7, 8). MAOA is exclusively expressed in the epithelial cells of prostatic glands with relatively low levels in stromal counterparts (9). These observations collectively suggest that MAOA may function in an auto-crine manner to regulate the proliferation and differentiation of prostatic epithelial cells.

Prostate tumorigenesis and cancer development are regulated by several oncogenic cues leading to dysregulated growth and increased stemness and plasticity by which cancer cells acquire increased migratory, invasive, and metastatic potential through epithelial-to-mesenchymal transition (EMT) (10). Evidence also supports the ability of cancer cells to adapt a HIF1 α pathway to resist oxidative stress, which cooperatively promotes an increasingly aggressive phenotype in cancer cells (11, 12).

In this study, we proposed that increased MAOA expression in high-grade PCa may be an important contributor to its dysregulated growth and dedifferentiation of the glandular epithelial phenotype. We demonstrated the ability of MAOA to induce mesenchymal transition, with PCa cells gaining increased proliferative, invasive, and metastatic potentials. Moreover, genetic targeting of MAOA using shRNA effectively inhibited or even completely eliminated prostate tumorigenesis and cancer metastasis in mouse xenograft models. We showed mechanistically that MAOA potentiated aggressive PCa behavior by converging functional interplay among EMT, hypoxia, and oxidative stress. Additionally, evidence for MAOA functionality in PCa also extended to human clinical PCa specimens. These findings establish MAOA as a viable therapeutic target in PCa and provide a rationale for the development of MAOA-targeted therapeutics.

Results

MAOA suppresses epithelial phenotype and promotes mesenchymal transition. Although MAOA expression has been previously demonstrated in human PCa tissues (7), its mode of action and potential to drive aggressive PCa phenotypes such as increased EMT-mediated

Conflict of interest: The authors have declared that no conflict of interest exists.

Citation for this article: *J Clin Invest.* 2014;124(7):2891–2908. doi:10.1172/JCI70982.

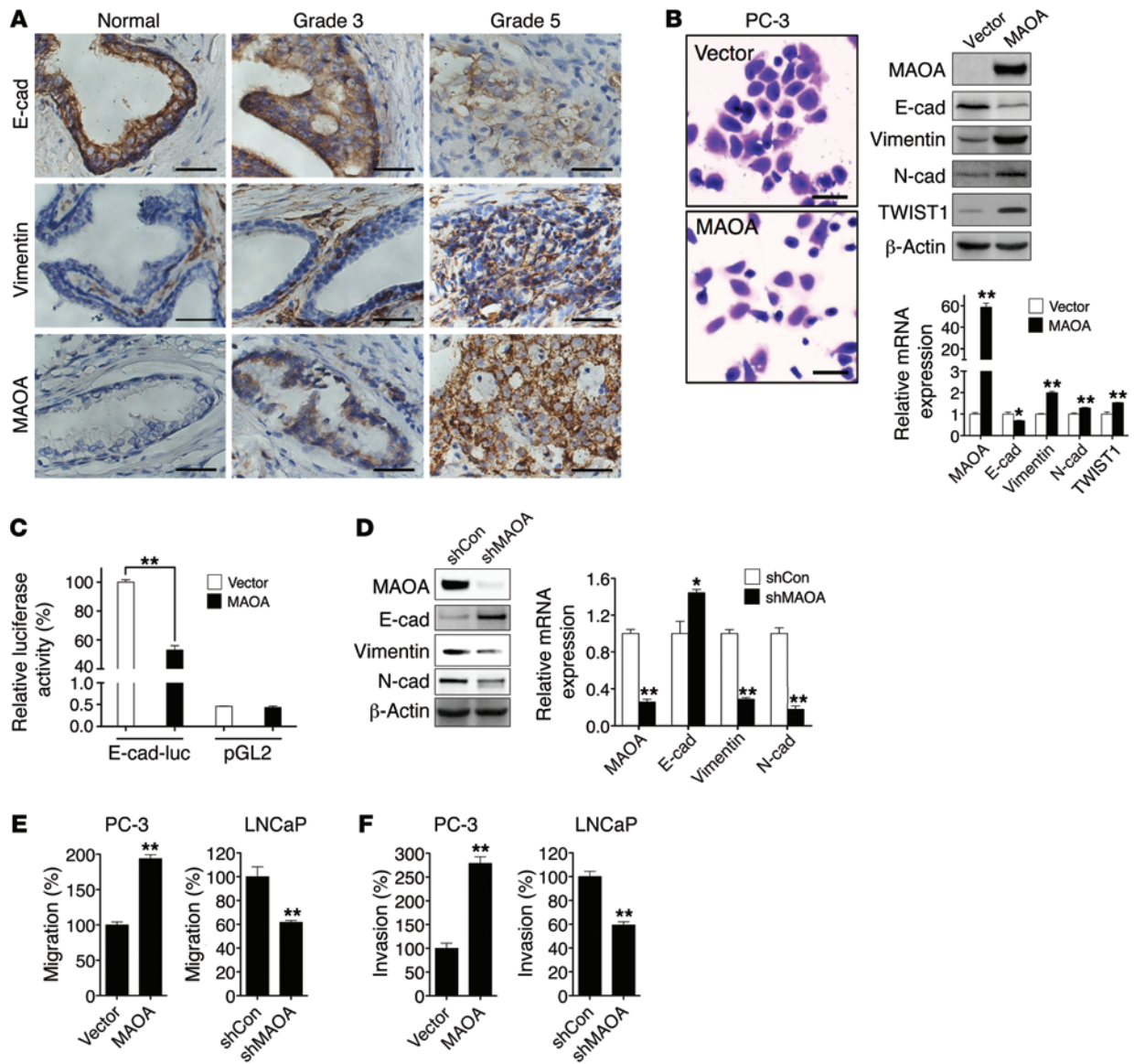


Figure 1

MAOA and EMT in PCa. (A) Clinical specimens of normal prostatic epithelium and Gleason grade 3 and 5 PCa were stained for E-cadherin, vimentin, and MAOA. Representative images from a tissue microarray are shown. Original magnification, $\times 400$; scale bars: 20 μm . (B) PC-3 cells stably overexpressing an empty vector or MAOA were photographed after crystal violet staining (left), and extracts were analyzed for the expression of MAOA and EMT markers by immunoblotting (middle) and qPCR (right). Original magnification, $\times 40$; scale bars: 200 μm . $*P < 0.05$, $**P < 0.01$. (C) Stable vector- and MAOA-overexpressing PC-3 cells were transfected with either an *E-cadherin* promoter reporter construct (*E-cad-luc*, expressing *Firefly* luciferase) or a promoterless pGL2 vector (expressing *Firefly* luciferase), cotransfected with a pRL-TK (expressing *Renilla* luciferase) construct as an internal standard for normalization of transfection efficiency. Data represent the mean \pm SEM ($n = 3$) of *Firefly* luciferase activity normalized to *Renilla* luciferase activity. The *E-cadherin* promoter activity in vector-expressing PC-3 cells was set as 100%. $**P < 0.01$. (D) Immunoblotting (left) and qPCR (right) analysis of LNCaP cells that express a MAOA-targeting shRNA (shMAOA) or a scrambled shRNA (shCon) for the expression of MAOA and EMT markers. $*P < 0.05$, $**P < 0.01$. (E and F) Paired PC-3 and LNCaP cells as indicated were assayed for their ability to either migrate (E) or invade (F). The migration or invasion of respective control cells was set as 100%. Data represent the mean \pm SEM ($n = 3$). $**P < 0.01$.

ated signaling pathways have not been pursued. Using a series of clinical specimens as the gold standards, we observed consistently that high-Gleason grade (grade 5) PCa is distinguished from low-grade (grade 3) PCa by characteristic morphological features such as the merger of neoplastic glands and cytological dedifferentiation (13). High-Gleason grade tumors also expressed diminished levels

of E-cadherin (an epithelial marker) and increased expression of vimentin (a mesenchymal marker) and MAOA in the same clinical specimens (Figure 1A), which was further confirmed in a tissue microarray by quantification of the association of expression levels of these genes in different types of prostate tissues (Supplemental Figure 1, A and B; supplemental material available online with

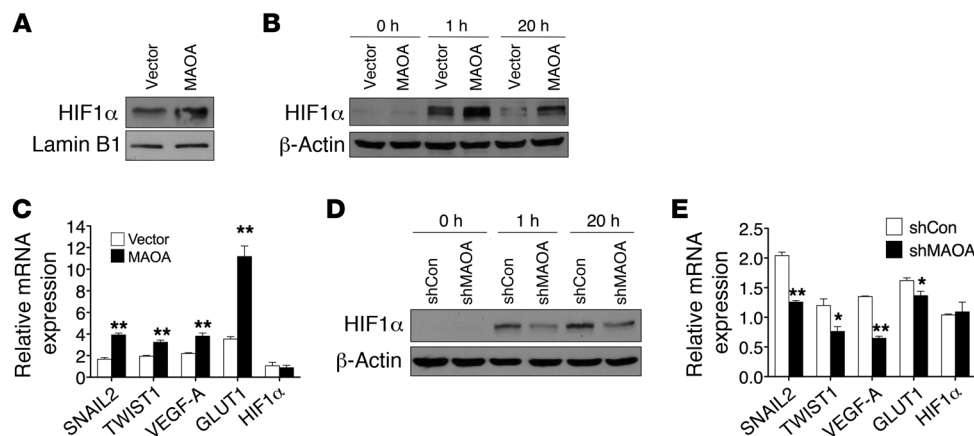


Figure 2
 MAOA regulates HIF1 α stability. (A) Immunoblots of nuclear extracts from PC-3 (vector and MAOA-overexpression) cells cultured at 21% O₂ for HIF1 α . (B and D) Immunoblots of paired PC-3 (B) or LNCaP (D) cells cultured at 1% O₂ for the indicated time. (C and E) Fold induction of HIF1 α target genes in response to hypoxia (1% O₂, 24 hours) measured by qPCR in PC-3 (vector and MAOA-overexpression) (C) or LNCaP (shCon and shMAOA) (E) cells. Normoxic gene expression in control PC-3 (vector-expressing) or LNCaP (shCon) cells was used as a control for normalization. Data represent the mean \pm SEM ($n = 3$). * $P < 0.05$, ** $P < 0.01$.

this article; doi:10.1172/JCI70982DS1). These results suggest that high-Gleason grade cancers exhibit EMT characteristics associated with increased MAOA expression and aggressive behaviors, which led us to hypothesize that MAOA may regulate EMT in PCa.

To address this hypothesis, we used human PC-3 and LNCaP PCa cell lines as models, since these cell lines express either low (PC-3) or high (LNCaP) basal levels of MAOA (Supplemental Figure 2, A–C). Stably enforced expression of a MAOA expression construct in PC-3 cells resulted in the transition to a dispersed morphology, a significant loss of E-cadherin, and increased expression of vimentin, N-cadherin, and TWIST1 at both protein and mRNA levels (Figure 1B). To establish that MAOA regulates *E-cadherin* transcription, we assayed the activity of *E-cadherin* promoter-luciferase reporter gene in PC-3 cells that stably expressed either an empty vector or a MAOA construct. MAOA-overexpressing cells displayed substantially diminished promoter activity compared with control cells (Figure 1C). By contrast, stable knockdown of MAOA in LNCaP cells with a MAOA-targeting shRNA (shMAOA) increased the expression of E-cadherin and downregulated vimentin and N-cadherin at both protein and mRNA levels compared with control cells given a scramble shRNA (shCon) (Figure 1D). Moreover, overexpression of MAOA also led to a significant increase in migration and invasion of PC-3 cells, a characteristic function of EMT. In contrast, knockdown of MAOA in LNCaP cells reduced the ability of cells to migrate or invade (Figure 1, E and F). In these studies, we did not observe significant changes in either cell proliferation or cell death in parallel to the analysis of cell migration and invasion in these cells with the manipulation of MAOA expression. Stable knockdown of MAOA in 2 other human PCa cell lines, C4-2 and ARCaP_M, supported the concept that MAOA is responsible for driving EMT in PCa cells, in which markedly attenuated mesenchymal features with changes in cell morphology, reduced mesenchymal marker expression, and reduced cell migratory and invasive behaviors were observed (Supplemental Figure 3, A–C).

MAOA stabilizes HIF1 α via ROS generation and PHD destruction. Hypoxia, a common condition found in a wide range of solid tumors including PCa, is often associated with poor prognosis and frequent expression of an aggressive phenotype promoted by EMT. HIF1 α , a master mediator of hypoxia, mediates hypoxic effects by activating relevant downstream target genes involved in many aspects of tumor progression, such as increased tumor glycolysis, angiogenesis, invasion, migration, and metastasis (14). Since increased MAOA expression promotes EMT, we assessed a possible relationship between MAOA and HIF1 α .

This possibility was evaluated first by investigation of whether MAOA directly regulates HIF1 α stability under normoxic conditions. In the presence of physi-

ological levels of oxygen, HIF1 α is rapidly degraded, which prevents a direct measurement in whole-cell lysates, but HIF1 α is detectable from isolated nuclei (15). As shown in Figure 2A, nuclei isolated from MAOA-overexpressing PC-3 cells during normoxia revealed elevated levels of HIF1 α relative to the vector-expressing control cells. Likewise, when these cells were cultured under hypoxic conditions at 1% O₂, HIF1 α was stabilized earlier and to a higher degree in MAOA-overexpressing cells when compared with control cells in whole-cell lysates (Figure 2B). Consistently, PC-3 tumors grown as subcutaneous xenografts from MAOA-overexpressing cells demonstrated increased staining of HIF1 α protein compared with control tumors by immunohistochemical (IHC) analysis (Supplemental Figure 4D). Moreover, select HIF1 α target genes, including the EMT-promoting genes *SNAIL2* and *TWIST1*, *VEGFA*, and glucose transporter 1 (*GLUT1*), were significantly upregulated in MAOA-overexpressing cells compared with control cells under hypoxia. Enforced expression of MAOA and hypoxia further showed additive effects on the expression of these genes (Figure 2C). In contrast, stable knockdown of MAOA reduced HIF1 α stabilization as well as expression of its target genes (*SNAIL2*, *TWIST1*, *VEGFA*, and *GLUT1*) in hypoxia-treated LNCaP cells, indicating that MAOA is required for HIF1 α function (Figure 2, D and E). Notably, the *HIF1A* mRNA level was not affected by differential MAOA expression (Figure 2, C and E), suggesting that MAOA may regulate HIF1 α stability via translational or posttranslational modifications. We assessed further the potential involvement of HIF1 α in MAOA-induced EMT and cell behaviors by genetically knocking down HIF1 α in hypoxia-treated MAOA-overexpressing PC-3 cells. We found that HIF1 α knockdown attenuated MAOA-induced EMT characteristics by decreasing mesenchymal marker expression and cell migration, invasion, and proliferation (Supplemental Figure 5, A–C). These data in aggregate suggest that MAOA modulates the stabilization of HIF1 α protein and the induction of crucial HIF1 α target genes that coordinate EMT and cancer progression.

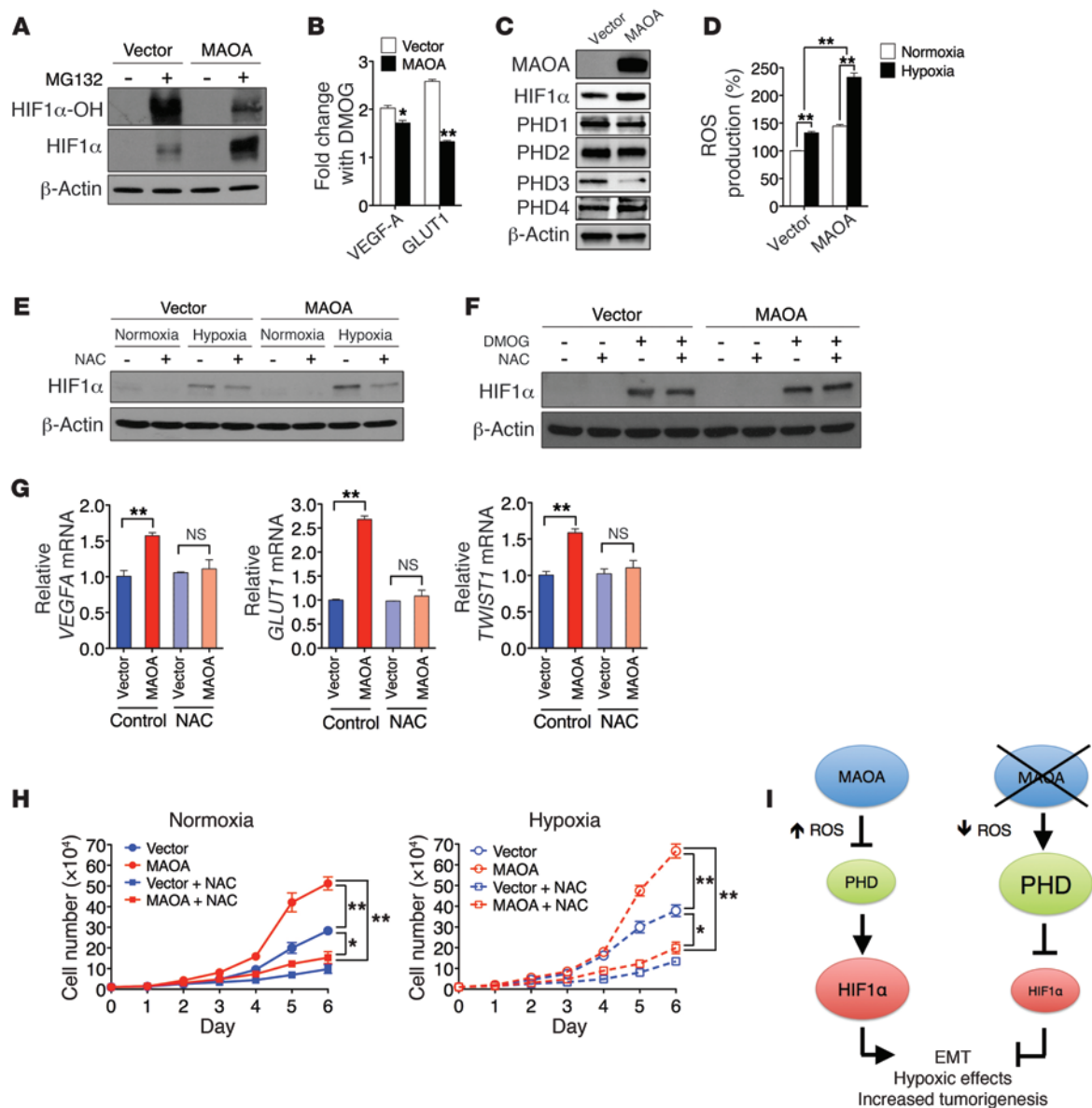


Figure 3

MAOA regulates HIF1 α stability through ROS. **(A)** Immunoblots of PC-3 (vector and MAOA-overexpression) cells treated with or without MG132 (1 μ M, 6 hours) for hydroxylated HIF1 α (HIF1 α -OH) and total HIF1 α . **(B)** Fold induction of HIF1 α target genes in PC-3 (vector and MAOA-overexpression) cells treated with DMOG (1 mM, 24 hours) was measured by qPCR, and the ratio (mean \pm SEM, $n = 3$) of DMOG-treated to untreated gene expression is shown. $*P < 0.05$, $**P < 0.01$. **(C)** Immunoblots of PC-3 (vector and MAOA-overexpression) cells with hypoxia for PHD1–4. **(D)** The increase in ROS production in PC-3 (vector and MAOA-overexpression) cells with hypoxia was calculated as the percentage changes (mean \pm SEM, $n = 3$) in ROS levels in hypoxic cells relative to normoxic cells. $**P < 0.01$. **(E)** Immunoblots of PC-3 (vector and MAOA-overexpression) cells incubated with 10 mM NAC and cultured under normoxia and hypoxia. **(F)** Immunoblots of PC-3 (vector and MAOA-overexpression) cells cultured at 21% O $_2$ with 10 mM NAC or 1 mM DMOG as indicated. **(G)** qPCR analysis of *VEGFA*, *GLUT1*, and *TWIST1* expression (mean \pm SEM, $n = 3$) in PC-3 (vector and MAOA-overexpression) cells incubated with 10 mM NAC and cultured under hypoxia. $**P < 0.01$. **(H)** Growth curves of PC-3 (vector and MAOA-overexpression) cells cultured in standard media supplemented or not supplemented with 10 mM NAC under either normoxia (left panel) or hypoxia (right panel) (mean \pm SEM, $n = 3$). $*P < 0.05$, $**P < 0.01$. **(I)** A schematic diagram outlining MAOA stabilization of HIF1 α by repression of PHD activity through ROS production.

The regulation of HIF1 α is complex and has not been fully elucidated. During normoxia, HIF1 α is hydroxylated at 2 proline residues by a family of oxygen-dependent prolyl hydroxylases (PHD1–4), which enables the tumor suppressor von Hippel-Lindau (vHL) to bind to and target HIF1 α for ubiquitination and protea-

somal degradation (16). Since the *HIF1A* mRNA level remained unchanged by MAOA expression (Figure 2, C and E), we tested whether MAOA exerted a posttranslational effect on HIF1 α protein stability. We ruled out the direct interaction between these 2 proteins because of their distinct cellular localization. MAOA appears

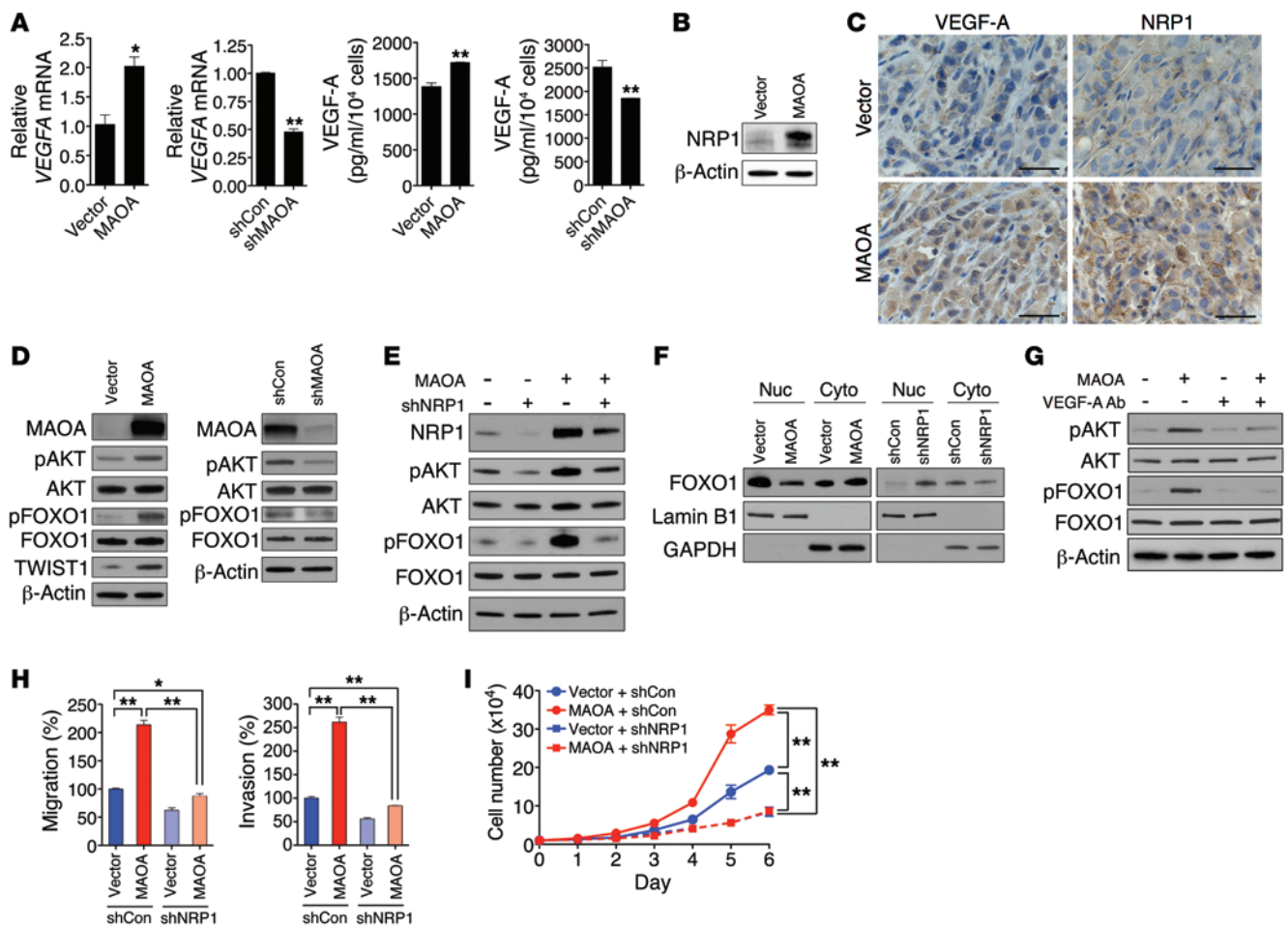


Figure 4

MAOA promotes VEGF-A/NRP1-mediated activation of AKT/FOXO1 signaling. (A) qPCR analysis of *VEGFA* mRNA expression (mean \pm SEM, $n = 3$) in paired PC-3 and LNCaP cells as indicated (left). VEGF-A secretion (mean \pm SEM, $n = 3$) in culture media from these cells was quantified by ELISA (right). * $P < 0.05$, ** $P < 0.01$. (B) Immunoblots of PC-3 (vector and MAOA-overexpression) cells for NRP1. (C) IHC analysis of PC-3 (vector and MAOA-overexpression) tumor xenografts for VEGF-A and NRP1 expression. Representative images from 5 separate samples are shown. Original magnification, $\times 400$; scale bars: 20 μm . (D) Immunoblots of paired PC-3 and LNCaP cells as indicated for pAKT (Ser473), pFOXO1 (Thr24), total AKT, and FOXO1. (E) Immunoblots of PC-3 (vector and MAOA-overexpression) cells that express *NRP1*-targeting shRNAs (shNRP1) or a scrambled shRNA (shCon) for NRP1, pAKT (Ser473), and pFOXO1 (Thr24). (F) Immunoblots of nuclear and cytoplasmic extracts from different groups of paired PC-3 cells as indicated for FOXO1. Lamin B1 and GAPDH serve as nuclear and cytoplasmic protein markers, respectively. (G) Immunoblots of PC-3 (vector and MAOA-overexpression) cells treated with either anti-VEGF-A antibody or a control IgG (0.5 $\mu\text{g/ml}$, 24 hours) for pAKT (Ser473) and pFOXO1 (Thr24). (H) PC-3 cells as established in E were assessed for their ability to either migrate (left) or invade (right). Data represent the mean \pm SEM ($n = 3$). * $P < 0.05$, ** $P < 0.01$. (I) Growth curves of PC-3 cells as established in E. Data represent the mean \pm SEM ($n = 3$). ** $P < 0.01$.

in the outer membrane of mitochondria to execute enzymatic reactions (17) (Supplemental Figure 6, A–C), whereas HIF1 α , when activated, functions as a nuclear transcription factor (18).

To test the hypothesis that MAOA regulates HIF1 α stability by directly affecting PHD activity, we determined PHD activity in control and MAOA-overexpressing PC-3 cells by measuring hydroxylated HIF1 α level, and these cells were pretreated with the proteasomal inhibitor MG132 to prevent hydroxylated HIF1 α from being degraded. More HIF1 α but significantly less hydroxylated HIF1 α was accumulated during MG132 treatment in MAOA-overexpressing cells (Figure 3A), suggesting lower PHD activity in the presence of MAOA. The hypothesis that MAOA regulates HIF1 α through the PHDs was further validated by determination of the

effect of treatment with dimethylxalylglycine (DMOG), a potent PHD inhibitor, on HIF1 α protein stability and the expression of HIF1 α target genes in MAOA-overexpressing cells. If MAOA affects HIF1 α stability by modulating PHD activity, DMOG treatment would overcome the effects of MAOA overexpression and produce equivalent levels of HIF1 α stabilization in control and MAOA-overexpressing cells. Indeed, the control and MAOA-overexpressing cells demonstrated equal levels of HIF1 α stabilized in response to DMOG treatment (Figure 3F, lane 3 vs. lane 7). Moreover, DMOG treatment relatively reduced the induction of the HIF1 α target genes *VEGFA* and *GLUT1* in MAOA-overexpressing cells compared with the control cells (Figure 3B). These data support a model in which PHD activity is already reduced in MAOA-overexpressing

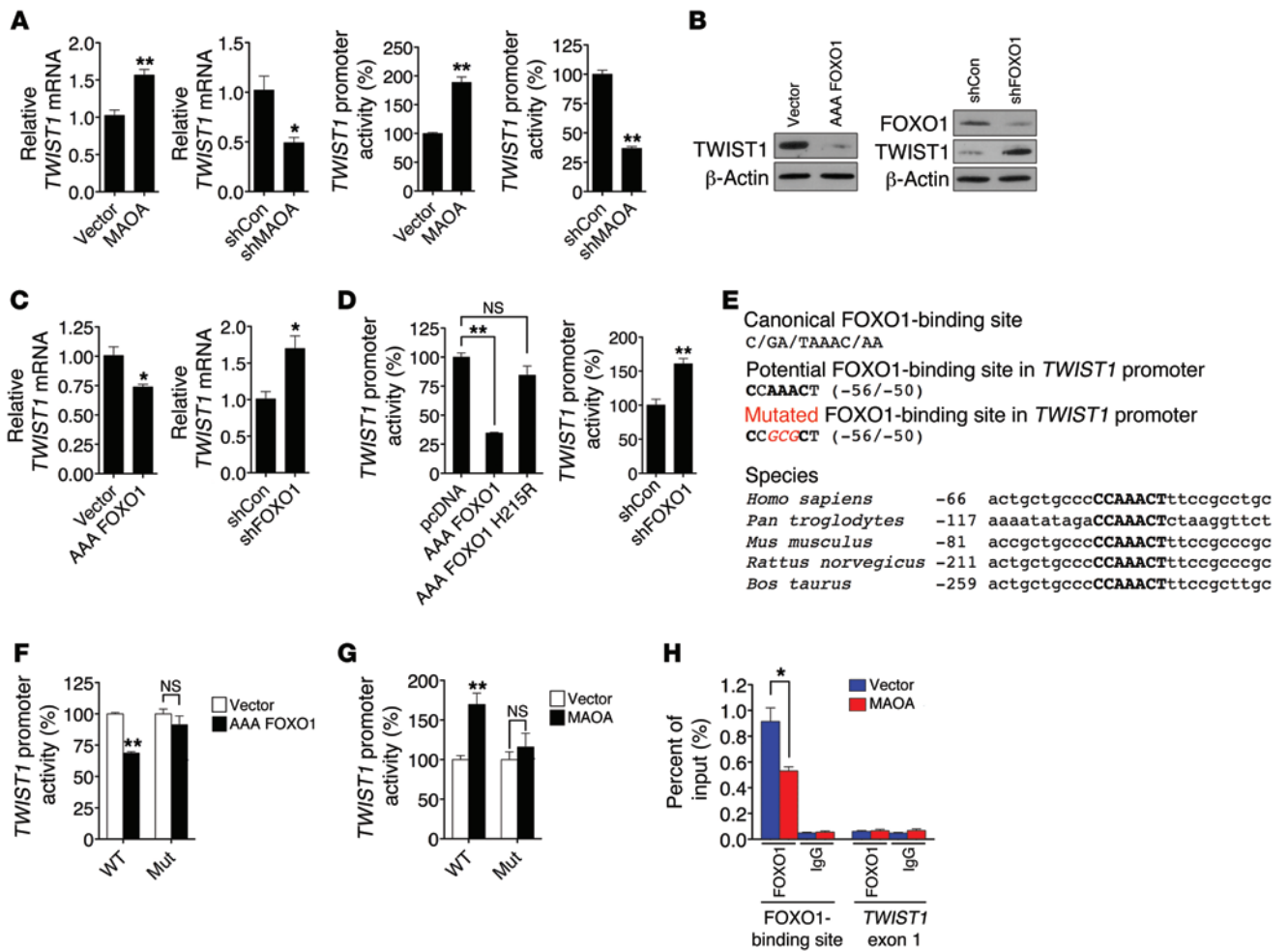


Figure 5

MAOA activates TWIST1 by reducing FOXO1 activity. (A) qPCR analysis of *TWIST1* mRNA expression (mean \pm SEM, $n = 3$) in paired PC-3 and LNCaP cells (left). A human *TWIST1* promoter reporter construct was transfected into these cells, and the luciferase activity (mean \pm SEM, $n = 3$) was assayed (right). (B) Immunoblots of paired PC-3 cells for TWIST1. AAA FOXO1 and shFOXO1 indicate a constitutively active form of FOXO1 expression construct and FOXO1-targeting shRNAs, respectively. (C) qPCR analysis of *TWIST1* mRNA expression (mean \pm SEM, $n = 3$) in different pairs of PC-3 cells. (D) Determination of *TWIST1* promoter activity (mean \pm SEM, $n = 3$) in different groups of PC-3 cells as indicated. AAA FOXO1 H215R is defective in DNA-binding ability. (E) Top box: The canonical sequence of the FOXO1-binding site (top), a potential FOXO1-binding site in the *TWIST1* promoter (middle), and introduced point mutations (bottom, italic and red) used to inactivate the potential FOXO1-binding site are shown. Bottom box: Alignment of the conserved FOXO1-binding site (bold) in the *TWIST1* promoter across different species is shown, with the number indicating the distance from transcription initiation sites. (F and G) Determination of WT and mutated (Mut) *TWIST1* promoter activity (mean \pm SEM, $n = 3$) in different pairs of PC-3 cells. (H) ChIP analysis of PC-3 (vector and MAOA-overexpression) cells immunoprecipitated by anti-FOXO1 or IgG antibody followed by qPCR using 2 primer sets for the FOXO1-binding site in the *TWIST1* promoter and *TWIST1* exon 1, respectively. Data represent the percent of input (mean \pm SEM, $n = 3$). * $P < 0.05$, ** $P < 0.01$.

cells. Consequently, when PHD activity is potently blocked by DMOG, MAOA-overexpressing cells have a smaller change in PHD activity and, thus, a smaller fold induction of HIF1 α target genes. To determine which isoforms of PHDs are involved in MAOA regulation of HIF1 α , the protein expression of all 4 PHD isoforms was measured in hypoxia-treated MAOA-overexpressing PC-3 cells. Specifically, PHD3 was repressed by MAOA overexpression at both protein and mRNA levels, whereas the expression of other PHDs remained unchanged (Figure 3C and Supplemental Figure 7A). Moreover, genetic knockdown of PHD3 but not other PHDs via siRNA recapitulated DMOG effects on HIF1 α target gene expression in MAOA-overexpressing cells compared with control cells

(Supplemental Figure 7, B and C). Taken together, our results suggest that MAOA-overexpressing PCa cells selectively reduced PHD3 activity, thus enhancing HIF1 α stability and activity, culminating in increased downstream target gene expression.

In addition to intracellular oxygen concentration, PHD activity can also be regulated by several intracellular signals, including ROS, which have been shown to inhibit the PHDs and stabilize HIF1 α (15, 16). Moreover, hypoxia enhances ROS production, a seemingly required step for the hypoxic activation of HIF1 α (19). Because MAOA-mediated enzymatic reactions produce hydrogen peroxide, which is responsible for the generation of ROS as a by-product (3), we hypothesized that increased ROS in MAOA-overexpressing



cells contribute to PHD inhibition and consequent HIF1 α stabilization in PCa cells. As expected, MAOA overexpression increased the generation of both mitochondrial hydrogen peroxide and ROS in PC-3 cells, while these were reduced in MAOA-knockdown LNCaP cells (Supplemental Figure 8, A–D). We found further that hypoxia triggered a significantly higher increase in ROS production in MAOA-overexpressing cells than control cells (Figure 3D), providing a mechanistic explanation for why MAOA-overexpressing cells have exaggerated responses to hypoxia. We next treated cells with the antioxidant N-acetylcysteine (NAC) to suppress ROS and hence block the downstream effects of MAOA mediated potentially by intracellular ROS. Indeed, the higher HIF1 α level in hypoxia-treated MAOA-overexpressing cells could be significantly attenuated by NAC treatment (Figure 3E, lane 8 vs. lane 7). Moreover, when PHD activity was blocked by DMOG treatment, control and MAOA-overexpressing cells both demonstrated comparable HIF1 α level, and NAC failed to destabilize HIF1 α (Figure 3F). Consistent with decreased HIF1 α expression in NAC-treated MAOA-overexpressing cells, the expression of the HIF1 α target genes *VEGFA*, *GLUT1*, and *TWIST1* was reduced to control levels in NAC-treated MAOA-overexpressing cells (Figure 3G). Furthermore, NAC treatment of cells reversed MAOA-induced EMT characteristics by decreasing mesenchymal marker expression and cell migratory and invasive behaviors (Supplemental Figure 5, D and E). To test whether increased ROS contribute to the proliferation of MAOA-overexpressing cells, we determined the growth profiles in cells cultured with NAC. Strikingly, we observed that NAC blunted the enhanced proliferation in MAOA-overexpressing cells under both normoxic and hypoxic conditions, restoring their growth rates to that of the control cells (Figure 3H). Together, MAOA regulation of ROS augmented hypoxic responses by increasing the steady-state HIF1 α level and its target gene expression, including *VEGFA*, *GLUT1*, and *TWIST1*, which converge the cell signaling network toward a mesenchymal transition and enhanced cell proliferation in MAOA-overexpressing cells (Figure 3I).

MAOA activates VEGF-A/neuropilin-1 signaling and its downstream AKT/FOXO1 pathway. Given that hypoxia reportedly can affect cell behavior by promoting EMT, we hypothesized that the HIF1 α target gene *VEGFA* in conjugation with its receptor(s) may play a crucial mediating role in controlling the downstream signaling for the MAOA-induced EMT and associated increased aggressive phenotype in PCa cells. VEGF has been implicated in poor prognosis and survival in PCa patients, and an elevated level of VEGF could be the trigger for an angiogenic switch in the lethal progression of advanced PCa (20). *VEGFA* expression was assessed in control/MAOA-overexpressing PC-3 or control/MAOA-knockdown LNCaP cells by quantitative PCR (qPCR), and there was a positive correlation between *VEGFA* and MAOA expression (Figure 4A, left). We further quantified VEGF-A expression in the culture media of MAOA-manipulated PCa cells by ELISA and confirmed that MAOA upregulated expression of VEGF-A and its extracellular secretion (Figure 4A, right). By contrast, we did not observe any VEGF effect on MAOA gene expression (Supplemental Figure 9, A–C). Autocrine VEGF signaling in tumor cells can occur through a nonangiogenic cell proliferative mechanism via increased autocrine VEGF-A and interaction with its coreceptor neuropilin-1 (NRP1), and such interaction has been implicated in cancer cell autonomy and aggressive behaviors (21). We showed that overexpression of MAOA significantly increased NRP1 expression in PC-3 cells (Figure 4B), which was further demonstrated

in parallel in MAOA-overexpressing PC-3 xenograft tumors with concurrently increased VEGF-A expression (Figure 4C).

To elucidate the mechanism(s) by which MAOA activation of VEGF-A and NRP1 mediates downstream signaling to promote EMT, select kinases that are implicated in PCa progression were examined in PCa cells previously subjected to MAOA manipulation. As shown in Figure 4D (left panel), there was a significant increase in the relative phosphorylation of both AKT and its downstream target FOXO1 by MAOA overexpression. AKT plays a central role by activating its many downstream target genes in regulating PCa initiation and progression (22). FOXO1, a member of the O subclass of the forkhead family of transcription factors, can be regulated via the phosphorylation of AKT upon PI3K/AKT signaling activation, and has demonstrated proapoptotic function in a variety of cancers (23). We further showed that AKT/FOXO1 signaling was conversely attenuated in MAOA-knockdown LNCaP cells (Figure 4D, right panel). These results suggest that the AKT/FOXO1 signaling pathway is downstream of MAOA.

Given that NRP1 can regulate AKT activity (24), which was reproduced in NRP1-overexpressing PC-3 cells with concurrent induction of EMT and cell proliferation (Supplemental Figure 10, A–D), we examined autocrine VEGF/NRP1-mediated signaling and evaluated the relationship between MAOA and AKT/FOXO1 signaling in PC-3 cells with stable knockdown of NRP1 using a lentiviral shRNA-mediated approach. As shown in Figure 4E, NRP1 knockdown significantly reduced both the basal and MAOA-induced phosphorylation of AKT and FOXO1 in PC-3 cells. Moreover, we demonstrated that MAOA facilitated the nuclear export of FOXO1 by altering the ratios of FOXO1 toward enhanced levels in the cytoplasmic fraction (Figure 4F, left panel), and this was confirmed by the IHC staining pattern of FOXO1 and phospho-FOXO1 in control and MAOA-overexpressing PC-3 tumor xenograft samples (Supplemental Figure 4E). Conversely, genetic silencing of NRP1 increased nuclear but decreased cytoplasmic FOXO1 expression (Figure 4F, right panel). To determine whether VEGF-A acts as the major ligand to mediate NRP1 effect in the MAOA context, we treated control and MAOA-overexpressing PC-3 cells with anti-VEGF-A antibody. This targeted blockade of receptor binding of secreted VEGF-A attenuated the MAOA-induced phosphorylation of both AKT and FOXO1 toward that of the control cells (Figure 4G). Unlike VEGF-A, we found that another potential NRP1 receptor ligand, semaphorin 3A (SEMA3A), was not elevated in MAOA-overexpressing PC-3 cells (Supplemental Figure 11), further confirming the mediating role of VEGF-A in controlling the MAOA/NRP1 axis. By examining the functional roles of NRP1 in determining cell behavior, we showed that NRP1 knockdown resulted in a significant decrease of MAOA-induced migration and invasion in PC-3 cells (Figure 4H). Likewise, NRP1 knockdown also dramatically reduced the cell proliferation rate in MAOA-overexpressing cells to a level lower than that of the control (Figure 4I). Taken together, these functional characteristics indicate that the VEGF-A/NRP1 system mediates MAOA-induced EMT and cell proliferation via the downstream AKT/FOXO1 signaling.

***TWIST1* expression is directly regulated by transcription factor FOXO1.** We screened a spectrum of key transcription factors known to promote EMT in our present model system, and identified TWIST1 as 1 of the downstream targets of MAOA (Figure 1B). TWIST1, a basic helix-loop-helix transcription factor, is a master regulator of EMT, and its expression in tumors often correlates with aggressive disease and poor outcome (25, 26). We showed that genetic silencing of

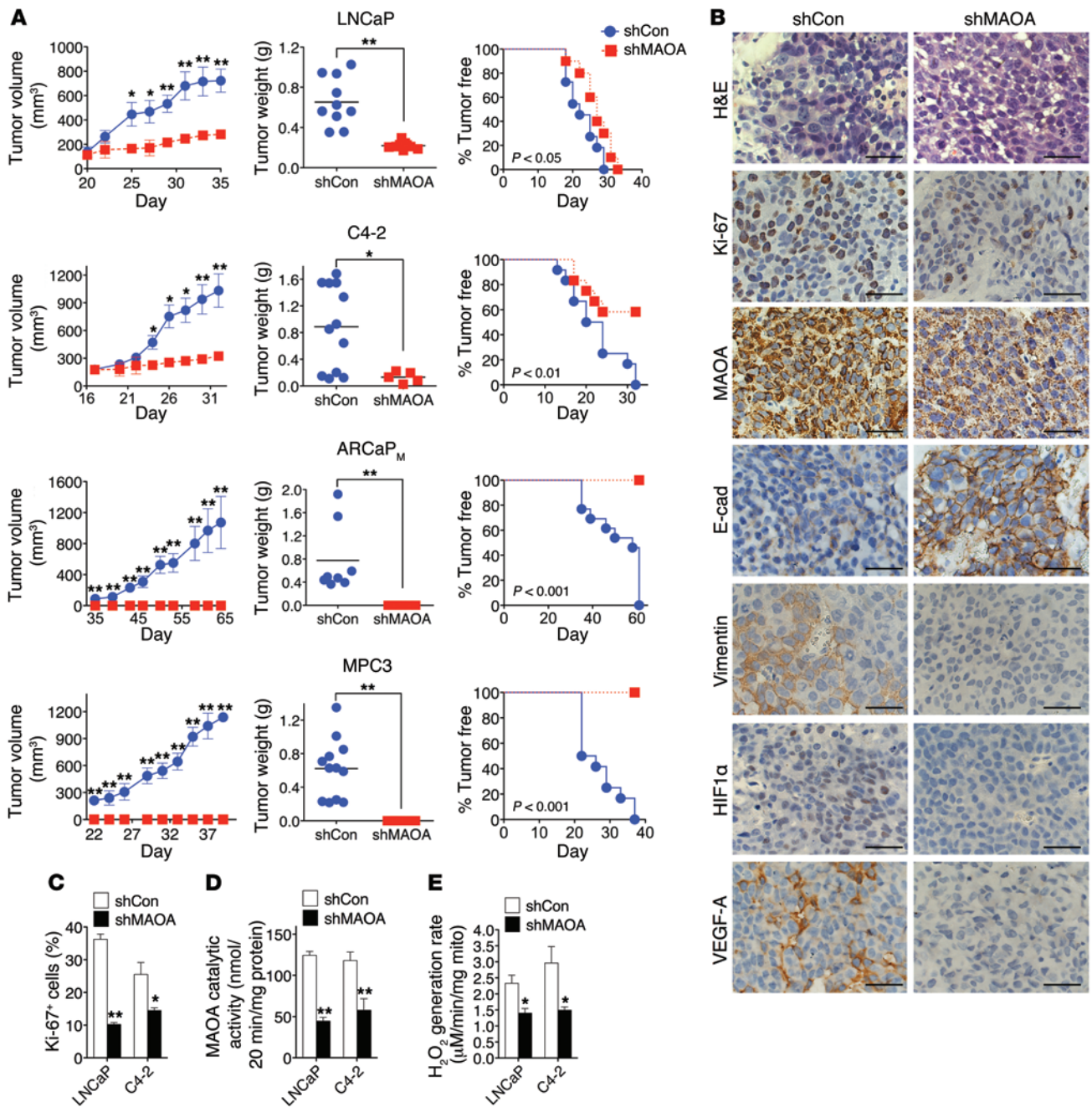
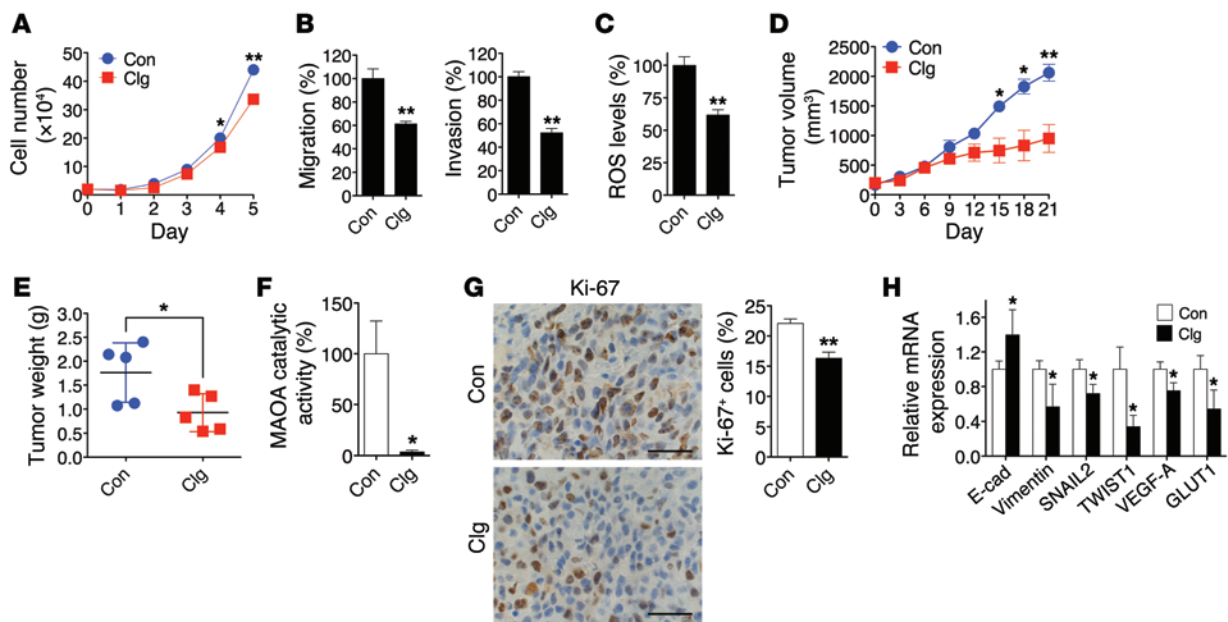


Figure 6

MAOA is essential for the growth of prostate tumor xenografts by regulating EMT, hypoxia, and ROS. **(A)** LNCaP, C4-2, ARCaP_M, or MPC3 cells that stably express a MAOA-targeting shRNA (shMAOA) or a scrambled shRNA (shCon) were injected s.c. into male nude mice (*n* = 4–7 mice for each group; details are given in Supplemental Table 1) for the growth of tumor xenografts. Tumor growth was determined by measurement of tumor volume, tumor weight, and the frequency of tumor formation. The graphs show the mean (± SEM) tumor size and tumor-free percentages at the indicated times. **P* < 0.05, ***P* < 0.01. **(B)** H&E and IHC analysis of Ki-67, MAOA, E-cadherin, vimentin, HIF1α, and VEGF-A expressions in LNCaP (shCon and shMAOA) tumor xenografts. Representative images from 5 separate samples are shown. Original magnification, ×400; scale bars: 20 μm. **(C)** Quantification of percentage of Ki-67⁺ tumor cells in paired LNCaP and C4-2 tumor xenografts from 5 distinct images of each tumor sample (*n* = 5 tumor samples for each group). Data represent the mean ± SEM. **P* < 0.05, ***P* < 0.01. **(D)** Determination of MAOA enzymatic activity in paired LNCaP and C4-2 tumor xenografts. Data represent the mean ± SEM from all tumors obtained at mouse necropsy (*n* = 5–12 tumors for each group; details are given in Supplemental Table 1). ***P* < 0.01. **(E)** Determination of H₂O₂ generation rate in intact mitochondria isolated from paired LNCaP and C4-2 tumor xenografts (*n* = 3 tumor samples for each group) by Amplex Red hydrogen peroxide assay. Data represent the mean ± SEM. **P* < 0.05.

**Figure 7**

Clorgyline inhibits the growth of PCa cells and tumor xenografts. (A) Growth curves of LNCaP cells treated with either clorgyline (1 μ M, Clg) or vehicle (PBS, Con) for 5 days (mean \pm SEM, $n = 3$). * $P < 0.05$, ** $P < 0.01$. (B) LNCaP cells treated with either clorgyline (1 μ M) or vehicle were assessed for their ability to either migrate (left) or invade (right) (mean \pm SEM, $n = 3$). ** $P < 0.01$. (C) Determination of ROS levels in LNCaP cells treated with clorgyline (1 μ M, 48 hours) or vehicle (mean \pm SEM, $n = 3$). ** $P < 0.01$. (D) Determination of the growth of C4-2 subcutaneous tumor xenografts in mice ($n = 5$ mice for each group) treated with clorgyline (10 mg/kg, i.p.) or saline on a daily basis for 21 days. The graph shows the mean (\pm SEM) tumor size at the indicated time. * $P < 0.05$, ** $P < 0.01$. (E) Determination of tumor weight at mouse necropsy. * $P < 0.05$. (F) Determination of MAOA enzymatic activity (mean \pm SEM) in clorgyline- or vehicle-treated tumor xenografts ($n = 5$ tumor samples for each group). * $P < 0.05$. (G) Quantification of percent of Ki-67+ (mean \pm SEM) tumor cells in clorgyline- or vehicle-treated tumor xenografts from 5 distinct images of each tumor sample ($n = 5$ tumor samples for each group) (right). Representative IHC images are shown (left). ** $P < 0.01$. Original magnification, $\times 400$; scale bars: 20 μ m. (H) qPCR analysis of clorgyline- or vehicle-treated tumor xenografts ($n = 5$ tumor samples for each group) for the expression of EMT marker and HIF1 α target genes. Data represent the mean \pm SEM. * $P < 0.05$.

TWIST1 reversed MAOA-induced EMT by decreasing mesenchymal marker expression and cell migratory, invasive, and proliferative behavior (Supplemental Figure 12, A–C), which suggests that TWIST1 is functional for the induction of EMT by MAOA. To assess the potential regulation of TWIST1 by MAOA, we determined both *TWIST1* mRNA and its promoter activity in PCa cells with manipulated MAOA expression. Overexpression of MAOA increased *TWIST1* mRNA and promoter activity in PC-3 cells, whereas these TWIST1-related activities were reduced upon MAOA knockdown in LNCaP cells (Figure 5A), suggesting that MAOA may regulate TWIST1 expression at the transcriptional level.

AKT drives EMT and cancer progression by regulating many downstream target genes, including TWIST1 (27, 28), but the specific AKT-responsive signaling pathways that regulate TWIST1 remain to be clarified. The transcription factor forkhead box (FOX) proteins capable of being phosphorylated by AKT play a dominant role in cancer progression (23). Moreover, FOX proteins have been demonstrated to mediate EMT by regulating EMT-inducing factors (29), which led us to speculate that FOXO1 may regulate TWIST1 in PCa cells. We established PC-3 cells that stably overexpressed a constitutively active FOXO1 expression construct (AAA FOXO1) with 3 mutated phosphorylation sites (T24A, S256A, and S319A). AAA FOXO1 is sequestered in the nucleus without degradation (30). Enforced expression of AAA FOXO1 significantly reduced TWIST1 protein expression, whereas sta-

ble shRNA-mediated silencing of FOXO1 increased TWIST1 levels in PC-3 cells (Figure 5B), suggesting a negative regulatory link between these 2 proteins. We also assessed whether FOXO1 directly participates in EMT induced by MAOA. We showed that stable knockdown of FOXO1 in MAOA-overexpressing cells further enhanced EMT characteristics by increasing mesenchymal marker expression and corresponding cell behavior including migration, invasion, and proliferation (Supplemental Figure 12, D–F), which provides a functional basis underlying the FOXO1 repression of TWIST1.

Considering the innate feature of FOXO1 as a transcription factor, we next determined whether FOXO1 transcriptionally regulates *TWIST1* expression, and we showed a reproducible negative regulation of *TWIST1* mRNA by FOXO1 in PC-3 cells (Figure 5C). To explore the possible direct influence of FOXO1 on the promoter of the *TWIST1* gene, a 1-kb DNA segment located upstream of the transcription initiation site of *TWIST1* was introduced as a luciferase reporter construct into PC-3 cells (31). Since FOXO1 can affect the transcription of target genes either through direct binding to their consensus DNA sequences in the promoter or via indirect protein-protein interactions with other transcription factors or cofactors (32), we distinguished these 2 alternative mechanisms by using a FOXO1 mutant (AAA FOXO1 H215R) that is deficient in DNA binding (30). In contrast to its WT counterpart, which strongly repressed *TWIST1* promoter activity, the FOXO1 mutant

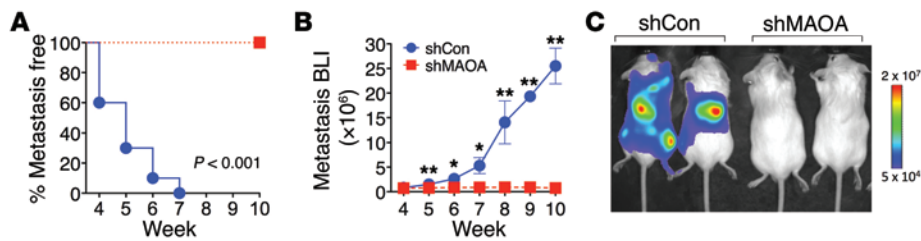


Figure 8

MAOA is essential for PCa metastasis. (A) Kaplan-Meier curves of metastasis development of control (shCon) and MAOA-knockdown (shMAOA) ARCaP_M cells ($n = 10$ mice for each group). (B) Normalized BLI curves of metastasis development for each experimental group. Data represent the mean \pm SEM ($n = 10$). * $P < 0.05$, ** $P < 0.01$. (C) Representative BLI (week 10) images of 2 of 10 mice in each group from B.

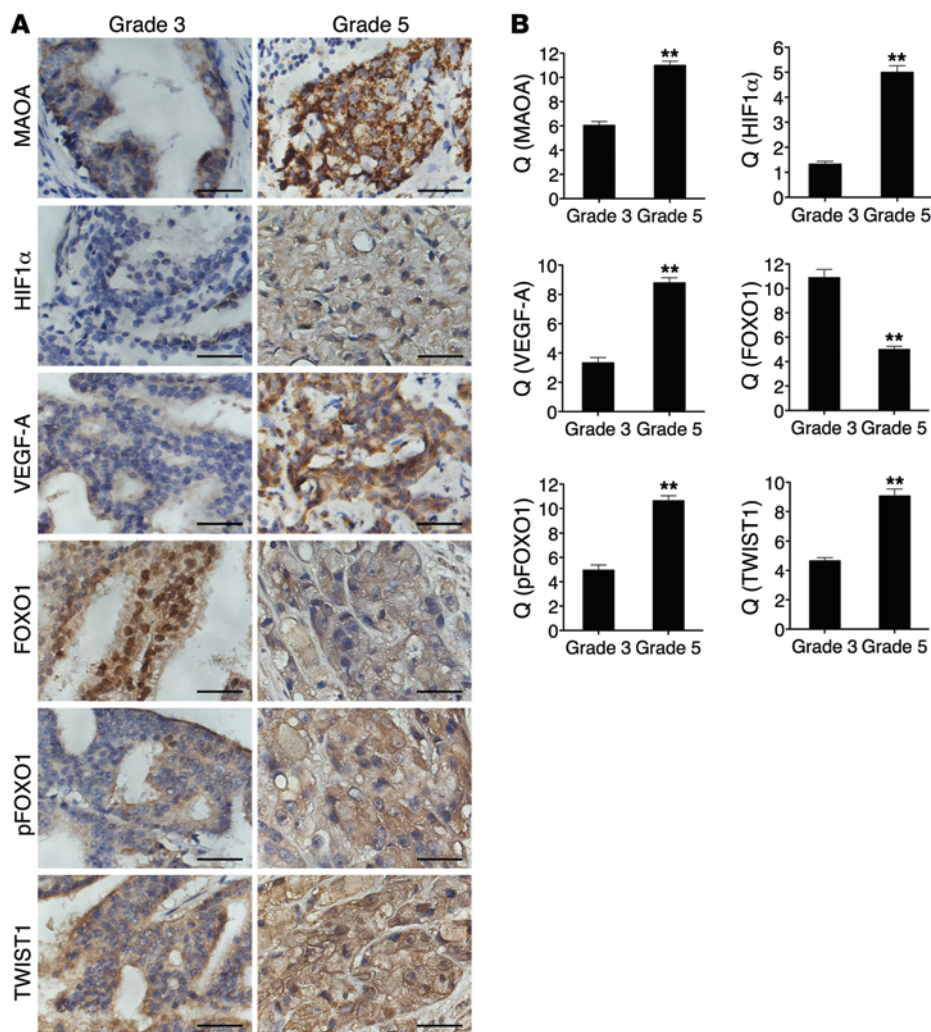
failed to do so (Figure 5D, left panel). Hence, the FOXO1 action on the *TWIST1* promoter appeared to require the intact DNA-binding activity of FOXO1. This regulation is further supported by the observation that genetic silencing of FOXO1 increased *TWIST1* promoter activity in PC-3 cells (Figure 5D, right panel).

It remained unclear whether the observed repression is mediated by direct binding of FOXO1 to the *TWIST1* promoter. To address this issue, we attempted to identify a FOXO1-response element in the *TWIST1* promoter. Serial deletion of the *TWIST1* promoter combined with sequence analysis revealed a region within the *TWIST1* promoter (-56/-50) that exhibits strong sequence similarity to the canonical AT-rich FOXO1-binding site (Figure 5E, top panel) (33, 34). To test whether the potential direct regulation of *TWIST1* by FOXO1 is conserved throughout evolution, we searched for the consensus FOXO1-binding site and its surrounding sequences in the human *TWIST1* promoter across species. Interestingly, we found that this element (CCAAACT) is highly conserved among amniotic genomes examined, including chimpanzees, mice, rats, and cows (Figure 5E, bottom panel). Accordingly, we generated a mutant *TWIST1* promoter reporter construct harboring 3 point mutations in the center of the putative FOXO1-response element. The resulting mutated *TWIST1* promoter was no longer repressed by ectopic expression of FOXO1 in PC-3 cells (Figure 5F). This *TWIST1* promoter reporter mutant construct was further introduced into MAOA-overexpressing PC-3 cells, and in contrast to its WT counterpart, the mutant did not respond to MAOA overexpression (Figure 5G). To confirm the direct occupancy of FOXO1 with the sequences in the *TWIST1* promoter in vivo, we extended these studies by performing ChIP analysis. We isolated chromatin-nuclear protein complexes immunoprecipitated with anti-FOXO1 antibody from both control and MAOA-overexpressing PC-3 cells, and analyzed it by qPCR using primers that specifically encompass the putative FOXO1-response element in the *TWIST1* promoter. We were able to detect the physical association of FOXO1 with the *TWIST1* promoter sequences, and such association was reduced in the presence of MAOA overexpression (Figure 5H), which is consistent with the observation of less nuclear FOXO1 expression in MAOA-overexpressing PC-3 cells (Figure 4F, left panel). Moreover, limited signals were detected from the negative controls, in which either nonspecific IgG antibody was used in the immunoprecipitation step or the *TWIST1* exon 1 was probed in order to confirm the targeting specificity of the primer set used in PCR. These results in sum provide evidence that MAOA negatively mediates *TWIST1* gene activation via direct interaction of FOXO1 with a specific element located

in the *TWIST1* promoter. In the case of MAOA overexpression in PCa cells, increased *TWIST1* gene activation that drives EMT was the result of sequestration of FOXO1 from nucleus to cytoplasm, reducing the overall suppression of *TWIST1* gene expression.

MAOA function in prostate tumorigenesis and cancer metastasis. The MAOA effects on promotion of EMT, hypoxia, and ROS production described above shed light on how MAOA supports PCa growth and development. To test this hypothesis, we established multiple prostate tumor xenograft mouse models to determine the functional roles of MAOA in controlling tumor growth (Supplemental Table 1). We used 3 human PCa cell lines that show different MAOA expression levels, aggressiveness, and invasiveness as well as other innate features such as responses to androgen (35, 36). Considering the importance of the immune system in PCa growth and progression, we also extended our analysis by using a highly tumorigenic mouse prostate carcinoma MPC3 cell line in an immunocompetent mouse model. The MPC3 line was derived from mouse primary prostate tumors harboring double loss of *Pten* and *p53* tumor suppressors. To assess MAOA function in these tumor xenograft models, we first infected these cells with a lentiviral construct expressing an shRNA directed against the mRNA encoding MAOA, or a control that targets no known mammalian genes. Stable introduction of MAOA-specific shRNAs decreased MAOA enzymatic activity by more than 50%–70% in all cell lines (Supplemental Figure 13A). In line with the observation that enforced MAOA expression significantly induced PC-3 cell proliferation (Supplemental Figure 4A), cells expressing MAOA-targeting shRNAs had consistently reduced cell proliferation rates in comparison with control cells (Supplemental Figure 13B). In these studies, we observed no significant apoptotic changes in either MAOA-overexpressing PC-3 or MAOA-knockdown LNCaP cells compared with their respective control cells (Supplemental Figure 14, A and B). These complementary results suggest that MAOA affects PCa cell growth mainly through its proliferation-enhancing functions.

After being implanted s.c. into male nude mice, LNCaP and its lineage-derived androgen-independent C4-2 cells expressing MAOA-targeting shRNAs showed slower tumor growth rates and formed fewer tumors than controls. Cells stably expressing MAOA-targeting shRNA that did form tumors formed tumors that were quite small, with an average tumor weight of 221 ± 36 mg and 132 ± 81 mg for LNCaP and C4-2 tumors, respectively, compared with larger tumors, with an average weight of 653 ± 232 mg and 888 ± 632 mg for LNCaP and C4-2 control tumors, respectively (Figure 6A). Strikingly, stable knockdown of MAOA in ARCaP_M,

**Figure 9**

The HIF1 α /VEGF-A/FOXO1/TWIST1 pathway is manifested in high-Gleason grade PCa. **(A)** Sixty specimens of human PCa including 30 Gleason grade 3 tumors and 30 Gleason grade 5 tumors were immunostained for MAOA, HIF1 α , VEGF-A, FOXO1, pFOXO1, and TWIST1. Original magnification, $\times 400$; scale bars: 20 μm . **(B)** Semiquantitative analysis of IHC staining was performed for all specimens to assess both the percentage of cells stained and the intensity of each staining. This analysis is reported as the quotient (Q) of these 2 parameters (mean \pm SEM). Details are given in Supplemental Methods. Images representative of the mean Q for each IHC staining are shown. ** $P < 0.01$.

an aggressive human PCa cell line, and MPC3 cells completely eliminated their *in vivo* growth, in sharp contrast to the expected explosive tumor growth in mice inoculated with the control cells.

As a comparison, we next analyzed the protein expression patterns of select markers in tumor specimens from LNCaP and C4-2 xenograft tumors by IHC. Ki-67 staining of tumor specimens revealed a 40%–70% decrease of Ki-67⁺ cells in the MAOA-knockdown group of both LNCaP and C4-2 tumors (Figure 6, B and C). MAOA protein staining also showed decreased intensity in MAOA-knockdown tumor samples for both lines (Figure 6B), which is consistent with the results of reduced MAOA enzymatic activity in harvested tumors expressing MAOA-targeting shRNAs (Figure 6D), supporting the concept that genetically silencing MAOA gene expression by an shRNA-mediated protocol is highly effective and sustainable under *in vivo* conditions. Moreover, MAOA-knockdown xenograft tumors showed EMT reversal by increased staining of E-cadherin as well as reduced expression of vimentin, and repressed tumor hypoxia by less HIF1 α and VEGF-A staining (Figure 6B and Supplemental Figure 15). These results from tumor xenograft mouse models provide further evidence that MAOA drives EMT and augments PCa cell response to hypoxia.

We further examined the levels of ROS in both control and MAOA-knockdown tumor samples. MAOA is located in the outer

membrane of mitochondria and directly engaged in hydrogen peroxide production via the oxidative deamination of its substrates, which can be subsequently converted into other forms of ROS (3). We determined the rate of hydrogen peroxide generation in intact tumor mitochondria, which represents specifically the differences in MAOA-originated ROS production, from both control and MAOA-knockdown tumors. LNCaP and C4-2 tumors that expressed MAOA-targeting shRNAs showed slower rates of hydrogen peroxide generation in comparison with control tumors (Figure 6E), suggesting that increased ROS production could be a crucial factor underlying MAOA's role in PCa development, in line with *in vitro* studies.

We next evaluated the therapeutic effect of small-molecule inhibitors of MAOA capable of interfering with MAOA enzymatic activity in PCa xenograft mouse models. Treatment of LNCaP cells with clorgyline, a potent MAOA inhibitor (37), decreased cell proliferation, migration, and invasion (Figure 7, A and B), and suppressed cellular ROS levels (Figure 7C). Mice bearing subcutaneously androgen-independent and aggressive C4-2 xenograft tumors (36, 38), when receiving clorgyline treatment via the *i.p.* route, showed reduced tumor growth by both slower growth rate and smaller tumor weight within a 3-week treatment period (Figure 7, D and E). In the meanwhile, we did not observe significant differences of

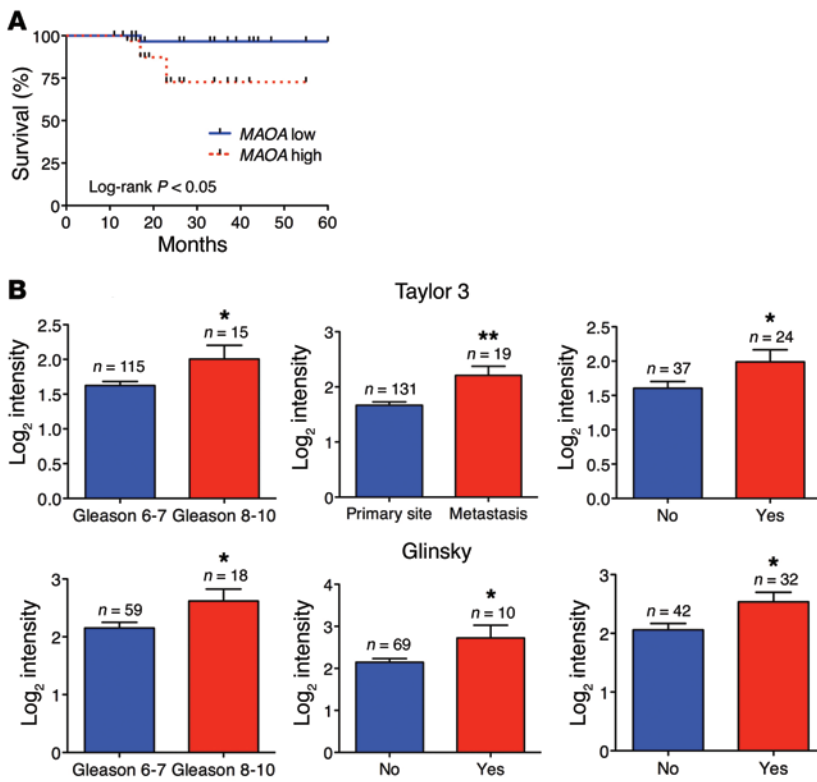


Figure 10

Increased MAOA expression is associated with poor prognosis in PCa patients. **(A)** Kaplan-Meier plots of survival of PCa patients stratified by the expression of MAOA from tissue microarrays (74 patients in total; MAOA-low, $n = 37$; MAOA-high, $n = 37$). Detailed patient information is given in Supplemental Table 3. The P value was calculated by a log-rank test. **(B)** OncoPrint analysis of MAOA transcript level in 2 publicly available DNA microarray data sets (top, Taylor 3; bottom, Glinsky) regarding Gleason score (Taylor 3, left; Glinsky, left), cancer sample site (Taylor 3, middle), seminal vesicle involvement (Glinsky, middle), and 5-year recurrence status (Taylor 3, right; Glinsky, right). $*P < 0.05$, $**P < 0.01$.

mouse body weight between the control and treatment groups. The efficacy of inhibition of MAOA enzymatic activity was confirmed in tumor samples at mouse necropsy (Figure 7F). By closely characterizing tumor samples, we demonstrated less Ki-67 staining, with a 26% drop of Ki-67⁺ cells, in the tumor specimens of the treatment group (Figure 7G). Moreover, qPCR analysis of tumor samples further revealed consistent changes in select markers of MAOA-knockdown effects, demonstrating reduced EMT and hypoxic responses to clorgyline treatment (Figure 7H).

In addition to the participation of MAOA in determining prostate tumorigenesis and cancer growth, our accumulated evidence that MAOA induced EMT and invasiveness in multiple lines of PCa cells further led us to speculate that MAOA may mediate PCa metastasis. To directly test whether MAOA is functionally important for PCa metastasis, we used ARCaP_M cells, a highly metastatic human PCa cell line (35, 39), which expressed either a control shRNA or a MAOA-specific shRNA to stably silence MAOA expression. The progression of cancer metastasis after intracardiac injection of tumor cells in mice was monitored by weekly bioluminescence imaging (BLI) using a stably expressed *Firefly* luciferase reporter. BLI analysis showed that MAOA knockdown significantly abrogated cancer metastasis in mice within a 10-week period after injection (Figure 8, A–C). In contrast, we observed significant metastases of control cells to various organs, including bone, adrenal gland, lymph node, lung, and liver, by BLI imaging with results confirmed by routine necrotic protocols (Supplemental Table 2). Taken together, these data strongly demonstrate that MAOA is a key determinant of tumor growth and metastasis in mice, potentially coordinating the regulation of EMT, hypoxia, and oxidative stress.

The HIF1 α /VEGF-A/FOXO1/TWIST1 pathway is manifested in high-Gleason grade PCa. A critical question that arises from our in vivo

data is whether the expression of HIF1 α , VEGF-A, and pFOXO1/FOXO1 and the activation of TWIST1 correlate with clinical grading in human PCa, and whether the expression of these proteins correlates with MAOA in the same specimens as predicted by our hypothesis. To address this question, we used a semiquantitative analysis of IHC staining to assess the expression of these proteins in specimens from 60 PCa patients, of which 30 were Gleason grade 3 and 30 were grade 5. Expression of MAOA was significantly higher in the cytoplasm of grade 5 compared with grade 3 PCa (Figure 9A), confirming previous studies. We observed intense widespread nuclear HIF1 α expression in grade 5 cells that was absent in grade 3 cells. Intense VEGF-A immunostaining was also evident in Gleason grade 5 tumor cells compared with grade 3 tumor cells (Figure 9A).

FOXO1 expression was observed in both the nucleus and cytoplasm, and there was a significant decrease of nuclear expression of FOXO1 in grade 5 tumor cells compared with grade 3 cells. pFOXO1 expression was present in both the nucleus and cytoplasm as well, but predominantly in cytoplasm. Cytoplasmic pFOXO1 showed higher staining in grade 5 cells in contrast to grade 3 cells. The differences seen in FOXO1/pFOXO1 expression patterns between Gleason grade 3 and grade 5 tumors indicate a dynamic nuclear exclusion of FOXO1 corresponding with disease progression. Moreover, intense widespread nuclear TWIST1 staining was evident in the majority of grade 5 tumor cells concurrently accompanied by a decline of nuclear FOXO1 expression (Figure 9A). These results are consistent with the hypothesis that MAOA increases TWIST1 expression by facilitating the phosphorylation and nuclear export of FOXO1 to activate the TWIST1 transcription. These IHC differences were all further confirmed by semiquantitative analysis of multiple specimens (Figure 9B).

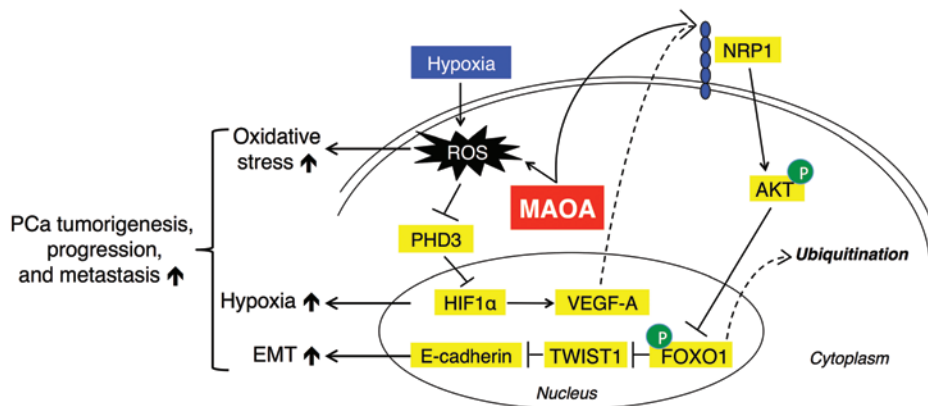


Figure 11

A proposed working model for how MAOA regulates prostate tumorigenesis, progression, and metastasis by engaging EMT, hypoxia, and ROS. MAOA induces EMT by generating ROS that inhibit PHD3 activity and stabilizing HIF1 α . Stimuli, such as hypoxia, can exacerbate MAOA-mediated production of ROS. MAOA further mediates the activation of VEGF-A/NRP1 signaling to upregulate the AKT/FOXO1 pathway, which results in the nuclear export of transcription repressor FOXO1 to activate nuclear TWIST1 expression. Together, increased MAOA expression promotes EMT, hypoxia, and ROS production, which in concert drive PCa tumorigenesis, progression, and metastasis.

Increased MAOA expression is associated with poor prognosis in PCa patients. To determine whether high MAOA expression exhibited by high-grade PCa is associated with poor patient outcome, we used a tissue microarray containing 74 cases with multiple disease progression (e.g., Gleason score 6–10, T2, or T3). After semiquantitative IHC analysis of these clinical samples, the Kaplan-Meier survival curves indicated that MAOA-low patients had significantly enhanced survival times when compared with MAOA-high patients (log-rank $P = 0.0267$) (Figure 10A and Supplemental Table 3). We further evaluated the prognostic value of MAOA in multiple public clinical DNA microarray data sets using OncoPrint 4.4. Considering that PCa is a biologically and clinically heterogeneous disease, we investigated whether high MAOA expression was related to multiple clinical indices in a subset of cases using Cancer Outlier Profile Analysis (COPA), a methodology that has been validated for uncovering candidate oncogenes, such as *ERG* (40). COPA identified MAOA as significantly overexpressed in a subset of tumor samples in 15 of 27 available data sets (gene rank, top 20%; fold change, >2 ; $P < 1 \times 10^{-4}$). Using the same statistical filters, MAOA displayed a COPA score comparable to or higher than that of *ERG* in several data sets (Supplemental Table 4).

The Gleason grading system for PCa is a key parameter for clinically assessing prognosis and choice of therapy, and cancers with a higher Gleason score are more aggressive along with a worse prognosis (13). Analysis of 2 data sets (Taylor 3 and Glinsky) indicated that high-level expression of MAOA was strongly associated with advanced Gleason score (8 to 10) (Figure 10B, left panels in both rows). We further correlated MAOA expression profiling with other clinical indices indicating poor prognosis of PCa, including metastasis (lymph node, bone, and soft tissues), seminal vesicle invasion, and biochemical recurrence. MAOA expression was increased when cancer cells formed metastatic lesions after dissemination from the primary site (Figure 10B, top middle panel). Invasion of the muscular wall of the seminal vesicles by PCa is considered as another marker for poor prognosis, metastatic disease, and quick biochemical recurrence (41). Examining the Glinsky data set, we

found that PCa patients with seminal vesicle invasion demonstrated higher MAOA expression than patients with intact seminal vesicles (Figure 10B, bottom middle panel). Additionally, analysis of 2 data sets (Taylor 3 and Glinsky) revealed increased MAOA expression in PCa patients who had biochemical recurrence at 5 years (Figure 10B, right panels in both rows). Overall, these clinical data support the experimentally described functional roles of MAOA in PCa and further indicate its prognostic value for distinguishing aggressive from indolent PCa.

In summary, our data suggest that the increased intrinsic MAOA in high-Gleason grade PCa activates a mesenchymal transition and consequent invasive behavior by a mechanism that involves its ability to stabilize HIF1 α via ROS production and activate the VEGF-A/

NRP1-mediated signaling network, which drives EMT by activating AKT/FOXO1 signaling and enhancing nuclear TWIST1 expression via sequestration of FOXO1 in the cytoplasm (Figure 11). Our data further show the key features of this enhanced cell signaling network in prostate tumor xenograft samples and in clinical high-Gleason grade PCa specimens, supporting the essential roles of MAOA in prostate tumorigenesis and cancer metastasis.

Discussion

Our study explores extensively how MAOA affects PCa growth and metastasis and demonstrates, for the first time to our knowledge, that MAOA induces EMT and augments hypoxic responses to increase the migratory, invasive, and metastatic potential of PCa cells. Increased MAOA expression has been previously reported in several types of cancer, including PCa (7) and renal cell carcinoma (42). Downregulation of MAOA has also been linked with the majority of other cancer types according to a preliminary analysis of an ensemble of cancer data sets (43). The fact that MAOA is expressed differentially in various cancers suggests that MAOA may be regulated differently in the context of specific cancer types. By examining what signaling events may upregulate MAOA in PCa specifically, we demonstrated that select oncogenic events (*c-Myc* overexpression and the loss of PTEN and p53) that appear to show high frequency in PCa (44–46) as well as activated androgen signaling were able to induce MAOA in PCa (Supplemental Figure 16). These regulations, particularly the induction of androgen by MAOA, may be an important underlying clue for the expression and function of MAOA in PCa distinct from other types of cancer. Moreover, serotonin, a monoamine neurotransmitter degraded preferentially by MAOA, has been shown to act as a growth factor for several types of cancer (47, 48), including melanoma (49) and cholangiocarcinoma (50). Inhibition of MAOA by clorgyline, which elevated serotonin levels, showed protection of melanoma cells against cell death (51). In addition, a suppression of MAOA expression that correlates with worse clinical prognosis and survival was associated with abnormally high levels of seroto-



nin in cholangiocarcinoma, which stimulate cholangiocarcinoma cell growth, and this condition is responsive to the blockade by the inhibition of serotonin synthesis (50, 52). In contrast, serotonin by itself plays a marginal role in regulating the growth of PCa cells in general (53), and there was no significant clinical correlation of serotonin levels with PCa disease progression (54, 55). The different effects of serotonin in diverse cancers therefore also provide insights into the differential functions of MAOA in PCa and other cancers. In addition, given the differential expressions of MAOA in multiple cancers, it would be worthwhile to examine MAOA effects on EMT and hypoxia in other types of cancer to gain a more comprehensive in-depth understanding of how MAOA functions in cancer generally.

MAOA was shown to stabilize HIF1 α , activate the VEGF-A/NRP1 system, and induce the expression of TWIST1, an EMT master transcription factor commonly associated with EMT promotion. These signaling components downstream from MAOA were shown to be clinically relevant, as revealed by the differential expressions of these genes in PCa specimens of different Gleason grades. The clinical relevance of EMT has been shown during tumor progression, and certain typical characteristics, including poor differentiation, correlated with aggressive and invasive behavior in high-Gleason grade PCa can result from EMT and EMT-like processes (56). We observed both increased MAOA expression and EMT in the same specimens of high-grade PCa, which, in line with our other results showing that MAOA can drive EMT (Figure 1), provides a molecular basis for the acquisition of a more aggressive phenotype in high-Gleason grade PCa. Our observation is consistent with previous studies showing that pharmacological inhibition of MAOA in PCa cells kept basal prostatic epithelial cells from differentiating into matured glandular structures by reorganizing cell structures and decreasing the expression of basal cytokeratins (9). In addition, a recent clinical survey assessing EMT marker levels in clinical samples with organ-confined PCa revealed that vimentin and TWIST1, among 13 other EMT markers, showed the most promising predictive potential for poor prognosis including biochemical recurrence (57). Our study mechanistically documented the induction of these 2 EMT markers, along with EMT promotion, by MAOA, and higher MAOA expression correlated with poor clinical outcomes in PCa patients, again suggesting its potential prognostic value (Figure 10).

Elevated ROS levels in MAOA-overexpressing cells contributed to increased HIF1 α stabilization and activity (Figures 2 and 3 and Supplemental Figure 8). Conversely, knockdown of MAOA in both cancer cells and xenograft tumors, resulting in reduced ROS levels, decreased HIF1 α /VEGF-A expression and exerted less hypoxic effects (Figures 2 and 6 and Supplemental Figure 8), which was further recapitulated by pharmacological inhibition of MAOA enzymatic activity (Figure 7). Several groups have reported the capability of both endogenous and added ROS to either transcriptionally (58) or posttranslationally (15) regulate HIF1 α activity. We demonstrated that MAOA-produced ROS could modulate HIF1 α activity by suppressing PHD activity, without changes in *HIF1A* transcription (Figures 2 and 3). MAOA, when catalyzing oxidative reactions in the outer membrane of mitochondria, immediately produces hydrogen peroxide as a by-product that can be further converted into other species of ROS (3). In the present system, we were able to pinpoint the intracellular hydrogen peroxide released specifically from intact mitochondria as well as extracellular general ROS regulated by MAOA in PCa cells (Figure 6 and Supple-

mental Figure 8). The secreted ROS in the extracellular environment may largely serve as paracrine stimuli to further enhance HIF1 α activity via PHD repression in a heterogeneous tumor cell population. Subsequently, the increased HIF1 α expression has the potential to further induce mitochondrial activity including the formation of specific ROS during hypoxia (19, 59), potentially programming a “vicious cycle” or feed-forward loop among MAOA, ROS, and HIF1 α to further drive PCa tumorigenesis. The vigorous characterization of the role of MAOA-regulated ROS solely contributed by enzymatic reactions led us further to investigate whether MAOA enzymatic activity or the protein is the determinant for mediating MAOA function in PCa. By conducting a comparative study using WT and a mutated MAOA expression construct that is defective in MAOA enzymatic activity but maintains intact protein expression (60), we demonstrated that MAOA enzymatic activity rather than the protein is the major player driving the migration, invasion, proliferation, and colonization of PCa cells by enhanced EMT and hypoxia (Supplemental Figure 17), which reinforces the role of MAOA-regulated ROS as an important mediator for MAOA functions in PCa.

The ability of MAOA to control VEGF-A/NRP1 signaling by upregulating the expression of both establishes a connection between this system and downstream signaling pathways. Since the seminal observation that NRP1 can function as a VEGF coreceptor (21), subsequent studies have demonstrated its functional importance in angiogenesis and cancer development (61). MAOA upregulates both the ligand and receptor and mediates receptor function mainly through the angiogenic aspect, which activates the VEGF-A/NRP1 system, particularly its EMT-enhancing ability (Figure 4). These findings support the potential role of MAOA in PCa tissues with high Gleason grade, distinguished by high tumor angiogenesis activity from low-grade PCa. In addition to interactions with angiogenic factors, NRP1 also cooperates with other growth factor receptors, such as c-Met (62, 63) and TGF- β receptors (64, 65), to mediate relevant pathways that contribute to tumorigenesis, and therefore could serve as a prognostic marker as well as an attractive target for cancer therapy. This establishes an additional rationale for targeting MAOA in PCa therapy, since patients with high-Gleason grade PCa may benefit from the blockade of VEGF-A/NRP1-mediated tumor angiogenesis along with other neuropilin-dependent pathways.

One of the salient features of our study is the discovery that MAOA represses *E-cadherin* transcription and promotes EMT in PCa cells by activating the transcription of *TWIST1* via AKT/FOXO1 signaling. We found that MAOA regulated *TWIST1* most robustly among the several master EMT transcription factors we screened. Given the prominent effect of *TWIST1* on the repression of the epithelial phenotype by direct suppression of *E-cadherin* transcription (66), the MAOA/*TWIST1* axis can thus be considered an effective regulatory node for the downregulation of *E-cadherin* by MAOA (Figure 1). The activation of *TWIST1* by MAOA is associated with the regulation of FOXO1 activity by AKT signaling, a transcription factor important for cell death and survival. The direct transcriptional regulation of *TWIST1* by FOXO1, proposed here for the first time to our knowledge, involves a key response element within the *TWIST1* promoter, which is highly conserved in the amniote genomes examined. This finding is supported by our mutational analysis of this element in the *TWIST1* promoter as well as the observation that FOXO1 can be recruited to this site in vivo (Figure 5). Moreover, we also



took into account other possible mechanisms that may contribute to TWIST1 activation in the MAOA context, such as HIF1 α activation of TWIST1 by binding directly to a hypoxia-response element in the *TWIST1* promoter as described in a recent study (67). We showed that MAOA was capable of inducing TWIST1 expression in response to effective knockdown of HIF1 α , suggesting diverse regulations of TWIST1 in the MAOA context (Supplemental Figure 18). This result further supports our mechanistic finding on the regulation of TWIST1 by MAOA/AKT/FOXO1 signaling in a HIF1 α -independent manner. Despite their all being a consequence of the activation of VEGF-A/NRP1 and AKT signaling to drive EMT, the mechanisms we elucidated for the regulation of TWIST1 by MAOA are distinct from those exerted by other genes, such as ER β , which is engaged in the activation of GSK-3 β and SNAIL1 to promote EMT (68). In our studies, we did not detect ER β changes in the context of MAOA overexpression (Supplemental Figure 19), suggesting that MAOA's effects in PCa are independent of ER β signaling. Notably, the complex but select activation of different pathways for EMT initiation suggests a context-dependent regulation of EMT. In addition to the profound effect on promoting and maintaining EMT (25), TWIST1 has also been implicated in the regulation of cell growth. Recent evidence has indicated that persistent TWIST1 expression induced growth arrest in EMT-like breast cancer cells mimicked by transient TGF- β treatment, which was mechanistically associated with cooperation with SNAIL1 and a signal feedback loop involving p38 and extracellular signal-regulated kinase (ERK) (69). By contrast, we observed an opposite effect of TWIST1 on cell proliferation (Supplemental Figure 12C), which, however, is consistent with the findings reported by several other groups where genetic interference with TWIST1 expression decreased PCa cell proliferation independent of cellular androgen levels and responses (70, 71). Furthermore, we did not find any changes in SNAIL1 level and p38 and ERK1/2 activity in the context of MAOA (Supplemental Figure 20), which could be an underlying mechanism accounting for the TWIST1 effect in the present system. These controversial results suggest, once again, a potential cell context-dependent role for TWIST1 in cell growth, related possibly to cell types, relevant gene expression profiling, and the responses of cancer cells to environmental cues.

Our study shows that genetic intervention with MAOA expression, by avoiding the potential off-target effects of pharmacological inhibitors, significantly impeded PCa progression or even eliminated prostate tumorigenesis in mice, using tumor xenograft models established from multiple human and murine prostate carcinoma cell lines (Figure 6). Moreover, inhibition of MAOA enzymatic activity by the small-molecule clorgyline achieved growth-inhibitory effects on xenograft tumors (Figure 7). The mechanisms discussed here suggest that targeting MAOA blocks PCa tumor growth by disrupting or disengaging the convergent signaling network involving EMT, hypoxia, and oxidative stress (Figure 11). In addition, genetic silencing of MAOA abolished the metastasis of an aggressive androgen-independent PCa cell line in mice (Figure 8), reinforcing the critical roles of MAOA in EMT initiation and cell invasiveness.

In summary, we have uncovered the underlying molecular mechanisms contributing to MAOA-initiated PCa progression. MAOA was shown to induce EMT, stabilize HIF1 α , and mediate hypoxia-elicited elevation of ROS in prostate carcinomas. Elevated MAOA signaling also increased the expression of VEGF-A

and its coreceptor NRP1, which together enhance EMT by stimulating AKT/FOXO1 signaling and promoting TWIST1 expression through sequestration of FOXO1 in the cytoplasm. The molecular basis of MAOA action could serve as a prognostic biomarker for poor differentiation and increased aggressiveness in PCa. Targeting MAOA and disengaging its downstream signaling network driving EMT, hypoxia, and oxidative stress provides a promising mechanistic rationale for therapeutic development.

Methods

Clinical specimens. All tissue specimens used in this study were archived formalin-fixed paraffin-embedded (FFPE) PCa tissues. These FFPE primary PCa specimens of defined Gleason grades were obtained from the Department of Pathology, Xijing Hospital, Fourth Military Medical University (FMMU). PCa tissue microarrays, including a total of 74 primary adenocarcinomas with patient overall survival data, were obtained from Imgenex and US Biomax. Specimens were stained with antibodies specific for MAOA (Santa Cruz), E-cadherin (Cell Signaling), vimentin (Santa Cruz), HIF1 α (Novus Biologicals), VEGF-A (Santa Cruz), FOXO1 (Millipore), pFOXO1 (Millipore), and TWIST1 (Sigma-Aldrich) following our published protocol (72, 73) with minor modifications as described below. Additional details on the clinical specimens used and methods of IHC analysis are provided in the Supplemental Methods online.

Cells and reagents. Human PCa PC-3 and LNCaP cell lines were obtained from American Type Culture Collection. Human PCa C4-2 (36) and ARCaP_M (35, 39) cell lines were established by our laboratory. The murine PCa MPC3 cell line, bearing a double knockout of *Pten* and *p53*, was provided by Neil Bhowmick (Cedars-Sinai Medical Center). For hypoxia experiments, cells were grown in a hypoxic chamber (1% O₂, 5% CO₂). Human MAOA expression construct was generated by insertion of the human MAOA coding region at *EcoRI*-*BglII* sites in 3xFLAG-pCMV vector (Sigma-Aldrich) containing a neomycin-resistant gene. Human *E-cadherin* promoter luciferase reporter construct (pGL2Basic-EcadK1) was provided by Eric Fearon (University of Michigan, Ann Arbor, MI) and obtained from Addgene. Human constitutively active (AAA) FOXO1 expression construct was provided by Kun-Liang Guan (University of California, San Diego, CA) and obtained from Addgene. Human TWIST1 promoter luciferase reporter constructs of various lengths were provided by Lu-Hai Wang (Mount Sinai Hospital, New York, NY). The *Renilla* luciferase plasmid was purchased from Promega. Human MAOA, NRP1, and nontargeting control shRNA lentiviral particles were purchased from Sigma-Aldrich or Santa Cruz. NAC and clorgyline were purchased from Sigma-Aldrich. DMOG and MG132 were purchased from Millipore. Additional details on cells and reagents used in this study are provided in the Supplemental Methods.

Biochemical analyses. Total RNA was isolated using the RNeasy Mini Kit (Qiagen) and reverse-transcribed to cDNA by M-MLV reverse transcriptase (Promega) as described previously (74). Details on primers and methods used for qPCR are provided in the Supplemental Methods. For immunoblots, cells were extracted with radioimmunoprecipitation assay buffer in the presence of a protease and phosphatase inhibitor cocktail (Thermo Scientific), and blots were performed as described previously (75, 76) using primary antibodies against MAOA (Santa Cruz), E-cadherin (Cell Signaling), vimentin (Santa Cruz), N-cadherin (Santa Cruz), TWIST1 (Santa Cruz), β -actin (Sigma-Aldrich), HIF1 α (BD Biosciences), hydroxy-HIF1 α (Cell Signaling), PHD1-4 (Novus Biologicals), NRP1 (Santa Cruz), phospho-AKT (Ser473) (Cell Signaling), AKT (Cell Signaling), phospho-FOXO1 (Thr24) (Cell Signaling), FOXO1 (Santa Cruz), lamin B1 (Cell Signaling), or GAPDH (Cell Signaling). Immunoblots were further subjected to morphometric and statistical analysis by ImageJ software (NIH) (Supplemental Figure 21). Nuclear/cytoplasmic and mitochondrial/cytoplasmic extracts used



for immunoblots were prepared with individual kits (Thermo Scientific). VEGF-A levels in culture media were quantified by ELISA (R&D Systems).

Migration and invasion assays. Assays were performed using 6.5-mm transwell inserts (8- μ m pore size) coated with either collagen I or Growth Factor Reduced Matrigel (BD Biosciences) for the migration and invasion assays, respectively. Cells were serum-starved overnight before seeding to eliminate the interference of proliferative effect with cell migration or invasion. Cells were seeded inside transwell inserts containing culture medium without serum. After 18–24 hours, the cells that translocated to the lower surface of the filters were fixed in 4% formaldehyde. The fixed membranes were stained using 1% crystal violet. Assays were quantified by counting of the number of stained nuclei in 5 independent fields in each transwell.

Luciferase assays. PC-3 cells were transfected with the desired *Firefly* luciferase reporter plasmids and the *Renilla* luciferase construct to normalize for transfection efficiency. Relative light units were calculated as the ratio of *Firefly* luciferase to *Renilla* luciferase activity. The protocol used for transfection and measurement of luciferase activity has been described previously (77).

ROS measurement. Cellular ROS was measured according to published protocols (78, 79). Briefly, cells were washed with PBS and incubated with 5 μ M CM-H₂DCFDA (Life Technologies) for 30 minutes. Cells were trypsinized, and mean FL1 fluorescence was measured by flow cytometry. Intact cellular or tumor mitochondria were isolated with a kit (Thermo Scientific) or according to published protocols (80), respectively, and the hydrogen peroxide generation rate was measured for a period of 30 minutes using the Amplex Red Hydrogen Peroxide Assay Kit (Life Technologies) by a spectrophotometer.

Analyses of *Twist1* promoter. Serial deletion analysis of *TWIST1* promoter was used to locate the putative FOXO1-response element. Site-directed mutagenesis was used to mutate the DAF-16 binding element (DBE) sequence from CCAAACCT to CCGCGCT. ChIP analysis was used to determine the direct association of endogenous FOXO1 protein with the native *TWIST1* promoter in control and MAOA-overexpressing PC-3 cells. Details of these analyses are provided in Supplemental Methods.

Animal studies. Male 4- to 6-week-old athymic nude mice, SCID-beige mice, and immune-intact C57BL/6 mice were purchased from Taconic, housed in the animal research facility at Cedars-Sinai Medical Center (CSMC), and fed a normal chow diet. For xenograft studies, 1×10^6 LNCaP, C4-2, ARCaP_M (shCon and shMAOA), or PC-3 (vector and MAOA-overexpression) cells were mixed 1:1 with Matrigel (BD Biosciences) and injected s.c. into nude mice, and 1×10^6 MPC3 (shCon and shMAOA) cells were injected s.c. into immune-intact C57BL/6 mice. Each mouse was injected on both flanks. Four to seven mice were used for each group. Details on the number of mice and injection sites used for each cell line to establish subcutaneous tumor xenografts are provided in Supplemental Table 1. Tumor size was measured every 2–3 days by caliper from the time of the formation of palpable tumors, and tumors were dissected and weighed after 3–6 weeks. Tumor volume was calculated by the formula of length \times width² \times 0.52 (81). Tumors were fixed in 4% formaldehyde and embedded in paraffin. Sections were stained with H&E in accordance with standard procedures (82).

For determining the effect of clorgyline on tumor growth, 1×10^6 C4-2 cells were mixed 1:1 with Matrigel and injected s.c. into nude mice, with each mouse bearing 1 tumor on the right flank. Mice were randomly assigned to 2 groups (clorgyline treatment vs. control, $n = 5$ for each) when the tumors reached a measurable size of 100–200 mm³. Daily i.p. injection of clorgyline (10 mg/kg) was given to mice of the treatment group for 21 days, and saline injection was used for the control group. Tumor size was measured every 3 days by caliper, and tumors were weighed when mice were subjected to necropsy on day 21.

For metastatic studies, 1×10^6 ARCaP_M cells tagged with a *Firefly* luciferase reporter construct (Promega) were injected into the left cardiac ventricle of anesthetized SCID-beige mice as described previously (39). Development of metastases was monitored by BLI. Anesthetized mice were injected i.p. with 30 mg D-Luciferin per mouse (Gold Biotech). Bioluminescence images were acquired with a Xenogen IVIS Spectrum Imaging System (PerkinElmer). Analysis was performed with Living Image software (PerkinElmer) by measurement of photon flux in the whole bodies of mice. Data were normalized to the signal in week 1.

Immunohistochemistry. IHC analysis of tumor xenograft or mouse primary tumor samples was performed using antibodies against Ki-67 (Dako), MAOA (Santa Cruz), E-cadherin (Cell Signaling), vimentin (Santa Cruz), HIF1 α (BD Biosciences), or VEGF-A (Santa Cruz) following our published protocol (72) with minor modifications. Briefly, FFPE sections (4 μ m) were deparaffinized, rehydrated, and subjected to antigen retrieval. After incubation in Dual Endogenous Enzyme Block solution (Dako) for 10 minutes, the section was treated with primary antibody diluted by different folds with Antibody Diluent solution (Dako) at 4°C overnight. The section was then washed 3 times in PBST (PBS containing 0.2% Tween-20) for 5 minutes per washing. To detect specific staining, the section was treated for 30 minutes with EnVision + Dual Link System-HRP (Dako), which contained HRP-conjugated goat antibodies against mouse and rabbit IgG. The section was washed 3 times for 5 minutes each, and specific stains were developed with 3'-diaminobenzidine (Dako). Image acquisition was performed using a Nikon camera and software. Magnification was $\times 400$ (scale bars $\sim 20 \mu$ m).

MAOA enzymatic activity assay. MAOA enzymatic activity was determined in control and MAOA-knockdown cells and tumor samples as described previously (83). Briefly, 100 μ g of total protein was incubated with 1 mM [¹⁴C]5-HT in the assay buffer at 37°C for 20 minutes, and the reaction was terminated by the addition of ice-cold 6 N HCl. The reaction products were extracted with benzene/ethyl acetate (1:1) and centrifuged at 4°C for 7 minutes. The organic phase containing the reaction products was extracted, and radioactivity was determined by liquid scintillation spectroscopy.

Microarray data sets. Two PCa DNA microarray data sets, Taylor 3 (84) and Glinisky (85), were downloaded directly from the Oncomine database by licensed access. Microarray data of the Taylor 3 data set are also publicly available in Gene Expression Omnibus (GEO GSE21032).

Statistics. Data are presented as the mean \pm SEM as indicated in the figure legends. Comparisons between Kaplan-Meier curves were performed using the log-rank test. All other comparisons were analyzed by unpaired 2-tailed Student's *t* test. A *P* value less than 0.05 was considered statistically significant.

Study approval. All animal studies received prior approval by the IACUC of CSMC and were conducted in compliance with its recommendations. All human studies were reviewed and approved by the IRB of CSMC and FMMU, and written informed consent was provided for human samples.

Acknowledgments

This work was supported by NIH/National Cancer Institute grants 5P01CA098912 and R01CA122602, the Board of Governors Cancer Research Chair, and the Steven Spielberg Fund in Prostate Cancer Research (to L.W.K. Chung); Department of Defense Prostate Cancer Research Program grant W81XWH-12-1-0282 (to H.E. Zhou and J.C. Shih); and the Daniel Tsai Family Fund (to J.C. Shih). We thank Lei Zhang (FMMU, Xi'an, Shaanxi, China) for providing clinical specimens, Pradip Roy-Burman (Department of Pathology, University of Southern California, Los Angeles, CA) for providing mouse prostate-specific *Pten*-knockout tumor specimens, and Bin Qian and Jenny Wu (Department of Pharmacology and Pharmaceuticals, University of Southern California, Los



Angeles, CA) for providing technical assistance. We also thank Gary Mawyer for editorial assistance.

Received for publication May 20, 2013, and accepted in revised form April 3, 2014.

Address correspondence to: Leland W.K. Chung, Cedars-Sinai Medical Center, 8750 Beverly Boulevard, Atrium 103, Los Angeles,

California 90048, USA. Phone: 310.423.7622; Fax: 310.423.8543; E-mail: leland.chung@cshs.org. Or to: Jean C. Shih, University of Southern California, 1985 Zonal Avenue, PSC 518, Los Angeles, California 90089, USA. Phone: 323.442.1441; Fax: 323.442.3229; E-mail: jcsih@usc.edu. Or to: Haiyen E. Zhou, Cedars-Sinai Medical Center, 8750 Beverly Boulevard, Atrium 103, Los Angeles, California 90048, USA. Phone: 310.423.8179; Fax: 310.423.8543; E-mail: haiyen.zhou@cshs.org.

- Siegel R, Naishadham D, Jemal A. Cancer statistics, 2013. *CA Cancer J Clin*. 2013;63(1):11–30.
- Partin AW, et al. Combination of prostate-specific antigen, clinical stage, and Gleason score to predict pathological stage of localized prostate cancer. A multi-institutional update. *JAMA*. 1997; 277(18):1445–1451.
- Shih JC, Chen K, Ridd MJ. Monoamine oxidase: from genes to behavior. *Annu Rev Neurosci*. 1999; 22:197–217.
- Shih JC, Wu JB, Chen K. Transcriptional regulation and multiple functions of MAO genes. *J Neural Transm*. 2011;118(7):979–986.
- Bortolato M, Chen K, Shih JC. Monoamine oxidase inactivation: from pathophysiology to therapeutics. *Adv Drug Deliv Rev*. 2008;60(13–14):1527–1533.
- Trachootham D, Alexandre J, Huang P. Targeting cancer cells by ROS-mediated mechanisms: a radical therapeutic approach? *Nat Rev Drug Discov*. 2009;8(7):579–591.
- True L, et al. A molecular correlate to the Gleason grading system for prostate adenocarcinoma. *Proc Natl Acad Sci U S A*. 2006;103(29):10991–10996.
- Peehl DM, Coram M, Khine H, Reese S, Nolley R, Zhao H. The significance of monoamine oxidase-A expression in high grade prostate cancer. *J Urol*. 2008;180(5):2206–2211.
- Zhao H, Nolley R, Chen Z, Reese SW, Peehl DM. Inhibition of monoamine oxidase A promotes secretory differentiation in basal prostatic epithelial cells. *Differentiation*. 2008;76(7):820–830.
- Nauseef JT, Henry MD. Epithelial-to-mesenchymal transition in prostate cancer: paradigm or puzzle? *Nat Rev Urol*. 2011;8(8):428–439.
- Stewart GD, Ross JA, McLaren DB, Parker CC, Habib FK, Riddick AC. The relevance of a hypoxic tumour microenvironment in prostate cancer. *BJU Int*. 2010;105(1):8–13.
- Gupta-Elera G, Garrett AR, Robison RA, O'Neill KL. The role of oxidative stress in prostate cancer. *Eur J Cancer Prev*. 2012;21(2):155–162.
- Gleason DF, Mellinger GT. Prediction of prognosis for prostatic adenocarcinoma by combined histological grading and clinical staging. *J Urol*. 1974;111(1):58–64.
- Lu X, Kang Y. Hypoxia and hypoxia-inducible factors: master regulators of metastasis. *Clin Cancer Res*. 2010;16(24):5928–5935.
- Finley LW, et al. SIRT3 opposes reprogramming of cancer cell metabolism through HIF1 α destabilization. *Cancer Cell*. 2011;19(3):416–428.
- Kaelin WG Jr, Ratcliffe PJ. Oxygen sensing by metazoans: the central role of the HIF hydroxylase pathway. *Mol Cell*. 2008;30(4):393–402.
- Schnaitman C, Erwin VG, Greenawalt JW. The sub-mitochondrial localization of monoamine oxidase. An enzymatic marker for the outer membrane of rat liver mitochondria. *J Cell Biol*. 1967;32(3):719–735.
- Wang GL, Jiang BH, Rue EA, Semenza GL. Hypoxia-inducible factor 1 is a basic-helix-loop-helix-PAS heterodimer regulated by cellular O₂ tension. *Proc Natl Acad Sci U S A*. 1995;92(12):5510–5514.
- Chandel NS, Maltepe E, Goldwasser E, Mathieu CE, Simon MC, Schumacker PT. Mitochondrial reactive oxygen species trigger hypoxia-induced transcription. *Proc Natl Acad Sci U S A*. 1998;95(20):11715–11720.
- Antonarakis ES, Carducci MA. Targeting angiogenesis for the treatment of prostate cancer. *Expert Opin Ther Targets*. 2012;16(4):365–376.
- Soker S, Takashima S, Miao HQ, Neufeld G, Klagsbrun M. Neuropilin-1 is expressed by endothelial tumor cells as an isoform-specific receptor for vascular endothelial growth factor. *Cell*. 1998;92(6):735–745.
- Bartholomeusz C, Gonzalez-Angulo AM. Targeting the PI3K signaling pathway in cancer therapy. *Expert Opin Ther Targets*. 2012;16(1):121–130.
- Zhang Y, Gan B, Liu D, Paik JH. FoxO family members in cancer. *Cancer Biol Ther*. 2011;12(4):253–259.
- Bachelder RE, et al. Vascular endothelial growth factor is an autocrine survival factor for neuropilin-expressing breast carcinoma cells. *Cancer Res*. 2001;61(15):5736–5740.
- Yang J, et al. Twist, a master regulator of morphogenesis, plays an essential role in tumor metastasis. *Cell*. 2004;117(7):927–939.
- Wallerand H, et al. The epithelial-mesenchymal transition-inducing factor TWIST is an attractive target in advanced and/or metastatic bladder and prostate cancers. *Urol Oncol*. 2010;28(5):473–479.
- Vichalkovski A, Gresko E, Hess D, Restuccia DF, Hemmings BA. PKB/AKT phosphorylation of the transcription factor Twist-1 at Ser42 inhibits p53 activity in response to DNA damage. *Oncogene*. 2010;29(24):3554–3565.
- Xue G, et al. Akt/PKB-mediated phosphorylation of Twist1 promotes tumor metastasis via mediating cross-talk between PI3K/Akt TGF-beta signaling axes. *Cancer Discov*. 2012;2(3):248–259.
- Shiota M, et al. Foxo3a suppression of urothelial cancer invasiveness through Twist1, Y-box-binding protein 1, E-cadherin regulation. *Clin Cancer Res*. 2010;16(23):5654–5663.
- Tang ED, Nunez G, Barr FG, Guan KL. Negative regulation of the forkhead transcription factor FKHR by Akt. *J Biol Chem*. 1999;274(24):16741–16746.
- Cheng GZ, et al. Twist is transcriptionally induced by activation of STAT3 and mediates STAT3 oncogenic function. *J Biol Chem*. 2008;283(21):14665–14673.
- Glauser DA, Schlegel W. The emerging role of FOXO transcription factors in pancreatic β cells. *J Endocrinol*. 2007;193(2):195–207.
- Allen DL, Unterman TG. Regulation of myostatin expression and myoblast differentiation by FoxO and SMAD transcription factors. *Am J Physiol Cell Physiol*. 2007;292(1):C188–C199.
- Fan W, et al. FoxO1 regulates Tlr4 inflammatory pathway signalling in macrophages. *EMBO J*. 2010;29(24):4223–4236.
- Zhou HY, et al. Androgen-repressed phenotype in human prostate cancer. *Proc Natl Acad Sci U S A*. 1996; 93(26):15152–15157.
- Thalmann GN, et al. Androgen-independent cancer progression and bone metastasis in the LNCaP model of human prostate cancer. *Cancer Res*. 1994;54(10):2577–2581.
- Green AR, Youdim MB. Effects of monoamine oxidase inhibition by clorgyline, deprenil or tranlycypromine on 5-hydroxytryptamine concentrations in rat brain hyperactivity following subsequent tryptophan administration. *Br J Pharmacol*. 1975;55(3):415–422.
- Wu TT, et al. Establishing human prostate cancer cell xenografts in bone: induction of osteoblastic reaction by prostate-specific antigen-producing tumors in athymic and SCID/bg mice using LNCaP and lineage-derived metastatic sublines. *Int J Cancer*. 1998;77(6):887–894.
- Xu J, et al. Prostate cancer metastasis: role of the host microenvironment in promoting epithelial to mesenchymal transition and increased bone and adrenal gland metastasis. *Prostate*. 2006;66(15):1664–1673.
- Tomlins SA, et al. Recurrent fusion of TMPRSS2 and ETS transcription factor genes in prostate cancer. *Science*. 2005;310(5748):644–648.
- Potter SR, Epstein JI, Partin AW. Seminal vesicle invasion by prostate cancer: prognostic significance and therapeutic implications. *Rev Urol*. 2000; 2(3):190–195.
- Hodorova I, et al. Comparison of expression pattern of monoamine oxidase A with histopathological subtypes and tumour grade of renal cell carcinoma. *Med Sci Monit*. 2012;18(12):BR482–BR486.
- Rybaczuk LA, Bashaw MJ, Pathak DR, Huang K. An indicator of cancer: downregulation of monoamine oxidase-A in multiple organs and species. *BMC Genomics*. 2008;9:134.
- Gurel B, et al. Nuclear MYC protein overexpression is an early alteration in human prostate carcinogenesis. *Mod Pathol*. 2008;21(9):1156–1167.
- McMenamin ME, Soung P, Perera S, Kaplan I, Loda M, Sellers WR. Loss of PTEN expression in paraffin-embedded primary prostate cancer correlates with high Gleason score and advanced stage. *Cancer Res*. 1999;59(17):4291–4296.
- Chi SG, deVere White RW, Meyers FJ, Siders DB, Lee F, Gumerlock PH. p53 in prostate cancer: frequent expressed transition mutations. *J Natl Cancer Inst*. 1994;86(12):926–933.
- Pratesi G, Cervi S, Balsari A, Bondiolotti G, Vicentini LM. Effect of serotonin and nicotine on the growth of a human small cell lung cancer xenograft. *Anticancer Res*. 1996;16(6B):3615–3619.
- Soll C, et al. Serotonin promotes tumor growth in human hepatocellular cancer. *Hepatology*. 2010; 51(4):1244–1254.
- Lee HJ, Park MK, Kim SY, Park Choo HY, Lee AY, Lee CH. Serotonin induces melanogenesis via serotonin receptor 2A. *Br J Dermatol*. 2011;165(6):1344–1338.
- Alpini G, et al. Serotonin metabolism is dysregulated in cholangiocarcinoma, which has implications for tumor growth. *Cancer Res*. 2008;68(22):9184–9193.
- Malorni W, et al. Protection against apoptosis by monoamine oxidase A inhibitors. *FEBS Lett*. 1998; 426(1):155–159.
- Huang L, et al. Monoamine oxidase A expression is suppressed in human cholangiocarcinoma via coordinated epigenetic and IL-6-driven events. *Lab Invest*. 2012;92(10):1451–1460.
- Pirozhok I, Meye A, Hakenberg OW, Fuessel S, Wirth MP. Serotonin and melatonin do not play a prominent role in the growth of prostate cancer cell lines. *Urol Int*. 2010;84(4):452–460.
- Jungwirth N, Haerberle L, Schrott KM, Wullich B, Krause FS. Serotonin used as prognostic marker of urological tumors. *World J Urol*. 2008;26(5):499–504.
- Heinrich E, et al. Neuroendocrine tumor cells in prostate cancer: evaluation of the neurosecretory products serotonin, bombesin, and gastrin – impact on angiogenesis and clinical follow-up. *Prostate*. 2011;71(16):1752–1758.
- Savagner P. The epithelial-mesenchymal tran-



- sition (EMT) phenomenon. *Ann Oncol.* 2010; 21(suppl 7):vii89–vii92.
57. Behnsawy HM, Miyake H, Harada K, Fujisawa M. Expression patterns of epithelial-mesenchymal transition markers in localized prostate cancer: significance in clinicopathological outcomes following radical prostatectomy. *BJU Int.* 2013;111(1):30–37.
58. Bonello S, et al. Reactive oxygen species activate the HIF-1 α promoter via a functional NF κ B site. *Arterioscler Thromb Vasc Biol.* 2007;27(4):755–761.
59. Chandel NS, et al. Reactive oxygen species generated at mitochondrial complex III stabilize hypoxia-inducible factor-1 α during hypoxia: a mechanism of O₂ sensing. *J Biol Chem.* 2000;275(33):25130–25138.
60. Geha RM, Chen K, Wouters J, Ooms F, Shih JC. Analysis of conserved active site residues in monoamine oxidase A and B and their three-dimensional molecular modeling. *J Biol Chem.* 2002;277(19):17209–17216.
61. Guttman-Raviv N, Kessler O, Shraga-Heled N, Lange T, Herzog Y, Neufeld G. The neuropilins and their role in tumorigenesis and tumor progression. *Cancer Lett.* 2006;231(1):1–11.
62. Matsushita A, Gotze T, Korc M. Hepatocyte growth factor-mediated cell invasion in pancreatic cancer cells is dependent on neuropilin-1. *Cancer Res.* 2007; 67(21):10309–10316.
63. Hu B, et al. Neuropilin-1 promotes human glioma progression through potentiating the activity of the HGF/SF autocrine pathway. *Oncogene.* 2007; 26(38):5577–5586.
64. Glinka Y, Prud'homme GJ. Neuropilin-1 is a receptor for transforming growth factor β -1, activates its latent form, promotes regulatory T cell activity. *J Leukoc Biol.* 2008;84(1):302–310.
65. Cao S, et al. Neuropilin-1 promotes cirrhosis of the rodent human liver by enhancing PDGF/TGF- β signaling in hepatic stellate cells. *J Clin Invest.* 2010; 120(7):2379–2394.
66. Vesuna F, van Diest P, Chen JH, Raman V. Twist is a transcriptional repressor of E-cadherin gene expression in breast cancer. *Biochem Biophys Res Commun.* 2008;367(2):235–241.
67. Yang MH, et al. Direct regulation of TWIST by HIF-1 α promotes metastasis. *Nat Cell Biol.* 2008; 10(3):295–305.
68. Mak P, et al. ERbeta impedes prostate cancer EMT by destabilizing HIF-1 α and inhibiting VEGF-mediated snail nuclear localization: implications for Gleason grading. *Cancer Cell.* 2010;17(4):319–332.
69. Tran DD, Corsa CA, Biswas H, Aft RL, Longmore GD. Temporal and spatial cooperation of Snail1 and Twist1 during epithelial-mesenchymal transition predicts for human breast cancer recurrence. *Mol Cancer Res.* 2011;9(12):1644–1657.
70. Shiota M, et al. Castration resistance of prostate cancer cells caused by castration-induced oxidative stress through Twist1 and androgen receptor overexpression. *Oncogene.* 2010;29(2):237–250.
71. Shiota M, et al. Twist promotes tumor cell growth through YB-1 expression. *Cancer Res.* 2008; 68(1):98–105.
72. Zhou HE, et al. Epithelial to mesenchymal transition (EMT) in human prostate cancer: lessons learned from ARCaP model. *Clin Exp Metastasis.* 2008; 25(6):601–610.
73. Zeng N, et al. PTEN controls beta-cell regeneration in aged mice by regulating cell cycle inhibitor p16(ink4a). *Aging Cell.* 2013;12(6):1000–1011.
74. Wu JB, Chen K, Ou XM, Shih JC. Retinoic acid activates monoamine oxidase B promoter in human neuronal cells. *J Biol Chem.* 2009; 284(25):16723–16735.
75. Zeng N, et al. Adaptive basal phosphorylation of eIF2 α is responsible for resistance to cellular stress-induced cell death in Pten-null hepatocytes. *Mol Cancer Res.* 2011;9(12):1708–1717.
76. Chen K, Ou XM, Wu JB, Shih JC. Transcription factor E2F-associated phosphoprotein (EAPP), RAM2/CDC47L/JPO2 (R1), simian virus 40 promoter factor 1 (Sp1) cooperatively regulate glucocorticoid activation of monoamine oxidase B. *Mol Pharmacol.* 2011;79(2):308–317.
77. Wu JB, Shih JC. Valproic acid induces monoamine oxidase A via Akt/forkhead box O1 activation. *Mol Pharmacol.* 2011;80(4):714–723.
78. Eruslanov E, Kusmartsev S. Identification of ROS using oxidized DCFDA and flow-cytometry. *Methods Mol Biol.* 2010;594:57–72.
79. Li Y, et al. Phosphatase and tensin homolog deleted on chromosome 10 (PTEN) signaling regulates mitochondrial biogenesis respiration via estrogen-related receptor α (ERR α). *J Biol Chem.* 2013; 288(35):25007–25024.
80. Graham JM. Isolation of mitochondria from tissues and cells by differential centrifugation. *Curr Protoc Cell Biol.* 2001;3:Unit 3.3.
81. Tomayko MM, Reynolds CP. Determination of subcutaneous tumor size in athymic (nude) mice. *Cancer Chemother Pharmacol.* 1989;24(3):148–154.
82. Fischer AH, Jacobson KA, Rose J, Zeller R. Hematoxylin and eosin staining of tissue and cell sections. *CSH Protoc.* 2008;2008.pdb.prot4986.
83. Wu JB, Chen K, Li Y, Lau YF, Shih JC. Regulation of monoamine oxidase A by the SRY gene on the Y chromosome. *FASEB J.* 2009;23(11):4029–4038.
84. Taylor BS, et al. Integrative genomic profiling of human prostate cancer. *Cancer Cell.* 2010;18(1):11–22.
85. Glinsky GV, Glinskii AB, Stephenson AJ, Hoffman RM, Gerald WL. Gene expression profiling predicts clinical outcome of prostate cancer. *J Clin Invest.* 2004;113(6):913–923.

Published in final edited form as:

Biomaterials. 2014 September ; 35(28): 8175–8185. doi:10.1016/j.biomaterials.2014.05.073.

Near-infrared fluorescence imaging of cancer mediated by tumor hypoxia and HIF1 α /OATPs signaling axis

Jason Boyang Wu^{a,§}, Chen Shao^{a,b,§}, Xiangyan Li^a, Changhong Shi^{a,c}, Qinlong Li^a, Peizhen Hu^a, Yi-Ting Chen^a, Xiaoliang Dou^b, Divya Sahu^d, Wei Li^d, Hiroshi Harada^e, Yi Zhang^f, Ruoxiang Wang^a, Haiyen E. Zhau^a, and Leland W.K. Chung^{a,*}

^aUro-Oncology Research Program, Department of Medicine, Cedars-Sinai Medical Center, Los Angeles, CA 90048, USA

^bDepartment of Urology, Xijing Hospital, Fourth Military Medical University, Xi'an, Shaanxi 710032, China

^cLaboratory Animal Center, Fourth Military Medical University, Xi'an, Shaanxi 710032, China

^dDepartment of Dermatology, Keck School of Medicine, University of Southern California, Los Angeles, CA 90089, USA

^eDepartment of Radiation Oncology and Image-Applied Therapy, Kyoto University Graduate School of Medicine, Kyoto 606-8507, Japan

^fBiomedical Imaging Research Institute, Cedars-Sinai Medical Center, Los Angeles, CA 90048, USA

Abstract

Near-infrared fluorescence (NIRF) imaging agents are promising tools for noninvasive cancer imaging. Here, we explored the mechanistic properties of a specific group of NIR heptamethine carbocyanines including MHI-148 dye we identified and synthesized, and demonstrated these dyes to achieve cancer-specific imaging and targeting via a hypoxia-mediated mechanism. We found that cancer cells and tumor xenografts exhibited hypoxia-dependent MHI-148 dye uptake *in vitro* and *in vivo*, which was directly mediated by hypoxia-inducible factor 1 α (HIF1 α). Microarray analysis and dye uptake assay further revealed a group of hypoxia-inducible organic anion-transporting polypeptides (OATPs) responsible for dye uptake, and the correlation between OATPs and HIF1 α was manifested in progressive clinical cancer specimens. Finally, we demonstrated increased uptake of MHI-148 dye *in situ* in perfused clinical tumor samples with activated HIF1 α /OATPs signaling. Our results establish these NIRF dyes as potential tumor

© 2014 Elsevier Ltd. All rights reserved.

*Corresponding Author. Uro-Oncology Research Program, Cedars-Sinai Medical Center, 8750 Beverly Blvd., Atrium 103, Los Angeles, CA 90048, USA. Tel.: +1 310 4237622. Leland.Chung@cshs.org.

§These authors contributed equally to this work.

Publisher's Disclaimer: This is a PDF file of an unedited manuscript that has been accepted for publication. As a service to our customers we are providing this early version of the manuscript. The manuscript will undergo copyediting, typesetting, and review of the resulting proof before it is published in its final citable form. Please note that during the production process errors may be discovered which could affect the content, and all legal disclaimers that apply to the journal pertain.

hypoxia-dependent cancer-targeting agents and provide a mechanistic rationale for continued development of NIRF imaging agents for improved cancer detection, prognosis and therapy.

Keywords

cancer imaging; HIF1 α ; hypoxia; near-infrared dyes; organic anion-transporting polypeptides

1. Introduction

Near-infrared fluorescence (NIRF) imaging has recently emerged as a useful tool for noninvasive cancer imaging [1]. NIRF agents show very limited autofluorescence from intrinsic chromophores, but upon binding to biomolecules they display drastically increased fluorescence due to rigidization of the fluorophores [2, 3]. Polymethine carbocyanine dyes, such as pentamethine and heptamethine carbocyanines, are representative NIRF contrast agents that have shown great potential for both experimental and clinical NIRF imaging [4]. These organic dyes feature high extinction coefficients and relatively large Stokes' shift, and in the presence of emission wavelengths ranging from 700–1,000 nm their fluorescence can be readily captured from deep tissues by commercially available imaging modalities [2, 3].

Most conventional approaches for utilizing NIRF dyes in cancer imaging require chemical conjugation of NIR fluorophores with appropriate tumor-specific ligands, including metabolic substrates, aptamers, growth factors, and antibodies [5–7]. A number of surface molecules have been tested as targets, including membrane receptors, extracellular matrices, cancer cell surface-specific markers, and neovascular endothelial cell-specific markers [8, 9]. These approaches have created agents with a narrower spectrum for cancer imaging since the NIRF moieties only detect specific types of cancer cells with well-characterized surface properties [10]. Moreover, the specificity and affinity of targeting ligands could also be affected by chemical conjugation [3]. Hence, there is an unmet need for developing NIRF dyes with simpler and more straightforward use to advance noninvasive cancer imaging, taking into account the heterogeneous nature of cancer.

We previously identified and synthesized a specific class of NIRF heptamethine carbocyanines as dual imaging and cancer targeting agents. Two prototypic heptamethine carbocyanine dyes including MHI-148 demonstrated promising biological activity [11, 12]. However, how these dyes achieve cancer-specific targeting properties are largely unclear. Tumor cells, though display heterogeneity in general, still share select common features for proliferation and survival such as responses to environmental hypoxic stimuli through certain epigenetic alterations. In this study, utilizing genitourinary cancers as a model system, we investigated the intrinsic features of these dyes by linking the dye uptake with tumor hypoxia and explored the possible molecular mechanisms that may mediate the preferential uptake of this class of NIRF dyes by cancer cells.

2. Materials and methods

2.1. Cell culture and reagents

The human prostate cancer (PCa) cell lines PC-3, PC-3M and LNCaP, human breast cancer cell line MDA-MB-231, and human leukemia cell line K562 were purchased from American Type Culture Collection (ATCC, Manassas, VA). The normal prostatic epithelial PrEC cells were purchased from Lonza (Allendale, NJ). The human PCa cell lines C4-2, ARCaP_E and ARCaP_M were established by our laboratory [13–15], and the murine prostate cancer cell line MPC3 was kindly provided by Dr. Neil Bhowmick (Cedars-Sinai Medical Center, Los Angeles, CA) [16]. For hypoxia treatment, cells were grown in a hypoxic chamber (1% O₂, 5% CO₂). PC-3 cells stably overexpressing *5HREp-ODD-luc* were established by lipofectamine-mediated transfection of the construct followed by 2-week G418 (500 µg/ml) selection as described previously [17]. PC-3 cells overexpressing a constitutively active *HIF1α* construct were established by retroviral infection as described previously [18]. *HIF1α*, *OATP1B3* and non-targeting control shRNA lentiviral particles used to establish stable knockdown cell lines were purchased from Santa Cruz (Santa Cruz, CA). The heptamethine carbocyanine MHI-148 dye was synthesized and purified as described previously [11]. Cobalt chloride, rifampicin, gemfibrozil and bromosulfophthalein were purchased from Sigma-Aldrich (St. Louis, MO). DMOG was purchased from Millipore (Billerica, MA).

2.2. Tumor xenograft studies

Male 4- to 6-week-old athymic nude mice were purchased from Taconic (Oxnard, CA), housed in the animal research facility at Cedars-Sinai Medical Center (CSMC), and fed a normal chow diet. For xenograft studies, 1×10^6 cells were injected subcutaneously into nude mice. Each mouse was injected on either one or both flanks, and at least five mice were used for each group. Tumors were dissected 4–6 weeks after inoculation and fixed in 4% formaldehyde and embedded in paraffin for subsequent histological analysis.

2.3. Clinical specimens

Archival formalin-fixed paraffin-embedded (FFPE) PCa clinical specimens were obtained from the Department of Pathology, Xijing Hospital, Fourth Military Medical University (FMMU). All renal cell carcinoma (RCC) patients enrolled in the present study were from the Department of Urology, Xijing Hospital, FMMU, and the exclusion criteria included kidney cysts, renal pelvis carcinoma and other inflammatory diseases.

2.4. Analysis of NIRF dye uptake in cancer cells, tumor xenografts and clinical tumor specimens

2.4.1. Cancer cell model—After exposure to different treatments, cells were incubated with MHI-148 dye at a concentration of 5 µM at 37°C for 10 min and washed twice with PBS to remove excess dyes. Cells were fixed in 10% formaldehyde and subjected to analysis of NIRF dye uptake by a BD Accuri C6 flow cytometer (BD Biosciences, San Jose, CA) equipped with a 780/30 nm filter for NIRF detection, and the data was analyzed by FlowJo software (Tree Star Inc., Ashland, OR).

2.4.2. Tumor xenograft model—Mice bearing xenografted tumors, when tumor sizes reached 2–6 mm in diameter assessed by palpation, were injected intraperitoneally with MHI-148 dye at a dose of 50 nmol/mouse. Whole-body or organ-specific optical imaging was taken at 24 hour using an IVIS Lumina XR imaging system (PerkinElmer, Waltham, MA) equipped with fluorescent filter sets (excitation/emission, 783/840 nm) as described previously [11, 12].

2.4.3. Clinical RCC specimens—RCC patients who were histopathologically confirmed underwent complete retroperitoneal laparoscopic nephrectomy. Immediately subsequent to the surgical removal, the kidney was administered intra-arterially with 5000 units of heparin for anti-coagulation, and then subjected to perfusion with 300 ml saline at a rate of 20 ml/min at 4°C. Next, the kidney was perfused with MHI-148 dye (0.5 nmol/g) in 500 ml saline at a rate of 20 ml/min at 4°C, and further infused with 500 ml Ringer's solution to remove excess dyes. Uptake of MHI-148 dye in the kidney was determined by NIRF imaging as described in 2.4.2. RCC and adjacent normal tissues were further excised and cut into small blocks followed by NIRF imaging and signal intensity quantification. All procedures were performed either on ice or at 4°C.

2.5. Luciferase assay and bioluminescence imaging

PC-3 cells that stably carry *5HREp-ODD-luc* after receiving different treatments were subjected to cell lysis, and the cell lysates were incubated with D-luciferin (Promega, Madison, WI) for luciferase readout using a Monolight luminometer (BD Biosciences) as described previously [17]. Bioluminescence imaging of either PC-3 cells or tumor xenografts that carry *5HREp-ODD-luc* after receiving D-luciferin (3 mg/mouse via intraperitoneal delivery) was performed using a Xenogen IVIS Spectrum imaging system (PerkinElmer).

2.6. Immunohistochemical (IHC) and double quantum dot labeling (QDL) analysis of tumor xenograft and clinical tumor specimens

FFPE tissue specimens were stained with antibodies specific for HIF1 α (1:30) (H1alpha67, Novus Biologicals, Littleton, CO or 54, BD Bioscience), VEGF-A (1:40) (A-20, Santa Cruz), or OATP1B3 (1:50, Sigma-Aldrich or 1: 30, H-52, Santa Cruz) by IHC or double QDL as described previously [19].

2.7. cDNA microarray analysis

RNA samples were prepared from control and constitutively active HIF1 α overexpressing PC-3 cells using a RNeasy Mini kit (Qiagen, Valencia, CA) and processed for cDNA microarray analysis. Human U133plus2.0 array hybridizations were performed by the University of California, Los Angeles (UCLA) Clinical Microarray Core following the standard Affymetrix GeneChip Expression Analysis protocol. The acquisition of array images was undertaken using the Affymetrix GeneChip Command Console 1.1 (AGCC).

2.8. Biochemical analyses

Total RNA was isolated using a RNeasy Mini kit and reverse-transcribed to cDNA using M-MLV reverse transcriptase (Promega) as described previously [17, 20]. qPCR was conducted using SYBR Green PCR Master Mix and run with Applied Biosystems 7500 Fast Real-Time PCR System (Applied Biosystems, Carlsbad, CA). PCR conditions included an initial denaturation step of 3 min at 95°C, followed by 40 cycles of PCR consisting of 30 s at 95°C, 30 s at 60°C, and 30 s at 72°C. The PCR data were analyzed by $2^{\Delta\Delta CT}$ method [21]. Details on primers for qPCR are provided in Supplemental Table 2.

For immunoblotting, cells were extracted with RIPA buffer in the presence of a protease and phosphatase inhibitor cocktail (Thermo Scientific, Rockford, IL), and immunoblotting were performed as described previously [22, 23] using primary antibodies as follows: HIF1 α (1:500) (54, BD Bioscience), OATP1B3 (1:500) (Sigma-Aldrich, or H-52, Santa Cruz), or β -Actin (1:2000) (AC-15, Sigma-Aldrich).

2.9. Chromatin immunoprecipitation (ChIP) analysis and qPCR

ChIP assay was used to determine the *in vivo* association of HIF1 α protein with *OATP1B3* promoter in PC-3 cells treated with either vehicle or cobalt chloride (200 μ M, 16 h, dissolved in PBS) by a SimpleChIP Enzymatic Chromatin IP Kit (Cell Signaling, Danvers, MA). Briefly, chromatin that was cross-linked with nuclear proteins, enzymatically digested with micrococcal nuclease and sonicated was immunoprecipitated with anti-HIF1 α antibody. After being pelleted with agarose beads and purified, immunoprecipitated chromatin was subsequently subjected to qPCR with a pair of primers specifically targeting the *OATP1B3* promoter region that encompasses a HRE. IgG included in the kit was used as a negative control for IP. A control primer set for *OATP1B3* exon1 was used as a negative control for PCR. Primer sequences for the *OATP1B3* promoter were forward 5'-AAAACAATTAGCCGGGCGTTG-3' and reverse 5'-CTTATCCAGAAATCTGGTATGC-3', and for *OATP1B3* exon1 were forward 5'-ATGTTCTTGGCAGCCCTGTC-3' and reverse 5'-CAATTTCAAAGCTTCCATCAATTA-3'. Two percent of chromatin prior to IP was saved as input, and data were presented as the percent of input from three independent experiments

2.10. Statistical analysis

Data were presented as the mean \pm SEM from at least three independent experiments and analyzed with an unpaired Student's t test. A *p* value less than 0.05 was considered as statistically significant.

2.11. Study approval

All animal studies received prior approval by the IACUC of CSMC and were conducted in compliance with its recommendations. All human studies were reviewed and approved by the IRB of CSMC and FMMU, and written informed consent was provided for human samples.

Results

3.1. MHI-148, a NIRF dye, targets tumor hypoxia *in vivo*

We sought to determine the association of tumor hypoxia with NIRF imaging of cancer cells and tumor xenografts given that hypoxia is a common condition found in a wide range of cancer cells or solid tumors [24]. At the cellular level, cancer cells within the tumors or as circulating tumor cells in contrast to normal cells can survive hypoxic conditions and show increased expression of hypoxia-inducible factors (HIFs), such as HIF1 α [25]. To assess intratumoral hypoxia, we used a HIF1 α -dependent reporter construct, *5HREp-ODD-luc* [26], in which 5 copies of the hypoxia-response element (HRE) enhance the expression of a luciferase (luc) protein fused with the oxygen-dependent degradation (ODD) domain under hypoxia (Fig. 1B, top panel), to monitor the hypoxic status and HIF1 α activity in a real-time manner in cancer cells and tumor xenografts. Under normoxic conditions, the ODD domain of HIF1 α is modified by 4-prolyl hydroxylases (PHDs) and von Hippel-Lindau tumor suppressor (VHL), which require oxygen and subsequently result in the rapid degradation of HIF1 α protein. In contrast, HIF1 α is stabilized under hypoxia that destroys PHD activity due to the lack of oxygen [27]. Therefore, the expression of *5HREp-ODD-luc*, by modulating the oxygen-sensitive ODD-luc fusion protein levels, produces a marginal leak of luminescence under normoxia but increases markedly under hypoxia, reflecting dynamic and real-time HIF1 α activity correlating to the levels of hypoxia.

To validate this construct in the present system, we stably overexpressed *5HREp-ODD-luc* in human prostate cancer (PCa) PC-3 cells, which showed a time-dependent increase of luminescence signals in parallel with stabilized HIF1 α protein under hypoxia (Fig. 1B, middle and bottom panels). These observations were further recapitulated under treatment with either cobalt chloride or dimethylxalylglycine (DMOG), both acting as HIF1 α stabilizers by inhibiting PHD activity (Fig. S1). Notably, there was barely detectable luminescence in cells either under normoxia or without the treatment (Fig. 1B and S1), suggesting the specificity of this construct for hypoxia or HIF1 α activation. To determine the potential hypoxic effects on the tumor uptake of MHI-148 dye (chemical structure shown in Fig. 1A) *in vivo*, we established a subcutaneous tumor xenograft mouse model using *5HREp-ODD-luc*-overexpressing PC-3 cells and subjected mice to dual bioluminescence and fluorescence imaging. As shown in Fig. 1C (left panel), bioluminescence signals were concurrently accumulated centrally with NIRF signals of MHI-148 in tumor xenografts. Slim tumor slices (1–1.5 mm), dissected from tumor tissues immediately after whole-body optical imaging, were analyzed *ex vivo*, and superimposed bioluminescence and NIRF images were also observed (Fig. 1C, right panel). The co-registration of bioluminescence and NIRF signals in tumor xenografts suggested a correlation between tumor hypoxia and the uptake of NIRF dyes by tumors.

3.2. NIRF dye uptake by cancer cells and tumor xenografts is enhanced by hypoxia

To determine if hypoxia is responsible for the preferential uptake of NIRF dyes by cancer cells, we examined a wide spectrum of human and murine carcinomas including prostate carcinoma (PC-3, PC-3M, LNCaP, C4-2, ARCaP_E, ARCaP_M and MPC3), breast carcinoma (MDA-MB-231), colorectal carcinoma (CT26) and leukemia (K562) cell lines under

hypoxic conditions. After exposure to hypoxia, these cells were incubated with MHI-148 dye followed by flow cytometric analysis to quantify the NIRF intensity. As shown in Fig. 2A, hypoxia increased the accumulation of MHI-148 dye in all cancer cell lines by 30% to more than 2 fold relative to their incubation under normoxic conditions. In contrast, the normal prostatic epithelial PrEC cells, serving as a negative control, did not show significant changes in dye uptake under hypoxia, which is consistent with our previous observations that normal cells retain little of these NIRF dyes [11]. We further showed that cobalt chloride treatment, a chemical mimicker of hypoxia, induced the uptake of MHI-148 dye in select cancer cells lines (PC-3, ARCaP_E and MDA-MB-231) in a time-dependent manner (Fig. 2B).

To determine whether HIF1 α protein directly mediates NIRF dye uptake by cancer cells, we stably introduced a constitutively active *HIF1 α* expression construct (*CA-HIF1 α*), which lacks the ODD domain and hence escapes degradation under normoxia, into cancer cells (PC-3, PC-3M and MDA-MB-231) by retroviral infection. Successful enforced expression of HIF1 α , confirmed by immunoblotting, enhanced the ability of cancer cells to take up MHI-148 dye by more than 50% under normoxic conditions (Fig. 2C). Conversely, stable targeted silence of *HIF1 α* gene expression via lentiviral shRNAs in select cancer cell lines (PC-3, PC-3M, C4-2, ARCaP_E and MDA-MB-231) blunted the hypoxia-induced increase of dye uptake to lower levels comparable to those observed under normoxic conditions (Fig. 2D).

Next, we studied the hypoxic effects on the uptake of NIRF dyes in tumor-bearing mice. PC-3 cells that stably overexpressed either *CA-HIF1 α* construct or an empty vector were used to establish subcutaneous tumor xenografts in nude mice. Each mouse carried both control and HIF1 α -overexpressing tumors with one on each flank for a simultaneous comparison of the extent of dye uptake between the tumors. We observed that tumor HIF1 α protein expression correlated progressively with tumor growth, concurring with the observations from other groups [28]. To ensure that tumor size did not interfere with the assessment of tumor uptake of NIRF dyes, tumor NIRF intensity was normalized to tumor weight at the end of the study. HIF1 α overexpression enhanced the uptake of MHI-148 dye by PC-3 tumor xenograft relative to control tumor, leading to a 60% increase of NIRF signals after normalization to tumor weight (Fig. 3A and 3B, left panel). On the other hand, stable knockdown of *HIF1 α* via lentiviral shRNAs (shHIF1 α) reduced the ability of PC-3 tumors to take up and retain MHI-148 dye by 56% subsequent to normalization of NIRF signals to tumor weight, compared with control tumor that expressed a scrambled shRNA (shCon) (Fig. 3A and 3B, right panel). The accumulation of MHI-148 dye was found specific to tumors but not normal organs including the liver, lung, spleen, kidney, heart, prostate and testis by both *in vivo* and *ex vivo* NIRF imaging modalities, reinforcing the tumor-specific targeting ability of NIRF dyes (Fig. 3A). Tumor HIF1 α expression was confirmed by immunohistochemical (IHC) analysis by probing protein expression of HIF1 α and its target genes, such as vascular endothelial growth factor A (VEGF-A) [24] (Fig. 3C). These data collectively suggest that hypoxia, through its key mediator HIF1 α , mediates the uptake of NIRF dyes by cancer cells.

3.3. Regulation of OATPs by hypoxia and HIF1 α in PCa

To elucidate the effectors downstream of the hypoxia/HIF1 α -mediated signals and responsible for the preferential uptake of NIRF dyes by cancer cells, we conducted cDNA microarray analysis with control and HIF1 α -overexpressing PC-3 cells. Preliminary results, confirmed later by qPCR, identified a family of organic anion-transporting polypeptide (*OATP*) genes induced by constitutive activation of HIF1 α protein (Fig. 4A). OATPs represent a superfamily of solute carrier transporters. Currently there are 11 known human OATPs classified into 6 families and subfamilies on the basis of their amino acid sequence homologies. OATPs facilitate the transport of a large number of substrates, including organic acids, drugs and hormones, into cells in a highly substrate- and pathophysiologic-dependent manner [29]. Hypoxia induction of *OATPs* was further demonstrated in 4 human PCa cell lines (LNCaP, PC-3, DU-145 and ARCaP_E), which all showed an increasing trend of mRNA expression for most *OATPs* under hypoxia (Fig. S2A, left panel). *VEGF-A* and glucose transporter 1 (*Glut1*), known for HIF1 α target genes [24], were used as a positive control for validating hypoxic effects. Considering the reported association of dysregulated expression of OATPs with cancer progression [29, 30], we conducted a survey of the expression of all OATPs in 10 human PCa cell lines. Most of *OATPs* demonstrated higher mRNA expression in PCa cells relative to normal prostatic epithelial PrEC cells (Fig. S2A, right panel).

Recent evidence has indicated the aberrant expression and genetic variants of select *OATPs*, such as *OATP1B3* [31], in different types of human cancer [30], which led us to speculate a potential regulatory link between OATPs and hypoxia signals in human cancer progression. To test this idea, we examined the protein expression of HIF1 α and OATP1B3 as a representative in PCa clinical specimens with either low or high Gleason grades. We observed that the expression of both HIF1 α and OATP1B3 proteins were well correlated with prostate tumor Gleason grades (Fig. 4B), which was further confirmed by double quantum dot labeling (QDL) analysis, enabling quantification of staining intensity of each protein at the single cellular level. As shown in Fig. 4C, the increased co-expression of HIF1 α and OATP1B3 was progressively associated with higher Gleason grades (left and middle panels), and HIF1 α protein expression further showed significant correlation with OATP1B3 expression in high-grade cancer patient samples (right panel). These data in aggregate establish a molecular correlation between HIF1 α and OATP1B3 in clinical cancer settings.

To examine further the relationship between HIF1 α and OATP1B3, we analyzed OATP1B3 protein and mRNA expression in PCa cells and tumor xenografts subsequent to the change of hypoxic or HIF1 α protein expression levels. In response to hypoxic stimuli, both OATP1B3 protein and mRNA expression were induced in PC-3 and ARCaP_E cells (Fig. 4D and 4E), which was recapitulated in cancer cells and tumor xenografts by enforced HIF1 α protein expression (Fig. S2B, S2C and S2D, left panel). Conversely, stable knockdown of HIF1 α protein expression reduced OATP1B3 protein and mRNA expression (Fig. S2B, S2C and S2D, right panel). To investigate whether HIF1 α directly regulates *OATP1B3* gene, we attempted to identify a functional HRE in the *OATP1B3* promoter. Sequence analysis of a 2-kb DNA segment located upstream of the transcription initiation site of *OATP1B3* gene

revealed a region (-926/-923) that exhibits strong sequence identity to a canonical HRE [32] (Fig. 4F). By conducting chromatin immunoprecipitation assay coupled with qPCR analysis, we were able to detect the physical interaction of HIF1 α protein with the *OATP1B3* promoter region that harbors a HRE in cobalt chloride-treated cells, whereas this association was absent in control cells (Fig. 4G). These results provide evidence that hypoxia mediates *OATP1B3* gene activation by facilitating the cis-trans interactions between a specific HRE in the *OATP1B3* promoter and HIF1 α protein.

3.4. OATP1B3 mediated NIRF dye uptake by cancer cells and tumor xenografts

To investigate whether OATP1B3 directly mediates the uptake of NIRF dyes in cancer cells, we used PC-3 and ARCaP_E cells, which were stably infected with either *OATP1B3*-targeting shRNAs (shOATP1B3) or a scrambled shRNA (shCon). Stable knockdown of OATP1B3 protein expression resulted in a 30% decrease in MHI-148 dye uptake by cancer cells under normoxia (Fig. 5A), indicating that OATP1B3 can mediate the transport of NIRF dyes into cancer cells in a hypoxia-independent manner. Moreover, pharmacological interference with OATP1B3 activity in cancer cells by pre-treatment with different inhibitors compromised the hypoxia-induced uptake of MHI-148 dye by up to 65% and 31% in PC-3 and ARCaP_E cells, respectively (Fig. 5B). To determine the OATP1B3 effect on NIRF dye uptake by xenograft tumors, nude mice were inoculated subcutaneously with PC-3 or ARCaP_E cells (shCon vs. shOATP1B3). We observed parallel growth of control and OATP1B3-knockdown tumors, suggesting that OATP1B3 did not affect cell proliferation even though its expression correlated with clinical cancer progression. Importantly, knockdown of OATP1B3 protein expression, confirmed by IHC analysis (Fig. 5C), significantly reduced MHI-148 dye intensity after normalization to tumor weight in both PC-3 and ARCaP_E tumor xenografts, by 40% and 15% respectively (Fig. 5D and 5E). These results suggest that OATP1B3 directly mediates NIRF dye uptake and retention in tumors, which can be independent of hypoxia signaling.

3.5. Assessment of NIRF dye uptake and HIF1 α /OATP signaling axis in clinical renal cell carcinoma (RCC) samples

A critical issue that arises from the experimental studies is whether the HIF1 α /OATPs signaling axis participates in the clinical tumor imaging by NIRF dyes. To address this issue, we applied MHI-148 dye to detect clear cell RCC (CCRCC) in three complete nephrectomy specimens confirmed by imaging (CT and 2D/3D phase-contrast MRI) and histopathological (H&E stain) methods (Fig. S3 and Table S1). CCRCC, accounting for approximately 75% of all RCCs, is frequently characterized by the inactivation of the *VHL* tumor suppressor gene, which subsequently contributes to the stabilization of HIF1 α and induction of hypoxia signaling [33]. In the present study, RCC patients underwent the surgical removal of the entire kidney, which was perfused immediately with MHI-148 dye in saline and subsequently subjected to *ex vivo* NIRF imaging. NIRF was detected specifically in the tumor regions referring to the diagnostic images in sharp contrast to the normal counterpart (Fig. 6A). With a further quantification analysis of small blocks of RCC versus normal tissues from three nephrectomy samples by normalizing NIRF intensity to tissue weight, we found up to 6-fold increase of MHI-148 dye uptake in tumor relative to normal tissues (Fig. 6B and 6C). To confirm the co-activation of HIF1 α and OATPs in clinical RCC samples, we

conducted IHC analysis and demonstrated intense widespread nuclear HIF1 α and cytoplasmic OATP1B3 expression in RCC samples but absent in adjacent normal tissues (Fig. 6D). These clinical observations reinforce the regulatory roles of HIF1 α /OATPs signaling axis in mediating tumor uptake of NIRF dyes.

4. Discussion

In this study, we demonstrated the use of a specific group of NIRF heptamethine carbocyanines, identified originally to enable tumor-specific imaging and targeting, for assessing tumor hypoxia (Fig. 1). We also provided mechanistic insights into the preferential uptake of these NIRF dyes by cancer cells using genitourinary cancers as a representative model system. The mechanisms primarily involve the activation of hypoxia signaling through a key transcription factor, HIF1 α , which is frequently observed in a variety of types of cancers and often associated with a poor prognosis and rapid disease progression expressing aggressive phenotypes [24]. Currently, few biomarkers to reliably detect and predict tumor hypoxia are available for clinical use, and therefore extending the application of these NIRF dyes for assessing tumor hypoxia and predicting hypoxia-regulated disease prognosis in cancer patients merits further exploration.

In a subsequent analysis of our imaging results, we compared in parallel MHI-148 with indocyanine green (ICG), the only NIRF agent approved by the Food and Drug Administration in the United States for clinical application. ICG functions *in vivo* primarily through binding to plasma proteins and enables tumor diagnosis by NIRF lymphatic imaging [34, 35], but there is little evidence showing its direct association with tumor hypoxia. Regarding the tumor-to-background ratio of NIRF signals at 24 hours for tumor detection in mice, ICG has a ratio of 1.4–1.7 [36], whereas MHI-148 shows a median of 9.1, which can be further exacerbated by 2 fold in the presence of HIF1 α protein overexpression, suggesting that tumor hypoxia is an important mechanism for facilitating tumor detection by NIRF imaging. In addition, another mechanism that may contribute to the preferential accumulation of contrast agents in tumors is the disorganized tumor vasculature that can coincidentally result from tumor hypoxia [37, 38], which is able to activate the expression of VEGF to further increase vascular disorganization [24]. This scenario supports our mechanistic findings and also provides a rationale for elucidating the advantages of our dyes over other NIRF agents for cancer imaging.

We find that a group of *OATP* genes induced by hypoxia participate in mediating the uptake of NIRF dyes in cancer cells, which can be either dependent or independent from hypoxia signaling. OATPs function in the uptake of amphipathic compounds, including drugs, hormones, and other xenobiotics that cannot freely diffuse through cellular membranes, and can be either tissue-specific or expressed ubiquitously [29]. Recent studies have implicated altered *OATP* expressions and variants in many different types of cancers [30], including OATP1B3 that can serve as a testosterone transporter in PCa [39]. Our study showed the correlation of OATP1B3 expression with HIF1 α expression as well as PCa progression, providing a rationale for its role in mediating the uptake of NIRF dyes by cancer cells (Fig. 4 and Fig. 5). An important finding of our study is that HIF1 α directly upregulates *OATPs*, which is supported by the co-expression of these two proteins in clinical prostate and renal

cancer samples (Fig. 4 and Fig. 6). Under hypoxic conditions, active nuclear HIF1 α protein interacts with a HRE in the *OATP1B3* promoter, resulting in the increased transcription of *OATP1B3* (Fig. 4). HIF1 α is destabilized under normoxia due to the rapid degradation initiated by the PHD/VHL pathway [27], which is likely a mechanism responsible for the relatively low levels of OATPs in normal tissues (Supplemental Fig. 2). Hence, inactivation of HIF1 α /OATPs signaling in normal cells and tissues blunts their sensitivity to recruit NIRF dyes; conversely, NIRF dyes acquire the ability to target hypoxic cancer cells. Although we used PCa as the major model system in the present study, these mechanistic findings could be extended to other types of cancers by determining the potential concerted effects exerted by HIF1 α along with other OATPs on the uptake of NIRF dyes in future studies. In addition, the mechanisms by which NIRF dyes are specifically taken up by cancer cells may extend beyond the present study, and further investigation is warranted to explore other properties of NIRF dyes for targeting cancer cells, such as their long-lasting retention and preferential organelle-specific cellular localization in cancer cells.

It has been shown that NIRF heptamethine carbocyanines enter cells and form complexes with nucleic acids [40, 41] or proteins [42, 43] through non-covalent interactions, which might be potentially modulated by hypoxia either in the tumor cells or the microenvironment. Further investigation would advance our understanding of this process. To delineate the functional groups associated with dye uptake by cancer cells, the structure-activity properties of these dyes were closely examined. The bridging atoms between the two aromatic heterocycles serve as a part of rigid cyclic ring which allows conformational stability and enhanced excitations/emission properties. The nitrogen atom in heterocyclic rings is amenable for modification to a variety of functional groups including negatively-charged carboxylic acid, sulfonic acid as well as uncharged alcohol, amine and ester, which can be used for manipulating physical properties of NIRF dyes such as water solubility and conjugation with other molecular entities [44, 45]. We found that the charged dyes were well retained in cancer cells with intact imaging capability by observing fluorescence signals, while the uncharged dyes were shown to be inactive with poor retention in cells. Further chemical modifications of the functionally charged moieties via covalent conjugation with either ligands for radiolabeling or drugs showed minimal effects on their cancer-specific propensity [46, 47] and anti-cancer activity [45, 48] in tumor xenografts in mice. Moreover, structural modifications of the two heteroaromatic rings or the central meso position of the cyclohexyl ring seemed to retain the activity of NIRF dyes as well. In addition to the direct chemical modifications, the mechanistic insights provided in the present study may also shed light on the dye activity. Specifically, the potential effect of hypoxia on the net charge of dye molecules by regulating either intracellular or extracellular pH conditions may need to be taken into account for future improvements in the design of NIRF imaging dyes [49, 50]. Following these observations, we anticipate that chemical modifications of this attractive class of NIRF imaging agents will produce a wide variety of cancer imaging and targeting agents in the near future.

5. Conclusions

In this study, we elucidated the molecular mechanisms underlying the uptake of a specific class of NIRF dyes by cancer cells through hypoxia and activation of a HIF1 α /OATPs

signaling axis, which provides a mechanistic rationale for targeting tumor hypoxia and cancer cells with these NIRF dyes. These findings also have great significance for the future development and application of NIRF agents in the clinic for better cancer detection, prognosis and therapy.

Supplementary Material

Refer to Web version on PubMed Central for supplementary material.

Acknowledgments

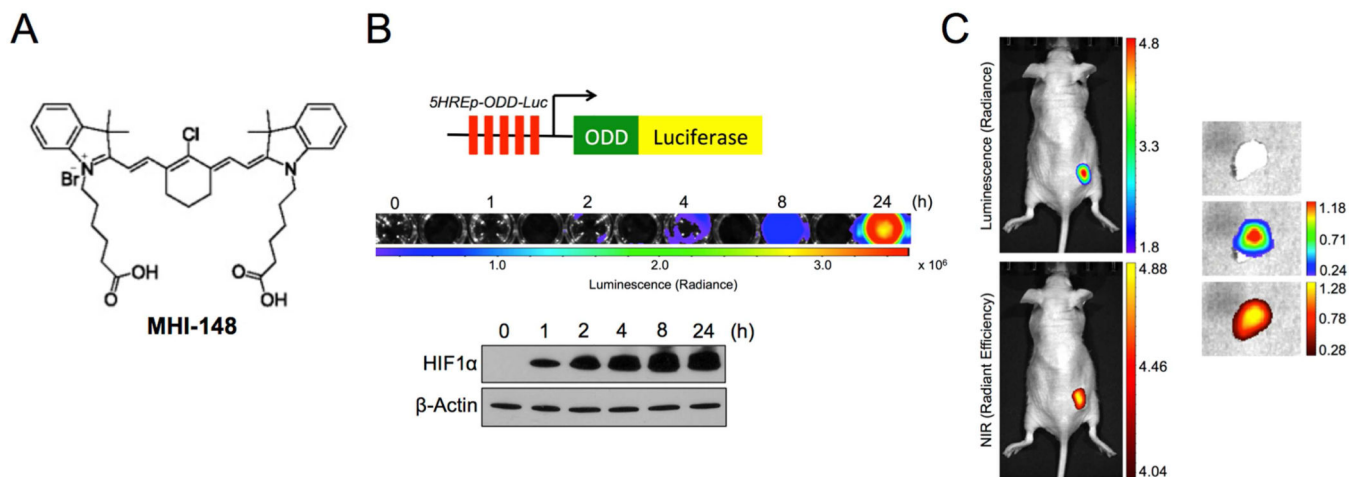
This work was supported by NIH/NCI Grant 5P01CA098912, R01CA122602, the Board of Governors Cancer Research Chair and Steven Spielberg Fund in Prostate Cancer Research (L.W.-K.C.), and by the Program of International Science and Technology Cooperation of China (No. 2011DFA33110) (C.S.). We thank Dr. Lei Zhang (Fourth Military Medical University, Xi'an, Shaanxi, China) for providing clinical specimens, and Chunyan Liu for providing technical assistance. We also thank Mr. Gary Mawyer for editorial assistance.

References

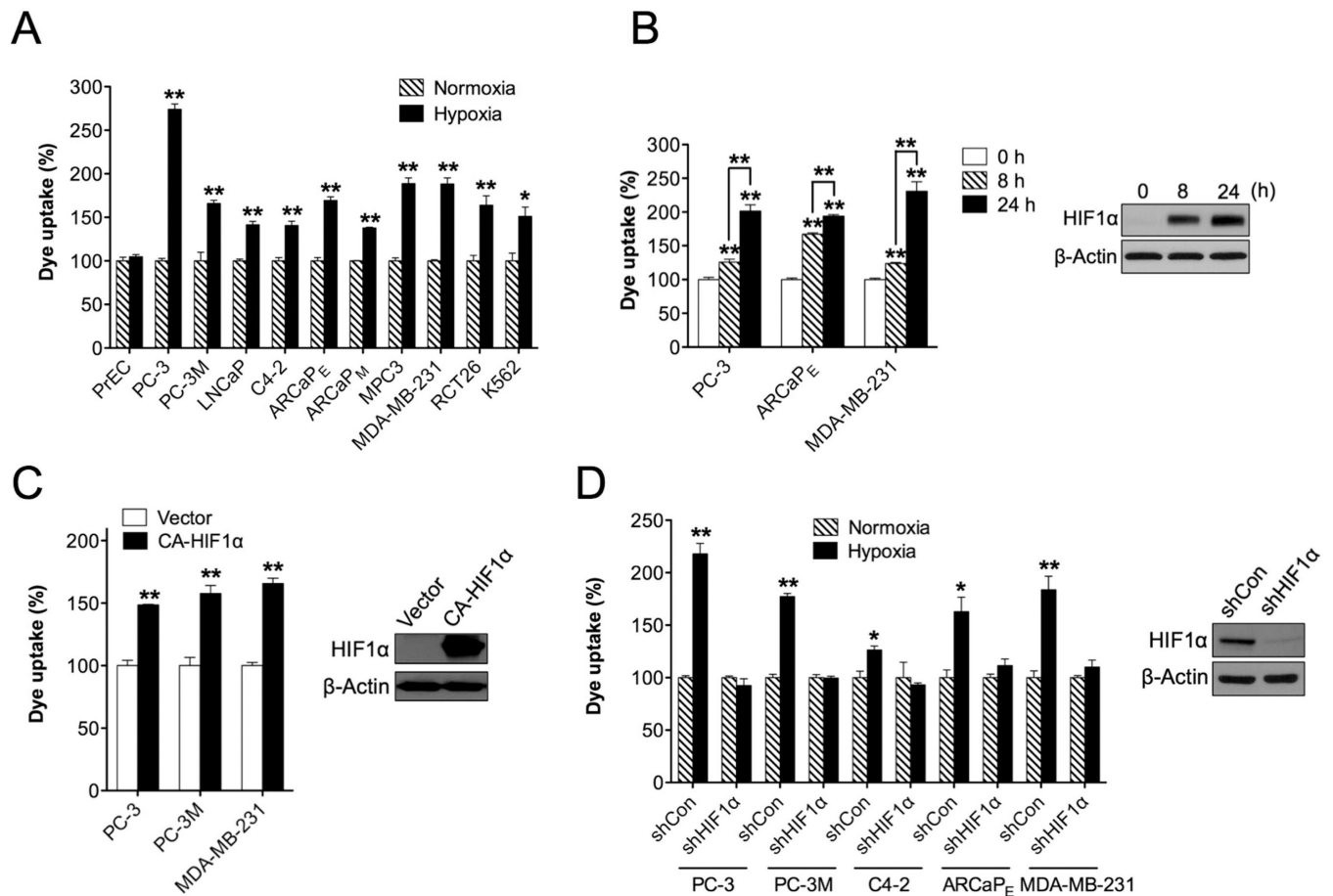
1. Wu J, Pan D, Chung LW. Near-infrared fluorescence and nuclear imaging and targeting of prostate cancer. *Transl Androl Urol*. 2014; 2:254–264.
2. Frangioni JV. In vivo near-infrared fluorescence imaging. *Curr Opin Chem Biol*. 2003; 7:626–634. [PubMed: 14580568]
3. Rao J, Dragulescu-Andrasi A, Yao H. Fluorescence imaging in vivo: recent advances. *Curr Opin Biotechnol*. 2007; 18:17–25. [PubMed: 17234399]
4. Hawrysz DJ, Sevick-Muraca EM. Developments toward diagnostic breast cancer imaging using near-infrared optical measurements and fluorescent contrast agents. *Neoplasia*. 2000; 2:388–417. [PubMed: 11191107]
5. Hintersteiner M, Enz A, Frey P, Jatton AL, Kinzy W, Kneuer R, et al. In vivo detection of amyloid-beta deposits by near-infrared imaging using an oxazine-derivative probe. *Nat Biotechnol*. 2005; 23:577–583. [PubMed: 15834405]
6. Wu X, Liu H, Liu J, Haley KN, Treadway JA, Larson JP, et al. Immunofluorescent labeling of cancer marker Her2 and other cellular targets with semiconductor quantum dots. *Nat Biotechnol*. 2003; 21:41–46. [PubMed: 12459735]
7. Humblet V, Lapidus R, Williams LR, Tsukamoto T, Rojas C, Majer P, et al. High-affinity near-infrared fluorescent small-molecule contrast agents for in vivo imaging of prostate-specific membrane antigen. *Mol Imaging*. 2005; 4:448–462. [PubMed: 16285907]
8. Frangioni JV. New technologies for human cancer imaging. *J Clin Oncol*. 2008; 26:4012–4021. [PubMed: 18711192]
9. Pierce MC, Javier DJ, Richards-Kortum R. Optical contrast agents and imaging systems for detection and diagnosis of cancer. *Int J Cancer*. 2008; 123:1979–1990. [PubMed: 18712733]
10. Edwards PA. Heterogeneous expression of cell-surface antigens in normal epithelia and their tumours, revealed by monoclonal antibodies. *Br J Cancer*. 1985; 51:149–160. [PubMed: 2578284]
11. Yang X, Shi C, Tong R, Qian W, Zhou HE, Wang R, et al. Near IR heptamethine cyanine dye-mediated cancer imaging. *Clin Cancer Res*. 2010; 16:2833–2844. [PubMed: 20410058]
12. Yang X, Shao C, Wang R, Chu CY, Hu P, Master V, et al. Optical imaging of kidney cancer with novel near infrared heptamethine carbocyanine fluorescent dyes. *J Urol*. 2013; 189:702–710. [PubMed: 23000848]
13. Zhou HY, Chang SM, Chen BQ, Wang Y, Zhang H, Kao C, et al. Androgen-repressed phenotype in human prostate cancer. *Proc Natl Acad Sci U S A*. 1996; 93:15152–15157. [PubMed: 8986779]
14. Zhou HE, Odero-Marrah V, Lue HW, Nomura T, Wang R, Chu G, et al. Epithelial to mesenchymal transition (EMT) in human prostate cancer: lessons learned from ARCaP model. *Clin Exp Metastasis*. 2008; 25:601–610. [PubMed: 18535913]

15. Wu HC, Hsieh JT, Gleave ME, Brown NM, Pathak S, Chung LW. Derivation of androgen-independent human LNCaP prostatic cancer cell sublines: role of bone stromal cells. *Int J Cancer*. 1994; 57:406–412. [PubMed: 8169003]
16. Qi J, Tripathi M, Mishra R, Sahgal N, Fazli L, Ettinger S, et al. The E3 ubiquitin ligase Siah2 contributes to castration-resistant prostate cancer by regulation of androgen receptor transcriptional activity. *Cancer Cell*. 2013; 23:332–346. [PubMed: 23518348]
17. Wu JB, Chen K, Li Y, Lau YF, Shih JC. Regulation of monoamine oxidase A by the SRY gene on the Y chromosome. *Faseb J*. 2009; 23:4029–4038. [PubMed: 19661285]
18. Sahu D, Zhao Z, Tsen F, Cheng CF, Park R, Situ AJ, et al. A potentially common peptide target in secreted heat shock protein-90alpha for hypoxia-inducible factor-1alpha-positive tumors. *Mol Biol Cell*. 2012; 23:602–613. [PubMed: 22190738]
19. Hu P, Chu GC, Zhu G, Yang H, Luthringer D, Prins G, et al. Multiplexed quantum dot labeling of activated c-Met signaling in castration-resistant human prostate cancer. *PLoS One*. 2011; 6:e28670. [PubMed: 22205960]
20. Chen K, Ou XM, Wu JB, Shih JC. Transcription factor E2F-associated phosphoprotein (EAPP), RAM2/CDCA7L/JPO2 (R1), and simian virus 40 promoter factor 1 (Sp1) cooperatively regulate glucocorticoid activation of monoamine oxidase B. *Molecular pharmacology*. 2011; 79:308–317. [PubMed: 20980443]
21. Livak KJ, Schmittgen TD. Analysis of relative gene expression data using real-time quantitative PCR and the 2(-Delta Delta C(T)) Method. *Methods*. 2001; 25:402–408. [PubMed: 11846609]
22. Wu JB, Chen K, Ou XM, Shih JC. Retinoic acid activates monoamine oxidase B promoter in human neuronal cells. *J Biol Chem*. 2009; 284:16723–16735. [PubMed: 19401466]
23. Wu JB, Shih JC. Valproic acid induces monoamine oxidase A via Akt/forkhead box O1 activation. *Mol Pharmacol*. 2011; 80:714–723. [PubMed: 21775495]
24. Lu X, Kang Y. Hypoxia and hypoxia-inducible factors: master regulators of metastasis. *Clin Cancer Res*. 2010; 16:5928–5935. [PubMed: 20962028]
25. Ameri K, Luong R, Zhang H, Powell AA, Montgomery KD, Espinosa I, et al. Circulating tumour cells demonstrate an altered response to hypoxia and an aggressive phenotype. *Br J Cancer*. 2010; 102:561–569. [PubMed: 20051957]
26. Harada H, Kizaka-Kondoh S, Itasaka S, Shibuya K, Morinibu A, Shinomiya K, et al. The combination of hypoxia-response enhancers and an oxygen-dependent proteolytic motif enables real-time imaging of absolute HIF-1 activity in tumor xenografts. *Biochem Biophys Res Commun*. 2007; 360:791–796. [PubMed: 17624305]
27. Kaelin WG Jr, Ratcliffe PJ. Oxygen sensing by metazoans: the central role of the HIF hydroxylase pathway. *Mol Cell*. 2008; 30:393–402. [PubMed: 18498744]
28. Li J, Shi M, Cao Y, Yuan W, Pang T, Li B, et al. Knockdown of hypoxia-inducible factor-1alpha in breast carcinoma MCF-7 cells results in reduced tumor growth and increased sensitivity to methotrexate. *Biochem Biophys Res Commun*. 2006; 342:1341–1351. [PubMed: 16516853]
29. Obaidat A, Roth M, Hagenbuch B. The expression and function of organic anion transporting polypeptides in normal tissues and in cancer. *Annu Rev Pharmacol Toxicol*. 2012; 52:135–151. [PubMed: 21854228]
30. Pressler H, Sissung TM, Venzon D, Price DK, Figg WD. Expression of OATP family members in hormone-related cancers: potential markers of progression. *PLoS One*. 2011; 6:e20372. [PubMed: 21625523]
31. Yang M, Xie W, Mostaghel E, Nakabayashi M, Werner L, Sun T, et al. SLCO2B1 and SLCO1B3 may determine time to progression for patients receiving androgen deprivation therapy for prostate cancer. *J Clin Oncol*. 2011; 29:2565–2573. [PubMed: 21606417]
32. Semenza GL, Agani F, Booth G, Forsythe J, Iyer N, Jiang BH, et al. Structural and functional analysis of hypoxia-inducible factor 1. *Kidney Int*. 1997; 51:553–555. [PubMed: 9027737]
33. Zbar B, Klausner R, Linehan WM. Studying cancer families to identify kidney cancer genes. *Annu Rev Med*. 2003; 54:217–233. [PubMed: 12525673]
34. Hirche C, Murawa D, Mohr Z, Kneif S, Hunerbein M. ICG fluorescence-guided sentinel node biopsy for axillary nodal staging in breast cancer. *Breast Cancer Res Treat*. 2010; 121:373–378. [PubMed: 20140704]

35. Cherrick GR, Stein SW, Leevy CM, Davidson CS. Indocyanine green: observations on its physical properties, plasma decay, and hepatic extraction. *J Clin Invest.* 1960; 39:592–600. [PubMed: 13809697]
36. Kosaka N, Mitsunaga M, Longmire MR, Choyke PL, Kobayashi H. Near infrared fluorescence-guided real-time endoscopic detection of peritoneal ovarian cancer nodules using intravenously injected indocyanine green. *Int J Cancer.* 2011; 129:1671–1677. [PubMed: 21469142]
37. Less JR, Skalak TC, Sevick EM, Jain RK. Microvascular architecture in a mammary carcinoma: branching patterns and vessel dimensions. *Cancer Res.* 1991; 51:265–273. [PubMed: 1988088]
38. Jin H, Kang KA. Fluorescence-mediated detection of a heterogeneity in a highly scattering media. *Adv Exp Med Biol.* 2005; 566:167–172. [PubMed: 16594149]
39. Hamada A, Sissung T, Price DK, Danesi R, Chau CH, Sharifi N, et al. Effect of SLC01B3 haplotype on testosterone transport and clinical outcome in caucasian patients with androgen-independent prostatic cancer. *Clin Cancer Res.* 2008; 14:3312–3318. [PubMed: 18519758]
40. Ihmels H, Thomas L. Light up G-quadruplex DNA with a [2.2.2]heptamethinecyanine dye. *Organic & biomolecular chemistry.* 2013; 11:480–487. [PubMed: 23203349]
41. Karlsson HJ, Eriksson M, Perzon E, Akerman B, Lincoln P, Westman G. Groove-binding unsymmetrical cyanine dyes for staining of DNA: syntheses and characterization of the DNA-binding. *Nucleic acids research.* 2003; 31:6227–6234. [PubMed: 14576310]
42. Volkova KD, Kovalska VB, Balanda AO, Vermeij RJ, Subramaniam V, Slominskii YL, et al. Cyanine dye-protein interactions: looking for fluorescent probes for amyloid structures. *Journal of biochemical and biophysical methods.* 2007; 70:727–733. [PubMed: 17467807]
43. Patonay G, Kim JS, Kodagahally R, Strekowski L. Spectroscopic study of a novel bis(heptamethine cyanine) dye and its interaction with human serum albumin. *Applied spectroscopy.* 2005; 59:682–690. [PubMed: 15969815]
44. Yeh CS, Su CH, Ho WY, Huang CC, Chang JC, Chien YH, et al. Tumor targeting and MR imaging with lipophilic cyanine-mediated near-infrared responsive porous Gd silicate nanoparticles. *Biomaterials.* 2013; 34:5677–5688. [PubMed: 23639532]
45. Henary M, Pannu V, Owens EA, Aneja R. Near infrared active heptacyanine dyes with unique cancer-imaging and cytotoxic properties. *Bioorganic & medicinal chemistry letters.* 2012; 22:1242–1246. [PubMed: 22177785]
46. Zhang Y, Xiao L, Popovic K, Xie X, Chordia MD, Chung LW, et al. Novel cancer-targeting SPECT/NIRF dual-modality imaging probe (99m)Tc-PC-1007: synthesis and biological evaluation. *Bioorganic & medicinal chemistry letters.* 2013; 23:6350–6354. [PubMed: 24125889]
47. Xiao L, Zhang Y, Yue W, Xie X, Wang JP, Chordia MD, et al. Heptamethine cyanine based (64)Cu-PET probe PC-1001 for cancer imaging: synthesis and in vivo evaluation. *Nuclear medicine and biology.* 2013; 40:351–360. [PubMed: 23375364]
48. Tan X, Luo S, Wang D, Su Y, Cheng T, Shi C. A NIR heptamethine dye with intrinsic cancer targeting, imaging and photosensitizing properties. *Biomaterials.* 2012; 33:2230–2239. [PubMed: 22182749]
49. Hulikova A, Harris AL, Vaughan-Jones RD, Swietach P. Regulation of intracellular pH in cancer cell lines under normoxia and hypoxia. *Journal of cellular physiology.* 2013; 228:743–752. [PubMed: 22949268]
50. Brahim-Horn MC, Pouyssegur J. Hypoxia in cancer cell metabolism and pH regulation. *Essays in biochemistry.* 2007; 43:165–178. [PubMed: 17705800]

**Fig. 1.**

MHI-148, a NIRF dye, assessed tumor hypoxia. (A) Chemical structure of NIR heptamethine carbocyanine MHI-148 dye. (B) Generation and validation of human PCa PC-3 cells that stably expressed the *5HRE-pODD-Luc* construct (top). Stable cells were treated with hypoxia (1% O₂) for different times as indicated and then subjected to either luminescence imaging (middle) or immunoblotting of HIF1α protein expression (bottom). (C) *In vivo* and *ex vivo* images of PC-3 tumor xenografts that expressed *5HRE-pODD-Luc* construct by both bioluminescence (top) and NIRF (bottom) imaging, which showed superimposed signal distribution. Scale bars represent x10⁵ and x10⁹ for *in vivo* bioluminescence and NIRF, respectively; x10⁴ and x10⁹ for *ex vivo* bioluminescence and NIRF, respectively, in the unit of radiant efficiency.

**Fig. 2.**

Hypoxia and HIF1 α mediated the uptake of MHI-148 dye by cancer cells. (A)

Determination of MHI-148 dye uptake in multiple cancer cell lines under either normoxic or hypoxic (1% O₂, 4 hr) conditions (N=3, mean \pm SEM). Normal human prostatic epithelial PrEC cells were used as a negative control. Dye uptake by cells under normoxia was set as 100%. (B) Determination of MHI-148 dye uptake in select cancer cell lines under CoCl₂ (200 μ M) treatment for different time periods as indicated (N=3, mean \pm SEM). The CoCl₂ effect in PC-3 cells as a representative was examined by immunoblotting HIF1 α protein expression. (C, D) Determination of MHI-148 dye uptake in cancer cells either overexpressing constitutively active HIF1 α (C) or with stable knockdown of HIF1 α (D) (N=3, mean \pm SEM). The efficacy of overexpression or knockdown of HIF1 α in PC-3 cells as a representative was examined by immunoblotting HIF1 α protein expression. * p <0.05, ** p <0.01.

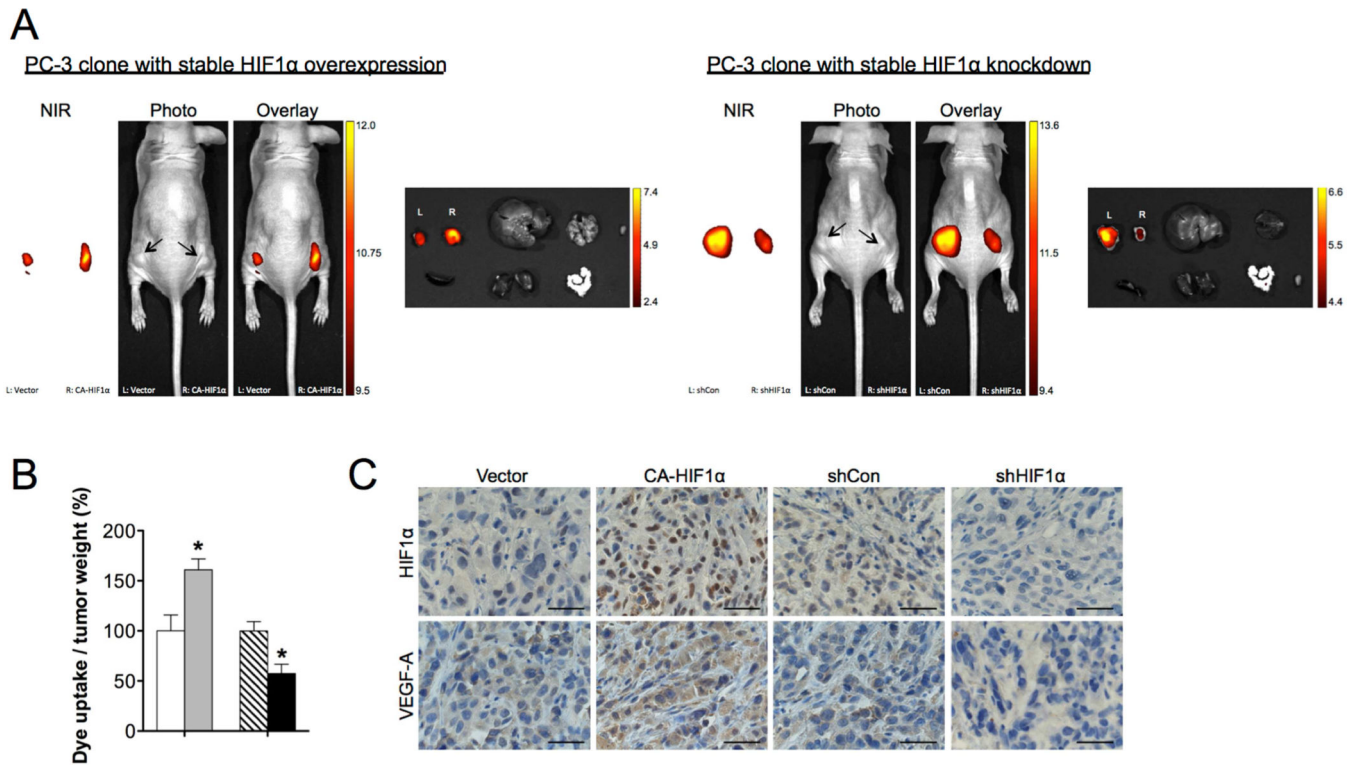


Fig. 3. Hypoxia and HIF1 α mediated the uptake of MHI-148 dye by tumor xenografts. (A) Representative *in vivo* and *ex vivo* NIRF images of control (left flank) vs. HIF1 α -overexpressing (right flank) (left panel) and control (left flank) vs. HIF1 α -knockdown (right flank) PC-3 tumor xenografts. Scale bars represent $\times 10^8$ for both *in vivo* and *ex vivo* NIRF in the unit of radiant efficiency. (B) Quantitation of tumor uptake of MHI-148 dye (N=5, mean \pm SEM) presented as the ratio of dye intensity to tumor weight. * $p < 0.05$, ** $p < 0.01$. (C) IHC analysis of HIF1 α and VEGF-A expression in PC-3 tumor xenografts with different manipulation of HIF1 α levels as indicated. Representative images are shown. Original magnification, $\times 400$; scale bars represent $20 \mu\text{m}$.

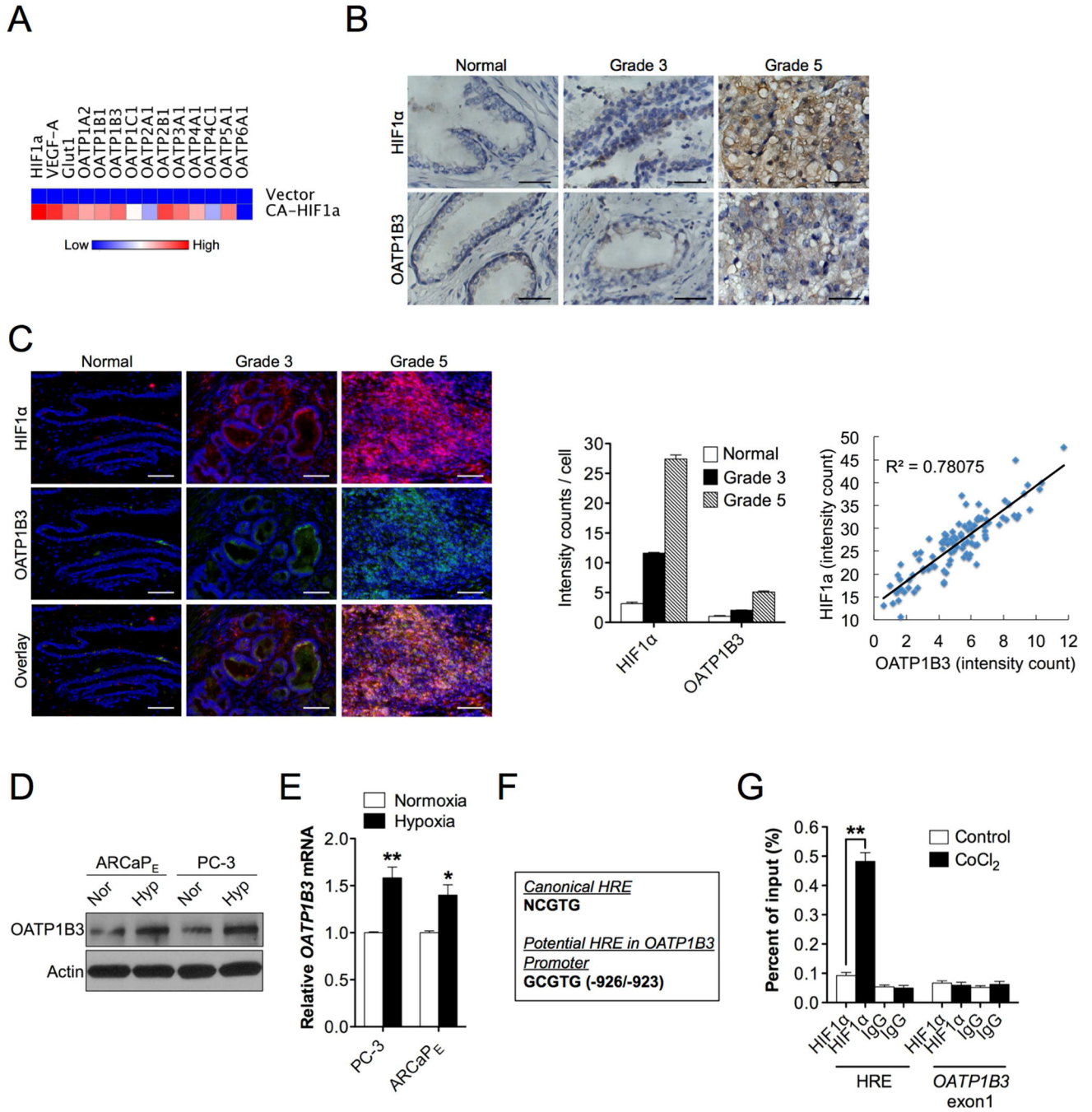


Fig. 4. Co-expression and regulation of HIF1α and OATPs in human PCa. (A) Heat map depicting OATPs mRNA expression profiling in constitutively active HIF1α-overexpressing PC-3 cells by qPCR. (B, C) IHC (B) and double QDL (C, left panel) staining of HIF1α and OATP1B3 expression in clinical specimens of normal prostatic epithelium, Gleason grade 3 and 5 PCa (N=15 for each). Representative images are shown. Original magnification, x400; scale bars represent 20 μm. Cell-based average intensity counts of HIF1α and OATP1B3 stain from 1,000 each of normal, grade 3 and 5 samples were quantified using in Form

software (C, middle panel). Intensity of HIF1 α and OATP1B3 co-expression in 100 single cells from a representative high-grade individual patient was analyzed for gene expression correlation (C, right panel). (D, E) Determination of OATP1B3 protein (D) and mRNA (E) expression in PC-3 and ARCaP_E cells in response to hypoxia (1% O₂) for 24 hrs and 4 hrs, respectively. (F) Sequences of the canonical HRE (top sequence) and a potential HRE in *OATP1B3* promoter (bottom sequence). (G) Chromatin from either vehicle- or CoCl₂-treated (200 μ M, 16 hr) PC-3 cells was immunoprecipitated using anti-HIF1 α or IgG antibodies followed by qPCR using 1 primer set for the HRE in *OATP1B3* promoter and 1 control primer set for *OATP1B3* exon1. Data represent the mean \pm SEM of three separate experiments. * p <0.05, ** p <0.01.

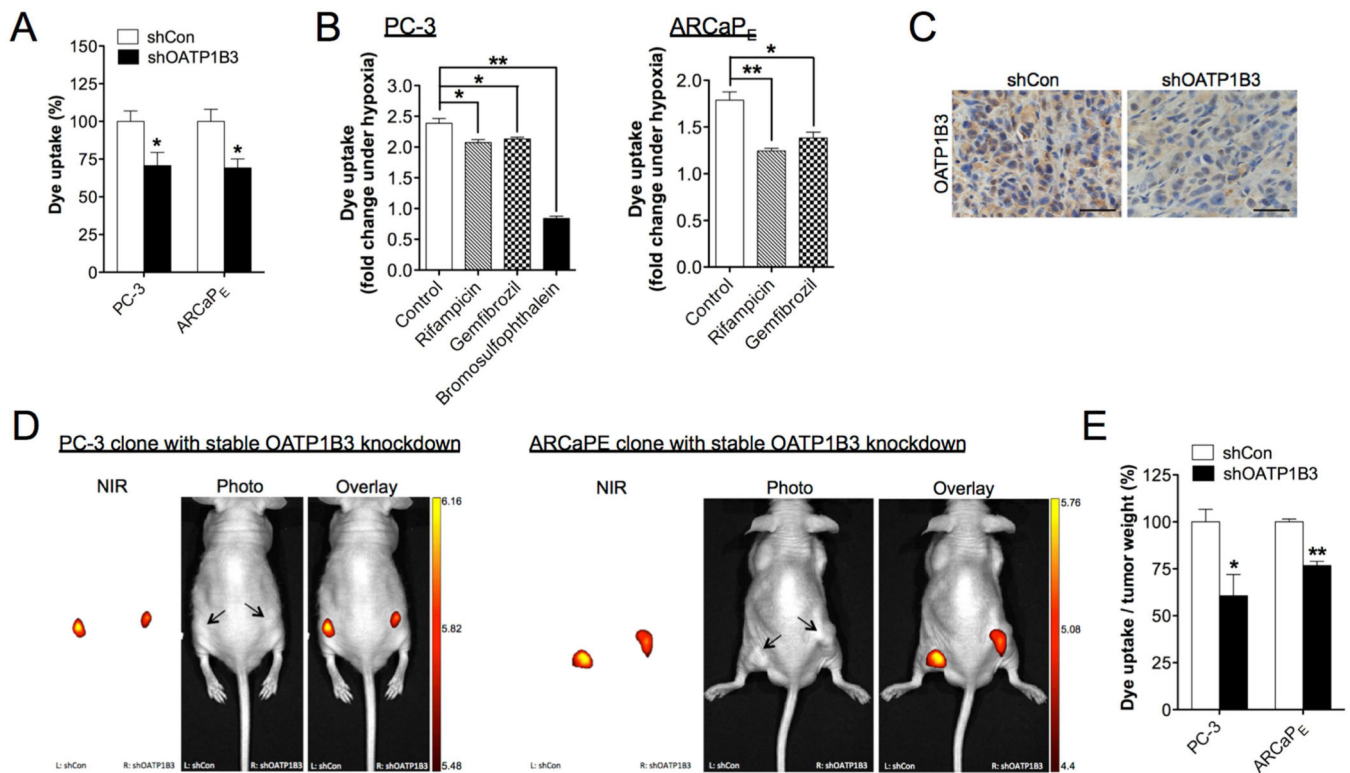


Fig. 5. OATP1B3 mediated the uptake of MHI-148 dye by cancer cells and tumor xenografts. (A) Determination of MHI-148 dye uptake in PC-3 and ARCaPE cells with stable knockdown of OATP1B3 (N=3, mean \pm SEM). (B) Determination of MHI-148 dye uptake in PC-3 (left panel) and ARCaPE (right panel) cells pre-treated with different OATP1B3 selective inhibitors as indicated for 1 hr followed by hypoxia treatment (1% O₂, 4 hr). Data was presented as fold change of MHI-148 dye uptake with hypoxia (N=3, mean \pm SEM). (C) IHC analysis of OATP1B3 expression in control and OATP1B3-knockdown PC-3 tumor xenograft. Original magnification, x400; scale bars represent 20 μ m. (D) Representative *in vivo* NIRF images of control (left flank)/OATP1B3-knockdown (right flank) PC-3 (left panel) and ARCaPE (right panel) tumor xenografts. Scale bars represent $\times 10^9$ for *in vivo* NIRF imaging of both PC-3 and ARCaPE tumor xenografts in the unit of radiant efficiency. (E) Quantitation of MHI-148 dye uptake in tumor xenografts (N=5, mean \pm SEM), presented as the ratio of dye intensity to tumor weight. * $p < 0.05$, ** $p < 0.01$.

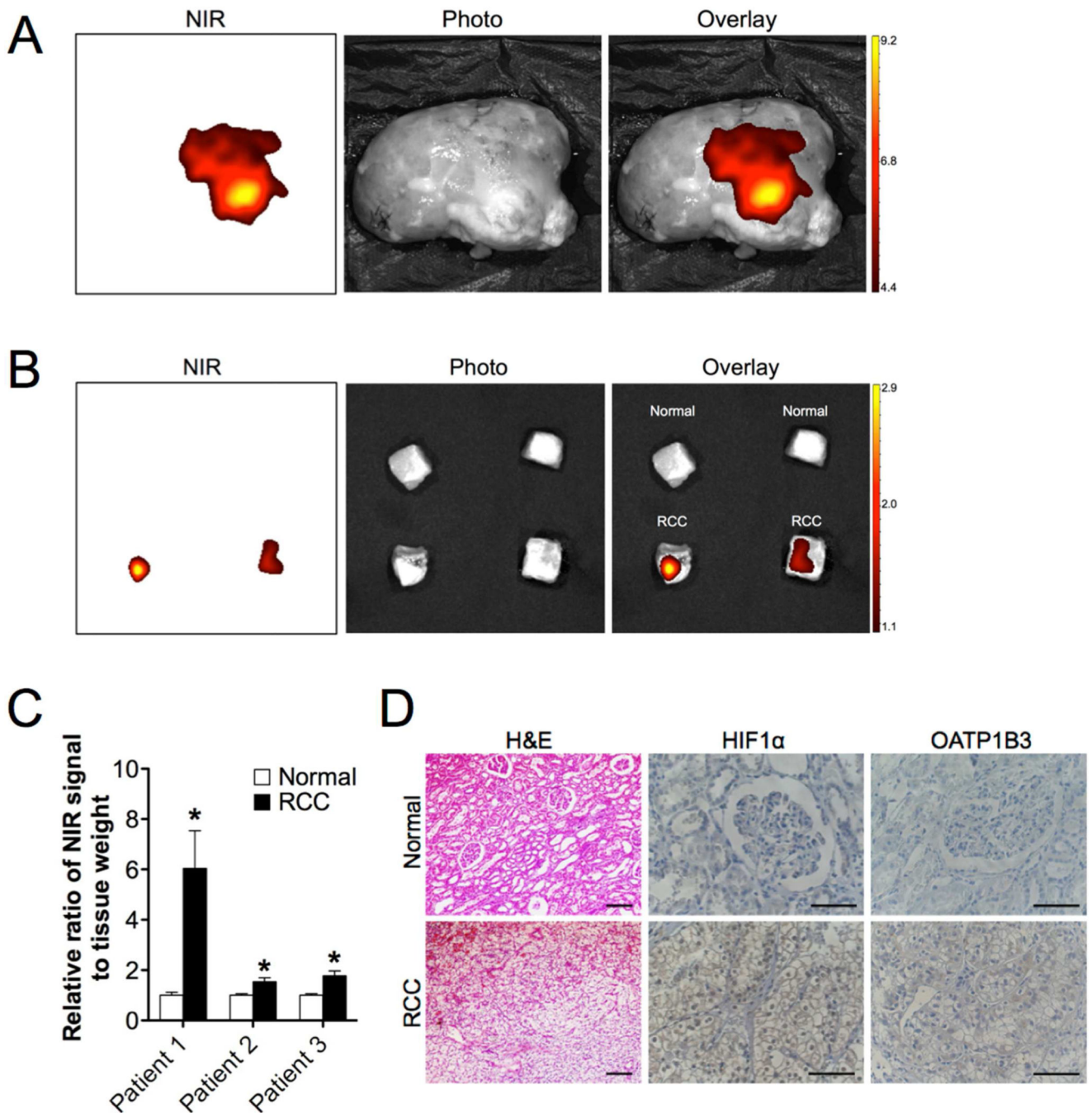


Fig. 6. NIRF imaging of clinical RCC samples. (A, B) Representative NIRF images of excised kidney by complete nephrectomy (A) as well as small cuts of normal (B, top) and RCC tissues (B, bottom) from an individual patient. Scale bars represent $\times 10^9$ and $\times 10^8$ for (A) and (B), respectively, in the unit of radiant efficiency. (C) Quantitation of MHI-148 dye uptake in normal and tumor tissues from three RCC patients, presented as the ratio of dye intensity to tissue weight from five cuts of tissues of each patient (mean \pm SEM). (D) H&E stain and IHC analysis of HIF1 α and OATP1B3 expression in normal and RCC samples.

Representative images are shown. Original magnification, x200 (H&E) and x400 (IHC); scale bars represent 20 μm . * $p < 0.05$.

Monoamine Oxidase A Inhibitor–Near-Infrared Dye Conjugate Reduces Prostate Tumor Growth

Jason Boyang Wu,[†] Tzu-Ping Lin,^{‡,§} John D. Gallagher,[‡] Swati Kushal,[‡] Leland W. K. Chung,[†] Haiyen E. Zhau,^{*,†} Bogdan Z. Olenyuk,^{*,‡,||} and Jean C. Shih^{*,‡,⊥}

[†]Uro-Oncology Research Program, Department of Medicine, Samuel Oschin Comprehensive Cancer Institute, Cedars-Sinai Medical Center, Los Angeles, California 90048, United States

[‡]Department of Pharmacology and Pharmaceutical Sciences, School of Pharmacy, University of Southern California, Los Angeles, California 90089, United States

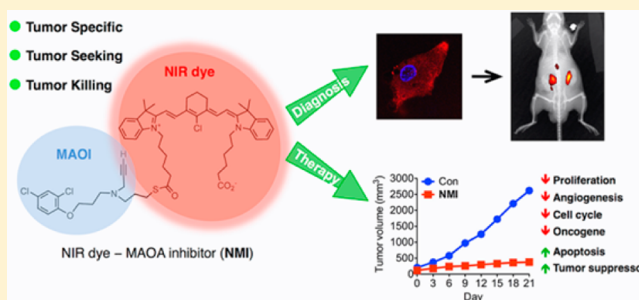
[⊥]Department of Cell and Neurobiology, Keck School of Medicine, University of Southern California, Los Angeles, California 90033, United States

^{||}USC Norris Comprehensive Cancer Center, Los Angeles, California 90033, United States

S Supporting Information

ABSTRACT: Development of anti-cancer agents with high tumor-targeting specificity and efficacy is critical for modern multidisciplinary cancer research. Monoamine oxidase A (MAOA), a mitochondria-bound enzyme, degrades monoamine neurotransmitters and dietary monoamines. Recent evidence suggests a correlation between increased MAOA expression and prostate cancer (PCa) progression with poor outcomes for patients. MAOA induces epithelial–mesenchymal transition (EMT) and augments hypoxic effects by producing excess reactive oxygen species. Thus, development of MAOA inhibitors which selectively target tumors becomes an important goal in cancer pharmacology. Here we describe the design, synthesis, and *in vitro* and *in vivo* evaluation of NMI, a conjugate that combines a near-infrared dye for tumor targeting with the moiety derived from the MAOA inhibitor clorgyline.

NMI inhibits MAOA with low micromolar IC_{50} , suppresses PCa cell proliferation and colony formation, and reduces migration and invasion. In mouse PCa xenografts, NMI targets tumors with no detectable accumulation in normal tissues, providing effective reduction of the tumor burden. Analysis of tumor specimens shows reduction in Ki-67⁺ and CD31⁺ cells, suggesting a decrease of cell proliferation and angiogenesis and an increase in M30⁺ cells, indicating increased apoptosis. Gene expression profiles of tumors treated with NMI demonstrate reduced expression of oncogenes *FOS*, *JUN*, *NFKB*, and *MYC* and cell cycle regulators *CCND1*, *CCNE1*, and *CDK4/6*, along with increases in the levels of tumor suppressor gene *TP53*, cell cycle inhibitors *CDKN1A* and *CDKN2A*, and MAOA-downstream genes that promote EMT, tumor hypoxia, cancer cell migration, and invasion. These data suggest that NMI exerts its effect through tumor-targeted delivery of a MAOA-inactivating group, making NMI a valuable anti-tumor agent.



INTRODUCTION

The search for new targets and development of anti-cancer agents with high tumor-targeting specificity and efficacy are critical goals underpinning the urgent, unmet need for more effective, mechanism-based cancer therapies. Monoamine oxidase A (MAOA) is a mitochondria-bound enzyme which catalyzes the degradation of monoamine neurotransmitters and dietary amines by oxidative deamination.^{1,2} This process is accompanied by production of hydrogen peroxide, a major source of reactive oxygen species (ROS), which can predispose cancer cells to DNA damage and can be a main cause of tumor initiation and progression.^{3,4} Recent studies performed by us⁵ and others⁶ have shown that increased MAOA levels are associated with prostate cancer (PCa) progression and poor prognosis for patients, and pharmacological inhibition of

MAOA reduces the growth of PCa cells *in vitro* and tumor xenografts *in vivo*.^{5,7,8} PCa is the second most common cause of death from cancer in American men of all ages.⁹ Despite its widespread occurrence, current treatments that include hormonal therapy,¹⁰ radiation therapy,¹¹ and surgery¹² are beneficial only for patients in the early stages of the disease and result in undesired side effects. These treatments have limited effectiveness for patients with advanced stages of castration-resistant and metastatic PCa. The urgent, unmet need for novel, effective mechanism-based therapies with reduced side effects has prompted a search for both novel targets in PCa and their pharmacological inhibitors.

Received: December 11, 2014

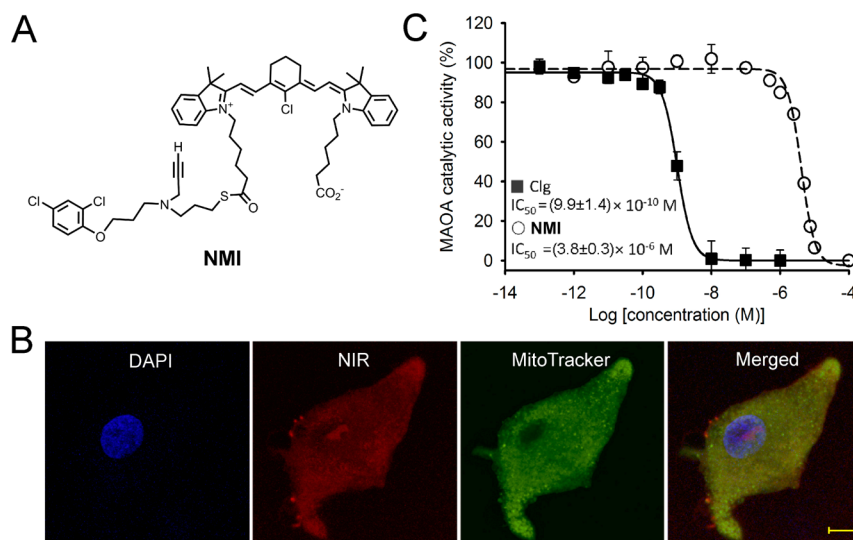
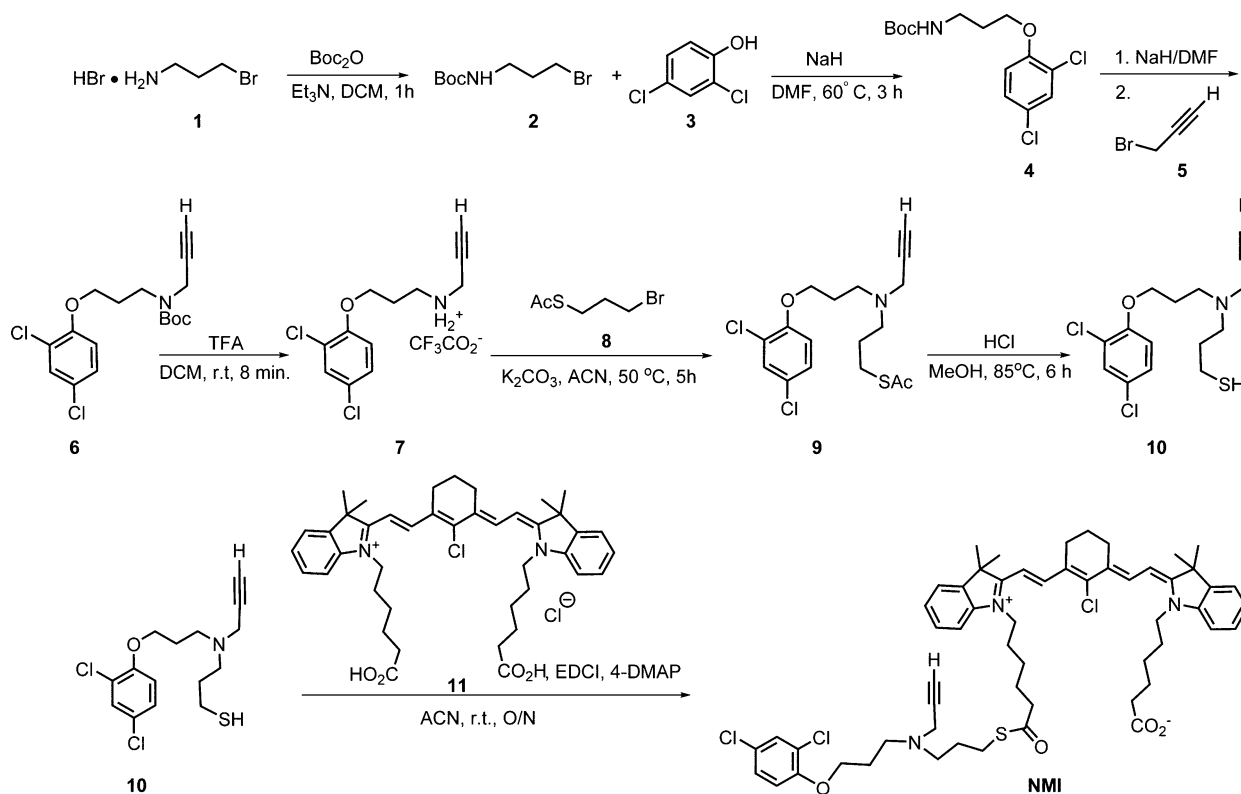


Figure 1. Structure and *in vitro* characterization of NMI. (A) Chemical structure of NMI. (B) Confocal images of a single LNCaP cell incubated with NMI. DAPI and MitoTracker agent were used to stain the nucleus and mitochondria of cells, respectively. Scale bar, 10 μm. (C) Inhibition of MAOA activity was determined in C4-2B cells (see Experimental Section). Clorgyline (Clg) or NMI was pre-incubated at 37 °C for 20 min at indicated doses, and IC₅₀ values were determined. The assay was performed in triplicate.

Scheme 1. Synthesis of NIR Dye–MAOA Inhibitor Conjugate NMI



We found that overexpression of MAOA in human PCa cell lines results in a loss of cell polarity, cell–cell adhesion, and gain of migratory and invasive properties, indicating that MAOA induces epithelial–mesenchymal transition (EMT).⁵ Moreover, MAOA-dependent activation of oncogenic pathways was consistently detected in high-grade PCa specimens, and knockdown of MAOA reduced or even eliminated prostate tumor growth and metastasis in a variety of PCa xenograft mouse models. By conducting site-directed mutagenesis, we found that MAOA catalytic activity is the major reason for

enhancing growth and metastasis of PCa.⁵ MAOA produces hydrogen peroxide as a byproduct of oxidative deamination reactions taking place in the outer membrane of mitochondria. Hydrogen peroxide and products of its conversion as other forms of ROS stabilize hypoxia-inducible factor 1 α (HIF1α).^{13–15} HIF1α increases tumor angiogenesis and survival responses as well as invasion and metastasis through the overexpression of hypoxia-inducible genes.^{16,17} These results are fully consistent with the clinical data, where elevated

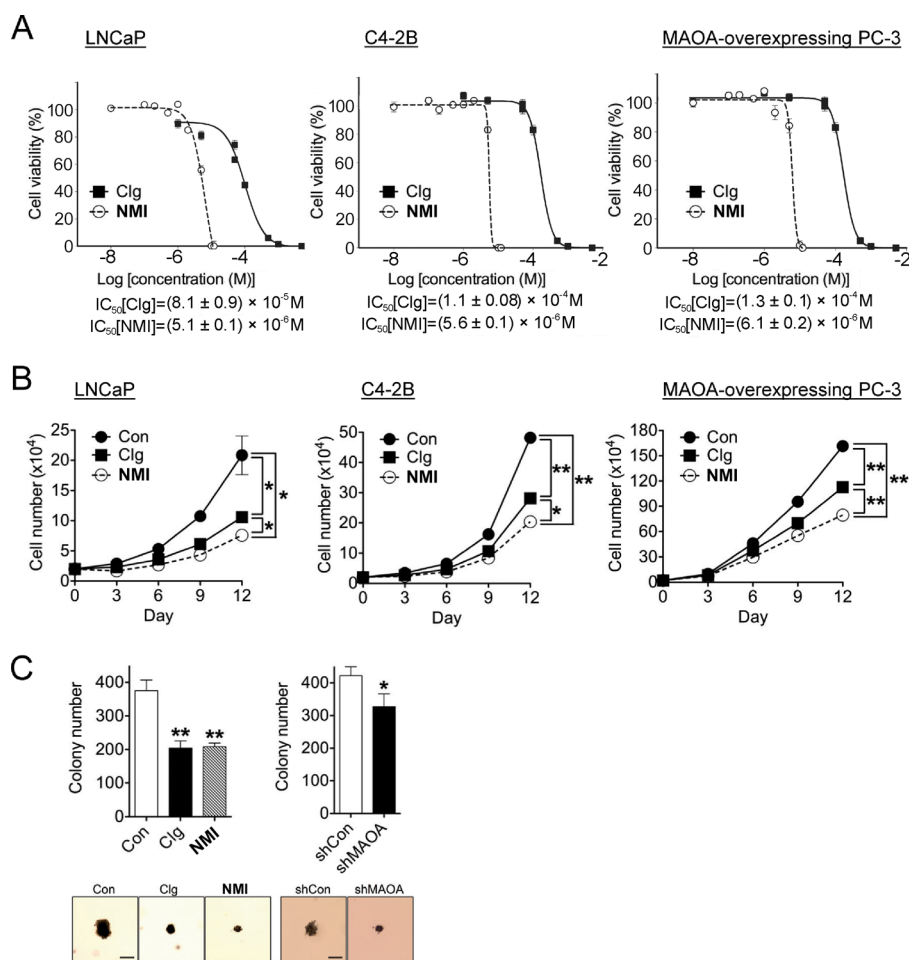


Figure 2. NMI inhibits PCa cell proliferation and colony formation. (A) Effect of clorgyline (Clg) and NMI on cell viability in LNCaP, C4-2B, and MAOA-overexpressing PC-3 cells as measured by an MTS assay. (B) Cell number counting assay with LNCaP, C4-2B, and MAOA-overexpressing PC-3 cells treated with Clg or NMI (1 μ M) for 12 days. Compound-added medium was replenished every 3 days; PBS was used as the vehicle. * p < 0.05, ** p < 0.01. (C) Colony formation assays in either LNCaP cells treated with Clg or NMI (1 μ M, left panel) or LNCaP cells targeted by either a scrambled shRNA (shCon) or a MAOA-targeting shRNA (shMAOA). Representative colonies are shown. Original magnification, \times 100; scale bar, 50 μ m. * p < 0.05, ** p < 0.01.

MAOA expression in PCa tissues is correlated with poor prognosis for PCa patients.^{5,6}

In keeping with these observations, we investigated MAOA as a potential novel pharmacological target for the treatment of human PCa. MAOA inhibitors, many of which are currently on the market as anti-depressants,¹ target central nervous system and other peripheral tissues where MAOA is present. This reduces the effective systemic concentration of MAOA inhibitors, limiting their delivery into the tumor where they could be most effective. To circumvent these problems, we designed a novel tumor-targeted MAOA inhibitor that would preferentially accumulate in the cancerous lesions. This inhibitor contains a tumor-targeting near-infrared (NIR) dye and a moiety of a MAOA inhibitor. We reasoned that including an NIR imaging functionality could be useful for measuring uptake and cellular localization of the conjugate and possibly for future image-guided diagnosis and drug delivery. We chose the small molecule clorgyline as a MAOA-targeting functionality because of the high affinity and selectivity of this compound toward MAOA. The availability of a high-resolution crystal structure of a clorgyline–MAOA complex¹⁸ facilitated our design. For tumor targeting and NIR imaging, we chose a recently developed class of nontoxic, fluorescent heptamethine

carbocyanine dyes with NIR emission maxima.^{19–21} The high selectivity in targeting of these dyes to tumors, mediated by tumor hypoxia and organic anion-transporting polypeptides (OATPs),²² has been demonstrated for many types of cancers, including human PCa.²³ Here we report the first study on PCa targeting and inhibition of xenograft growth in mice with a designed dual-function NIR dye–MAOA inhibitor conjugate (Figure 1A), abbreviated as NMI.

RESULTS

Design and Synthesis of NMI. NMI was synthesized in a sequence of steps outlined in Scheme 1. The synthesis started with commercially available 3-bromopropylamine hydrobromide (1). This compound was converted into *tert*-butyl (3-bromopropyl)carbamate (2), which was used in the subsequent step to alkylate the commercially available 2,4-dichlorophenol, giving an intermediate, 4. Deprotonation of the amide in 4 was carried out with sodium hydride, followed by alkylation with propargyl bromide 5, producing Boc-protected alkyne 6. The protecting group was removed under acidic conditions using trifluoroacetic acid (TFA) in dichloromethane (DCM). The product 7 was alkylated with 1-bromo-3-thioacetylpropane (8), resulting in the formation of compound

9. Removal of the acetyl protective group in **9** was carried out in methanolic HCl, affording an intermediate, **10**. This intermediate was then coupled to MHI-148 dye **11** using 1-ethyl-3-(3-dimethylaminopropyl)carbodiimide (EDCI) and 4-(dimethylamino)pyridine (4-DMAP) to give the product **NMI** in good yield (Scheme 1). The compound was purified by preparative thin-layer chromatography (TLC), and its identity and purity were confirmed by NMR and mass spectrometry.

NMI Localizes in PCa Cells and Inhibits MAOA. Recent reports suggested that the NIR heptamethine carbocyanine dyes IR-783 and MHI-148 can be retained in cancer cells but not normal cells, in tumor xenografts, and in spontaneous tumors in transgenic mice.²³ The two dyes have strong emission maxima at 820–860 nm upon excitation at 750–780 nm, which can be easily detected by NIR imaging. MAOA inhibitor–monomethine carbocyanine conjugates have fluorescence properties similar to those of the NIR dye MHI-148 itself. Therefore, a laser-scanning confocal microscope equipped with the appropriate laser and filters for NIR imaging was used to examine the cellular uptake of **NMI** in human PCa LNCaP cells which have high MAOA levels. Images of a single cell treated with **NMI** are shown in Figure 1B (*vide supra*). This compound rapidly accumulated in LNCaP cells and localized in the mitochondria, as determined by co-staining with the mitochondria-specific dye MitoTracker Green. In order to test the inhibitory activity of **NMI**, an MAOA activity assay was carried out in LNCaP-derived C4-2B cells using radiolabeled MAOA-specific substrate serotonin. The results indicate that **NMI** inhibits MAOA activity with a mean 50% inhibitory concentration (IC_{50}) of $(3.8 \pm 0.3) \times 10^{-6}$ M (Figure 1C).

NMI Reduces Colony Formation, Migration, and Invasion of PCa Cells. PCa LNCaP, C4-2B and MAOA-overexpressing PC-3 cells⁵ were used for cell viability (Figure 2A) and cell proliferation assays (Figure 2B). Treatment with clorgyline produced dose–response curves with $IC_{50} = 80.7 \pm 8.8 \mu\text{M}$ in LNCaP, $113.5 \pm 8.0 \mu\text{M}$ in C4-2B, and $129.3 \pm 9.6 \mu\text{M}$ in MAOA-overexpressing PC-3 cells. By comparison, treatment with **NMI** produced curves with $IC_{50} = 5.1 \pm 0.1 \mu\text{M}$ in LNCaP, $5.6 \pm 0.1 \mu\text{M}$ in C4-2B, and $6.1 \pm 0.2 \mu\text{M}$ in MAOA-overexpressing PC-3 cells, indicating 12–20 times higher efficacy for **NMI** in inhibiting PCa cells growth as compared to clorgyline (Figure 2A).

Most PCa cell lines, including LNCaP, C4-2B, and MAOA-overexpressing PC-3, possess undetectably low levels of monoamine oxidase B (MAOB), the second known MAO isoform.²⁴ However, given the important role MAOB plays in the normal physiology of the central nervous system and peripheral tissues,² we first decided to ascertain that MAOA is selectively inhibited with minimal interference to MAOB. Given that clorgyline is selective for MAOA and produces dose-sensitive inhibition,² in our preliminary cell-based assays we used a range of clorgyline concentrations (10 nM–10 μM) that are inhibitory for MAOA but below the IC_{50} for MAOB inhibition.²⁵ We determined 1 μM as the lowest concentration required for clorgyline to show efficacy in suppressing cell proliferation. This concentration was also consistent with the data from other reported study.²⁴ Thus, we chose 1 μM as the concentration at which the efficacies of both clorgyline and **NMI** could be assessed and compared in the subsequent *in vitro* studies.

In cell number counting assays, we observed that both clorgyline and **NMI** reduced the number of proliferating cells after 12 days. **NMI** also showed higher efficacy as compared to

clorgyline (Figure 2B). Colony formation assays were performed in LNCaP cells treated with clorgyline or **NMI** (Figure 2C). In a parallel setup, LNCaP cells were targeted by either MAOA-targeting shRNA (shMAOA) or a scrambled shRNA (shCon). Treatment with clorgyline and **NMI** resulted in a reduction of the colony number by as much as 45%, although in this assay the difference between the activities of clorgyline and **NMI** was not statistically significant (Figure 2C, left panel). Treatment with MAOA-targeting shRNA reduced the colony number by only 25%, as compared to treatment with scrambled shRNA (right panel). Because clorgyline has consistently shown lower efficacy in these experiments, we focused on **NMI** in the subsequent studies.

We tested the ability of **NMI** to inhibit migration of LNCaP and C4-2B cells. After treatment with compounds at 1 μM concentration for 48 h, the LNCaP cells showed statistically significant reduction in migration of 35% for **NMI** (Figure 3A,

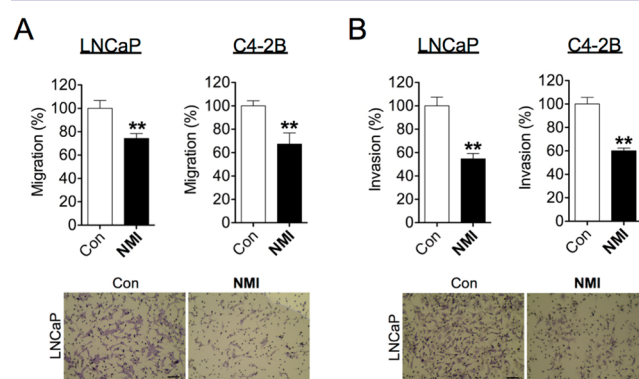


Figure 3. **NMI** reduces the migration and invasion of PCa cells. (A) Migration assays and (B) invasion assays of LNCaP and C4-2B cells treated with **NMI** (1 μM , 48 h). Representative images from LNCaP cells are shown. Original magnification, $\times 200$; scale bars, 200 μm . ** $p < 0.01$.

left panel). A similar result was observed for C4-2B cells (Figure 3A, right panel). In invasion assays, cells treated with **NMI** also showed 50% reduction in LNCaP and 40–45% reduction in C4-2B cells (Figure 3B).

NMI Reduces the Rate of Growth of PCa Xenografts in Nude Mice. In order to assess the efficacy of **NMI** *in vivo*, subcutaneous tumor xenograft mouse models were used. After being implanted subcutaneously into male nude mice, C4-2B cells formed tumors in 3–4 weeks. After tumors reached 200 mm^3 , mice were randomly assigned into two groups to receive treatments every other day: (1) control and (2) **NMI**. Two routes of administration were used to test the tumor-specific targeting ability of **NMI**: intratumoral and intraperitoneal. Tumors were measured with calipers, and tumor volume was calculated every 3 days during the 21-day treatment. Serum prostate-specific antigen (PSA) levels in mice were determined on day 11 (the middle of the treatment course), and tumor MAOA activity was determined at the end of treatment. Mice body weights were monitored on a weekly basis from the time of inoculation. At the experiment end point, mice were euthanized, tumors were excised, and tumor weights were determined. **NMI**-treated mice showed significant delays in tumor growth (Figure 4A), reduction in PSA levels (Figure 4B), and decreases in tumor weight as compared to control mice (Figure 4C). NIR imaging of the whole body *in vivo* and individual tumor and normal organs *ex vivo* clearly showed

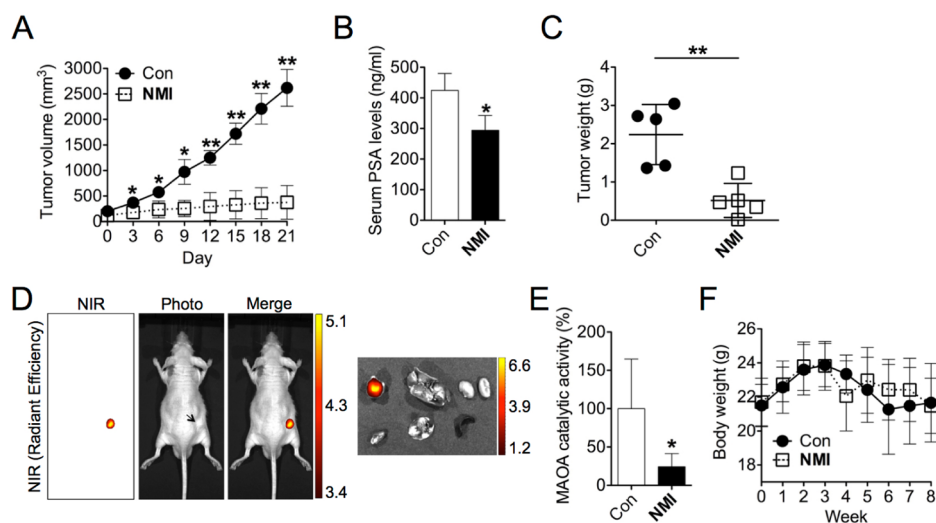


Figure 4. NMI inhibits the growth of C4-2B tumor xenografts in mice. (A) C4-2B cells were subcutaneously injected into male nude mice ($n = 5$ for each group) to establish tumor xenografts. After tumor size reached 200 mm^3 , mice were given intratumoral treatments (saline and NMI; 750 nmol/mouse) every other day for a 21-day period. Tumor size was determined by calipers, and tumor volume was calculated as described in the Supporting Information. $*p < 0.05$, $**p < 0.01$. (B) Serum PSA levels in mice were determined on day 11 after the treatment by ELISA. $*p < 0.05$. (C) Tumor weight, determined at the time of euthanasia of mice. $**p < 0.01$. (D) *In vivo* and *ex vivo* NIR imaging of mice given NMI treatment. Representative images are shown. NIR fluorescence color scales denote $\times 10^9$ and $\times 10^8$ for *in vivo* and *ex vivo* imaging, respectively, in the units of radiant efficiency ($[\text{p/sec/cm}^2/\text{sr}]/[\mu\text{W/cm}^2]$). (E) Tumor MAOA catalytic activity, determined at the time of euthanasia. $*p < 0.05$. (F) Mice body weight, determined every week after tumor implantation.

NMI localization within the tumor (Figure 4D). Measurements of MAOA activity in tumors showed its significant reduction in NMI-treated mice (Figure 4E). All mice in treated and control groups showed similar changes in body weight that did not exceed 18% throughout the entire duration of experiment (Figure 4F), suggesting that this treatment regimen was well tolerated by the animals.

We next performed hematoxylin and eosin (H&E) staining and immunohistochemical analysis of protein expression patterns of Ki-67 (a cell proliferation marker), M30 (a cell apoptosis marker), and CD31 (an angiogenesis marker) in tumor specimens from control and treated groups (Figure 5A). H&E staining showed a decrease in the nucleus-to-cytoplasm ratios in cells from tumors treated by NMI as compared to the control group, suggesting reduced malignancy in treated tumors.²⁶ Ki-67 staining of tumor specimens revealed a 25% decrease of Ki-67⁺ cells in NMI-treated tumors (Figure 5B, left panel). We observed an 11-fold increase of M30⁺ area (middle panel) and a 48% decrease in CD31⁺ area (right panel) in the treated specimens as compared to controls (Figure 5B), suggesting increased apoptosis and reduced angiogenesis occurring in treated tumors.

Gene expression profiling further indicated down-regulation in expression of such proto-oncogenes or oncogenes as *FOS*, *JUN*, *NFKB1*, and *MYC* and up-regulation of *TP53* tumor suppressor gene expression in response to treatment. Cell-cycle regulator genes that activate cell cycle progression, such as *CCND1*, *CCNE1*, *CDK4*, and *CDK6*, were also down-regulated, whereas expression of select cell-cycle inhibitors, including *CDKN1A* and *CDKN2A*, increased in the NMI-treated tumors as compared to controls. In contrast, decreased expression of anti-apoptotic *BCL2* gene was revealed in treated tumor samples. In addition, genes involved in MAOA-downstream signaling demonstrated to promote EMT (*VIM*, *SNAI1*, *SNAI2*, and *TWIST1*), tumor hypoxia (*VEGFA* and *GLUT1*), and cancer cell migration, invasion, and metastasis (*IL6*, *IL8*,

MMP2, *MMP9*, and *MET*)⁵ all showed reduced expression by treatment (Figure 5C).

To further evaluate the tumor-targeting properties of NMI, C4-2B cells were subcutaneously implanted contralaterally into both flanks of male nude mice. After the formation of two tumor xenografts in each mouse, NMI was injected intratumorally into one of the lesions. NIR imaging conducted after three injections performed every other day showed localization of the conjugate in both tumors (Figure 6A), which reveals tumor-targeting properties of NMI. Remarkably, the intensities of the NIR signals originating from the injected and contralateral tumor were comparable, suggesting rapid redistribution of the injected compound between two tumors. Figure 6B further shows that NMI selectively targets two tumors when administered in an intraperitoneal injection. NIR imaging shows no observable NIR signals in other body parts, further confirming the tumor-specific targeting of NMI and its systemic circulation.

DISCUSSION

The search for effective therapies based on pharmacological targeting and inhibition of increased MAOA expression in PCa and potentially other cancers is in its infancy. This study is our first report on the design, synthesis, and *in vitro* and *in vivo* evaluation of the therapeutic efficacy of NMI, a novel conjugate that targets tumors and reduces MAOA activity in mouse PCa xenograft models. The conjugate consists of the MAOA targeting functionality and a NIR dye. It was synthesized in eight steps in a scalable procedure from commercially available starting materials to give hundreds of milligrams of material. The conjugate was shown to target PCa cells, localize in mitochondria, and inhibit MAOA activity in the low micromolar IC_{50} range. It has shown efficacy that exceeds that of clorgyline, a known MAOA inhibitor, in suppressing the growth of three PCa cell lines with high levels of MAOA: LNCaP, C4-2B, and MAOA-overexpressing PC-3. It inhibited colony

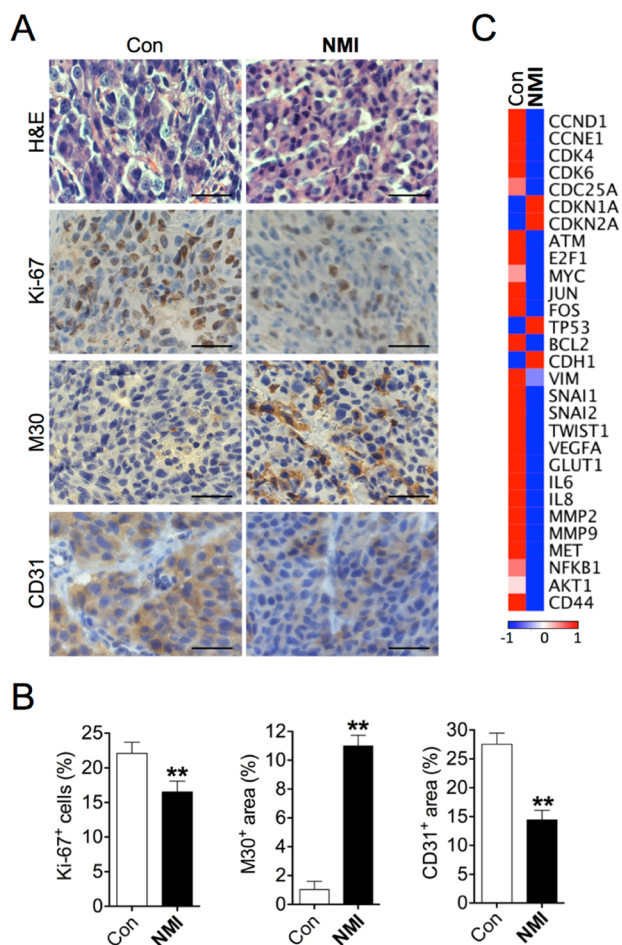


Figure 5. Analysis of tumor specimens obtained from treated and control mice. (A) H&E and immunohistochemical analysis of Ki-67, M30, and CD31 expression in respective tumor specimens. Representative images are shown. Original magnification, $\times 400$; scale bars, $20\ \mu\text{m}$. (B) Quantification of percent of Ki-67⁺, M30⁺, and CD31⁺ tumor cells or areas of five distinct images from each group. The data represent mean \pm SD. $**p < 0.01$. (C) Heat map depicting gene expression profiling of tumor samples from each group. Red and blue colors indicate high and low relative expression levels, respectively, with the numbers indicating \log_2 -transformed ratios.

formation for LNCaP cells similarly to MAOA-targeting shRNA. NMI also inhibited invasion and migration of PCa cells, which is consistent with the demonstrated mechanism that high MAOA activity is associated with aggressive cell behavior and induced EMT. The diminished levels of an epithelial marker, E-cadherin, and increased expression of a mesenchymal marker, vimentin, indicate EMT suppression. By conducting a comparative study using NMI and clorgyline, we have shown that the tumor-targeting property of NMI makes it a superior pharmacological inhibitor, as compared to clorgyline, in nearly all cases.

Our *in vivo* studies using PCa xenograft mouse models show that NMI localizes in the tumors, reduces the rate of tumor growth, and decreases levels of PSA and MAOA catalytic activity in mice engrafted with C4-2B cells. At a final dose of 6 nmol per mouse, NMI shows significant inhibitory efficacy on tumor xenograft growth. One of the unexpected findings is the discovery that an intratumorally injected compound would redistribute itself into the neighboring tumors, suggesting that its redistribution *in vivo* is facilitated by the rapid circulation in

the bloodstream. This is further supported by the observation of tumor-specific targeting made by an intraperitoneal administration.

We previously shown that tumor hypoxia is one of the major factors that mediates uptake of heptamethine carbocyanine NIR dyes by tumor cells.²² Hypoxia, through stabilization of HIF1 α , also underlies one of the key MAOA functions in promoting tumor progression and metastasis in PCa.⁵ The increased uptake and retention of NMI in tumors is likely due to tumor hypoxia through an activated HIF1 α /OATPs signaling axis,²² which is supported by our observation that the tumor-targeting effect of NMI could be enhanced in PCa expressing high levels of MAOA associated with increased tumor hypoxia. Indeed, the higher accumulation of NMI in MAOA-overexpressing PC-3 tumors as compared to a control tumor is paralleled by the increase in HIF1 α immunostaining in those tumor samples with elevated expression of MAOA (see Supporting Information, Figure S1). These observations suggest that a synergistic strategy based on the use of tumor-targeting MAOA inhibitors such as NMI and inhibitors of hypoxia-inducible transcription could result in an improved efficacy and reduced side effects in treating hypoxic, high-grade PCa.

CONCLUSION

We have demonstrated that a tumor-targeting NIR dye–MAOA inhibitor conjugate has the highest efficacy among all the MAOA inhibitors tested in PCa, and it may become a novel pharmacological agent for treatment and diagnosis of this type of cancer. Such an agent, after the proper preclinical development, could become an important platform for future generation of anti-cancer therapeutics. Such a conjugate also possesses a diagnostic potential, in that it can differentiate the prostate tumors with high MAOA activity, high hypoxia, and elevated malignant potential from the indolent neoplasms. Its anti-tumor effect, largely derived through MAOA targeting, makes it a valuable addition to the anti-cancer therapeutic armamentarium.

EXPERIMENTAL SECTION

General. All reagents and solvents were obtained from commercial sources and were used as received unless otherwise stated. Molecular biology grade salts and buffers were obtained from Sigma-Aldrich. MitoTracker Green and 4',6-diamidino-2-phenylindole (DAPI) dyes were obtained from Life Technologies. All reactions involving moisture-sensitive reagents were conducted under argon atmosphere with anhydrous solvents and flame-dried glassware. Hygroscopic liquids were transferred via a syringe and were introduced into reaction vessels through rubber septa. Reaction product solutions were concentrated using a rotary evaporator at 30–150 mmHg. Column chromatography was performed on silica gel (230–400 mesh) using reagent grade solvents. Analytical TLC was performed on glass-backed, pre-coated plates (0.25 mm, silica gel 60, F-254, EM Science). Analytical high-performance liquid chromatography (HPLC) was performed on Microsorb-MV C₈ reverse-phase columns (250 \times 4.6 mm, Varian) using a Shimadzu LC-10A VP pump and a Shimadzu SPD 10A VP UV–vis variable-wavelength detector. Preparative HPLC purifications were carried out with C₈ reverse-phase preparative columns (Grace Davison). The flow rate for preparative reverse-phase HPLC was 4 mL/min. In all cases, 5%–95% gradients of acetonitrile (ACN) in 0.1% aqueous TFA were used as eluents. Water (18 M Ω) was obtained from a Barnstead water purification system, and all buffers were 0.2 μm filtered. NMR spectra were collected on instruments in the indicated solvents. The identity and purity of each intermediate and the final product were confirmed by ¹H and ¹³C

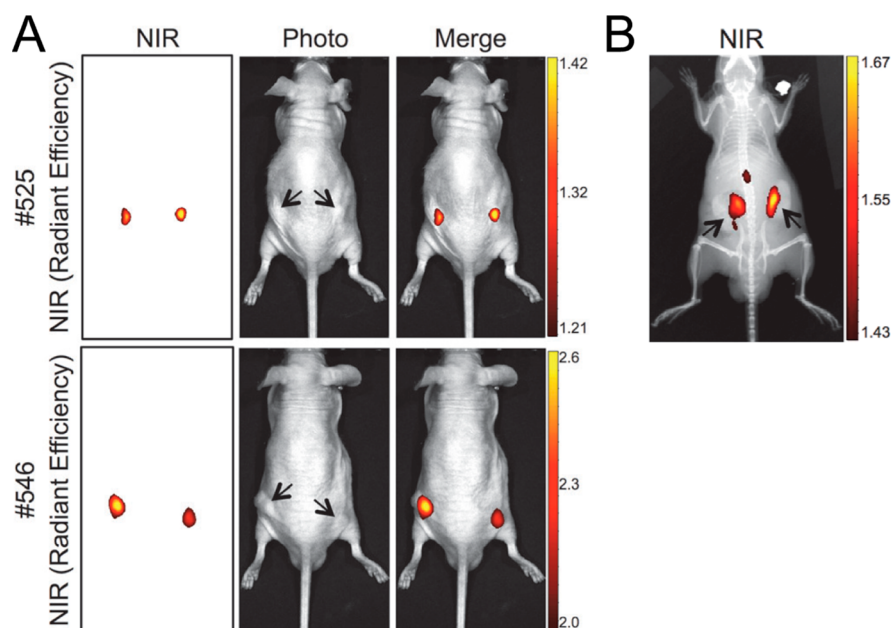


Figure 6. Tumor-targeting properties of NMI in mouse xenografts. (A) C4-2B cells were subcutaneously implanted into both flanks of male nude mice to form tumor xenografts, and only the tumor in one flank (right #525 or left #546) was given intratumoral injection of NMI (12 nmol/mouse) every other day for three injections, followed by NIR imaging. Representative images are shown. (B) Mice bearing C4-2B tumor xenografts as described in (A) were intraperitoneally injected with NMI (50 nmol/mouse) and 24 h later subjected to NIR imaging. One representative image is shown. Tumors are indicated by the arrows. NIR fluorescence color scales denote $\times 10^9$ and $\times 10^{10}$ for intratumoral and intraperitoneal injections, respectively, in the units of radiant efficiency ($[\text{p}/\text{sec}/\text{cm}^2/\text{sr}]/[\mu\text{W}/\text{cm}^2]$).

NMR (Varian Mercury 400 MHz instrument) and mass spectrometry (Agilent 6520 time-of-flight system).

Synthesis of Compounds. *tert-Butyl (3-Bromopropyl)-carbamate (2)*. To a 100 mL round-bottom flask equipped with a magnetic stirrer were added 3-bromopropylamine hydrobromide (**1**, 1.19 g, 5.44 mmol, 1.0 equiv) and DCM (30 mL). To the resultant solution was added *di-tert-butyl* dicarbonate (2.16 g, 9.90 mmol, 1.8 equiv) in DCM (20 mL), followed by triethylamine (0.866 mL, 6.21 mmol, 1.1 equiv). The solution was stirred at room temperature for 75 min. The reaction was diluted with DCM (50 mL) and washed twice with sodium bicarbonate (50 mL) and once with brine (50 mL). The organic phase was dried over sodium sulfate and filtered, and the solvent was removed *in vacuo* to yield **2** (1.35 g, 80%). ^1H NMR (400 MHz, CDCl_3): δ 4.65 (s, 1H), 3.37 (dt, 2H, $J_1 = 6.4$ Hz, $J_2 = 1.2$ Hz), 3.21 (dd, 2H, $J_1 = 12.4$ Hz, $J_2 = 6.4$ Hz), 1.98 (m, 2H), 1.37 (s, 9H).

tert-Butyl 3-(2,4-Dichlorophenoxy)propylcarbamate (4). To a 50 mL round-bottom flask equipped with a magnetic stirrer was added 2,4-dichlorophenol (**3**, 452 mg, 2.77 mmol, 1.0 equiv) followed by dimethylformamide (DMF, 3 mL). To the resultant solution was added sodium hydride portion-wise (111 mg, 2.77 mmol, 1.0 equiv) followed by **4** (661 mg, 2.77 mmol, 1.0 equiv) in DMF (2 mL). The mixture was stirred at 60 °C for 3 h. The reaction was diluted with DCM (50 mL) and washed three times with 10% sodium hydroxide (15 mL), once with HCl (25 mL), and once with brine (50 mL). The organic phase was dried over sodium sulfate and filtered, and the solvent was removed *in vacuo* to yield **4** (431 mg, 48%). ^1H NMR (400 MHz, CDCl_3): δ 7.36 (d, 1H, $J = 2.8$ Hz), 7.18 (dd, 1H, $J_1 = 8.8$ Hz, $J_2 = 2.8$ Hz), 6.83 (d, 1H, $J = 8.4$ Hz), 5.16 (s, 1H), 4.07 (t, 2H, $J = 5.6$ Hz), 3.38 (m, 2H), 2.03 (m, 2H), 1.44 (s, 9H).

tert-Butyl 3-(2,4-Dichlorophenoxy)propyl(prop-2-ynyl)carbamate (6). To a 20 mL scintillation flask equipped with a magnetic stirrer was added **4** (273 mg, 0.858 mmol, 1.0 equiv) followed by DMF (3 mL). To the resultant solution was added sodium hydride portion-wise (35 mg, 0.858 mmol, 1.0 equiv) followed by propargyl bromide (**5**, 130 μL , 0.858 mmol, 1.0 equiv). The mixture was stirred at room temperature for 2 h. The reaction was evaporated and the residue purified by column chromatography using a gradient of 2%–5%–50% EtOAc in hexanes to yield **6** (75.4 mg, 21% yield). ^1H NMR (400

MHz, CDCl_3): δ 7.36 (d, 1H, $J = 2.8$ Hz), 7.17 (dd, 1H, $J_1 = 8.4$ Hz, $J_2 = 2.4$ Hz), 6.83 (d, 1H, $J = 8.8$ Hz), 4.07 (t, 2H, $J = 6.0$ Hz), 4.04 (t, 1H, $J = 5.6$ Hz), 3.56 (t, 2H, $J = 6.8$ Hz), 2.18 (t, 2H, $J = 2.4$ Hz), 2.03 (m, 2H), 1.57 (s, 2H), 1.44 (s, 9H).

N-(3-(2,4-Dichlorophenoxy)propyl)prop-2-yn-1-aminium Tri-fluoroacetate (7). To a 20 mL scintillation flask equipped with a magnetic stirrer was added **6** (72.6 mg, 0.858 mmol, 1.0 equiv) followed by DCM (4 mL). To the resultant solution was added TFA (1 mL). The mixture was stirred at room temperature for 8 min. The reaction was evaporated and dried *in vacuo* to provide **7** without further purification (75 mg, quantitative yield).

S-3-Bromopropyl Ethanethioate (8). A 250 mL three-neck round-bottom flask equipped with a thermocouple in a glass sleeve, a magnetic stirrer, a vigreux column with an argon inlet (middle stem), and a sleeved rubber septum stopper was assembled and dried with a heat gun under flow of argon. Approximately 110–120 mL of anhydrous DMF was added via a cannula. Potassium thioacetate (11.68 g, 102.3 mmol) was added portion-wise into the flask while it was cooled with an ice-cold MeOH bath. The reaction was stirred for 7 h at about -10 °C. The ice-cold MeOH bath was removed after the reaction was quenched by addition of 165 mL of water. The reaction mixture was partitioned with 300 mL of methyl *tert*-butyl ether (MTBE) and 700 mL of water. The water layer was washed with 200 mL of MTBE. The MTBE layers were washed sequentially with water, saline, and NaHCO_3 , dried over MgSO_4 , filtered, and evaporated to yield **8** (19.1 g, 98.7%). ^1H NMR (400 MHz, CDCl_3): δ 3.45 (t, 2H, $J = 6.4$ Hz), 3.01 (t, 2H, $J = 7.2$ Hz), 2.35 (s, 3H), 5.16 (s, 1H), 2.13 (m, 2H).

S-3-((3-(2,4-Dichlorophenoxy)propyl)(prop-2-ynyl)amino)propyl Ethanethioate (9). To a 20 mL scintillation vial equipped with a magnetic stirrer was added **7** (12 mg, 0.032 mmol, 1.0 equiv) followed by ACN (2.5 mL). To the resultant solution was added potassium carbonate (186 mg, 1.343 mmol, 10.0 equiv) followed by **8** (12.6 mg, 5.66 mmol, 17.7 equiv). The mixture was stirred at 80 °C overnight. The reaction was then filtered, the solvent was removed under reduced pressure, and the residue was dried *in vacuo*. The crude material was purified by preparative TLC using 5% ethyl acetate in hexanes as an eluent to yield **9** (4.7 mg, 39%). ^1H NMR (400 MHz, CDCl_3): δ 7.35

(d, 1H, $J = 2.4$ Hz), 7.16 (dd, 1H, $J = 8.4$ Hz, $J = 2.4$ Hz), 7.35 (d, 1H, $J = 8.8$ Hz), 4.07 (t, 2H, $J = 6.0$ Hz), 4.04 (t, 1H, $J = 5.6$ Hz), 3.40 (s, 2H), 2.87 (t, 2H, $J = 6.8$ Hz), 2.70 (t, 2H, $J = 6.4$ Hz), 2.56 (t, 2H, $J = 6.8$ Hz), 2.30 (m, 3H), 2.17 (s, 1H), 1.95 (m, 2H), 1.71 (m, 2H).

3-((3-(2,4-Dichlorophenoxy)propyl)(prop-2-ynyl)amino)propane-1-thiol (10). A solution of **9** (1.17 mg, 3.10 μmol) in 200 μL of ACN was added into a 20 mL vial equipped with a stir bar, evaporated, and then co-evaporated with MeOH three times to remove ACN. MeOH/HCl (200 μL) was added into the vial, and then the vial was heated on an oil bath at 85 $^{\circ}\text{C}$ for 6 h. The reaction mixture was co-evaporated sequentially with MeOH three times and ACN three times to give **10**, which was used in the next step without further purification.

6-((Z)-2-((E)-2-(2-Chloro-3-((E)-2-(1-(6-((3-(2,4-dichlorophenoxy)propyl)(prop-2-yn-1-yl)amino)propyl)thio)-6-oxohexyl)-3,3-dimethyl-3H-indol-1-ium-2-yl)vinyl)cyclohex-2-en-1-ylidene)ethylidene)-3,3-dimethylindolin-1-yl)hexanoate (NMI). MHI-148 **11** (170 mg, 242 μmol , 1.10 equiv), dry DCM (10 mL), EDCI hydrochloride (45 mg, 235 μmol , 1.04 equiv), and DMAP (8 mg, 6.5 μmol , 0.03 equiv) were added to a 20 mL round-bottom flask equipped with a stir bar and stirred for 15 min. Compound **10**, obtained in the previous step (75 mg, 226 μmol , 1.00 equiv), was added to the mixture as a solution in ACN (2 mL), and the reaction was stirred at room temperature overnight. The solvent was then removed under reduced pressure. The compound was dissolved in 5 mL of DCM and purified on preparative silica gel plates using 7.5% MeOH in DCM as an eluent. Yield: 83.2 mg, 37%. Alternatively, the reaction mixture aliquot was dissolved in methanol and purified by HPLC using a YMC HPLC column (C_{18} 5- μm column, 50 mm length \times 20 mm i.d.) and a 5%–95% gradient of ACN in 0.1% aqueous TFA over 30 min to yield NMI (0.144 mg recovery). $^1\text{H NMR}$ (400 MHz, CDCl_3): δ 1.49 (m, 2H, $\gamma\text{-CH}_2(\text{COOH})$), 1.56 (m, 2H, $\gamma\text{-CH}_2(\text{COSCH}_2\text{-})$), 1.67 (s, 6H, CH_3), 1.71 (s, 6H, CH_3), 1.80 (m, 2H, $\beta\text{-CH}_2$), 1.82 (m, 2H, $\beta\text{-CH}_2$), 1.86 (m, 2H, $\delta\text{-CH}_2$), 1.88 (m, 2H, $\delta\text{-CH}_2$), 1.94 (s, 2H, $\text{O-CH}_2\text{CH}_2\text{CH}_2\text{N-}$), 1.97 (s, 2H, $\text{S-CH}_2\text{CH}_2\text{CH}_2\text{N-}$), 2.09 (s, 2H, CH_2), 2.56–2.57 (m, 4H, $\alpha\text{-CH}_2$), 2.68–2.70 (m, 4H, CH_2NCH_2), 2.71 (s, 2H, $\text{CH}_2\text{C=}$), 2.75 (s, 2H, $\text{CH}_2\text{C=}$), 2.85 (m, 2H, -SCH_2), 4.04 (t, 1H, $\text{HC}\equiv\text{C-}$), 4.05 (t, 4H, N-CH_2), 4.05 (t, 2H, O-CH_2), 4.07 (t, 2H, $\text{CH}_2\text{C}\equiv$), 6.04 (d, 1H, $\text{CH}=\text{CH}$), 6.32 (d, 1H, $\text{CH}=\text{CH}$), 6.85 (d, 1H, Ar-H), 7.05 (d, 1H, Ar-H), 7.17–7.42 (m, 9H, Ar-H), 8.28 (d, 1H, $\text{CH}=\text{CH}$), 8.40 (d, 1H, $\text{CH}=\text{CH}$). HRMS: calcd for $\text{C}_{57}\text{H}_{69}\text{Cl}_3\text{N}_3\text{O}_4\text{S}$ m/z 996.4074; observed m/z 996.4068. λ_{max} absorption and fluorescence wavelengths in methanol were 780 and 802 nm, respectively.

Cell Lines and Cell Culture Conditions. Human PCa LNCaP cell line was obtained from American Type Culture Collection. Human PCa C4-2B cell line was established from LNCaP as described previously.²⁷ Human PCa MAOA-overexpressing PC-3 cell line was established as described previously.⁵ LNCaP and C4-2B cells were grown in RPMI 1640 medium (Life Technologies), and MAOA-overexpressing PC-3 cells were grown in T-medium (Life Technologies), with both media supplemented with 10% fetal bovine serum (FBS) and 1% penicillin/streptomycin.

Laser-Scanning Confocal Microscopy. Cells were plated in glass-bottom microscopy dishes (MatTek) at a density of 20 000 cells in 400 μL of medium supplemented with 10% FBS and were allowed to form a monolayer over 20 h. NMI at a concentration of 5 μM in 400 μL of fresh medium containing 10% FBS, MitoTracker Green (1 \times), and DAPI (1 \times) were added to the media, and the cells were incubated at 37 $^{\circ}\text{C}$ and 5% CO_2 for an additional 4 h. Imaging was performed on a Zeiss LSM 510 inverted laser-scanning confocal microscope, equipped with an oil-immersion $\times 63$ objective lens. Excitation wavelengths were set at $\lambda_{\text{max}} = 488$ nm (DAPI, blue excitation), 514 nm (MitoTracker Green, green-yellow excitation), and 790 nm (NMI, red excitation). The data were acquired in a multi-track mode. Images were taken using pinholes of 130–200 μm in order to capture fluorescence signals on a thin focus plane.

MAOA Catalytic Activity Assay. MAOA catalytic activity was determined in PCa cells and tumor samples treated with clorgyline or NMI at different concentrations. One hundred micrograms of total protein ($\sim 1 \times 10^6$ cells) were incubated with 1 mM ^{14}C -5-

hydroxytryptamine (5-HT) in the assay buffer (50 mM sodium phosphate buffer, pH 7.4) at 37 $^{\circ}\text{C}$ for 20 min, and the reaction was terminated by the addition of 100 μL of 6 N HCl. The reaction products were extracted with benzene/ethyl acetate and centrifuged. The organic phase containing the reaction products was extracted, and the radioactivity was determined by liquid scintillation spectroscopy.

Cell Proliferation Assays. Cells were seeded on 96-well plates in triplicate and treated with vehicle, clorgyline, or NMI at different concentrations for 96 h. Cell proliferation was determined by MTS assay (Promega) following the manufacturer's instructions. For cell number counting assays, cells were seeded on 6-well plates (2×10^4 cells/well) and treated with vehicle, clorgyline (1 μM), or NMI (1 μM) for 12 days, with compound-added medium replenished every 3 days. Cell numbers from triplicate wells were counted by a hemocytometer.

Colony Formation Assay. Cells were suspended in the culture media containing 0.3% agarose (FMC BioProducts) with vehicle, clorgyline (1 μM), or NMI (1 μM) and placed on top of solidified 0.6% agarose in 6-well plates. The developed colonies were counted and recorded under a microscope after a 3-week incubation.

Migration and Invasion Assays. Assays were performed using 6.5 mm transwells (8 μm pore size) coated with either collagen I or Growth Factor Reduced Matrigel (BD Biosciences) for the migration and invasion assays, respectively. Cells were serum-starved overnight before seeding to eliminate the interference of proliferative effect with cell migration or invasion. Cells were seeded inside transwell inserts containing culture medium without serum and with treatment. After 18–24 h, the cells that translocated to the lower surface of the filters were fixed in 4% formaldehyde. The fixed membranes were stained using crystal violet (1% solution). Assays were quantified by counting the number of stained nuclei in five independent fields in each transwell.

Mouse Subcutaneous Tumor Xenograft Studies. Male 4- to 6-week-old athymic nude mice were purchased from Taconic, Inc., housed in the animal research facility at University of Southern California (USC), and fed a normal diet. For xenograft studies, 2×10^6 C4-2B cells were mixed 1:1 with Matrigel (BD Biosciences) and injected subcutaneously into nude mice, with each mouse bearing one tumor on the right flank. After tumors reached a size of 100–200 mm^3 , mice were randomly assigned to two groups (saline or NMI, $n = 5$ per group). For the treatment group, intratumoral injections of NMI (2 μg /tumor, 250 nmol/mouse) were given to mice every other day for the first 10 days, and then the dose was increased to 6 μg /tumor (750 nmol/mouse). Intratumoral injections of saline were given to the control group. Tumor size was measured every 3 days by calipers, and tumor volume was calculated by the formula of length \times width² \times 0.52.²⁸ Mouse blood was collected from the retro-orbital sinus bleeding on day 11, and serum PSA level was determined by an ELISA kit (GenWay Biotech) in accordance with the manufacturer's instructions. Tumors were dissected and weighed when mice were euthanized on day 21. Mice body weight was measured on a weekly basis following tumor implantation. All animal studies received prior approval by the USC IACUC and were conducted in compliance with its recommendations.

Analysis of Tumor Uptake of NMI by NIR Fluorescence Optical Imaging. Mice bearing C4-2B subcutaneous tumors, when tumor size reached 2–6 mm in diameter assessed by palpation, were injected intratumorally (three consecutive injections every other day) with NMI at a dose of 12 nmol/mouse or intraperitoneally (one injection) at 50 nmol/mouse. Whole-body NIR fluorescence optical imaging was taken 24 h after the last injection using an IVIS Lumina XR imaging system (PerkinElmer) equipped with fluorescence filter sets (excitation/emission, 783/840 nm) as described previously.²⁹ During imaging, mice were maintained in an anesthetized state.

Immunohistochemistry. Immunohistochemical analysis of tumor xenograft samples was performed using antibodies against Ki-67 (Abcam), M30 (DiaPharma), or CD31 (Santa Cruz) following our published protocol³⁰ with minor modifications. Briefly, formalin-fixed paraffin-embedded sections (4 μm) were de-paraffinized, rehydrated, and subjected to antigen retrieval. After incubation in Dual

Endogenous Enzyme Block solution (Dako) for 10 min, the section was treated with primary antibody diluted by different folds with Antibody Diluent solution (Dako) at 4 °C overnight. The section was then washed three times in phosphate-buffered saline containing 0.2% Tween-20 for 5 min per washing. To detect specific staining, the section was treated for 30 min with EnVision + Dual Link System-HRP (Dako), which contained horseradish peroxidase-conjugated goat antibodies against mouse or rabbit IgG. The section was washed three times for 5 min each, and specific stains were developed with 3,3'-diaminobenzidine (Dako). Images were acquired using a Nikon camera and software. Magnification was $\times 400$ (scale bars $\sim 20 \mu\text{m}$). Percent of Ki-67⁺ cells and M30⁺ and CD31⁺ area were analyzed by ImageJ software (NIH).

Statistical Analysis. Data are presented as the mean \pm SD, as indicated in the figure legends. All comparisons were analyzed by unpaired two-tailed Student's *t*-test. A *p*-value less than 0.05 was considered to be statistically significant.

■ ASSOCIATED CONTENT

● Supporting Information

Figure S1, detailed description of reverse transcription and quantitative real-time PCR assays, and Table S1. This material is available free of charge via the Internet at <http://pubs.acs.org>.

■ AUTHOR INFORMATION

Corresponding Authors

*jcsih@usc.edu

*bogdan@usc.edu

*haiyen.zhau@cshs.org

Present Address

[§]T.-P.L.: Department of Urology, Taipei Veterans General Hospital, Taipei, Taiwan 11217, R.O.C., and Department of Urology, School of Medicine, and Shu-Tien Urological Research Center, National Yang-Ming University, Taipei, Taiwan 11217, R.O.C.

Notes

The authors declare no competing financial interest.

■ ACKNOWLEDGMENTS

This work was supported by the U.S. Department of Defense Prostate Cancer Research Program grant W81XWH-12-1-0282 (to J.C.S., B.Z.O., and H.E.Z.), the Daniel Tsai Family Fund (to J.C.S.), Boyd and Elsie Welin Professorship (to J.C.S.), NIH/National Cancer Institute grants 5P01CA098912 and R01CA122602, Board of Governors Endowed Cancer Chair and Margaret E. Early Medical Research Trust Award (to L.W.K.C.), and the University of Southern California (to B.Z.O.). We thank Bin Qian (Department of Pharmacology and Pharmaceutical Sciences, University of Southern California) and Yi-Ting Chen (Uro-Oncology Research Program, Department of Medicine, Cedars-Sinai Medical Center) for technical assistance. We also thank Dr. Ramin Dubey, Dr. Vladimir Neschadimenko, and Ms. Li Zhou (Department of Pharmacology and Pharmaceutical Sciences, University of Southern California) for help in synthesizing NMI and precursors.

■ REFERENCES

- (1) Bortolato, M.; Chen, K.; Shih, J. C. *Adv. Drug Delivery Rev.* **2008**, *60*, 1527.
- (2) Shih, J. C.; Chen, K.; Ridd, M. J. *Annu. Rev. Neurosci.* **1999**, *22*, 197.

- (3) Josson, S.; Nomura, T.; Lin, J. T.; Huang, W. C.; Wu, D.; Zhau, H. E.; Zayzafoon, M.; Weizmann, M. N.; Gururajan, M.; Chung, L. W. *Cancer Res.* **2011**, *71*, 2600.

- (4) Sung, S. Y.; Hsieh, C. L.; Law, A.; Zhau, H. E.; Pathak, S.; Multani, A. S.; Lim, S.; Coleman, I. M.; Wu, L. C.; Figg, W. D.; Dahut, W. L.; Nelson, P.; Lee, J. K.; Amin, M. B.; Lyles, R.; Johnstone, P. A.; Marshall, F. F.; Chung, L. W. *Cancer Res.* **2008**, *68*, 9996.

- (5) Wu, J. B.; Shao, C.; Li, X.; Li, Q.; Hu, P.; Shi, C.; Li, Y.; Chen, Y. T.; Yin, F.; Liao, C. P.; Stiles, B. L.; Zhau, H. E.; Shih, J. C.; Chung, L. W. *J. Clin. Invest.* **2014**, *124*, 2891.

- (6) True, L.; Coleman, I.; Hawley, S.; Huang, C. Y.; Gifford, D.; Coleman, R.; Beer, T. M.; Gelmann, E.; Datta, M.; Mostaghel, E.; Knudsen, B.; Lange, P.; Vessella, R.; Lin, D.; Hood, L.; Nelson, P. S. *Proc. Natl. Acad. Sci. U.S.A.* **2006**, *103*, 10991.

- (7) Flamand, V.; Zhao, H.; Peehl, D. M. *J. Cancer Res. Clin. Oncol.* **2010**, *136*, 1761.

- (8) Zhao, H.; Flamand, V.; Peehl, D. M. *BMC Med. Genomics* **2009**, *2*, 55.

- (9) Siegel, R.; Ma, J.; Jemal, A. *CA Cancer J. Clin.* **2014**, *64*, 9–29.

- (10) da Silva, F. C. *Curr. Opin. Urol.* **2011**, *21*, 248.

- (11) Wilkins, A.; Parker, C. *Nat. Rev. Clin. Oncol.* **2010**, *7*, 583.

- (12) Kapoor, D. A.; Zimberg, S. H.; Ohrin, L. M.; Underwood, W., 3rd; Olsson, C. A. *J. Urol.* **2011**, *186*, 860.

- (13) Wang, G. L.; Jiang, B. H.; Rue, E. A.; Semenza, G. L. *Proc. Natl. Acad. Sci. U.S.A.* **1995**, *92*, 5510.

- (14) Chandel, N. S.; Maltepe, E.; Goldwasser, E.; Mathieu, C. E.; Simon, M. C.; Schumacker, P. T. *Proc. Natl. Acad. Sci. U.S.A.* **1998**, *95*, 11715.

- (15) Kaelin, W. G., Jr.; Ratcliffe, P. J. *Mol. Cell* **2008**, *30*, 393.

- (16) Gerald, D.; Berra, E.; Frapart, Y. M.; Chan, D. A.; Giaccia, A. J.; Mansuy, D.; Pouyssegur, J.; Yaniv, M.; Mechta-Grigoriou, F. *Cell* **2004**, *118*, 781.

- (17) Lu, X.; Kang, Y. *Clin. Cancer Res.* **2010**, *16*, 5928.

- (18) De Colibus, L.; Li, M.; Binda, C.; Lustig, A.; Edmondson, D. E.; Mattevi, A. *Proc. Natl. Acad. Sci. U.S.A.* **2005**, *102*, 12684.

- (19) Luo, S.; Zhang, E.; Su, Y.; Cheng, T.; Shi, C. *Biomaterials* **2011**, *32*, 7127.

- (20) Tan, X.; Luo, S.; Wang, D.; Su, Y.; Cheng, T.; Shi, C. *Biomaterials* **2012**, *33*, 2230.

- (21) Luo, S.; Tan, X.; Qi, Q.; Guo, Q.; Ran, X.; Zhang, L.; Zhang, E.; Liang, Y.; Weng, L.; Zheng, H.; Cheng, T.; Su, Y.; Shi, C. *Biomaterials* **2013**, *34*, 2244.

- (22) Wu, J. B.; Shao, C.; Li, X.; Shi, C.; Li, Q.; Hu, P.; Chen, Y.-T.; Dou, X.; Sahu, D.; Li, W.; Harada, H.; Zhang, Y.; Wang, R.; Zhau, H. E.; Chung, L. W. *Biomaterials* **2014**, *35*, 8175.

- (23) Yang, X.; Shi, C.; Tong, R.; Qian, W.; Zhau, H. E.; Wang, R.; Zhu, G.; Cheng, J.; Yang, V. W.; Cheng, T.; Henary, M.; Streckowski, L.; Chung, L. W. *Clin. Cancer Res.* **2010**, *16*, 2833.

- (24) Gordon, R. R.; Wu, M. C.; Huang, C. Y.; Harris, W. P.; Sim, H. G.; Lucas, J. M.; Coleman, I.; Higano, C. S.; Gulati, R.; True, L. D.; Vessella, R.; Lange, P. H.; Garzotto, M.; Beer, T. M.; Nelson, P. S. *PLoS One* **2014**, *9*, e104271.

- (25) Murphy, D. L.; Lipper, S.; Slater, S.; Shiling, D. *Psychopharmacology* **1979**, *62*, 129.

- (26) Foraker, A. G. *Cancer* **1954**, *7*, 884.

- (27) Thalmann, G. N.; Anezinis, P. E.; Chang, S. M.; Zhau, H. E.; Kim, E. E.; Hopwood, V. L.; Pathak, S.; von Eschenbach, A. C.; Chung, L. W. *Cancer Res.* **1994**, *54*, 2577.

- (28) Tomayko, M. M.; Reynolds, C. P. *Cancer Chemother. Pharmacol.* **1989**, *24*, 148.

- (29) Yang, X.; Shi, C.; Tong, R.; Qian, W.; Zhau, H. E.; Wang, R.; Zhu, G.; Cheng, J.; Yang, V. W.; Cheng, T.; Henary, M.; Streckowski, L.; Chung, L. W. *Clin. Cancer Res.* **2010**, *16*, 2833.

- (30) Zhau, H. E.; Otero-Marrah, V.; Lue, H. W.; Nomura, T.; Wang, R.; Chu, G.; Liu, Z. R.; Zhou, B. P.; Huang, W. C.; Chung, L. W. *Clin. Exp. Metastasis* **2008**, *25*, 601.



Near-infrared fluorescence heptamethine carbocyanine dyes mediate imaging and targeted drug delivery for human brain tumor



Jason Boyang Wu^{a,1}, Changhong Shi^{a,b,1}, Gina Chia-Yi Chu^a, Qijin Xu^c, Yi Zhang^d,
Qinlong Li^a, John S. Yu^c, Haiyen E. Zhau^a, Leland W.K. Chung^{a,*}

^a Uro-Oncology Research Program, Department of Medicine, Cedars-Sinai Medical Center, Los Angeles, CA 90048, USA

^b Laboratory Animal Center, the Fourth Military Medical University, Xi'an, Shaanxi 710032, China

^c Department of Neurosurgery, Cedars-Sinai Medical Center, Los Angeles, CA 90048, USA

^d Biomedical Imaging Research Institute, Cedars-Sinai Medical Center, Los Angeles, CA 90048, USA

ARTICLE INFO

Article history:

Received 7 March 2015

Received in revised form

14 July 2015

Accepted 14 July 2015

Available online 16 July 2015

Keywords:

Blood brain barrier

Brain tumor

Drug delivery

Heptamethine carbocyanine

Hypoxia

Near-infrared fluorescence dye

ABSTRACT

Brain tumors and brain metastases are among the deadliest malignancies of all human cancers, largely due to the cellular blood–brain and blood–tumor barriers that limit the delivery of imaging and therapeutic agents from the systemic circulation to tumors. Thus, improved strategies for brain tumor visualization and targeted treatment are critically needed. Here we identified and synthesized a group of near-infrared fluorescence (NIRF) heptamethine carbocyanine dyes and derivative NIRF dye–drug conjugates for effective imaging and therapeutic targeting of brain tumors of either primary or metastatic origin in mice, which is mechanistically mediated by tumor hypoxia and organic anion-transporting polypeptide genes. We also demonstrate that these dyes, when conjugated to chemotherapeutic agents such as gemcitabine, significantly restricted the growth of both intracranial glioma xenografts and prostate tumor brain metastases and prolonged survival in mice. These results show promise in the application of NIRF dyes as novel theranostic agents for the detection and treatment of brain tumors.

© 2015 Elsevier Ltd. All rights reserved.

1. Introduction

Brain tumors and tumor brain metastases are extremely deadly diseases with poor prognosis and short patient survival. Due to high resistance to chemotherapy and radiotherapy, early surgical intervention after tumor detection by imaging is the standard first-line treatment for most types of brain tumors [1,2]. The effectiveness of current diagnostics, including computed tomography (CT), magnetic resonance imaging (MRI) and ¹⁸F-fluorodeoxyglucose positron emission tomography (FDG-PET) [3,4], is limited by insufficient specificity and sensitivity, due in part to the background tissue autofluorescence, tissue metabolism, and limited resolution and depth of signal penetration [5,6]. These limitations may result in significant errors when patients are subjected to imaging for tumor diagnosis, prognosis, and follow-up of therapeutic responses and recurrence. Alternative diagnostic approaches using

multimodality optical- and nuclear-imaging-based techniques for the detection of brain tumors and tumor metastatic deposits in the brain are needed.

One central challenge of brain tumor detection and therapy is to deliver diagnostic and therapeutic agents effectively to the tumor core and migratory cells in the infiltration zone [7]. The blood–brain barrier (BBB) and the blood–tumor barrier (BTB) between brain tumor cells and microvessels are major obstacles to the delivery of most agents to tumor tissues from the systemic circulation [7,8]. Thus, chemotherapy has been of limited benefit for brain tumor patients, due in large part to the poor penetration of drugs through these barriers and the undesired side effects caused by non-selective drug accumulation in healthy tissues [9,10]. To overcome these barriers, a number of noninvasive targeted approaches, such as peptide-based, nanoparticle-coated delivery platforms [11,12], have been recently developed as a potential way to deliver targeted agents to brain tumors.

Near-infrared fluorescence (NIRF) imaging agents have great potential for noninvasive tumor imaging [13]. NIRF agents can potentially increase the sensitivity and specificity of cancer diagnosis because NIRF agents have low background autofluorescence,

* Corresponding author. Uro-Oncology Research Program, Cedars-Sinai Medical Center, 8750 Beverly Blvd., Atrium 103, Los Angeles, CA 90048, USA.

E-mail address: Leland.Chung@cshs.org (L.W.K. Chung).

¹ These authors contributed equally to this work.

tissue absorbance and scatter at NIR wavelengths (700–1000 nm) [14]. These agents can also undergo a number of chemical modifications including conjugation with effective therapeutic drugs to target cancer cells at different progressive stages [13,14]. We previously identified and synthesized a unique group of NIRF heptamethine carbocyanines as dual imaging and targeting agents and demonstrated two prototypic heptamethine carbocyanine dyes including IR-783 and MHI-148. These NIRF and derivative agents show preferential uptake in tumor cells but not normal cells as demonstrated in a variety of cancer cell lines, tumor xenografts, spontaneous mouse tumors in transgenic animals and human tumor samples [15–18], mediated by tumor hypoxia and activated hypoxia-inducible factor 1 α (HIF1 α)/organic anion-transporting polypeptides (OATPs) signaling axis [17,19]. However, whether these dyes possess the potential to penetrate the BBB/BBB and target brain tumors had not been evaluated. In this study, using a number of *in vitro* and *in vivo* brain tumor models, we investigated the mechanisms and targeting potential of this group of NIRF agents for primary and metastatic brain tumors. We also evaluated the ability of these dyes as carriers to deliver dye-drug conjugates to brain tumors and the therapeutic efficacy of these conjugates in mouse models.

2. Materials and methods

2.1. Cell culture and reagents

Human glioblastoma cell lines U87, U251 and T98G, and normal human embryonic kidney cell line HEK293 were purchased from American Type Culture Collection (ATCC, Manassas, VA). Human prostate adenocarcinoma cell line CW22Rv1 was kindly provided by Dr. Michael Freeman (Cedars-Sinai Medical Center, Los Angeles). These cells were cultured in Dulbecco's modified Eagle's medium (DMEM; Life Technologies, Grand Island, NY) or RPMI 1640 medium (Life Technologies) supplemented with 10% FBS (Biowest, Kansas City, MO) and 1% penicillin/streptomycin (Life Technologies). Human brain cancer stem-like cells (CSCs) isolated from pituitary adenoma patients were prepared as described previously [20] and cultured in a DMEM/F12 (1:1) medium (Life Technologies) containing B27 (1 \times) supplement (Life Technologies), 1% penicillin/streptomycin, fungizone (250 ng/ml; Life Technologies), EGF (20 ng/ml; Peprotech, Rocky Hills, NJ) and bFGF (20 ng/ml; Peprotech). For hypoxia treatment, cells were grown in a hypoxic chamber (1% O₂, 5% CO₂). Lentiviral particles expressing both luciferase and GFP were purchased from GenTarget (San Diego, CA). Bromosulphophthalein (BSP), cobalt chloride (CoCl₂) and dimethyl-oxalylglycine (DMOG) were purchased from Sigma–Aldrich (St. Louis, MO). D-Luciferin sodium salt was purchased from Gold Biotechnology (St. Louis, MO). The heptamethine carbocyanine dye IR-783 was prepared and purified as described previously [15]. Gemcitabine was purchased from Ark Pharm, Inc. (Libertyville, IL). All other chemicals used in IR-783-gemcitabine (NIRG) synthesis were purchased from Sigma Aldrich. NIRG was synthesized in house with detailed synthesis procedures described below.

2.2. IR-783-gemcitabine (NIRG) synthesis

The preparation of the compound 4-(2-((E)-2-((E)-2-chloro-3-((phenylamino)methylene)-cyclohex-1-en-1-yl)vinylyl)-3,3-dimethyl-3H-indol-1-ium-1-yl)butane-1-sulfonate 3: To the mixture of **1a** (2 g, 6.78 mmol) and crude **2** (3 g, 8.36 mmol) in EtOH (25 ml) was added CH₃COONa (0.56 g, 6.78 mmol), the resulted mixture was heated to reflux for 3 h. The reaction mixture was concentrated and the residue was recrystallized from methanol/ether to afford desired product **3** (2 g, yield 56%). HRMS (ESI-TOF),

m/z 525.1979 (M+H)⁺ (C₂₉H₃₄ClN₂O₃S requires 525.1979).

The preparation of the compound cyanine dye 4: To the mixture of **1b** (0.5 g, 1.4 mmol) and crude **3** (1 g, 1.9 mmol) in EtOH (8 ml) was added CH₃COONa (128 mg, 1.5 mmol), the resulted reaction was heated to reflux for 3 h. The reaction mixture was concentrated and the residue was purified with C18-RP silica chromatography elution with methanol–water to afford desired product **4** (0.8 g, yield 73%). ¹H NMR (DMSO-d₆, 400 MHz) HRMS (ESI-TOF), 705.3122 (M+H)⁺ (C₄₀H₅₀ClN₂O₅S requires 705.3129).

The preparation of the compound dye-gemcitabine conjugate 5: The mixture of **4** (761 mg, 1.1 mmol) 1-ethyl-3-(3-dimethylaminopropyl) carbodiimidehydrochloride (310 mg, 1.6 mmol) and 1-hydroxy-7-azabenzotriazole (175 mg, 1.3 mmol) were dissolved in 5.0 ml DMF solution. The mixture was stirred for 15 min, then gemcitabine (340 mg, 1.3 mmol) was added and stirred for additional 15 h. Ethyl ether (50 ml) was added. The precipitate collected and purified by C18-RP silica chromatography was eluted with methanol–water to afford desired product 509 mg (41%). HRMS (ESI-TOF), *m/z* 948.3578 (M–H)[–] (C₄₉H₅₇ClF₂N₅O₈S requires 948.3585).

ESI-TOF-MS analysis was performed on compounds at the UCLA Mass Spectrometry Laboratory using a Waters LCT Premier Mass Spectrometer. Protein nuclear magnetic resonance (¹H NMR) spectra were recorded on a Bruker AV400 FT NMR Spectrometer (400 MHz).

2.3. Tumor xenograft studies

All animal studies received prior approval from the IACUC of Cedars-Sinai Medical Center (CSMC) and were conducted in compliance with its recommendations. Male 4- to 6-week-old athymic nude mice and SCID mice were purchased from Taconic (Oxnard, CA), housed in the animal research facility at CSMC, and fed a normal chow diet. For subcutaneous xenograft studies, 1, 3 or 9 \times 10⁶ of luc-labeled U87 in 50% Matrigel (BD Biosciences, San Jose, CA) were injected subcutaneously into nude mice. Each mouse was injected on the right flank only. Tumor size was measured by caliper. For intracranial xenograft studies, SCID or nude mice were anesthetized by intraperitoneal injection of ketamine and xylazine, and stereotactically implanted with U87 or pituitary adenoma CSC cells (10,000 cells per mouse), respectively, in the right forebrains. At the end of the studies, tumor-bearing whole mouse brains were excised and fixed in 10% formaldehyde and embedded in paraffin for subsequent histological analysis. For intracardiac xenograft studies, 1 \times 10⁶ luc-tagged CW22Rv1 cells were injected into the left cardiac ventricle of anesthetized SCID mice as described previously [21]. Development of brain metastasis was monitored by BLI and MRI.

2.4. Bioluminescence imaging

Bioluminescence imaging of luciferase-tagged U87 or CW22Rv1 tumor xenografts either *in vivo* or *ex vivo* after mice received D-luciferin (3 mg/mouse via intraperitoneal delivery) was performed on a Xenogen IVIS Spectrum Imaging System (PerkinElmer, Waltham, MA). Analysis was performed with Living Image software (PerkinElmer) by measurement of photon flux in the tumor region of interest in mice. Data was normalized to the background signal.

2.5. Magnetic resonance imaging

MRI experiments were performed on a 9.4T (94/20) Bruker BioSpec MRI scanner (Bruker, Billerica, MA) using 4 channel ¹H mouse brain receiver coil (Bruker). The tumor-bearing mouse brain was excised and placed in 10% formaldehyde for at least 24 h then

suspended in Fomblin[®] YLVAC (Sigma–Aldrich) for imaging. T1 weighted 0.5 mm axial slices, encompassing the whole brain (50 slices), were acquired with a fast spin echo sequence to delineate anatomic details with an in-plane resolution of 92 μm (field of view, 18 mm \times 12 mm; TE/TR, 8 ms/900 ms, 196 \times 128 matrix, 6 averages). MRI data were processed and analyzed using ParaVision software (Bruker).

2.6. Analysis of brain tumor imaging and targeting by NIRF dye and NIRG in cultured brain tumor cells and xenografts

For cultured brain and prostate tumor cells, after exposure to different treatments when necessary, cells were incubated with IR-783 at a concentration of 20 μM at 37 °C for 30 min and washed twice with PBS to remove excess dye. Cells were either fixed in 10% formaldehyde when cultured alone or incubated in PBS when present in co-culture, and subjected to analysis of NIRF dye uptake by NIRF microscopy (Olympus 1x71; Olympus, Melville, NY) using a 75 W Xenon lamp and an indo-cyanine green filter cube (excitation/emission: 750–800/820–860 nm) as described previously [15]. Cellular NIRF intensity was quantitated by ImageJ software (NIH). For tumor xenograft models, mice bearing xenograft tumors were injected intraperitoneally with IR-783 or NIRG at a dose of 50 nmol/mouse assuming the average body weight of mice is 20 g. Whole-body or organ-specific optical imaging was taken at 1 h or/and 24 h using an IVIS Lumina XR Imaging System (PerkinElmer, Waltham, MA) equipped with fluorescent filter sets (excitation/emission, 783/840 nm), with automatic subtraction of background fluorescence from the total dye uptake in tumors during the image acquisition, as described previously [15,22].

2.7. Biochemical analyses of brain tumor cells and tumor xenografts

Total RNA from cultured cells and formalin-fixed, paraffin-embedded tissue sections was isolated using the RNeasy Mini Kit and the RNeasy FFPE Kit (Qiagen), respectively; and reverse-transcribed to cDNA by M-MLV reverse transcriptase (Promega) following the manufacturer's instructions. qPCR was conducted using SYBR Green PCR Master Mix and run with Applied Biosystems 7500 Fast Real-Time PCR System (Applied Biosystems). PCR conditions include an initial denaturation step of 3 min at 95 °C, followed by 40 cycles of PCR consisting of 30 s at 95 °C, 30 s at 60 °C, and 30 s at 72 °C. The PCR data were analyzed by $2^{-\Delta\Delta\text{CT}}$ methods [23]. Details on primers used for qPCR are provided in the Supplementary Table 1.

2.8. Microarray data sets

Two brain cancer DNA microarray data sets, Bredel Brain 2 [24] and Sun Brain [25], were downloaded directly from the Oncomine database by licensed access. Microarray data of the Bredel Brain 2 (GSE2223) and Sun Brain (GSE4290) data set are also publicly available in Gene Expression Omnibus.

2.9. Cell proliferation assays

U87 cells were seeded at 3000/well in a 96-well plate and treated with either gemcitabine (200 nM) or IR-783-gemcitabine (200 nM) for 4 consecutive days. PBS was used as a vehicle. Cells were fixed and stained with crystal violet, and the OD value at the wavelength of 595 nm was read by a microplate reader on a daily basis.

2.10. Tumor xenograft therapeutic studies

For determining the therapeutic effect of NIRG on brain tumor or metastasis, mice bearing either intracranial U87 tumors or CW22Rv1 prostate tumor brain metastases as confirmed by BLI were randomly assigned to 2 groups. For U87 tumor model, 2 weeks after tumor cell inoculation, mice were injected intraperitoneally with either saline or NIRG (10 mg/kg) twice a week for 4–5 weeks. For CW22Rv1 prostate tumor brain metastatic model, after confirming the presence of tumor metastases in mouse brains, mice were injected intraperitoneally with either saline or NIRG (10 mg/kg) twice a week for 5 weeks. Tumor growth and development of brain metastasis were monitored by BLI.

2.11. Statistical analysis

Data were presented as the mean \pm SEM as indicated in the figure legends. Comparisons between Kaplan–Meier curves were performed using the long-rank test. All other comparisons were analyzed by unpaired 2-tailed Student's *t* test. A *p* value less than 0.05 was considered as statistically significant.

3. Results

3.1. Preferential accumulation of NIRF dye in brain tumor cells

Glioblastoma, the most common and aggressive malignant primary brain tumor arising from astrocytes [2], was chosen as a model to assess the ability of NIRF dye uptake by brain tumor cells and xenografts. To determine whether the NIRF dye specifically targets brain tumor cells but not normal cells, we established an *in vitro* co-culture model in which human glioblastoma U87 cells were engineered dually with green fluorescence protein (GFP) and luciferase (*luc*) and cultured together with normal human embryonic kidney HEK293 cells in a 2-dimensional culture on a plastic surface. Lentiviral infection-mediated labeling of U87 cells with GFP followed by puromycin selection ensured a 100% integrated rate of GFP in stable U87 cells, which was confirmed by fluorescence microscopy (Fig. S1). To examine the dye uptake, the co-culture was incubated with IR-783, a NIRF heptamethine carbocyanine dye we identified previously (chemical structure shown in Fig. 1A), and then subjected to fluorescence microscopy. The NIRF signals were exclusively observed in GFP⁺ U87 cells and not in the other GFP⁻ HEK293 cells (Fig. 1B), suggesting the preferential uptake and retention of IR-783 in brain tumor cells but not normal cells under the same culture conditions. We also examined the dye uptake in this co-culture model in a quantitative manner. A doubling series number of *luc*-tagged U87 cells were incubated with a fixed number of HEK293 cells, producing different cell number ratios (U87/HEK293 1:8, 1:4, 1:2 and 1:1). These co-cultures were exposed to IR-783 and subjected in parallel to luminescence and NIRF imaging, demonstrating a significant linear correlation ($R^2 = 0.9958$) between luminescence and NIRF signal intensities (Fig. 1C and D), which reinforces the finding of a preferential dye uptake by brain tumor cells relative to normal cells. These results in aggregate confirm the tumor-specific targeting ability of IR-783 dye in cultured brain tumor cells.

3.2. NIRF dye uptake correlates with brain tumor xenograft growth

To determine whether the preferential uptake of IR-783 by brain tumor cells *in vitro* can be recapitulated *in vivo*, we implanted different numbers (1×10^6 , 3×10^6 and 9×10^6) of *luc*-tagged U87 cells subcutaneously into nude mice to establish tumor xenografts. When tumors formed at different sizes as expected, we

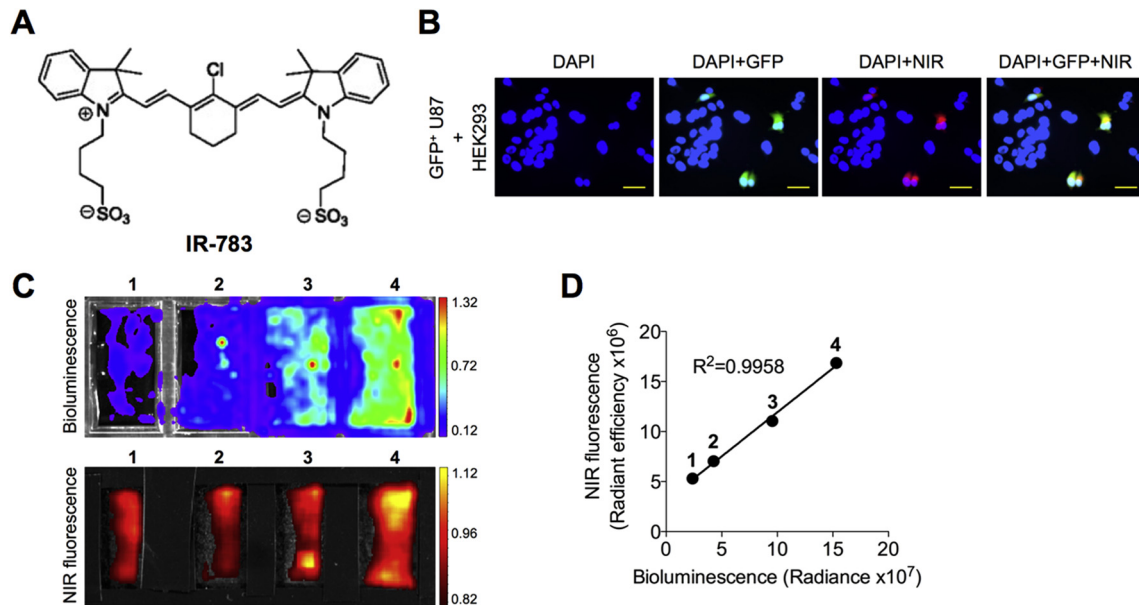


Fig. 1. Uptake of NIRF heptamethine carbocyanine IR-783 dye by human glioblastoma cells. (A) Chemical structure of IR-783 dye. (B) Uptake of IR-783 dye (20 μM , 30 min) by GFP-tagged human glioblastoma U87 cells co-cultured with normal human HEK293 cells. Nuclei from both U87 and HEK293 cells were stained by DAPI. Scale bars represent 50 μm . (C) Uptake of luc-tagged U87 cells co-cultured with HEK293 cells at different ratios (U87/HEK293: 1, 1:8; 2, 1:4; 3, 1:2; and 4, 1:1) determined by both luminescence and NIRF imaging. (D) Correlation of luminescence and NIRF signal intensity in (C).

demonstrated by whole-body NIRF imaging that IR-783 was specifically taken up by xenograft tumors in mice. This was further supported by the co-registered bioluminescence (BLI) and NIRF

signals in tumors, with a positive correlation ($R^2 = 0.9980$) of signal intensity between the two imaging modalities (Fig. 2B). Moreover, a significant correlation ($R^2 = 0.9811$) between tumor NIRF signal

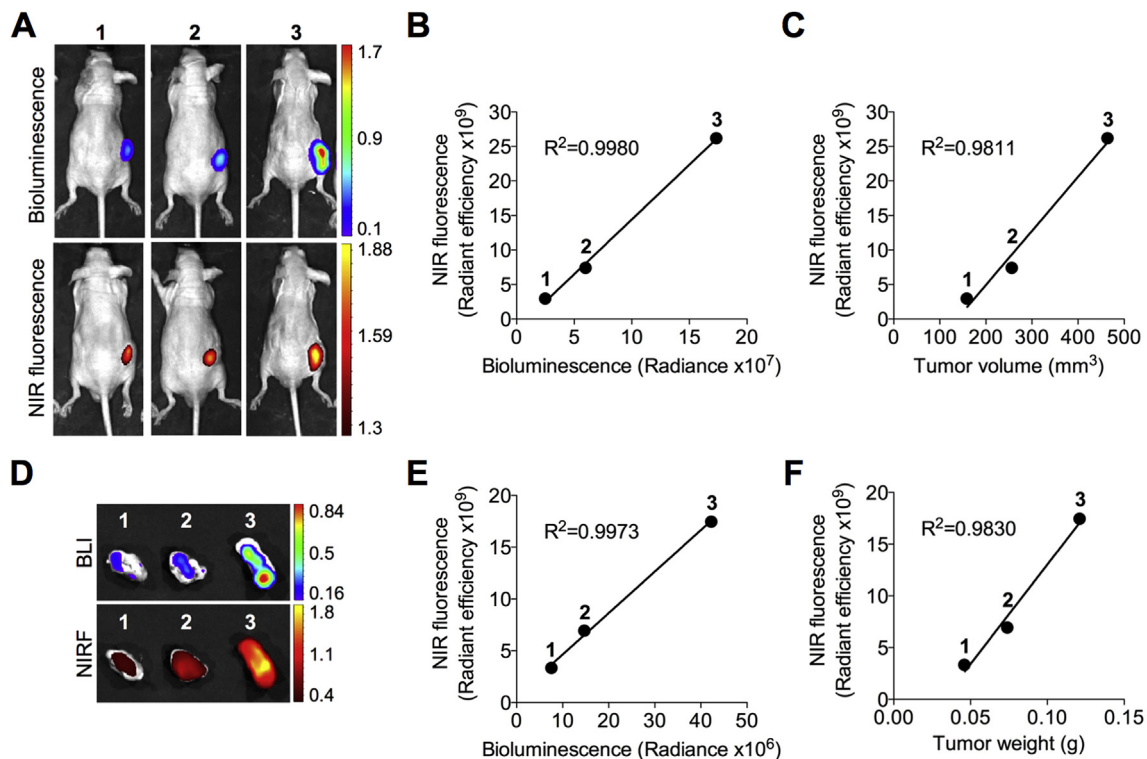


Fig. 2. Preferential uptake and retention of IR-783 dye in subcutaneous U87 glioblastoma xenografts. (A) Uptake of IR-783 dye (50 nmol/mouse, i.p.) by subcutaneous luc-tagged U87 glioblastoma xenografts of different sizes determined by *in vivo* BLI and NIRF imaging (cell number initially implanted to form xenograft tumors: 1, 1×10^6 ; 2, 3×10^6 ; and 3, 9×10^6). (B, C) Correlation of tumor NIRF signal intensity with either BLI signal intensity (B) or tumor volume determined by caliper (C) in (A). (D) Uptake of IR-783 dye by U87 xenograft tumors dissected from (A) and determined by *ex vivo* BLI and NIRF imaging. (E, F) Correlation of tumor NIRF signal intensity with either BLI signal intensity (E) or tumor weight (F) in (D). $n = 3$ for each experimental group. The mean was used to plot the correlation curves.

intensity and tumor volume was established (Fig. 2C). Immediately after *in vivo* imaging, tumors were dissected and analyzed *ex vivo* by both BLI and NIRF imaging simultaneously (Fig. 2D). Similarly, we showed that tumor NIRF signal intensity was well correlated with both tumor BLI intensity ($R^2 = 0.9973$) and tumor weight ($R^2 = 0.9830$) (Fig. 2E and F). In addition, we observed marginal dye uptake by other normal mouse organs, such as the lung, heart, spleen, kidney and liver, consistent with our previous results [15,22]. Together, these results indicate the ability of IR-783 to target specifically brain tumor in a subcutaneous model and more importantly to quantitatively estimate tumor burden in mice.

3.3. NIRF dye penetrates the BBB/BTB and targets intracranial brain tumor xenografts

A unique feature of brain tumors is the presence of tight barriers, termed BBB and BTB, which protect cancer cells from exposure to most chemical agents in circulation [8]. To assess whether IR-783 can target brain tumors at the primary site, we generated an intracranial brain tumor xenograft by stereotactically implanting U87 cells into the right hemisphere of immunocompromised mice. Once the intracranial tumor xenograft was established, mice were given IR-783 through the intraperitoneal route to allow the delivery of this NIRF dye by systemic circulation. At 1 h and 24 h after the dye injection, mice were subjected to NIRF imaging. The results showed that NIRF signals localized exclusively in the brain region in mice in a time-dependent manner (Fig. 3A, left panel), indicating that IR-783 was capable of passing through the BBB/BTB and entering the tumor core space. In contrast, we did not observe the accumulation of IR-783 dye in the sham-operated normal brain that did not harbor tumor by *in vivo* imaging (Fig. 3A, right panel). A signal-to-background ratio (tumor/no tumor) ranging from 2.9 to 5.6 was observed at different time points (Fig. 3B). We also assessed the brain tumor-targeting ability of IR-783 dye by *ex vivo* imaging of an alignment of individual mouse organs, demonstrating the

presence of NIRF signals only in the brain and not in other selected major organs including the lung, heart, spleen, kidney and liver (Fig. 3C). Quantitative analysis of the organ-specific accumulation of dye intensity showed an average of 81.6-fold higher NIRF intensity in the brain than the average intensity in other organs (Fig. 3D).

To better mimic the clinical situation, we implanted human pituitary adenoma stem-like cells prepared directly from patient samples into the brains of nude mice. As demonstrated by both *in vivo* and *ex vivo* NIRF imaging (Fig. 3E and F), IR-783 was taken up specifically by the tumor-bearing brains in mice, which further showed up to 82.6-fold higher NIRF signal intensity in the brain compared to that in other selected organs (Fig. 3G). In line with these data, we conclude that NIRF dye can be taken up by brain tumors after effectively penetrating the BBB/BTB.

3.4. Hypoxia and organic anion-transporting polypeptide (OATP) genes mediate NIRF dye uptake into brain tumor cells

We recently showed that hypoxia mediates the uptake of NIRF dye by cancer cells via activation of HIF1 α /OATP signaling in a series of genitourinary cancer models [22]. This provides insights into brain tumor, where hypoxia is also frequently observed due to inadequate vascular supply or inefficient microcirculation in vascularized tumor regions [26]. OATPs could also mediate the uptake of NIRF dyes including both IR-783 and MHI-148 [22]. OATPs represent a superfamily of solute carrier transporter, including 11 known human OATPs classified into 6 families and subfamilies on the basis of their amino acid sequence homologies [27]. Aberrant expression of OATPs has been reported in a spectrum of cancer types, including brain cancer [28,29]. OATPs facilitate the transport of a number of substances into cells, including organic acids, drugs and hormones, in a highly substrate- and pathophysiologic-including cancer-dependent manner [27]. Notably, select OATPs including OATP1A2 and OATP2B1 are highly expressed in

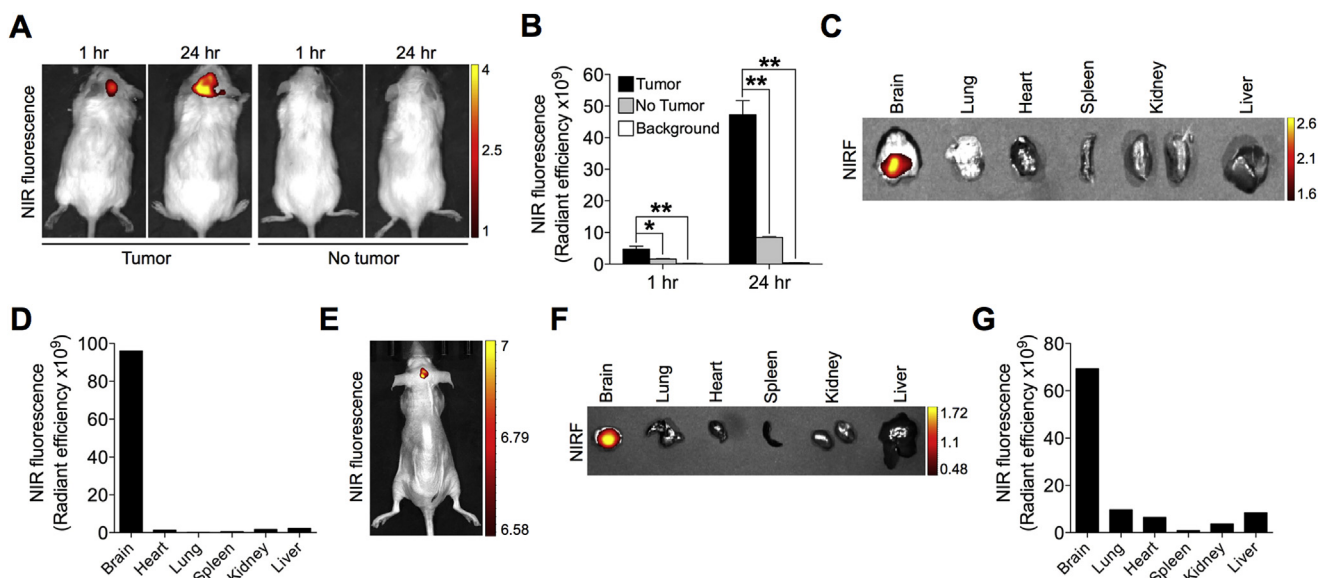


Fig. 3. Preferential uptake and retention of IR-783 dye in intracranial brain tumor xenografts. (A) Uptake of IR-783 dye (50 nmol/mouse, i.p.) by intracranial U87 tumor xenograft as determined by *in vivo* NIRF imaging at 1 h and 24 h time points after dye injection. Representative images are shown. (B) Quantitative analysis of uptake intensity in (A) ($n = 3$, mean \pm SEM). * $p < 0.05$, ** $p < 0.01$. (C) Uptake and retention of IR-783 dye by representative mouse brain and other indicated organs dissected from (A), as determined by *ex vivo* NIRF imaging 24 h after dye injection. (D) Quantitative analysis of NIRF signal intensity in (C). (E, F) Uptake of IR-783 dye (50 nmol/mouse, i.p.) by intracranial tumor developed originally from pituitary adenoma patient samples 24 h after dye injection, which was further removed and subjected to *ex vivo* NIRF imaging in parallel with other organs (F). (G) Quantitative analysis of organ-specific NIRF signal intensity in (F).

physiological barriers such as the BBB [30], and a significantly lower blood-to-brain transport of several agents was observed in *Oatp1a4* (corresponding to *OATP1A2* in humans) knockout mice compared to wild-type mice [31]. These studies in aggregate suggest a potential role of these OATPs in depositing contrast agents and drugs into brain tumors.

Given the common features, including hypoxia and aberrant expression of OATPs, shared by brain tumors and other types of tumors, we speculated whether brain tumor cells use similar mechanisms to take up and retain NIRF dyes. To test this, three human glioblastoma cell lines, U87, U251 and T98G, were exposed to IR-783 under hypoxic conditions (1% O₂). As shown in Figs. 4A, B and S2, there were significant increases in dye uptake varying from 41% to 149% after hypoxic stimuli in all three cell lines. Moreover, cells pre-treated with bromosulphophthalein (BSP), a potent competitive inhibitor of OATPs, reduced dye uptake by up to 64% in all cell lines (Figs. 4A, B and S2). These data collectively suggest that hypoxia and OATPs mediate the uptake of NIRF dye in brain tumor cells.

Next, we examined the expression levels of select brain-related OATPs in U87 intracranial tumor xenograft samples. As shown in Fig. S3A, higher mRNA expression of 3 OATPs, including *OATP1A2*, *OATP1C1*, and *OATP2B1*, was found in U87 tumor than nearby normal mouse brain tissue, which is supported by the observations of increased *OATP2B1* expression in glioblastoma samples compared with normal brain tissues in 2 brain cancer clinical data sets (Fig. S3B, Bredel Brain 2 and Sun Brain). To further determine if the hypoxia upregulation of OATP expression as we reported previously could be recapitulated in the scenario of brain tumor [19], we treated U87 cells with cobalt chloride or DMOG, two hypoxia-mimetic agents stabilizing the expression of HIF1 α , a master regulator of hypoxia signaling [19,32,33]. Induction of hypoxia, evidenced by increased expression of vascular endothelial growth factor A (*VEGFA*) and glucose transporter 1 (*Glut1*), two HIF1 α -target genes, activated the expression of select brain-expressing OATPs, including *OATP1A2*, *OATP1C1*, and *OATP2B1*, in U87 cells under both treatments (Fig. S3C). Furthermore, we demonstrated a significant correlation between HIF1 α and *OATP2B1* mRNA expression in the Sun Brain data set (Fig. S3D, $p = 0003$ and $p < 0.0001$ for Pearson and Spearman correlation, respectively). These results reinforce OATPs' function to facilitate the delivery of NIRF dyes across the BBB/BTB via an increased OATPs gradient across brain tumor cell membranes for dye uptake by brain tumors.

3.5. NIRF dye as a drug delivery carrier for therapeutically targeting brain tumors and brain metastases

Given the ability of IR-783 to target brain tumors specifically in different intracranial models (Fig. 3), we next investigated the potential of IR-783 as a drug delivery carrier covalently linked to a drug payload to serve as a theranostic agent for both imaging and antitumor capabilities. To develop IR-783 as a platform for drug delivery, we synthesized and characterized a modified compound that conjugates gemcitabine with a derivative of IR-783 backbone with one sulfonate moiety converted to carboxylate (IR-783-gemcitabine, abbreviated as NIRG) (Figs. 5A and S4), and tested its activity against the growth of brain tumor xenografts and prostate tumor metastasized to mouse brain. This conjugation with appropriate modification of one side chain of the heptamethine carbocyanine dye does not change the electronic properties of the aromatic backbones in order to maintain the fluorescence and tumor-specific targeting properties. On the other hand, conjugation of gemcitabine at the 4-(N)-amino group in the pyrimidine ring via amide bond has emerged as one of the most versatile methods for producing gemcitabine prodrugs without compromising drug activity [34,35]. Gemcitabine is a deoxycytidine analog that has shown a wide range of antitumor activity against the proliferation of different solid tumors, such as lung cancer, pancreatic cancer and breast cancer [36–38], by directly interfering with DNA replication to arrest tumor growth [39,40]. Gemcitabine at non-cytotoxic concentrations enables brain tumor radiosensitization [41]. However, it shows only modest potency to penetrate the BBB, resulting in limited therapeutic benefits for intracranial tumors [42]. We first characterized the fluorescence-emitting and cell-killing functions of NIRG. In parallel to IR-783, U87 cells retaining NIRG demonstrated strong NIRF signals (Fig. S5A, left panel), indicating the intact property of the carbocyanine dye to emit fluorescent photons for imaging. NIRG was also observed to inhibit the proliferation of U87 cells when compared to that of the vehicle-treated group (Fig. S5B), indicating its cytotoxic effect through the functional group of drug payload, gemcitabine. We next determined the uptake of NIRG by intracranial U87 tumors in mice. As shown by whole-body NIRF imaging (Fig. 5B), the conjugate was able to penetrate the BBB/BTB and was taken up specifically by tumor-bearing brains in mice with a time-dependent increase in signal intensity (1 h vs. 24 h), with signal-to-background ratios (tumor/no tumor) ranging from 3.5 to 4.2 at different time points (Fig. 5C). *Ex vivo* NIRF imaging confirmed significantly enhanced retention of NIRG in mouse brain relative to other organs with an increase up to

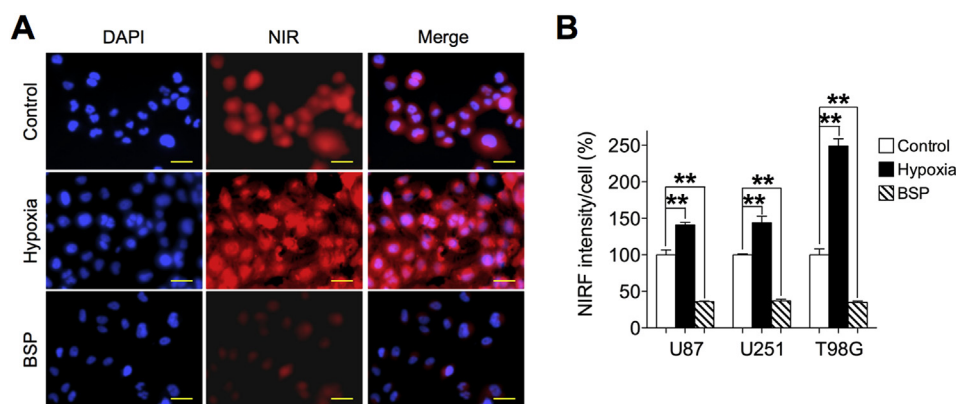


Fig. 4. Hypoxia and OATP genes mediated the uptake of IR-783 dye by human glioblastoma cells. (A) Uptake of IR-783 dye (20 μ M, 30 min) by U87 cells under pre-treatment with either hypoxia (1% O₂, 1 h) or bromsulphophthalein (BSP) (250 μ M, 1 h). Scale bars represent 50 μ m. (B) Quantitative analysis of NIRF signal intensity in U87, U251 and T98G cells. Intensity in control cells under normoxia and without treatment was set as 100% ($n = 5$, mean \pm SEM). ** $p < 0.01$.

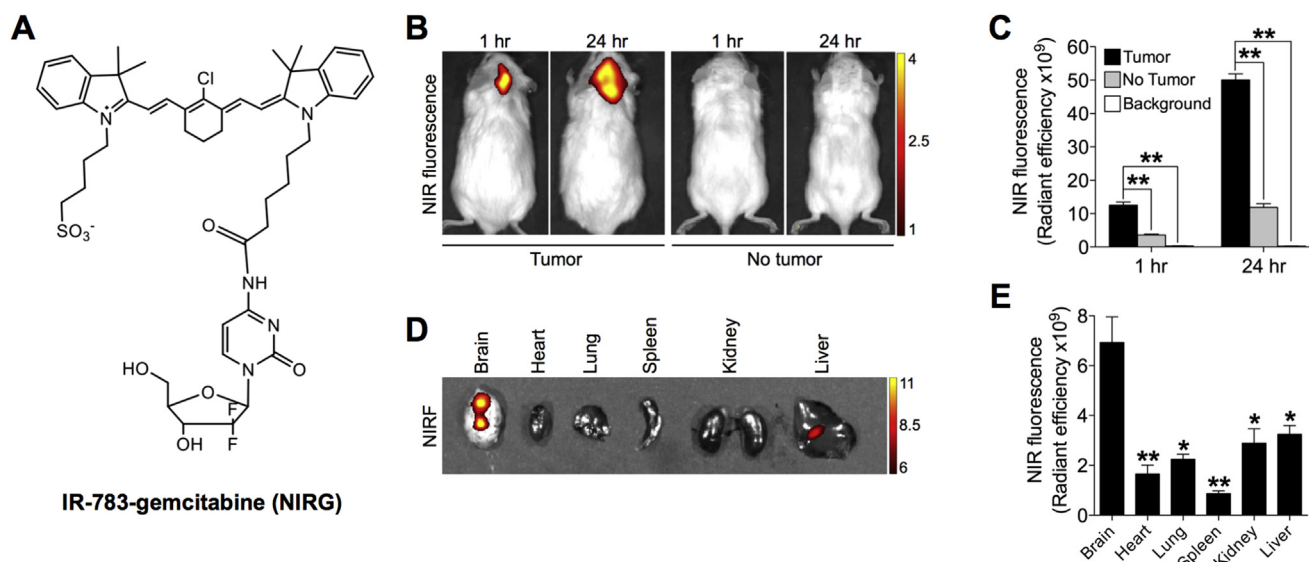


Fig. 5. Uptake and retention of IR-783-gemcitabine dye-drug conjugate (NIRG) in intracranial U87 tumor xenografts. (A) Chemical structure of NIRG. (B) Uptake of NIRG (50 nmol/mouse, i.p.) by intracranial U87 tumor xenograft as determined by *in vivo* NIRF imaging at 1 h and 24 h time points after dye injection. Representative images are shown. (C) Quantitative analysis of uptake intensity in (A) ($n = 3$, mean \pm SEM). $^{**}p < 0.01$. (D) Uptake and retention of NIRG by mouse brain and other indicated organs dissected from (B), as determined by *ex vivo* NIRF imaging 24 h after dye injection. (E) Quantitative analysis of organ-specific NIRF signal intensity in (D). ($n = 3$, mean \pm SEM). $^{*}p < 0.05$, $^{**}p < 0.01$ as compared to brain.

7.9-fold in signal intensity (Fig. 5D and E). Importantly, NIRG treatment significantly reduced the growth of intracranial U87 tumors in mice without affecting body weights of mice as compared to the control group (Fig. S5C and D), which suggests that NIRG has utility as an effective dual imaging and therapeutic agent for brain tumor.

In addition to the primary brain tumor, brain metastases can be developed by prostate, breast and lung cancers. Though brain is not as frequent a metastatic site as other distant organs, such as the skeleton, lethality from brain metastases occur frequently due in part to the lack of effective treatment strategies [43,44]. To test the potential of NIRG for targeting metastatic brain lesions, we first generated an intracardiac tumor xenograft model in immunodeficient mice by injecting a luc-tagged CW22Rv1 human prostate cancer cell line that is known to retain NIRG *in vitro* (Fig. S5A, right panel), as a model for the study of NIRG as a theranostic agent for prostate cancer brain metastases [45]. Mice that developed brain metastases after inoculation was confirmed by BLI received NIRG at 10 mg/kg intraperitoneally and were then subjected to dual modalities of BLI and NIRF imaging. Both *in vivo* and *ex vivo* imaging analyses showed co-registered BLI and NIRF signals accumulating specifically in the brain but not in other organs in mice (Fig. 6A and B), with a brain-to-kidney signal ratio of 102.5 and 30.6 for BLI and NIRF imaging, respectively (Fig. 6C). The brain lesions were confirmed by MRI (Fig. 6D) and H&E stain (Fig. 6E). Our results further demonstrated significantly improved survival in mice receiving NIRG for 5 consecutive weeks as compared to saline-treated control mice (Fig. S5E). These data in aggregate establish the potential use of NIRF dyes for guiding the targeted delivery of therapeutic drugs to brain tumors and brain metastases for effective therapeutic intervention.

4. Discussion

Brain tumors are one of the most deadly tumors in both adults and children [1,2]. Glioblastoma, the most common malignant primary brain tumor in adults, is the second cause of cancer death in adults less than 35 years of age and shows a survival rate of less

than 10% after diagnosis [46,47]. Despite surgical and medical advances achieved in recent years, the prognosis for brain tumor patients still remains poor. These dismal facts underscore the importance of pursuing alternative solutions for improved brain tumor diagnosis and therapy. In addition, since there are currently a plethora of different imaging techniques available, multimodality approaches are attractive by offering companion diagnostics while subjecting the patients to imaging-guided therapy. This was illustrated by recent studies using triple-modality MRI-photoacoustic imaging-Raman imaging nanoparticles for more accurate delineation of brain tumor margins for surgical resection compared to a single imaging modality [48].

In this study, we demonstrated that a group of NIRF heptamethine carbocyanine dyes, IR-783 dye and its conjugate, NIRG, provided highly effective tools for noninvasive brain tumor imaging and targeting. In contrast to conventional dyes in cancer imaging which require chemical conjugation of the imaging probes with appropriate tumor-specific ligands, such as chemical substrates, aptamers, growth factors or antibodies that recognize cell surface receptors in experimental mouse models [49–51], the uptake of NIRF dyes is dependent upon tumor hypoxia and the intrinsic expression of OATPs so that their entry into tumor cells does not require chemical conjugation [19]. These attractive features of NIRF dyes have distinct advantages to allow simple and straightforward detection of brain tumors and brain metastases by imaging agents with smaller sizes compared to other dyes where large molecules resulting from chemical conjugation often compromise their ability to penetrate the BBB/BTB [9]. We showed the preferential uptake of IR-783 by brain tumor cells and intracranial tumor xenografts in mice (Figs. 1 and 3). We also showed a significant correlation between tumor NIRF signal intensity and brain tumor burden in a subcutaneous tumor growth model (Fig. 2), indicating the potential uses of NIRF dye for tumor localization and quantitative imaging, which would greatly complement existing modalities for the imaging-assisted diagnosis and prognosis of brain tumors. Of note, not all cyanine dyes have tumor-targeting properties despite their structural resemblance to each other. Only heptamethine carbocyanine dyes that have charged side-chain terminal groups and a

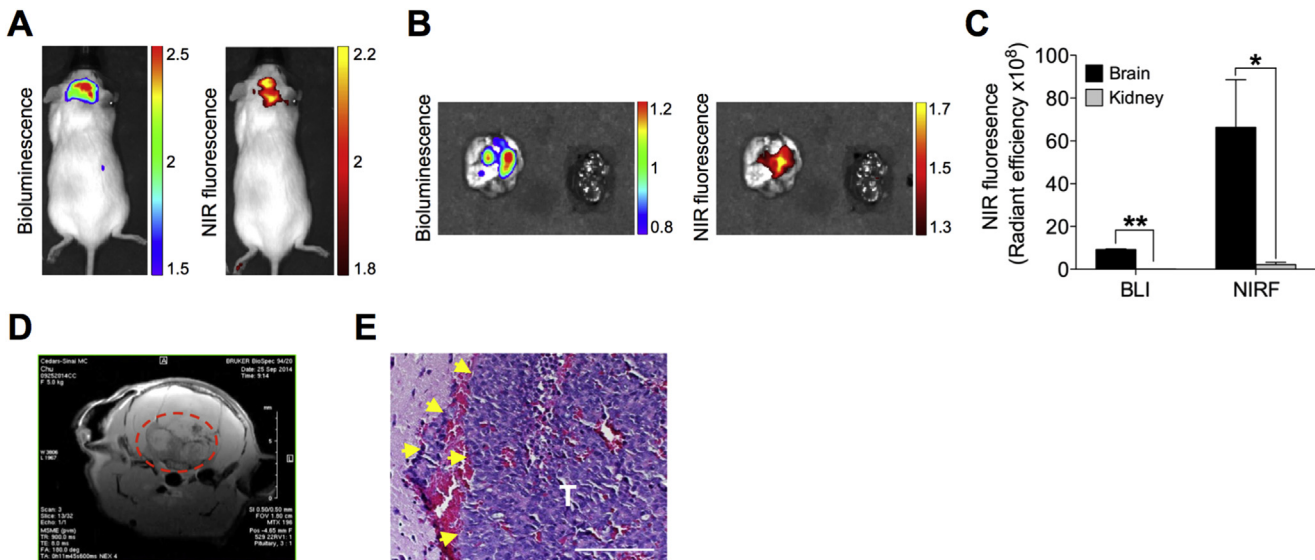


Fig. 6. Uptake and retention of IR-783-gemcitabine dye-drug conjugate (NIRG) in xenograft prostate tumor brain metastases. (A, B) Mice bearing CW22Rv1 prostate tumor brain metastases were subjected to both BLI and NIRF imaging *in vivo* 24 h after NIRG (50 nmol/mouse, *i.p.*) (A). Mouse brain and control kidney were subsequently excised and subjected *ex vivo* to both imaging modalities (B). (C) Quantitative analysis of both BLI and NIRF signal intensity in (B) ($n = 3$, mean \pm SEM). * $p < 0.05$, ** $p < 0.01$. (D) MRI T2 scan of tumor-bearing mouse brain. Tumor area is indicated in red dashed circle. (E) H&E stain of prostate tumor brain metastases (T). Yellow arrows indicate invasive edges. Original magnification, $\times 400$; scale bar: 20 μm .

chlorine atom at the central meso position of the cyclohexyl ring are cancer-specific and able to cross the BBB. In addition, the negative charges owned by IR-783 and its derivative dyes such as MHI-148 by possessing a sulfate or carboxyl group allow these dyes to be efficiently mediated by OATPs for BBB penetration [15,19].

In addition to primary brain tumors, the highly infiltrating nature of glioblastoma and the presence of migratory cells in the infiltration zone protected by the BBB is a major cause of brain tumor lethality in affected patients [1,9]. Conventional surgical methods cannot completely remove these invasive tumor cells outside the tumor bulk largely due to the intraoperative difficulties in delineating the brain tumor margins precisely, which inevitably leads to tumor relapse following surgery [1,48]. Given the high sensitivity and specificity of these NIRF dyes for targeting brain tumor cells at the cellular level (Fig. 1), extending the application of these dyes for assessing brain tumor margins for improved surgical outcomes merits further investigation.

We showed that hypoxia is one of the mechanisms responsible for the preferential uptake of NIRF dye by brain tumor cells (Fig. 4), a result consistent with our previous findings [22]. It is evident that hypoxia generally exists in brain tumors, with the obvious direct evidence being the presence of intratumoral necrosis, which in fact underlies the histological diagnosis of glioblastoma [52]. The hypoxia-mediated dye uptake mechanism may allow these NIRF dyes to target a broad range of brain tumor types despite their heterogeneous nature. One challenge to conventional imaging evaluation for brain tumor diagnosis is the occasional inability to distinguish radiation-induced necrosis or treatment-related pseudoprogression from recurrent high-grade tumor [52,53]. These post-treatment entities that mimic tumor recurrence have been suggested to correlate with treatment-related cellular hypoxia, leading to expression of hypoxia-regulated molecules in tumor and surrounding cells with subsequent increased vascular permeability and increased tumor enhancement [52]. We previously demonstrated a positive correlation between tumor uptake of NIRF dye and the extent of hypoxia using a HIF1 α -dependent luciferase reporter in mice [22,54]. These dyes collectively may be useful for evaluating residual or recurrent live brain tumors following

treatment by measuring the level of tumor hypoxia for improved diagnostic and prognostic accuracy and therapeutic responsiveness.

In addition to hypoxia, we showed that OATPs are another regulatory mechanism mediating NIRF dye uptake by brain tumor cells (Fig. 4). OATPs mediate the transmembrane uptake of amphipathic compounds, including drugs, hormones and other xenobiotics that cannot freely diffuse through cellular membranes, thereby affecting drug disposition and tissue penetration. Recent evidence has implicated altered OATP expressions and variants in many different types of cancers, including OATP1A2 and OATP2B1 in brain cancer [27–29,55]. Their expression in the luminal membrane of endothelial cells forming the BBB and BTB and the following evidence indicating reduced blood-to-brain transport of several agents in mice without *Oatp1a4*, a form corresponding to OATP1A2 in humans, suggest the role of these OATPs in facilitating the NIRF dye to penetrate the barriers and enter brain tumors [30,31]. We have previously demonstrated that tumor cell uptake of these NIRF dyes can be mediated by OATPs, which is further enhanced by tumor hypoxia through the direct upregulation of OATPs by HIF1 α at the transcriptional level, resulting in a concerted effect on increased uptake of NIRF dye by tumor cells [15,19,56,57]. In the present brain tumor study, we showed a similar dye uptake mechanism mediated by OATPs (Figs. 4 and S2), which could be either responsive to hypoxic effects or independent from tumor hypoxia. In agreement with our previous studies, the expression of several OATPs abundant in the BBB/BTB and brain tumor was elevated in brain tumor cells under hypoxia-mimicking conditions, which is further associated with a significant co-expression correlation between HIF1 α and OATP2B1, a representative OATP, in a clinical brain tumor data set (Fig. S3). On the other hand, we showed that pharmacological blockade of OATPs activities by a competitive inhibitor under normoxic conditions was sufficient to inhibit the dye uptake by brain tumor cells (Figs. 4 and S2). Importantly, we demonstrated increased expression of several brain-expressing forms of OATPs in the intracranial U87 tumor relative to nearby normal mouse brain tissue in mice subjected to NIRF imaging, which is consistent with the clinical observation of higher expression of these OATPs in glioblastoma than normal brain tissues (Fig. S3).

These results suggest that even without hypoxia the prevailing activation of OATPs in brain tumors is able to facilitate dye delivery across the BBB/BTB and dye uptake in brain tumors *in vivo*.

We demonstrated the preferential uptake of IR-783 by brain tumors in an intracranial xenograft model as early as 1 h after dye injection (Fig. 3), further with a time-dependent increase in dye uptake at 24 h, suggesting a tumor-attractive distribution of IR-783 in the body. We have previously reported the whole-body distribution of IR-783 dye at a series of time points starting from 0.5 h after dye administration in tumor-bearing mice. In addition to specific retention in tumors, IR-783 was shown to accumulate in liver, kidney, heart, lung and spleen for up to 6 h followed by clearance from these normal organs. However, normal organs displayed very low signals likely to be overshadowed by the more intense signals in tumors during imaging [15]. In addition, the observation of a time-dependent increase in dye uptake in tumors also fits the dye uptake model we demonstrated where IR-783 dye was progressively accumulated in brain tumors, mediated by OATP-based active transport, after the dye was rapidly diffused into the bloodstream and distributed in the whole body by circulation since injection. By contrast, normal organs and tissues retained dyes poorly due in large part to the lack of OATP involvement given the low expression of OATPs, thereby producing marginally detectable focal fluorescence signals by imaging. Increased dye uptake in brain tumors along with time supports an OATP-mediated redistribution of dyes from non-target normal organs to brain tumors in the body.

Chemotherapy is indispensable for brain tumor treatment after surgery [10], but its limited benefits are due to the ineffective delivery of therapeutic agents to the tumor tissues as well as undesired side effects elicited by nonspecific biodistribution [9,10]. In this study, we overcame these problems using NIRF dye as a drug carrier covalently conjugated to chemotherapeutic agents, facilitating the ability of drugs to penetrate the BBB/BTB. Using gemcitabine as an example, we demonstrated the exclusive accumulation of the NIRF conjugate in intracranial human tumors and brain tumor metastases in a human prostate cancer model (Figs. 5 and 6). We showed that NIRF is capable of restricting the growth of intracranial brain tumors and prostate tumor brain metastases and prolonging the survival of mice (Fig. S5). Because NIRF dye and NIRF can accumulate in tumor tissues and cells for a prolonged period due to their extensive interaction with cellular nucleic acids and proteins [58,59], these dyes and dye-drug conjugates could be further explored as promising imaging and targeting agents for the imaging and treatment of primary and metastatic brain tumors.

5. Conclusions

In this study, we demonstrated that NIRF dyes and derivative dye-drug conjugates, such as NIRF, are effective and promising new imaging and targeting agents for the detection and treatment of human brain tumors and brain metastases. The uptake and retention of these agents by brain tumors are mediated by tumor hypoxia and OATPs in the BBB/BTB compartments, and correlated quantitatively with tumor burden in mice. The NIRF dyes and derivative dye-drug conjugates could be developed and further evaluated in men for cancer imaging and targeting.

Acknowledgments

This work was supported by NIH/NCI Grants 2P01CA098912, 1R01CA122602, the Board of Governors Cancer Research Chair, the Steven Spielberg Fund in Prostate Cancer Research, and a Margaret E. Early Medical Research Trust Award (to L.W.K.C.). We thank Mr. Gary Mawyer for editorial assistance.

Appendix A. Supplementary data

Supplementary data related to this article can be found at <http://dx.doi.org/10.1016/j.biomaterials.2015.07.028>.

References

- [1] A. Behin, K. Hoang-Xuan, A.F. Carpentier, J.Y. Delattre, Primary brain tumours in adults, *Lancet* 361 (2003) 323–331.
- [2] M. Wrensch, Y. Minn, T. Chew, M. Bondy, M.S. Berger, Epidemiology of primary brain tumors: current concepts and review of the literature, *Neuro-oncology* 4 (2002) 278–299.
- [3] H.W. Kao, S.W. Chiang, H.W. Chung, F.Y. Tsai, C.Y. Chen, Advanced MR imaging of gliomas: an update, *BioMed Res. Int.* 2013 (2013) 970586.
- [4] T.Z. Wong, G.J. van der Westhuizen, R.E. Coleman, Positron emission tomography imaging of brain tumors, *Neuroimaging Clin. N. Am.* 12 (2002) 615–626.
- [5] A. de la Zerda, S. Bodapati, R. Teed, M.L. Schipper, S. Keren, B.R. Smith, et al., A comparison between time domain and spectral imaging systems for imaging quantum dots in small living animals, *Mol. Imaging Biol. MIB Off. Publ. Acad. Mol. Imaging* 12 (2010) 500–508.
- [6] S.R. Kantelhardt, H. Diddens, J. Leppert, V. Rohde, G. Huttmann, A. Giese, Multiphoton excitation fluorescence microscopy of 5-aminolevulinic acid induced fluorescence in experimental gliomas, *Lasers Surg. Med.* 40 (2008) 273–281.
- [7] S. Agarwal, P. Manchanda, M.A. Vogelbaum, J.R. Ohlfest, W.F. Elmquist, Function of the blood-brain barrier and restriction of drug delivery to invasive glioma cells: findings in an orthotopic rat xenograft model of glioma, *Drug Metab. Dispos. Biol. Fate Chem.* 41 (2013) 33–39.
- [8] D.R. Groothuis, The blood-brain and blood-tumor barriers: a review of strategies for increasing drug delivery, *Neuro-oncology* 2 (2000) 45–59.
- [9] S. Agarwal, R. Sane, R. Oberoi, J.R. Ohlfest, W.F. Elmquist, Delivery of molecularly targeted therapy to malignant glioma, a disease of the whole brain, *Expert Rev. Mol. Med.* 13 (2011) e17.
- [10] H.C. Lawson, P. Sampath, E. Bohan, M.C. Park, N. Hussain, A. Olivi, et al., Interstitial chemotherapy for malignant gliomas: the Johns Hopkins experience, *J. Neuro-oncol.* 83 (2007) 61–70.
- [11] G. Gu, X. Gao, Q. Hu, T. Kang, Z. Liu, M. Jiang, et al., The influence of the penetrating peptide iRGD on the effect of paclitaxel-loaded MT1-AF7p-conjugated nanoparticles on glioma cells, *Biomaterials* 34 (2013) 5138–5148.
- [12] B. Zhang, X. Sun, H. Mei, Y. Wang, Z. Liao, J. Chen, et al., LDLR-mediated peptide-22-conjugated nanoparticles for dual-targeting therapy of brain glioma, *Biomaterials* 34 (2013) 9171–9182.
- [13] J. Wu, D. Pan, L.W. Chung, Near-infrared fluorescence and nuclear imaging and targeting of prostate cancer, *Transl. Androl. Urol.* 2 (2013) 254–264.
- [14] E.M. Sevick-Muraca, Translation of near-infrared fluorescence imaging technologies: emerging clinical applications, *Annu. Rev. Med.* 63 (2012) 217–231.
- [15] X. Yang, C. Shi, R. Tong, W. Qian, H.E. Zhau, R. Wang, et al., Near IR heptamethine cyanine dye-mediated cancer imaging, *Clin. Cancer Res. Off. J. Am. Assoc. Cancer Res.* 16 (2010) 2833–2844.
- [16] X. Yang, C. Shao, R. Wang, C.Y. Chu, P. Hu, V. Master, et al., Optical imaging of kidney cancer with novel near infrared heptamethine carbocyanine fluorescent dyes, *J. Urol.* 189 (2013) 702–710.
- [17] C. Shi, J.B. Wu, G.C. Chu, Q. Li, R. Wang, C. Zhang, et al., Heptamethine carbocyanine dye-mediated near-infrared imaging of canine and human cancers through the HIF-1 α /OATPs signaling axis, *Oncotarget* 5 (2014) 10114–10126.
- [18] J.B. Wu, T.P. Lin, J.D. Gallagher, S. Kushal, L.W. Chung, H.E. Zhau, et al., Monoamine oxidase A inhibitor-near-infrared dye conjugate reduces prostate tumor growth, *J. Am. Chem. Soc.* 137 (2015) 2366–2374.
- [19] J.B. Wu, C. Shao, X. Li, C. Shi, Q. Li, P. Hu, et al., Near-infrared fluorescence imaging of cancer mediated by tumor hypoxia and HIF1 α /OATPs signaling axis, *Biomaterials* 35 (2014) 8175–8185.
- [20] Q. Xu, X. Yuan, P. Tunici, G. Liu, X. Fan, M. Xu, et al., Isolation of tumour stem-like cells from benign tumours, *Br. J. Cancer* 101 (2009) 303–311.
- [21] J. Xu, R. Wang, Z.H. Xie, V. Odero-Marab, S. Pathak, A. Multani, et al., Prostate cancer metastasis: role of the host microenvironment in promoting epithelial to mesenchymal transition and increased bone and adrenal gland metastasis, *Prostate* 66 (2006) 1664–1673.
- [22] J.B. Wu, C. Shao, X. Li, C. Shi, Q. Li, P. Hu, et al., Near-infrared fluorescence imaging of cancer mediated by tumor hypoxia and HIF1 α /OATPs signaling axis, *Biomaterials* 35 (28) (2014) 8175–8185.
- [23] K.J. Livak, T.D. Schmittgen, Analysis of relative gene expression data using real-time quantitative PCR and the 2(-Delta Delta C(T)) method, *Methods* 25 (2001) 402–408.
- [24] M. Bredel, C. Bredel, D. Juric, G.R. Harsh, H. Vogel, L.D. Recht, et al., Functional network analysis reveals extended gliomagenesis pathway maps and three novel MYC-interacting genes in human gliomas, *Cancer Res.* 65 (2005) 8679–8689.
- [25] L. Sun, A.M. Hui, Q. Su, A. Vortmeyer, Y. Kotliarov, S. Pastorino, et al., Neuronal and glioma-derived stem cell factor induces angiogenesis within the brain, *Cancer Cell* 9 (2006) 287–300.
- [26] P. Vajkoczy, M.D. Menger, Vascular microenvironment in gliomas, *Cancer*

- Treat. Res. 117 (2004) 249–262.
- [27] A. Obaidat, M. Roth, B. Hagenbuch, The expression and function of organic anion transporting polypeptides in normal tissues and in cancer, *Annu. Rev. Pharmacol. Toxicol.* 52 (2012) 135–151.
- [28] A. Bhowmik, R. Khan, M.K. Ghosh, Blood brain barrier: a challenge for effectual therapy of brain tumors, *BioMed Res. Int.* 2015 (2015) 320941.
- [29] M. Roth, A. Obaidat, B. Hagenbuch, OATPs, OATs and OCTs: the organic anion and cation transporters of the SLCO and SLC22A gene superfamilies, *Br. J. Pharmacol.* 165 (2012) 1260–1287.
- [30] H. Bronger, J. König, K. Kopplow, H.H. Steiner, R. Ahmadi, C. Herold-Mende, et al., ABC drug efflux pumps and organic anion uptake transporters in human gliomas and the blood-tumor barrier, *Cancer Res.* 65 (2005) 11419–11428.
- [31] A. Ose, H. Kusuhara, C. Endo, K. Tohyama, M. Miyajima, S. Kitamura, et al., Functional characterization of mouse organic anion transporting peptide 1a4 in the uptake and efflux of drugs across the blood-brain barrier, *Drug Metab. Dispos. Biol. Fate Chem.* 38 (2010) 168–176.
- [32] X. Lu, Y. Kang, Hypoxia and hypoxia-inducible factors: master regulators of metastasis, *Clin. Cancer Res. Off. J. Am. Assoc. Cancer Res.* 16 (2010) 5928–5935.
- [33] J.B. Wu, C. Shao, X. Li, Q. Li, P. Hu, C. Shi, et al., Monoamine oxidase A mediates prostate tumorigenesis and cancer metastasis, *J. Clin. Invest.* 124 (2014) 2891–2908.
- [34] X.M. Tao, J.C. Wang, J.B. Wang, Q. Feng, S.Y. Gao, L.R. Zhang, et al., Enhanced anticancer activity of gemcitabine coupling with conjugated linoleic acid against human breast cancer in vitro and in vivo, *Eur. J. Pharm. Biopharm. Off. J. Arbeitsgemeinschaft Pharm. Verfahrenstechnik eV* 82 (2012) 401–409.
- [35] Z. Daman, S. Ostad, M. Amini, K. Gilani, Preparation, optimization and in vitro characterization of stearoyl-gemcitabine polymeric micelles: a comparison with its self-assembled nanoparticles, *Int. J. Pharm.* 468 (2014) 142–151.
- [36] R.P. Abratt, W.R. Bezwoda, G. Falkson, L. Goedhals, D. Hacking, T.A. Rugg, Efficacy and safety profile of gemcitabine in non-small-cell lung cancer: a phase II study, *J. Clin. Oncol. Off. J. Am. Soc. Clin. Oncol.* 12 (1994) 1535–1540.
- [37] H.A. Burris 3rd, M.J. Moore, J. Andersen, M.R. Green, M.L. Rothenberg, M.R. Modiano, et al., Improvements in survival and clinical benefit with gemcitabine as first-line therapy for patients with advanced pancreas cancer: a randomized trial, *J. Clin. Oncol. Off. J. Am. Soc. Clin. Oncol.* 15 (1997) 2403–2413.
- [38] J. Carmichael, K. Possinger, P. Phillip, M. Beykirch, H. Kerr, J. Walling, et al., Advanced breast cancer: a phase II trial with gemcitabine, *J. Clin. Oncol. Off. J. Am. Soc. Clin. Oncol.* 13 (1995) 2731–2736.
- [39] L.W. Hertel, G.B. Boder, J.S. Kroin, S.M. Rinzler, G.A. Poore, G.C. Todd, et al., Evaluation of the antitumor activity of gemcitabine (2',2'-difluoro-2'-deoxycytidine), *Cancer Res.* 50 (1990) 4417–4422.
- [40] L.J. Ostruszka, D.S. Shewach, The role of DNA synthesis inhibition in the cytotoxicity of 2',2'-difluoro-2'-deoxycytidine, *Cancer Chemother. Pharmacol.* 52 (2003) 325–332.
- [41] J. Sigmund, R.J. Honeywell, T.J. Postma, C.M. Dirven, S.M. de Lange, K. van der Born, et al., Gemcitabine uptake in glioblastoma multiforme: potential as radiosensitizer, *Ann. Oncol. Off. J. Eur. Soc. Med. Oncol. ESMO* 20 (2009) 182–187.
- [42] T.L. Evans, J.H. Kim, F.A. Shepherd, K.N. Syrigos, K. Udud, V. Chubenko, et al., Cabazitaxel (Cbz) versus topotecan in patients (pts) with small cell lung cancer (SCLC) that has progressed during or after first-line treatment with platinum-based chemotherapy: A randomized phase II study, *J. Clin. Oncol. Off. J. Am. Soc. Clin. Oncol.* 31 (2013).
- [43] M. Preusser, A.S. Berghoff, D. Schandendorf, N.U. Lin, R. Stupp, Brain metastasis: opportunity for drug development? *Curr. Opin. Neurol.* 25 (2012) 786–794.
- [44] J. Seoane, L. De Mattos-Arruda, Brain metastasis: new opportunities to tackle therapeutic resistance, *Mol. Oncol.* 8 (2014) 1120–1131.
- [45] J.M. Drake, C.L. Gabriel, M.D. Henry, Assessing tumor growth and distribution in a model of prostate cancer metastasis using bioluminescence imaging, *Clin. Exp. Metastasis* 22 (2005) 674–684.
- [46] E. Allard, C. Passirani, J.P. Benoit, Convection-enhanced delivery of nano-carriers for the treatment of brain tumors, *Biomaterials* 30 (2009) 2302–2318.
- [47] A.D. Norden, J. Drappatz, P.Y. Wen, Antiangiogenic therapies for high-grade glioma, *Nat. Rev. Neurol.* 5 (2009) 610–620.
- [48] M.F. Kircher, A. de la Zerdá, J.V. Jokerst, C.L. Zavaleta, P.J. Kempen, E. Mittra, et al., A brain tumor molecular imaging strategy using a new triple-modality MRI-photoacoustic-Raman nanoparticle, *Nat. Med.* 18 (2012) 829–834.
- [49] M. Hintersteiner, A. Enz, P. Frey, A.L. Jatón, W. Kinzy, R. Kneuer, et al., In vivo detection of amyloid-beta deposits by near-infrared imaging using an oxazine-derivative probe, *Nat. Biotechnol.* 23 (2005) 577–583.
- [50] V. Humblet, R. Lapidus, L.R. Williams, T. Tsukamoto, C. Rojas, P. Majer, et al., High-affinity near-infrared fluorescent small-molecule contrast agents for in vivo imaging of prostate-specific membrane antigen, *Mol. Imaging* 4 (2005) 448–462.
- [51] X. Wu, H. Liu, J. Liu, K.N. Haley, J.A. Treadway, J.P. Larson, et al., Immunofluorescent labeling of cancer marker Her2 and other cellular targets with semiconductor quantum dots, *Nat. Biotechnol.* 21 (2003) 41–46.
- [52] R.L. Jensen, Brain tumor hypoxia: tumorigenesis, angiogenesis, imaging, pseudoprogression, and as a therapeutic target, *J. Neuro-oncol.* 92 (2009) 317–335.
- [53] I.F. Parney, S. Kunwar, M. McDermott, M. Berger, M. Prados, S. Cha, et al., Neuroradiographic changes following convection-enhanced delivery of the recombinant cytotoxin interleukin 13-PE38QQR for recurrent malignant glioma, *J. Neurosurg.* 102 (2005) 267–275.
- [54] H. Harada, S. Kizaka-Kondoh, S. Itasaka, K. Shibuya, A. Morinibu, K. Shinomiya, et al., The combination of hypoxia-response enhancers and an oxygen-dependent proteolytic motif enables real-time imaging of absolute HIF-1 activity in tumor xenografts, *Biochem. Biophys. Res. Commun.* 360 (2007) 791–796.
- [55] V. Buxhofer-Ausch, L. Secky, K. Wlcek, M. Svoboda, V. Kounnis, E. Briasoulis, et al., Tumor-specific expression of organic anion-transporting polypeptides: transporters as novel targets for cancer therapy, *J. Drug Deliv.* 2013 (2013) 863539.
- [56] S. Han, K. Kim, N. Thakkar, D. Kim, W. Lee, Role of hypoxia inducible factor-1alpha in the regulation of the cancer-specific variant of organic anion transporting polypeptide 1B3 (OATP1B3), in colon and pancreatic cancer, *Biochem. Pharmacol.* 86 (2013) 816–823.
- [57] B.J. Thompson, L. Sanchez-Covarrubias, L.M. Slosky, Y. Zhang, M.L. Laracuate, P.T. Ronaldson, Hypoxia/reoxygenation stress signals an increase in organic anion transporting polypeptide 1a4 (Oatp1a4) at the blood-brain barrier: relevance to CNS drug delivery, *J. Cereb. Blood Flow Metab. Off. J. Int. Soc. Cereb. Blood Flow Metab.* 34 (2014) 699–707.
- [58] H. Ihmels, L. Thomas, Light up G-quadruplex DNA with a [2.2.2]heptamethinecyanine dye, *Org. Biomol. Chem.* 11 (2013) 480–487.
- [59] K.D. Volkova, V.B. Kovalska, A.O. Balanda, R.J. Vermeij, V. Subramaniam, Y.L. Slominskii, et al., Cyanine dye-protein interactions: looking for fluorescent probes for amyloid structures, *J. Biochem. Biophys. Methods* 70 (2007) 727–733.